UNIVERSITÀ DEGLI STUDI DI MILANO

Scuola di Dottorato in Fisica, Astrofisica e Fisica Applicata
Dipartimento di Fisica

Corso di Dottorato in Fisica, Astrofisica e Fisica Applicata
Ciclo XXVI

Advances in models of Pulsar Glitches

Settore Scientifico Disciplinare FIS/05

Supervisore: Professor Pierre M. PIZZOCHERO

Coordinatore: Professor Marco BERSANELLI

Tesi di Dottorato di:
Stefano L. SEVESO

Anno Accademico 2014

Commission of the final examination:

External Referee:
Professor Jose A. Pons, Universitat d'Alacant, Departament de Fisica Aplicada

External Member:
Professor Valeria Ferrari, Università di Roma La Sapienza, Dipartimento di Fisica

External Member:
Professor Nicolas Chamel, Université Libre de Bruxelles, Institute of Astronomy and Astrophysics

Final examination:

Tuesday, January 20, 2015

Università degli Studi di Milano, Dipartimento di Fisica, Milano, Italy

A Daniela, Michela ed Eleonora
...ovviamente...

MIUR subjects:

FIS/05 - Astronomia e Astrofisica

PACS:

97.60.Gb	Pulsars
97.60.Jd	Neutron stars
26.60.-c	Nuclear matter aspects of neutron stars

Keywords: neutron stars, pulsars, glitch, Vela Pulsar, B0833-45, superfluidity, superconductivity, snowplow model, neutron stars masses, pinning force, flux-tube, drag force, mutual friction, dynamical model, two-fluids model

Contents

List of Figures

List of Tables

CHAPTER 1

Introduction

Neutron stars are surely one of the most interesting astronomical objects: in no other place of the observable universe, in fact, matter is so compressed that the density reaches and overcomes the nuclear saturation value. This is a such extreme condition that in no terrestrial laboratory we can directly reproduce it in order to study its properties. Neutron stars are therefore a very fascinating research field that can bring us to a deeper understanding of this exotic matter, by modeling the observations of peculiar phenomena related to these stars. In this work we focus on the *pulsar glitches*, which are rapid jumps in the rotation velocity of the star. Even if pulsars are known to be very stable clocks, many of them show sudden increase in their spin frequency that are instantaneous to the accuracy of the data.

To date several hundreds of glitches have been detected, with relative increases in the spin frequency ν that range from as low as $\Delta\nu/\nu \approx 10^{-11}$ to $\Delta\nu/\nu \approx 10^{-5}$. In particular a class of pulsars, of which the Vela pulsar is the prototype, exhibit what are known as "giant" glitches (Espinoza et al., 2011), large steps in the spin frequency ($\Delta\nu/\nu \approx 10^{-6}$) which are accompanied by an increase in the spindown rate $\dot{\nu}$ and exhibit a rough periodicity in their recurrence rate (for example giant glitches in the Vela occur roughly every three years).

Shortly after the first glitches were observed it was suggested that they could be due to a superfluid component in the stellar interior, weakly coupled to the normal component and to the electromagnetic emission, that could store angular momentum and then release it catastrophically, giving rise to a glitch (Baym et al., 1969; Anderson and Itoh, 1975; Alpar, 1977; Alpar et al., 1984b). Large scale superfluid components are, in fact, expected in neutron star interiors on theoretical grounds. The qualitative picture can be explained by considering that a superfluid rotates by forming an array of quantized vortexes which carry the circulation of the fluid. In the NS crust the vortexes can be strongly attracted, "pinned", to the nuclear lattice (Pines et al., 1980; Anderson et al., 1982) and cannot move outward. If the superfluid cannot remove vortexes it cannot spin down and it therefore acts as an angular momentum reservoir. As the crust spins down due to electromagnetic emission a lag will develop between the superfluid and the normal component, leading to a hydrodynamical lift force (Magnus force) acting on the vortexes. Eventually when the lag reaches a critical value the pinning force will no longer be able to contrast the hydrodynamical lift and the vortexes will unpin, transferring their angular momentum to the crust and giving rise to a glitch.

Although there is some evidence that smaller glitches in young active pulsars (like Crab) may be related to crust quakes, there is a growing consensus that the basic idea outlined above can be used to describe the main features of pulsar glitches. In this work we want to propose models which implement the superfluid framework realistically in order to reproduce the physical observable parameters of the event.

The picture outlined above indicates that the problem must be faced by merging results which come from the microphysics point of view into a more macroscopic simulation. Our research has been developed in parallel on these complementary aspects and the structure of the thesis reflects this approach. After the introductory **Chapter 2**, where we review the background concepts on which the models are built (superfluidity, hydrostatic equilibrium, TOV integration, stellar structure, entrainment), contents are divided in three main parts, described here.

Part I The first part of the thesis is focused on the microphysical ingredients of the problem, in particular on the pinning interaction. One of the main difficulties in performing calculations about glitches is the relative scarcity of realistic estimate of the pinning force between vortexes and nuclei, addressed on the *mesoscopic* scale. Although some authors have performed realistic calculations of the interaction between a vortex and a single nucleus of the lattice, the evaluation of the pinning force per unit length haven't been tackled deeply, and some work is required to fill this gap. In this part we propose our averaging procedure that allow us to move from the pinning per site towards the force over the whole vortex, which is the relevant quantity of the superfluid models. We call this approach "mesoscopic" because it's the fundamental bridge which brings our knowledge about nuclear physics into a macroscopic model of glitches.

Chapter 3 In this chapter we use the vortex–site interaction results of Donati and Pizzochero (2004, 2006) to propose the first realistic estimate of the pinning force per unit length in the inner crust of a neutron star. We take into account all possible vortex–lattice orientations and we obtain a force $f_{\rm crust} \sim 10^{15}$ dyn/cm, nearly two orders of magnitude less than previous naive estimates.

Chapter 4 If protons in the interior of NS are in a type II superconducting state, an interaction between magnetic flux tubes and rotational vortexes is possible and must be estimated (in case of type I superconductivity the interactions are much weaker). The same qualitative approach used for the crust is adopted also in this chapter to perform a calculation of the pinning interaction per unit length in the core of a neutron star. Our results indicate that even if the superconductivity is of type II, the interaction between vortexes and flux tubes will be significantly weaker than in the crust, because the force per unit length is $f_{\text{core}} \sim 10^{12}$–$10^{13}$ dyn/cm.

Part II The second part of the thesis is focused on static models of pulsar glitches, in particular the *snowplow* model. The pinning profiles of chapter 3 are implemented, together with spherical geometry and realistic background, in a macroscopic model that provides interesting hints about the interior of neutron stars.

Chapter 5 In this chapter the *snowplow* model of Pizzochero (2011) is implemented using realistic equations of state and therefore realistic density profiles for the pulsars. In this chapter we don't consider a pinning interaction in the core, thanks to the results of chapter 4. The main goal is to reproduce the typical order of magnitude of the observable quantities that are relevant in a giant glitch. The model described naturally explains the angular momentum storing mechanism that is responsible of the glitch, with minimal assumptions on the dynamic of vortexes. We find that the results are in agreement with observations and support the outcome of chapter 3 ($f_{\text{crust}} \sim 10^{15}$ dyn/cm).

Chapter 6 Even if the results of chapter 4 indicates that the pinning in the core of a pulsar is negligible, in this chapter we try to estimate with the *snowplow* model (with realistic physical inputs) what happens if a variable fraction of vorticity is blocked in the core by a strong pinning–like interaction. By comparing the results of the model with the observational data of the Vela 2000 glitch (step in frequency and in frequency derivative), we have constrained the pinned fraction of the core superfluid. Our conclusion is that both quantities cannot be fitted if a considerable fraction of vorticity is blocked: this means that either most of the core is a type I superconductor or the vortex/flux–tube interaction is very weak, in agreement with the mesoscopic result of chapter 4.

Chapter 7 Although there is still considerable debate on the real nature of the "trigger" of a glitch and several mechanisms have been proposed, we can anyway use the snowplow model to evaluate the amount of the angular momentum exchange as a function of the interglitch time between two events. By including also the entrainment in our calculations, this approach let us to fit well the observational data and infer the masses of the most frequent glitching stars. The model proposed in this chapter gives a unified description of the glitch phenomenon both for small and large glitchers and indicates an interesting correlation between mass and glitching strength.

Part III The last part of the thesis is focused on the development of dynamical model which can follow the whole time evolution of this phenomenon. We implement the multi–fluids formalism developed by Prix (2004); Andersson and Comer

(2006) in a consistent computer code, following the same approach of Haskell et al. (2012c), but using also realistic equations of state and the pinning profiles obtained in chapter 3. Moreover the entrainment effect is fully included in the model together with the most realistic benchmarks for the mutual friction between the components.

Chapter 8 In this chapter we derive the required formalism and describe in detail all physical ingredients of the model, like pinning, drag forces and entrainment, and how these inputs are encoded in the simulations.

Chapter 9 The results of the simulations are presented in this last chapter. The model allows us to study both the rise of a glitch and the recovery phase and analyze the dependency of these behaviors on the drag parameters used in the calculation. We perform a parameter study for the relevant physical quantities in order to understand more deeply all the aspects of this phenomenon. We also compare our simulations with the observational data of the frequent glitchers in order to estimate the masses of the pulsars. It's noteworthy the fact that the results are in good agreement with the ones of chapter 7, showing again the same mass–glitching strength relation.

CHAPTER **2**

Background concepts for superfluid glitch models

Neutron stars are commonly classified by the modern astrophysics as “compact object” for their exceptional density. If we look at the macroscopic characteristics we can immediately understand how strange these stars are. A typical neutron star in fact has a mass of the order of $(1 \div 2)\,\mathrm{M}_\odot$ but its radius is 10^5 times smaller (only about 10 km): this results in a very high central density that overcomes the value of the nuclear density $\rho_0 = 2.8\,\mathrm{g\ cm}^{-3}$, unreachable in any other place of the universe.

To construct models of pulsar glitches we must know the properties of matter at these densities: in other words we must have a valid equation of state that can be integrated to obtain the density profile inside the star. The high density is also responsible of the presence of superfluid matter inside the core of the star: this fact is very important for us because in this work we will focus on models that use precisely the superfluidity to explain the *glitch* phenomenon.

2.1 Neutron stars formation

The formation of a NS can be considered the last step of the entire evolution of a normal star that begins with its formation from a gas cloud. If the mass of this gas reaches a critical value, the conditions for the existence of a self–gravitating object are satisfied and the protostar begins its life. The Big Bang has produced a universe composed mainly by hydrogen (75%) and helium (25%) so we can consider that the cloud has the same composition. We have

$$E_G = -\frac{GM^2}{R} \qquad\qquad E_K = \frac{3}{2} N k_b T \tag{2.1}$$

where E_G is the gravitational energy of the cloud and E_K is the kinetic energy (assuming an ideal gas). In these equations M is the total mass involved in the process, R its

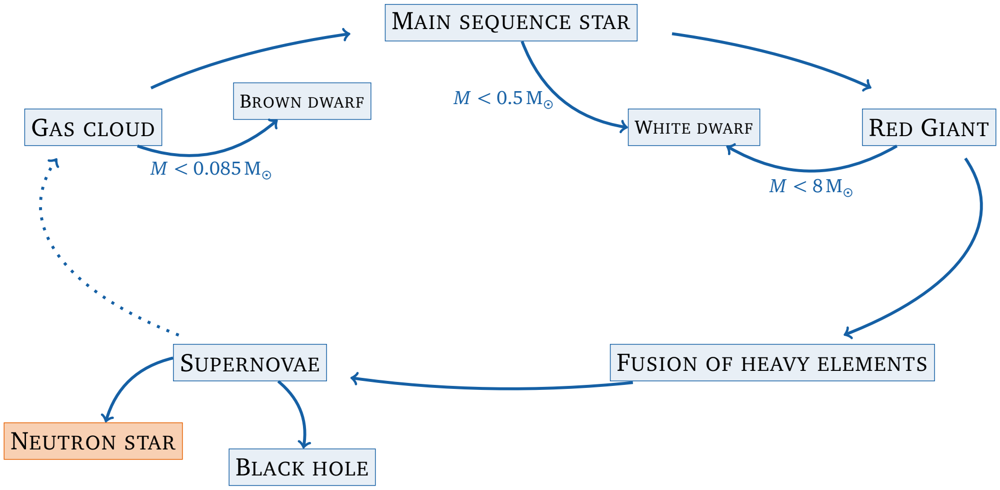

Figure 2.1: Diagram of the typical stellar evolution: the initial mass controls the entire life of a star. The neutron star is a possible final phase if the core mass is below of the critical value for the black hole collapse.

radius and T the temperature. The crucial condition for the star formation is that $|E_G| > E_K$ that lead us to the following critical values:

$$M > M_J \equiv \frac{3k_bTR}{2Gm} \tag{2.2}$$

$$R < R_J \equiv \frac{2GmM}{3k_b} \tag{2.3}$$

$$\rho > \rho_J \equiv \frac{3}{4\pi M^2}\left(\frac{3k_bT}{2Gm}\right)^2 \tag{2.4}$$

These values are commonly know as the Jeans' mass, radius and density.

If these conditions are met, there is a first phase of free collapse due to the fact that the loss in gravitational energy is used in the dissociation of the hydrogen molecules ($H_2 + \gamma \rightarrow H + H$) and in the following ionization of the atoms ($H + \gamma \rightarrow H^+ + e^-$). When the hydrogen is totally ionized, the hydrostatic equilibrium condition is reached and the protostar phase is completed. If the involved mass if above the threshold of $0.08\,\mathrm{M}_\odot$ the internal temperature of the object (which increase during the collapse) is enough to trigger nuclear fusion reactions. The longer phase of the life of the star begins now, and it's characterized by the conversion of hydrogen in helium: the star is said to be in "main sequence". When the core exhausts the reservoir of hydrogen, the star begins to evolve in order to restore the equilibrium: the outer envelope expands, while the inner part compresses as a consequence of the reduction of the rate of nuclear reaction; therefore the temperature rise triggers the fusion of helium in heavier nuclei bringing the star into a new burning phase. The whole life of the star is determined by the initial mass: if it's above the threshold of $\approx 8\,\mathrm{M}_\odot$ the process repeats several times, using each time the product of the previous phase, until the core of the star is made up of iron (if the initial mass is below the threshold, the star becomes a white dwarf, sustained by the electron degeneracy pressure). At this point, no nuclear reaction is energetically favorable and the core collapses in a hot, dense, neutron rich sphere of about 30 km, thanks to a fast neutronization process which produces a very high flux of neutrinos. This collapse is eventually halted by the short range nuclear force, while the outer parts of the star are involved in the process known as supernovae explosion.

Neutron stars are one possible end point of this evolution, when the remaining core is not too massive to overcome the neutron degeneracy pressure and becoming a black hole. This threshold is $M_{\max}$ and is about $2\,\mathrm{M}_\odot$; we will discuss this aspect later. The process described explains the name given to these objects: thanks to the inverse β–reactions most of protons and electrons are transformed in neutrons which form a high density degenerate gas.

2.2 Stellar structure

In this work we are interested in the glitch phenomenon that schematically is the exchange of angular momentum between the superfluid part of the star and the normal one (this aspect will be covered deeply later, see section 2.3). Is therefore important to calculate precisely the moment of inertia of the star and the distribution of matter (normal and superfluid) inside the compact object: in other words we must know the stellar structure.

The first step is to consider the *hydrostatic equilibrium* of the star. A neutron star doesn't collapse on itself and this means that exists a balance between the pressure and the gravitational force, in every point on the star. If we look at the figure section 2.2 we can see that a generic dV element at distance r from the center is subjected to a gravitational acceleration that can be written as

$$g(r) = \frac{G}{r^2}\int_0^r 4\pi r'^2 \rho(r')dr' \tag{2.5}$$

due to the fact that, for the Gauss theorem, the gravitational attraction in spherical symmetry at distance r is given only by the enclosed mass; here in fact $\rho(r)$ is the matter density. On the other hand, the force consequent to the pressure P acting of the element is

$$F_p(r) = P(r+dr)dA - P(r)dA = dA\left(\frac{dP}{dr}\right) = \frac{dP}{dr}dV \tag{2.6}$$

that produce an acceleration

$$a_p(r) = \frac{dP}{dr}\frac{dV}{dm} = \frac{1}{\rho(r)}\frac{dP}{dr} \tag{2.7}$$

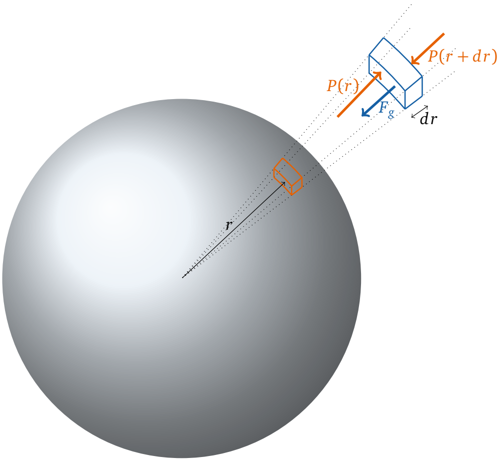

Figure 2.2: Schematic representation of the forces involved in the hydrostatic equilibrium: the gravitational force is balanced by the pressure inside the star.

The condition that the resulting force must be null leads us to the equation of the hydrostatic equilibrium in the newtonian case:

$$\frac{dP}{dr}(r) = -\rho(r)\frac{Gm(r)}{r^2} \tag{2.8}$$

2.2.1 TOV equations

Until now we have ignored the relativistic effects on the gravitational force. Anyway for a neutron star $GM/R \approx 0.2c^2$ and therefore these aspects must be taken into account. A full relativistic analysis of the hydrostatic equilibrium has been done by Tollman, Oppenheimer and Volkoff with the following set of equations (known as the *TOV equations*):

$$\frac{dm(r)}{dr} = 4\pi r^2 \rho(r) \tag{2.9}$$

$$\frac{d\phi(r)}{dr} = \left(\frac{Gm(r)}{r^2} + 4\pi G r\,\frac{P(r)}{c^2}\right)\left(1 - \frac{2Gm(r)}{c^2 r}\right)^{-1} \tag{2.10}$$

$$\frac{dP(r)}{dr} = -\left(\rho(r) + \frac{P(r)}{c^2}\right)\frac{d\phi}{dr}, \tag{2.11}$$

where $m(r)$ is the mass contained in a sphere of radius r, $\rho(r)$ is the density profile and $P(r)$ is the pressure. As already said, these differential equations model the hydrostatic equilibrium inside the star with relativistic approach and, of course, require the $P(\rho(r))$ function. The last two equations can be combined in one that gives an expression for the mass and pressure derivatives and the system can be solved with valid initial conditions. We obtain the functions that describe the star with the fourth–order Runge–Kutta method, starting at $r = 0$ with $m(0) = 0$ and $\rho(0) = \rho_c$, for a valid choice of the central density ρ_c. The integration stops when we reach the condition $\rho(R) = 10^{-8}\rho_c$ and we take R as the radius of the star. Of course the mass of the star is $M = m(R)$.

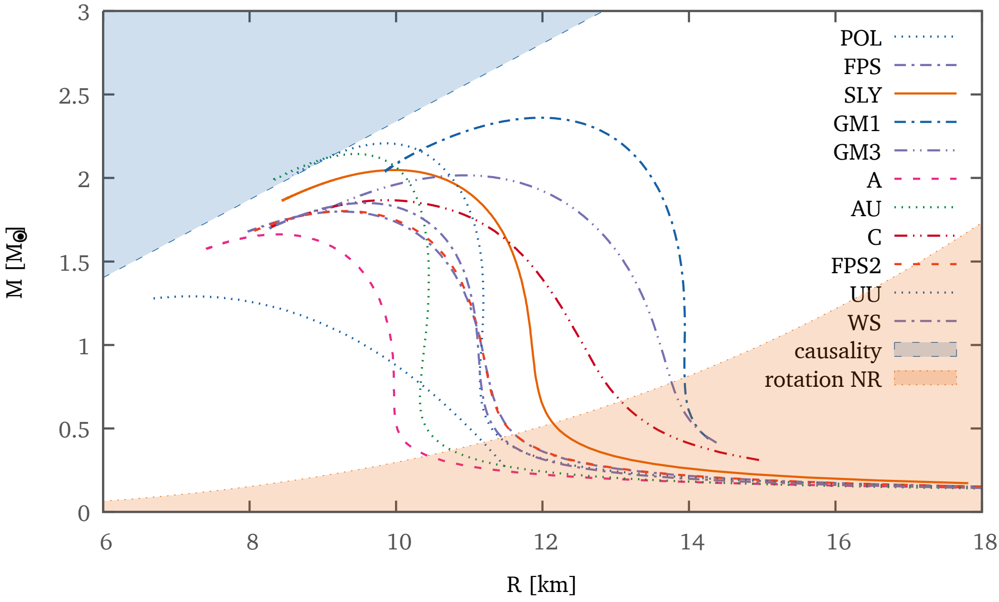

Figure 2.3: Mass–radius relation for different equations of state. Each EoS implies a precise value of the maximum mass for a neutron star. In this work we will consider SLy (moderate) and the stiffer GM1. References for the other EoSs can be found at `http://www.gravity.phys.uwm.edu/rns/source/eos/`

2.2.2 EoS and integration of TOV equations

The function $P(\rho(r))$ is called the equation of state (EoS) because is the relation between pressure and density and it is therefore linked to the microphysic at the typical densities of a NS. The formulation of a realistic EoS is a very challenging task, especially at so high densities: we cannot conduct an experiment to measure the pressure for such values of ρ. This means that an EoS is the result of a theoretical model about the microscopic nature of matter and depends strongly on the assumptions used. In literature there are many EoS and each one results in a different mass–radius $M(R)$ relation as we can see in fig. 2.3 This figure clearly identifies also the presence of a limit for the mass for a neutron star. The existence of a maximum mass M_{max} is an effect of the relativistic nature of the TOV equations, where pressure contributes to the gravitational field: above the critical value, the pressure required to contrast the collapse increases, in turn, the field and the object became a black hole (moreover the EoS can't violate causality requirement, as showed by the upper shaded region of fig. 2.3: the speed of sound must be less then the speed of light). Of course M_{max} depends on the EoS: a stiffer equation of state gives a higher M_{max}. The evidence of the existence of a $2\,\mathrm{M}_\odot$ neutron star (Demorest et al., 2010) allows, in fact, to reject soft equations of state that predict a maximum mass below this value. The fig. 2.3

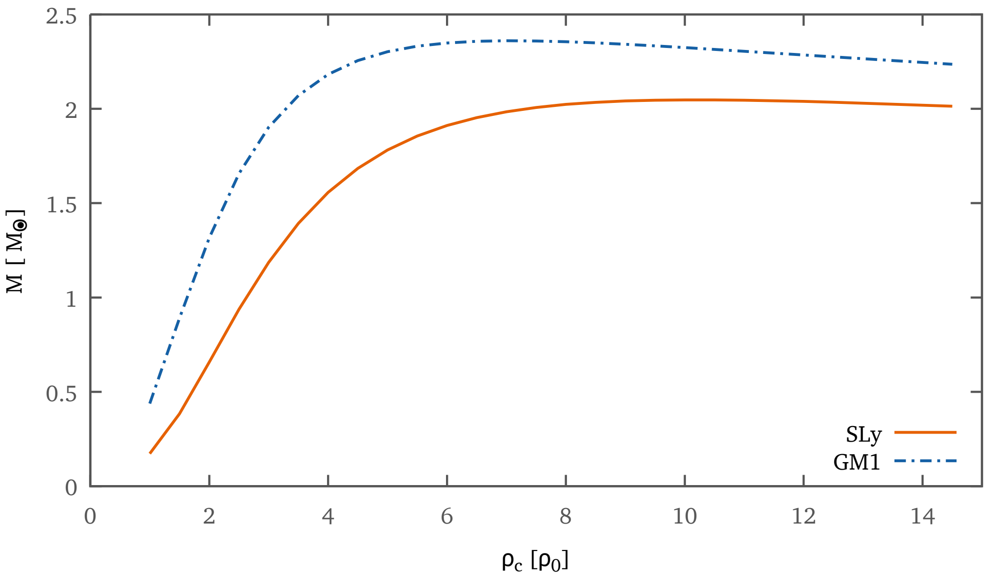

Figure 2.4: This plot shows the mass–central density relation for the EoSs considered. As expected, we find a maximum mass value above $2\,\mathrm{M}_\odot$ for each equation of state (see table 2.1).

indicates that there is a minimum mass for a neutron star (lower shaded region): below this limit the gravitational attraction is not enough to resist to the centrifugal force.

Therefore we have decided to use these two different EoSs:

1. SLy (Douchin and Haensel, 2001) is a moderate EoS, based on a non–relativistic parametrisation; this equation describes the whole star with a single analytical expression and so it is more convenient to integrate;

2. GM1 by Glendenning and Moszkowski (1991) is a stiff $P(\rho)$ relation that is very similar to SLy in the crust of star, but not in the core due to different microscopic approach used to describe hadrons at densities higher than ρ_0.

The fig. 2.4 shows the relation between the central density chosen as the initial condition for the TOV integration and the resulting final mass, showing again the existence of a limit mass M_{max} (see table 2.1 for numerical details). Considering two stars with the same total mass M, we can see in fig. 2.5 how the choice EoS affect the resulting star obtained after the TOV integration: the stiffer EoS (GM1) requires a lower central density and produce a larger radius. In this work we consider stars with masses from $1\,\mathrm{M}_\odot$ to M_{max}.

The interior of a neutron star can be divided in three shell shaped regions, each one characterized by a different composition. The outermost layer is called the *outer*

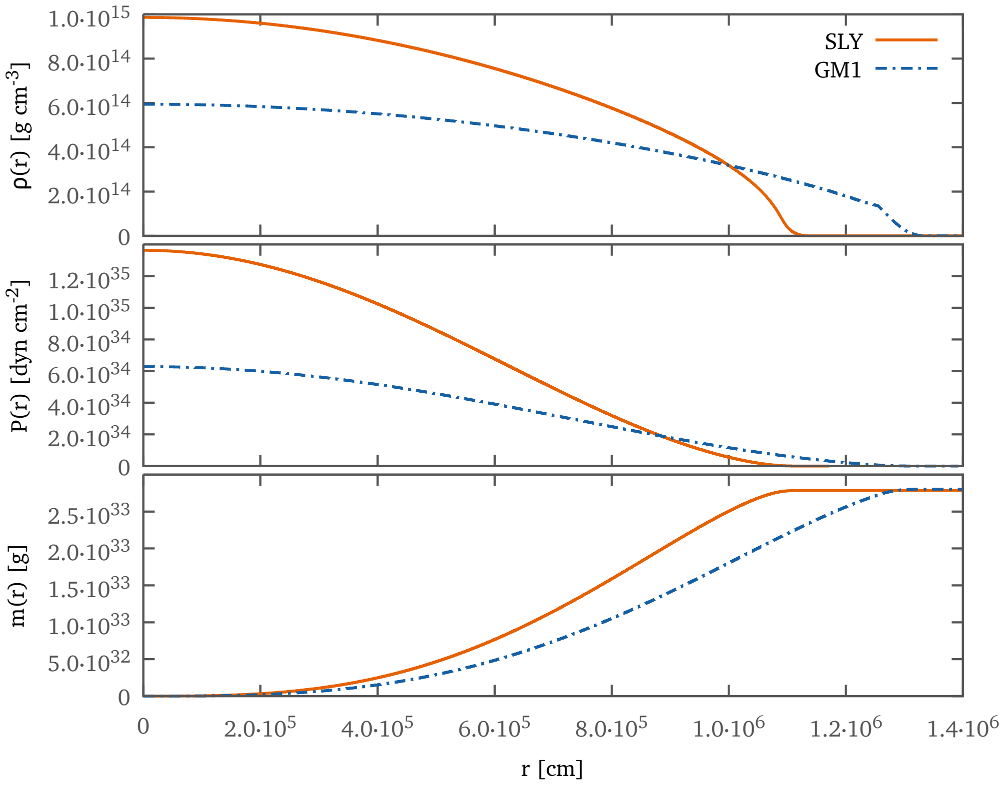

Figure 2.5: This plot shows the result of the TOV integration performed with SLy and GM1 in order to obtain a star of $1.4\,M_\odot$. We can see how the stiffness of the EoS controls the dependency on the radius r of the density ρ, the pressure P and the contained mass m.

Table 2.1: This table shows, for each EoS, the maximum allowed mass with the corresponding central density ρ_c (in units of nuclear saturation density ρ_0), radius of the star R, radius of the core R_c and radius of the inner crust R_{ic}.

EoS	ρ_c (ρ_0)	M ($\mathrm{M}_\odot$)	R (km)	R_c (km)	R_{ic} (km)
SLy	10.2	2.04	9.98	9.68	9.86
GM1	7.1	2.35	11.98	11.57	11.82

crust and it's composed mainly by iron and heavier nuclei which are arranged in a BCC lattice (the electrons form a degenerate gas); the Coulomb interaction between sites is very strong and this results in a very rigid crust, with thickness of $\lesssim 1\,\text{km}$. In this region matter is neutron–rich thanks to the inverse β–decay, but it's still in normal state because the density is not enough to produce superfluid condensates. The EoSs in this layer are constructed by taking into account the contributions to the total energy density that come from the electrons, lattice structure and of course the nuclei. This last term is generally based on the standard "liquid drop model".

The outer crust ends at the neutron drip density point $\rho_d \approx 4 \times 10^{11}\,\text{g/cm}^3$. Above this point the nuclei become unstable and release free neutrons: the BCC lattice is therefore immersed in a degenerate neutron superfluid. This region is the *inner crust* ($\approx 1\,\text{km}$ thick) in which coexists matter in normal and superfluid state. The model used for the outer crust to describe matter must be improved to consider this particular condition: the energy density expression gains another term to encompass the free neutron gas and for the nuclei the "compressible liquid drop model" is adopted (this approach takes into account the influence of the increase of density).

When the density approaches the nuclear saturation value $\rho_0 \approx 2.8 \times 10^{14}\,\text{g/cm}^3$, nuclei dissolve gradually in a homogeneous *n–p–e* gas. This transition phase is called "pasta phase" (because nuclei are deformed away from the spherical geometry) and it marks the beginning of the *core*, which contains most of the matter of the neutron star. In the inner part of the core, where density is highly above the saturation point, more exotic forms of matter are possible, like pions, hyperons and maybe even deconfined quarks: this is the most unknown region and all these considerations explain why it's difficult to describe precisely matter at so high density and why so many different EoSs has been proposed.

Thanks to the TOV integration, we obtain the density profile $\rho(r)$ and therefore it is possible to identify, for each star, the structural regions that are relevant for our models. In particular we calculate the radius of the core R_c as the distance from the center of the star where $\rho_{\text{core}} = \rho(R_c) = 0.5\rho_0$ (we fix $\rho_0 = 2.8\,\text{g/cm}^3$); the inner crust–outer crust interface R_{ic} corresponds, on the other hand, to the density value $\rho_d = 0.0015\rho_0$ that is the neutron drip point. It is easy also to calculate the moment of inertia of a shell delimited by radii r_1 and r_2:

$$I(r_1, r_2) = \frac{8\pi}{3} \int_{r_1}^{r_2} r^4 \rho(r)\, dr. \tag{2.12}$$

We can then calculate also the moment of inertia of every region, considering that $I_{\text{core}} = I(0, R_c)$, $I_{\text{ic}} = I(R_c, R_{\text{ic}})$ and $I_{\text{oc}} = I(R_{\text{ic}}, R)$.

Table 2.2 shows all the relevant parameters for the considered stars, obtained from the integration of the TOV equations with SLy and GM1.

Table 2.2: We give all the structural parameters (as defined in section 2.2.2) of the stars used to test our models, for both EoSs tested. See also fig. 2.6 for a graphical representation of these quantities.

EoS	M ($\mathrm{M}_\odot$)	R (km)	R_c (km)	$R_{\rm ic}$ (km)	I_{tot} (10^{45} g cm^2)	I_{core} (10^{45} g cm^2)	$I_{\rm ic}$ (10^{43} g cm^2)	$I_{\rm oc}$ (10^{40} g cm^2)
SLy	1.0	11.86	10.35	11.23	0.739	0.697	4.181	6.638
	1.1	11.83	10.49	11.28	0.827	0.788	3.923	5.945
	1.2	11.80	10.60	11.31	0.914	0.878	3.652	5.317
	1.3	11.76	10.69	11.32	0.999	0.965	3.370	4.738
	1.4	11.71	10.75	11.32	1.079	1.048	3.078	4.198
	1.5	11.64	10.79	11.29	1.154	1.126	2.777	3.685
	1.6	11.55	10.79	11.24	1.222	1.197	2.469	3.194
	1.7	11.42	10.76	11.16	1.279	1.258	2.150	2.718
	1.8	11.26	10.68	11.03	1.322	1.303	1.818	2.248
	1.9	11.03	10.54	10.83	1.339	1.324	1.463	1.769
	2.0	10.62	10.23	10.47	1.299	1.289	1.042	1.233
GM1	1.0	13.94	11.79	13.02	1.021	0.896	12.505	19.061
	1.1	13.94	12.01	13.12	1.146	1.025	12.068	17.532
	1.2	13.94	12.19	13.20	1.271	1.156	11.555	16.108
	1.3	13.93	12.35	13.27	1.395	1.285	10.991	14.780
	1.4	13.91	12.47	13.32	1.516	1.412	10.382	13.530
	1.5	13.89	12.58	13.34	1.634	1.536	9.738	12.340
	1.6	13.85	12.66	13.35	1.747	1.657	9.062	11.198
	1.7	13.79	12.71	13.35	1.854	1.771	8.362	10.099
	1.8	13.72	12.74	13.32	1.954	1.878	7.635	9.031
	1.9	13.62	12.74	13.26	2.043	1.974	6.885	7.987
	2.0	13.49	12.70	13.17	2.118	2.057	6.107	6.956
	2.1	13.33	12.63	13.05	2.173	2.120	5.292	5.922
	2.2	13.10	12.48	12.85	2.194	2.150	4.411	4.851
	2.3	12.71	12.20	12.51	2.146	2.113	3.371	3.631

2.3 The role of superfluidity

To understand the underlying mechanism of a glitch is necessary to frame some of the properties of a superfluid because, in the models discussed here, they are responsible for this phenomenon. The *superfluidity* is a special condition of the fluids in which they do not show signs of internal friction (viscosity). If we consider a fluid in the ground state ($T = 0$) flowing through a container, its energy can be expressed in the reference frame of the container to be due only by the kinetic contribution. If we suppose that a simple excitation arises in the fluid, we can characterize that by a momentum $\mathbf{p}$ and an energy contribution of $\varepsilon(p)$; then the total energy will be of course

$$E = \frac{1}{2}Mv^2 + \varepsilon(p) + \mathbf{p}\cdot\mathbf{v} \tag{2.13}$$

where we recognize the kinetic term (first one) and the change in energy due to the appearance of the excitation, $\varepsilon(p) + \mathbf{p}\cdot\mathbf{v}$. This change must be negative because

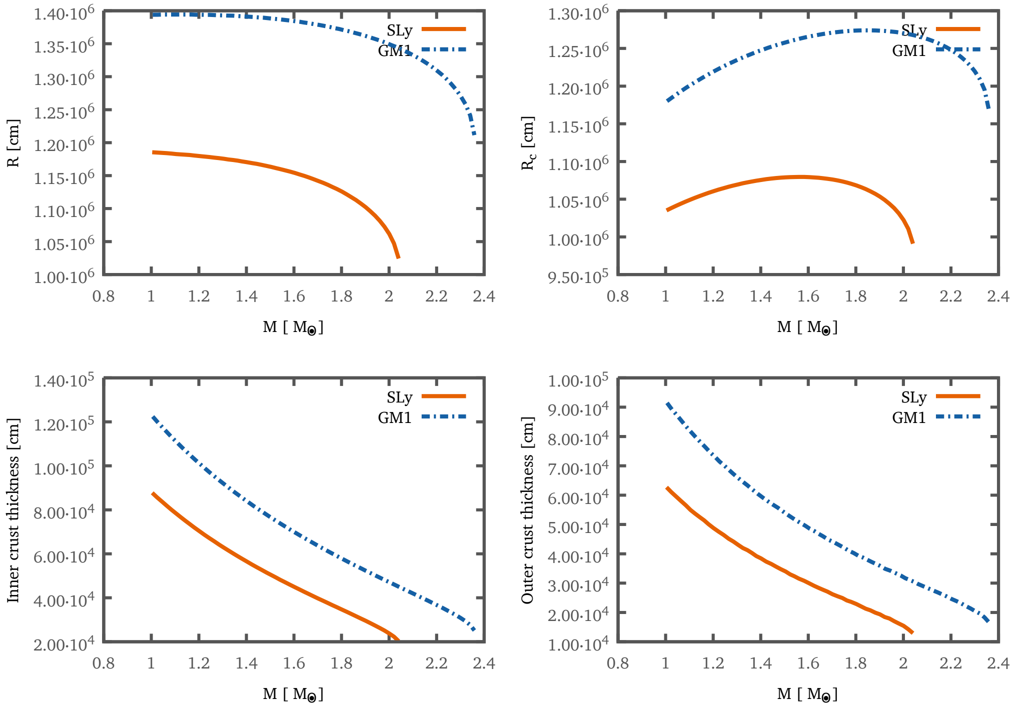

Figure 2.6: The first figure shows the dependence of the radius of the neutron star on the total mass, for the SLy and GM1 EoSs. The other plots represent the thicknesses of the stellar regions (core, inner crust and outer crust) as function of mass. As one can see, a more massive star has thinner crusts, while a stiffer equation of state produces a larger star.

otherwise the excited state would not be energetically favored. Bearing in mind that **p** and **v** are antiparallel the algebraic relation is

$$v > \frac{\varepsilon(p)}{p}. \tag{2.14}$$

It's easy to verify that when $\varepsilon(p) = \frac{p^2}{2m}$ this condition is always satisfied, in other words there is no chance for the fluid to remain in its ground state. But in a fermionic superfluid, the excitation energy can be expressed as

$$\varepsilon(p) = \sqrt{\left(\frac{p^2}{2m}\right)^2 + \Delta^2},$$

and this fact implies that the condition in eq. (2.14) can be rewritten as $v > \sqrt{2m\Delta}$. (In a bosonic superfluid the excitation are phonons and this means that $\varepsilon = c_s p$ and then $v > c_s$). In other words this means that if the velocity is below this threshold the excitement does not occur and we can refer to this state as *superfluidity*. As we will see in more detail, the presence of the dispersion term Δ in the excitation energy, also called *pairing gap*, it is crucial for the existence of superfluidity.

If we consider a superfluid in the ground state, we can describe its state with a single wave function

$$\psi = \sqrt{n_0}\, e^{i\phi}, \tag{2.15}$$

where ϕ is a global phase factor, as $|\psi|^2 = n_0$. We can immediately draw some important general properties of this class of fluids that will be crucial to understand the underlying mechanism of glitches. From quantum mechanics we know that $\mathbf{v} = \frac{\mathbf{p}}{m} = -\frac{i\hbar\nabla}{m}$, from which follows that

$$\mathbf{v}\psi = -\frac{i\hbar\nabla}{m}\psi = -i\sqrt{n_0}\frac{\hbar}{m}e^{i\phi}\nabla\phi = \frac{\hbar}{m}\nabla\phi\psi. \tag{2.16}$$

This means that $\frac{\hbar}{m}\nabla\phi$ is an eigenvector of the velocity; for a Cooper pair $m = 2m_n$ and then $\mathbf{v} = \frac{\hbar}{2m_n}\nabla\phi$. The result $\mathbf{v} \propto \nabla\phi$ implies that the macroscopic velocity field of a superfluid is irrotational, because its curl is null: $\nabla \times \mathbf{v} = \nabla \times \nabla\phi = 0$. In other words we can state that a superfluid will never rotate as a rigid body (namely $\nabla \times \mathbf{v} = 2\Omega$).

Consider now a cylinder rotating around its axis and a “normal” fluid inside, initially at rest: if there is a friction between the walls of the container and the fluid, this will be dragged and ultimately will rotate with its container. If instead we take a superfluid, this is not possible and it will persist in its groud state, as shown before, as long as this condition is thermodynamically favorable. In fact, if E is the total energy seen by a fixed “external” reference system, then when we move to the “rotating” coordinates, we have $E_{\text{rot}} = E - \mathbf{M}\cdot\boldsymbol{\Omega}$, where $\mathbf{M}$ is the angular momentum of the fluid and $\boldsymbol{\Omega}$ is the rotational angular velocity of the container. The preferred thermodynamic state is the one that minimizes E_{rot} and we can see that if $\boldsymbol{\Omega}$ is big enough, then it becomes favorable a configuration with $\mathbf{M} \neq 0$.

It’s important now to clarify the apparent contradiction with what has been explained above, namely the fact that the superfluid has always $\nabla \times \mathbf{v} = 0$ and therefore can not rotate. The contradiction is resolved if we introduce singularities in the velocity field. In other words, considering the circulation in place of the curl, we can write that

$$\oint_C \mathbf{v}\cdot d\mathbf{l} = \kappa, \tag{2.17}$$

where we consider a closed loop that encloses a straight singularity and it is centered with it. The value of the constant κ is obtained considering the relationship

$$\oint_C \mathbf{v}\cdot d\mathbf{l} = \kappa = \frac{\hbar}{2m_n}\Delta\phi,$$

where $\Delta\phi$ is the variation of the phase obtained by completing the circuit. Because of course this amount must be an integer multiple of 2π, we have

$$\kappa = n\frac{\pi\hbar}{M_N} = n\frac{h}{2m_n}. \tag{2.18}$$

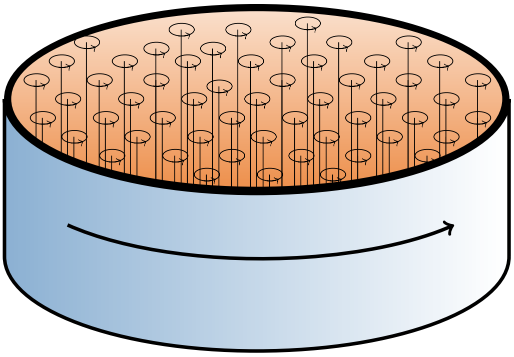

Figure 2.7: Schematic representation of a vortex bundle. The macroscopic rotation is quantized in vortexes, where each one carries a quantum of angular momentum.

Since the case $n = 1$ is energetically favorable compared with $n > 1$, from now on we assume $\kappa = \frac{h}{2m_n}$.

Talking again in terms of the curl, the relation in eq. (2.17) can be rewritten as

$$\nabla \times \mathbf{v} = \kappa\, \delta^2(\mathbf{r}_v)$$

and this is the starting point for deriving the expressions of " macroscopic" quantities of the superfluid: the system is in fact a lattice of "quantized vortex lines" (κ) that, from the macroscopic point of view, simulates a classical rotation.

It 's very interesting to see that the macroscopic quantities relevant to the proposed models of glitches can be written in a very general way as substantially dependent on the density of vortexes per unit area. These expressions are obtained easily if we imagine a cylinder rotating on its axis, with a superfluid inside. From what we have seen before, it's easy to see that, for azimuthal symmetry around the vortex,

$$2\pi x v(x) = \oint_C \mathbf{v} \cdot d\mathbf{l} = \frac{\hbar}{2m_n} \oint_C \nabla\phi \cdot d\mathbf{l} = \frac{\hbar}{2m_n} \Delta\phi = \frac{\hbar}{2m_n} 2\pi N(x), \tag{2.19}$$

where we take the circuit as a circle of radius x concentric and perpendicular to the axis of the cylinder: $N(x)$ then indicates the number of vortexes included within the radius x. If we write this quantity as $N(x) = \int_r n(x')da'$, where $da' = d(\pi x'^2)$, we can obtain that the velocity at a distance x from the axis is:

$$v(x) = \frac{\hbar}{2m_n} \frac{N(x)}{x} = \frac{\hbar}{2m_n} \frac{1}{x} \int_x n(x')da' \tag{2.20}$$

$$\Omega(x) = \frac{\hbar}{2m_n} \frac{N(x)}{x^2} = \frac{\hbar}{2m_n} \frac{1}{x^2} \int_x n(x')da'. \tag{2.21}$$

Note that the azimuthal symmetry and the Stokes' theorem ensure that the two formulas above apply to both cylinders that spheres: in the latter case x still represents the distance from the rotational axis and not the radius.

The last physical quantity important for the model is the angular momentum of the superfluid. His expression is obtained, of course, starting from $dL = \rho r v \sin\theta\, dV$.

If we consider a system with spherical symmetry, like a star with the density only dependent on the radius, then the above equation is integrated in the following way:

$$L = \frac{\hbar}{2m_n} \int_{r,\theta,\phi} \rho(r) N(r,\theta) r \sin\theta \, dr \, d\theta \, d\phi. \tag{2.22}$$

2.4 Superfluidity in neutron star and entrainment effect

A system of bosons, due to the fact that the excitations are phonons as described previously, can condense into a ground state at low temperatures, manifesting superfluid properties. Speaking instead of neutron stars, it is clear that we are interested in a superfluid of fermionic type: the existence of a ground state is guaranteed thanks to the formation of *Cooper pairs*. Basically, the neutrons near the Fermi surface are correlated in pairs so that they express bosonic features. The pairing gap Δ corresponds precisely to the binding energy per particle of these couples, and therefore it's the gap between the ground state and the first excited one. The value of this quantity is also linked to the critical temperature of the superfluid from the relation $k_b T_c = \Delta(T = 0)/1.76$. Above this temperature, the thermal energy is enough to break the pairs, bringing back the fluid to the "normal" condition.

Referring to what is described above with regard to the equation of state for neutron star matter, every region of the star has its own specific feature also in terms of superfluidity. The outer crust of course does not exhibit this behavior because, with the density less than the *drip* value (ρ_d), there is no "free" neutrons that can organize into Cooper pairs and then condensate to the ground state. The situation is different for the inner crust and the core, where $\rho > \rho_d$. The Fermi energy is density dependent and therefore it's easier for neutrons to form pairs: in the inner crust it's only possible the formation of neutron superfluid (no proton superconductor is present here), which are of type $^1S_0$ (S wave), since this condition with antialigned spins maximizes the binding energy, as shown by fig. 2.8. In the core, instead this state is possible only for protons (for their lower density compared to neutrons), while neutrons will be organized with the configuration $^3P_2$: a hypothetical $^1S_0$ pair would be broken by the nuclear repulsive interaction related to the high density, this does not happen in case of aligned spin, because the p–wave scattering length for neutrons is longer than the repulsive range.

The superfluid condition indicates that the fluid can flow without internal friction, thanks to the existence of the pairing gap. Anyway, as we will consider a system made up of two fluid (the superfluid and the "normal" one) for modeling NS glitches, we must also take into account the possible interactions between the two species. In chapter 8 we will consider the drag effects which are dissipative forces that occur both in the core and in the crust of a neutron star and are responsible of the glitch dynamic. But there is also a non–dissipative effect that can't be neglected: the *entrainment*. The entrainment in the crust (in this work we will not consider non–dissipative entrainment effects for the core) is related to the elastic scattering of neutrons by the nuclear lattice.

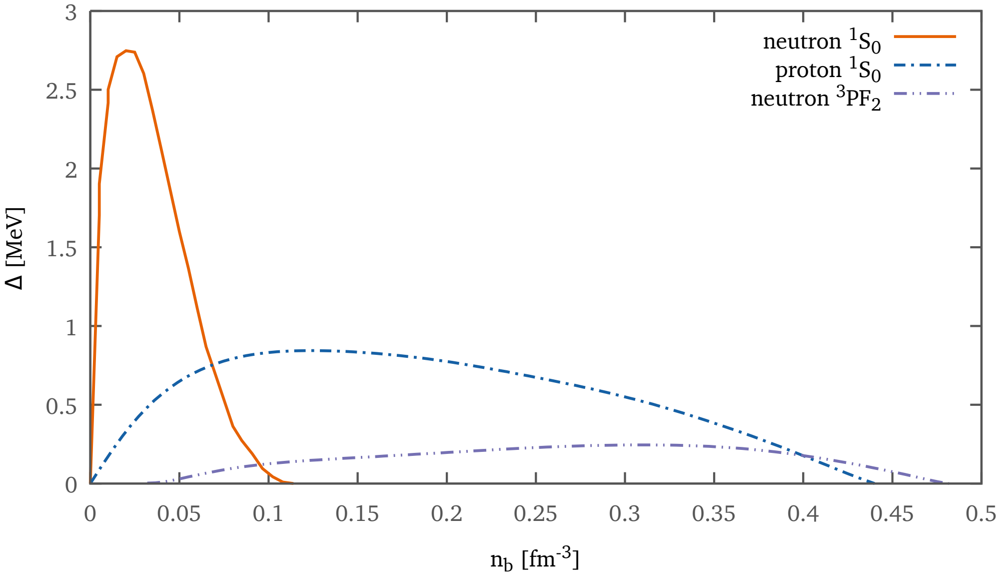

Figure 2.8: This plots shows the dependency of the pairing gap energy Δ on the barion density n_b, for different kinds of Cooper pairs. The $^3PF_2$ phase is a mixed wave pairing (Lombardo and Schulze, 2001).

This phenomenon has been successfully studied by using the band theory of solids (Chamel, 2012), applying the same ideas used in solid–state physics. As neutrons are Bragg–diffracted by the lattice, their motion is not free: a free neutron that is reflected cannot propagate as it is trapped in the crust.

Thanks to the band theory approach, it's possible to introduce an "effective neutron mass" m_n^* to encode this phenomenon. This parameter is related to the density n_n^c of the *conduction* neutrons (neutrons which are effectively free and therefore not entrained) and the total density of superfluid neutrons n_n with the following considerations. In the reference frame where the crust is at rest, the mass current $\mathbf{j}_n$ is written as

$$\mathbf{j}_n = n_n^c \mathbf{p}_n = n_n m_n \mathbf{v}_n \tag{2.23}$$

which implicitly define the average velocity of neutrons $\mathbf{v}_n$. We also define the effective mass m_n^* in such a way that $\mathbf{p}_n = m_n^* \mathbf{v}_n$ and we immediately obtain the relation

$$m_n^* = m_n \frac{n_n}{n_n^c}. \tag{2.24}$$

In an arbitrary frame where the lattice is moving with velocity $\mathbf{v}_p$, the mass current must be corrected as

$$\mathbf{j}_n = n_n^c \mathbf{p}_n + (n_n - n_n^c) m_n \mathbf{v}_p \tag{2.25}$$

because the fraction $(n_n - n_n^c)$ of "blocked" neutrons are moving with the crust. This leads directly to equation

$$\mathbf{p}_n = m_n^* \mathbf{v}_n + (m_n - m_n^*)\mathbf{v}_p = m_n \left[\mathbf{v}_n + \varepsilon_n (\mathbf{v}_p - \mathbf{v}_n) \right], \tag{2.26}$$

where we have defined $\varepsilon_n = (1 - m_n^*/m_n)$. This relation shows that the neutron mass current is no longer aligned with neutron momentum, and this fact has important consequences over the superfluid dynamics, and therefore over the glitch, as we will treat later in chapters 7 and 8. For a more detailed discussion about these aspects and the multi–fluid formalism for a NS, see Carter et al. (2006); Andersson et al. (2006).

A realistic calculation of the densities n_n and n_n^c has been performed by Chamel (2012): the results indicate that in the intermediate part of the inner crust, where $\rho \approx 4.5 \times 10^{13}\,\mathrm{g/cm^3}$, we have $m_n^* \approx 14\, m_n$. This means that most of the superfluid neutrons are actually entrained and therefore we cannot neglect this effect in our models.

PART I

THE PINNING FORCE

CHAPTER 3

Crustal pinning

The crust of a neutron star is thought to be comprised of a lattice of nuclei immersed in a sea of free electrons and neutrons. As the neutrons are superfluid their angular momentum is carried by an array of quantized vortexes. These vortexes can pin to the nuclear lattice and prevent the neutron superfluid from spinning down, allowing it to store angular momentum which can then be released catastrophically, giving rise to a pulsar glitch. A crucial ingredient for this model is the maximum pinning force that the lattice can exert on the vortexes, as this allows us to estimate the angular momentum that can be exchanged during a glitch. In this chapter we perform, a detailed and quantitative calculation of the pinning force *per unit length* acting on a vortex immersed in the crust and resulting from the mesoscopic vortex-lattice interaction. We consider realistic vortex tensions, allow for displacement of the nuclei and average over all possible orientation of the crystal with respect to the vortex. We find that, as expected, the mesoscopic pinning force becomes weaker for longer vortexes and is generally much smaller than previous estimates, based on vortexes aligned with the crystal. Nevertheless the forces we obtain still have maximum values of order $f_{\text{pin}} \approx 10^{15}$ dyn/cm, which would still allow for enough angular momentum to be stored in the crust to explain large Vela glitches, as will be deeply discussed in the next chapters.

3.1 Introduction

The physics of the Neutrons Star (NS) crust plays a crucial role when attempting to model these objects. First of all the outer layers of the star provide a heat blanket that shields the hot interior and determines the observable thermal emission from the surface (Gudmundsson et al., 1983). The elastic properties of the crust are also crucial, as "crust-quakes" have been invoked to explain a number of phenomena, such as magnetar flares (Thompson and Duncan, 1995) and pulsar glitches (Alpar et al., 1994; Middleditch et al., 2006). Furthermore the crust may sustain a large enough strain to build a "mountain" that leads to detectable gravitational wave emission (Bildsten, 1998). In this thesis we focus on the glitch phenomenon and therefore we want here to understand the role of the crust (in particular with the pinning interaction) in these events.

Glitches are sudden increases in frequency (instantaneous to the accuracy of the data) of an otherwise smoothly spinning down radio pulsar. Soon after the first observations, the long timescales associated with the post–glitch relaxation (up to months) were associated with the re-coupling of a loosely coupled superfluid component in the NS crust (Baym et al., 1969). Neutron superfluidity in NS interiors is, in fact, expected on a theoretical basis (Migdal, 1959) as most of the star will be cold enough for neutrons to form Cooper pairs and behave as a superfluid condensate, that can flow with little or no viscosity relative to the 'normal' component of the crust.

A crucial aspect of superfluid dynamics is that the neutron condensate can only rotate by forming an array of quantized vortexes, which determine an average rotation rate for the fluid. For the superfluid to spin-down it is necessary for vorticity to be expelled. If vortexes are, however, strongly attracted to the ions in the crust (i.e. they are 'pinned') their motion is impeded and the superfluid cannot follow the spin-down of the crust, and stores angular momentum, releasing it catastrophically during a glitch (Anderson and Itoh, 1975).

The nature of the trigger for vortex unpinning is still debated, with proposals ranging from vortex avalanches (Alpar et al., 1996; Warszawski and Melatos, 2012b) to hydrodynamical instabilities (Glampedakis and Andersson, 2009) or crust quakes (Ruderman, 1969, 1976; Alpar et al., 1994; Middleditch et al., 2006). Whatever the trigger mechanism, an important ingredient in this picture is the maximum pinning force that the crust can exert on a vortex, before hydrodynamical lift forces (the Magnus force) are able to free it. This quantity obviously determines the maximum amount of angular momentum that can be exchanged during a glitch. An understanding of how much angular momentum can be stored in different regions of the star would, in fact, allow detailed comparisons with observations of glitching pulsars and potentially constrain the equation of state of dense matter (Andersson et al., 2012; Chamel, 2013; Piekarewicz et al., 2014).

Early theoretical work focused on the microscopic interaction between a vortex and a single pinning site (Alpar, 1977; Epstein and Baym, 1988). The pinning force *per unit length* of a vortex depends, however, on the mesoscopic interaction between the vortex and many pinning sites, and thus on the rigidity of the vortex, on its radius (represented by the superfluid coherence length ξ) and on the lattice spacing. This naturally leads to the possibility of different pinning regimes in different regions of the crust. Alpar et al. (1984a,b) interpreted the slow post-glitch recovery of the Vela pulsar in terms of vortex "creep", i.e. thermally activated motion of pinned vortexes, and distinguished between three regimes: strong, weak and super weak pinning. The different regimes depend on the interplay between the quantities mentioned earlier: in strong pinning the coherence length ξ of a vortex is smaller than the lattice spacing, and the interaction is strong enough to displace nuclei; while in the weak pinning regime this is not the case. Superweak pinning, on the other hand, comes about when the coherence length ξ is greater than the lattice spacing and a vortex can encompass several nuclei. In this case there is little change in energy as the vortex moves and thus no preferred configuration for pinning. The pinning force is expected to be weak and, in the limit of infinitely long vortexes all configurations are equal and there would be no pinning Jones (1991b). Fits to the post-glitch relaxation of the Vela pulsar, within the vortex creep framework (Alpar et al., 1984a), were used to set observational constraints on some of these parameters, leading to the conclusion that only weak and super weak pinning are likely to be at work in a neutron star crust (Alpar et al., 1984b). The theoretical calculations of the mesoscopic pinning force relied, however, on estimates in the weak pinning case for the very particular configuration of vortexes *aligned* with the crystal axis. Although very little is known about the defect structure of the crust, one does not in general expect the crystal lattice to be oriented in the same direction over the whole length of a vortex (note also that a vortex will have cylindrical symmetry set by the rotation axis, while the only preferred direction for the crystal will be set by gravity and pressure which have spherical symmetry, slightly modified by rotation). More recently Link (2009) has performed simulations of motion of a vortex in a three-dimensional random potential, and found that the rigidity of the vortex does, indeed, play a fundamental role in setting the maximum superfluid flow above which vortexes cannot remain pinned.

In this chapter we perform a realistic calculation of the mesoscopic pinning force, that is the force per unit length acting on straight vortexes in the neutron star crust. We average over all possible vortex-crystal orientations and show that, although the force is considerably weaker than previous estimates based on particular configurations, it could still be strong enough to account for angular momentum transfer in large pulsar glitches.

3.2 Lattice properties

The crust of a NS is thought to form a crystal in which completely ionized neutron-rich nuclei form a *body centered cubic* (BCC) lattice, immersed in a sea of electrons and free neutrons. In this configuration each nucleus is at the center of a cubic cell of side $s = 2R_{\rm ws}$ with nuclei at each vertex. The separation between the ions (i.e. the potential pinning sites) thus depends on $R_{\rm ws}$, the radius of the Wigner-Seitz cell, which is a function of the density ρ. In our calculation we use the classic results from Negele and Vautherin (1973) where the crust is divided in five zone, each one characterized by a specific value of $R_{\rm ws}$ and R_N, which is the radius of the nucleus that occupies a single site of the lattice. Table 3.1 summarizes these results, together with the nuclear composition of the Wigner-Seitz cells.

Note that there is still significant uncertainty on the exact composition and structure of the crust (Steiner et al., 2014; Piekarewicz et al., 2014) and not only electrons, but also free neutrons, may partially screen the Coulomb interaction between the nuclear clusters, leading to different, and more inhomogeneous, configurations than a BCC lattice (Kobyakov and Pethick, 2014). Nevertheless the procedure we describe below

Table 3.1: Fiducial values of the quantities used in our calculations. These values are taken from Negele and Vautherin (1973): the NS crust is divided in five zone and here we give the baryon density ρ, the Wigner-Seitz cell radius ($R_{\rm ws}$), the element corresponding to the cell nuclear composition, the nuclear radius (R_N), the superfluid coherence length (ξ), which represents the vortex radius, and the pinning energy per site (E_p). The last two quantities are taken from the results of Donati and Pizzochero (2004, 2006)

#	ρ [g cm^{-3}]	Element	$R_{\rm ws}$ [fm]	R_N [fm]	ξ [fm]		E_p [MeV]	
					$\beta = 1$	$\beta = 3$	$\beta = 1$	$\beta = 3$
1	1.5×10^{12}	$^{320}_{40}$Zr	44.0	6.0	6.7	20.0	2.63	0.21
2	9.6×10^{12}	$^{1100}_{50}$Sn	35.5	6.7	4.4	13.0	1.55	0.29
3	3.4×10^{13}	$^{1800}_{50}$Sn	27.0	7.3	5.2	15.4	-5.21	-2.74
4	7.8×10^{13}	$^{1500}_{40}$Zr	19.4	6.7	11.3	33.5	-5.06	-0.72
5	1.3×10^{14}	$^{982}_{32}$Ge	13.8	5.2	38.8	116.4	-0.35	-0.02

can easily be adapted to different configurations.

To calculate the mesoscopic pinning force we need to identify the configurations in which the vortex is most strongly pinned to the lattice and the configurations in which it is ’free’. Once this has been done the *maximum* pinning force F_p simply follows from:

$$F_p = \frac{E_{\rm free} - E_{\rm pin}}{\Delta r} \tag{3.1}$$

where $E_{\rm pin}$ is the energy of the most strongly pinned configuration and $E_{\rm free}$ the energy of the free configuration. The average distance the vortex has to move between the configurations is Δr.

The energy of a particular vortex configuration will depend on the number of ions that it is able to pin to. Intuitively, the more sites it can pin to, the greater the energy gain, the stronger the pinning. In order to perform the calculation it is thus necessary to consider the pinning energy *per pinning site* E_p, i.e. the amount by which the energy of the system is changed when a single nucleus is inside the vortex. This quantity depends on the competition between the kinetic energy and the condensation energy of the superfluid, which is strongly density dependent and will thus change if a dense nucleus is introduced in the vortex. In this work we use the results of Donati and Pizzochero (2003, 2004, 2006), who calculate E_p consistently in the local density approximation. The values of E_p for different densities are given in the last columns of table 3.1. Note that in some regions E_p is positive, i.e. it costs energy to introduce a nucleus in a vortex. In these regions the vortex-nucleus interaction is repulsive and one has ’interstitial’ pinning (IP), in which the favored vortex configurations are in-between nuclei. We refer to the case in which the interaction between nuclei and vortexes is attractive as ’nuclear’ pinning (NP). We shall see in the following that the effect of attraction or repulsion does not strongly influence the calculation of the mesoscopic pinning force. The parameter β refers to the suppression factor for the neutron pairing gap used in the calculations: $\Delta = \frac{\Delta_0}{\beta}$, where Δ_0 is the pairing gap of the superfluid obtained by using the bare interaction (i.e. not accounting for in-medium corrections). This factor is related to the polarization effects of matter on the nuclear interaction. The case $\beta = 1$ describes the non–polarized interaction, while the case $\beta = 3$ describes the one in which the effect of the polarization is maximum. When $\beta = 1$ the mean pairing gap has a maximum of about 3 MeV, which corresponds to the strong pairing scenario, while when $\beta = 3$ the mean pairing gap has a maximum of about 1 MeV, as usually assumed in the weak pairing scenario. Realistic Montecarlo simulations of neutron matter (Gandolfi et al., 2008) indicate a reduction of the pairing gap consistent with the choice $\beta = 3$.

The total energy of the interaction between a given vortex portion and the lattice is calculated summing the contribution of each nucleus that can be captured by the pinning force. Naively this could be done by considering the vortex as a cylinder of radius ξ and counting how many nuclei are contained within it (we will discuss how to count nuclei at the boundary in the following). This approach can be improved to take into account the possible deformation of the nuclear lattice. The lattice has elastic properties, so it is possible for nuclei to be displaced from their equilibrium position under the action of the pinning force. The resulting energy per site can be expressed as

$$E(r) = E_p + E_l(r) \tag{3.2}$$

where r is the distance of the vortex axis from the equilibrium position of the considered nucleus. In this approach, the pinning energy per site E_p is corrected by the factor $E_l(r)$ that encodes the change in electrostatic energy due to the displacement of the nucleus. We will then define the capture radius r_c as the radius within which it is energetically favorable for the nuclei to be displaced: this will be the radius of the vortex to be used in the counting procedure. Let us now estimate r_c for both nuclear and interstitial pinning.

3.2.1 Nuclear pinning

In the nuclear pinning regime ($E_p < 0$) we define a pinning region assuming that a nucleus contributes to the total interaction by a factor E_p if it is completely inside the vortex: in other words its distance from the vortex axis must be less than $\gamma = \xi - R_N$ (fig. 3.1). If a site is at a distance $r > \gamma$ from the vortex axis, the nucleus must be dragged by a distance $\delta(r) = r - \gamma$. The electrostatic energy is calculated in a standard way using Gauss theorem together with the Wigner-Seitz approximation, which divides the lattice in independent spherical cells of radius R_{ws} each with an ion in the center surrounded by the electron and neutron gas:

$$E_l(r) = \frac{Z^2 e^2}{2R_{\mathrm{ws}}^3} \delta^2(r) \tag{3.3}$$

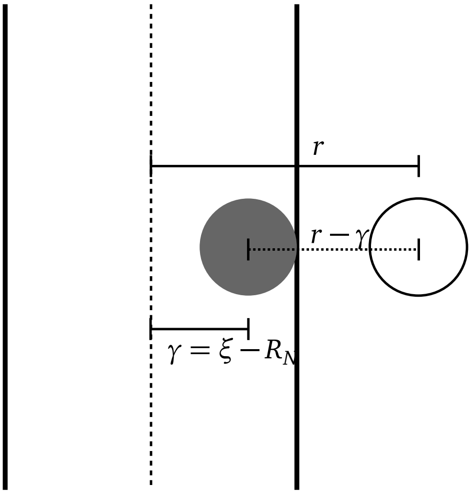

Figure 3.1: Representation of a nucleus displacement (NP case). The empty and full circles represent respectively the starting and final position of the nucleus. The dashed line represents the displacement $\delta(r)$.

where e is the elementary charge and Z is the number of protons and electrons in the cell. Of course, a nucleus whose equilibrium position is already inside the pinning region does not need to be dragged, so its energy contribution has no electrostatic term ($E(r) = E_p$ if $r < \gamma$). We can now define the maximum drag distance r_0 as the value of $\delta(r)$ for which the effective pinning interaction of eq. (3.2) becomes zero:

$$r_0 = \sqrt{-\frac{2E_p R_{\mathrm{ws}}^3}{Z^2 e^2}}. \tag{3.4}$$

From these consideration, it follows that the final *capture radius* that must be used in our calculation will be

$$r_c = \gamma + r_0 = \xi - R_N + r_0 \tag{3.5}$$

The total energy of the interaction between the considered vortex portion (of length L) and the lattice is calculated summing the contribution of each nucleus that can be captured by the pinning force. This energy is calculated through an integral over a uniform distribution of nuclei, that is valid when the number of nuclei which are taken into account becomes very large, so for $L \gg R_{\mathrm{ws}}$. Given N the number of pinning sites that fall inside a cylinder of radius r_c and length L, the superficial density will be $n_N = \frac{N}{\pi r_c^2}$. Then the total energy is calculated as

$$\begin{aligned} E &= \int_0^{\gamma} E_p n_N \, 2\pi r \, dr + \int_{\gamma}^{\gamma + r_0} \big(E_p + E_l(r)\big) n_N \, 2\pi r \, dr \\ &= \frac{N E_p}{(\gamma + r_0)^2} \left(\gamma^2 + \frac{4}{3}\gamma r_0 + \frac{1}{2} r_0^2\right) \end{aligned} \tag{3.6}$$

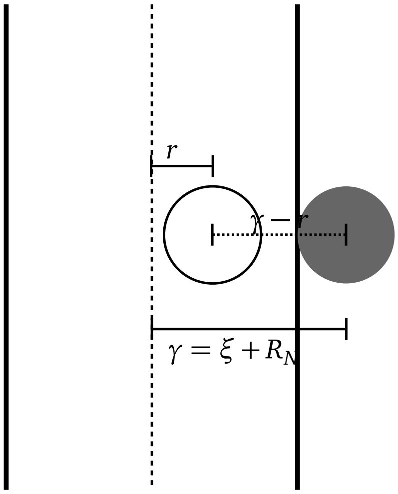

Figure 3.2: Representation of a nucleus displacement (IP case). The empty and full circles represent respectively the starting and final position of the nucleus. The dashed line represents the displacement $\delta(r)$.

From this equation we can immediately evaluate the effective interaction energy *per site* E_{eff}, defined by $E = NE_{\text{eff}}$:

$$E_{\text{eff}} = \frac{E_p}{(\gamma + r_0)^2}\left(\gamma^2 + \frac{4}{3}\gamma r_0 + \frac{1}{2}r_0^2\right) \tag{3.7}$$

In table 3.2 we give the values of the above quantities, which have been calculated using the fiducial inner crust and superfluid properties of table 3.1.

3.2.2 Interstitial pinning

The evaluation of r_c and E_{eff} in the interstitial pinning regime ($E_p > 0$) follows the same steps of the previous section, but taking into account the fact that in this case the interaction is repulsive and thence a nucleus that lies in the vortex core must be expelled instead of dragged into it in order to lower the energy. We define a nucleus as expelled if it is completely outside the vortex, that is if its distance from the vortex axis is larger than $\gamma = \xi + R_N$ (fig. 3.2); a nucleus which is expelled does not contribute to the pinning energy. The drag distance now is $\delta(r) = \gamma - r$ and the maximum value for this quantity, r_0, is given by the energy balance $E_p = E_l(\delta = r_0)$. This encodes the idea that the nuclear displacement is favorable until the energy of the dragged nucleus configuration is lower than the energy of the configuration where the nucleus is still in its equilibrium position in the lattice:

$$r_0 = \sqrt{\frac{2E_p R_{\text{ws}}^3}{Z^2 e^2}}. \tag{3.8}$$

The capture radius that must be used in the counting procedure in this case is equal to γ because the nuclei that contribute to the pinning energy are only those that lie in

Table 3.2: Lattice properties for the five zones of table 3.1. The values in table 3.1 are used here to calculate the capture radius r_c (in units of R_{ws}) and the effective pinning energy per site E_{eff} as explained in section 3.2

		$\beta = 1$				$\beta = 3$			
#	IP/NP	γ [fm]	r_0 [fm]	r_c [R_{ws}]	E_{eff} [MeV]	γ [fm]	r_0 [fm]	r_c [R_{ws}]	E_{eff} [MeV]
1	IP	12.7	14.0	0.289	0.36	26.0	3.9	0.591	0.17
2	IP	11.1	6.2	0.313	0.64	19.7	2.7	0.555	0.24
3	NP	0.0	7.6	0.204	-2.60	8.1	5.5	0.504	-2.08
4	NP	4.6	5.7	0.531	-3.46	26.8	2.1	1.490	-0.69
5	NP	33.6	1.1	2.514	-0.34	111.2	0.3	8.080	-0.02

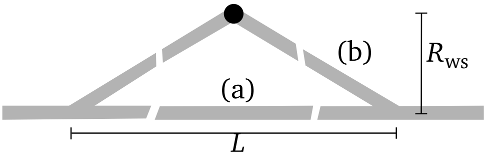

Figure 3.3: Representation of the vortex deformation. We sketch a rigid vortex (a) and a bent vortex (b). L is the vortex length and R_{ws} is the Wigner-Seitz radius.

the pinning region

$$r_c = \gamma = \xi + R_N \tag{3.9}$$

Now, if $r_0 < \gamma$ the total energy is calculated as

$$E = \int_0^{\gamma - r_0} E_p n_N \, 2\pi r \, dr + \int_{\gamma - r_0}^{\gamma} E_l(r) n_N \, 2\pi r \, dr \tag{3.10}$$

where the second term of the integral contains only the electrostatic contribution because the nuclei in that region have been expelled. If instead $r_0 > \gamma$ all the nuclei that contribute to the pinning energy are dragged outside the vortex: in this case we have

$$E = \int_0^{\gamma} E_l(r) n_N \, 2\pi r \, dr \tag{3.11}$$

Solving these integrals and defining again $E = N E_{\mathrm{eff}}$ we obtain the effective pinning energy *per site* (see table 3.2 for numerical results):

$$E_{\mathrm{eff}} = \begin{cases} E_p \frac{1}{\gamma^2} \left(\gamma^2 - \frac{4}{3} \gamma r_0 + \frac{1}{2} r_0^2 \right) & r_0 \leq \gamma \\ E_p \frac{\gamma^2}{6 r_0^2} & r_0 > \gamma \end{cases} \tag{3.12}$$

3.2.3 Vortex length

The length-scale over which a vortex can be considered straight corresponds the length L of the cylinder on which we perform the counting procedure described. We

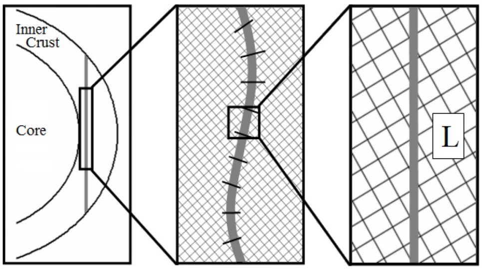

Figure 3.4: Representation of the vortex rigidity on different scales. L is the maximum length of the unbent vortex as discussed in section 3.2.3.

can estimate the order of magnitude of L with a simple argument based on energy considerations (we develop the argument in the NP regime, but the same result obtains in the IP regime). Assuming that the vortex, under tension T (self-energy per unit length), will bend under the influence of the pinning force, we can equate the energy of two limiting configurations: the straight (infinitely rigid) vortex (fig. 3.3a) and the vortex that has bent in order to pin to an additional nucleus at a typical distance $R_{\rm ws}$ (fig. 3.3b):

$$TL = E_p + T(L + \Delta L) \tag{3.13}$$

The difference ΔL of the vortex length in the two configuration is obviously

$$\Delta L = 2\sqrt{\left(\frac{L}{2}\right)^2 + R_{\rm ws}^2} - L \approx \frac{2R_{\rm ws}^2}{L} \tag{3.14}$$

where we have expanded the expression following the realistic assumption that $R_{\rm ws} \ll L$. Finally we have

$$\frac{L}{R_{\rm ws}} = \frac{2TR_{\rm ws}}{|E_p|} \sim 10^3 \tag{3.15}$$

where the standard neutron star values have been used: $T \sim 20$ MeV fm^{-1} (as in Jones (1990b)), $R_{\rm ws} \sim 30$ fm and $|E_p| \sim 1$ MeV. We will thus study the dependence of our results on variations of the parameter L around the estimate in eq. (3.15). Note that the ability of a vortex to bend and adapt to a pinned configuration plays an important role in determining the maximum of the pinning force, as also found by Link (2009).

3.3 Mesoscopic pinning force

The calculation of the pinning force per unit length is done here by counting the actual number of pinning sites intercepted by a randomly oriented vortex. We consider vortexes parallel to the rotation axis and that thread the whole star. Due to the finite rigidity of the vortex we assume that it can be considered straight only on a characteristic length-scale L, as described in the previous section (fig. 3.4). This idea, combined with the fact that the lattice is made up by macro-crystals with random direction (Jones, 1990b), indicates that a macroscopic portion of vortex immersed in the crust experiences all possible orientations with respect to the lattice. The force per unit length should then be calculated as an average over all angular directions. In following this procedure we neglect the effects of turbulence, which may arise in NS interiors (Peralta et al., 2005, 2006; Andersson et al., 2007), possibly due to modes of oscillations of the superfluid that may be unstable in the presence of pinning (Glampedakis and Andersson, 2009; Link, 2012b). In this case the vortex array is likely to form a complex tangle, that must, however, still be polarized due to the rotation of the star. Given that the problem of polarized turbulence is poorly understood (see Andersson et al. (2007) for the description of a possible approach to this issue) we shall focus on a regular vortex array, and leave the complex problem of turbulence for future work.

We consider an infinite BCC lattice with its symmetry axes oriented as $\hat{x}$, $\hat{y}$ and $\hat{z}$, and with a nucleus in $(0,0,0)$. A vortex is modeled as a cylinder of length L and radius r_c with its median point initially in the origin and the orientation is given by the angles θ and ϕ in spherical coordinates. For a given choice of θ and ϕ, we evaluate the pinning force per unit length $f_L(\theta,\phi)$ by a counting procedure: from the initial position the vortex is moved parallel to itself, covering a square region of side l in the plane perpendicular to the vortex axis, with steps of an amount dh. For each new position, identified by the displacement (λ,κ), it is possible to count the number $N(\lambda,\kappa)$ of lattice nuclei that are within the capture radius of the vortex. In figs. 3.5 and 3.6, we show two examples of a density plot where for each translation of the vortex (λ,κ) we plot the number of captured pinning sites $N(\lambda,\kappa)$. The difference between the cases of vortex aligned with the lattice and vortex with arbitrary orientation is evident from the figures.

As discussed in the previous section, the number of captured pinning sites N in a vortex-lattice configuration is directly related to the energy of the configuration by the expression $E = E_{\text{eff}}N$ where E_{eff} is the effective contribution of every single interaction. As previously discussed, the interaction between the vortex and the nuclei can be attractive (NP) or repulsive (IP) in different regions of the crust. The calculation procedure presented here is valid for both cases, with the following distinction: in the NP regime, the *bound* configuration (state of minimum energy) is identified by the positions (λ,κ) where the number of pinning site reach its maximum. This means that $N_{\text{bound}}(\theta,\phi) = \max(N(\lambda,\kappa))$. On the other hand, in the IP case, we must take the minimum: $N_{\text{bound}}(\theta,\phi) = \min(N(\lambda,\kappa))$.

This leads to the fact that, for both the NP and IP cases, the change in energy obtained by moving the vortex away from its bound configuration (unpinning energy) will be:

$$\begin{aligned}\Delta E(\theta,\phi) &= E_{\text{eff}}\Delta N(\theta,\phi)\\ &= E_{\text{eff}}\left(N_{\text{free}}(\theta,\phi) - N_{\text{bound}}(\theta,\phi)\right),\end{aligned} \tag{3.16}$$

where we take N_{free} as the average number of pinning sites counted in all visited displacements: $N_{\text{free}}(\theta,\phi) = \langle N(\lambda,\kappa)\rangle$. Obviously, we have $\Delta E(\theta,\phi) > 0$ for both the NP and IP cases, since it takes energy to remove the vortex from the location where it is

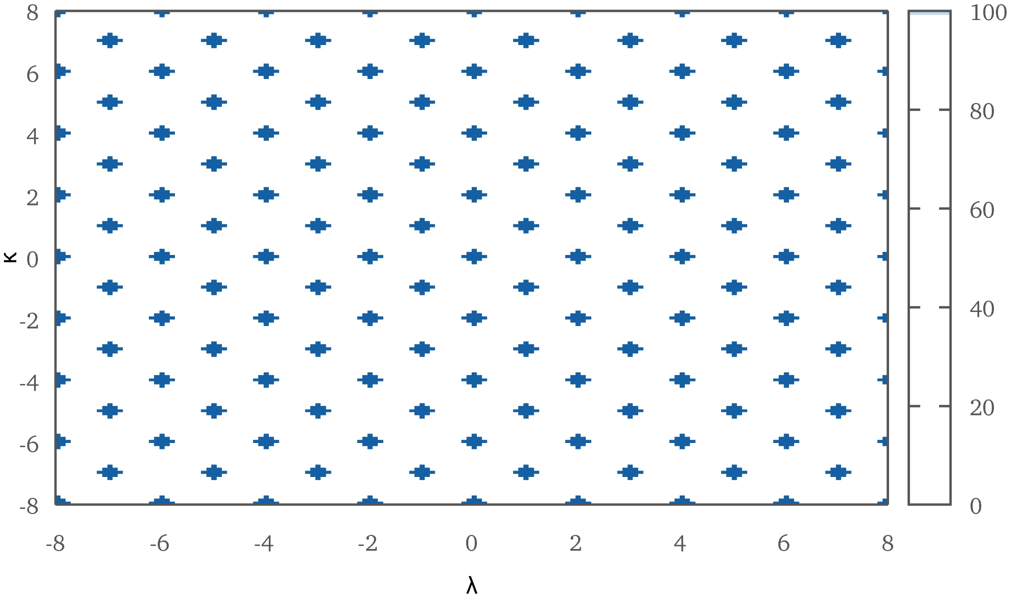

Figure 3.5: Number of captured pinning sites $N(\lambda,\kappa)$ when the vortex is *aligned* with the lattice. The color codes are described in the sidebar. The axes λ and κ represent the translation of the vortex with respect to the initial position, and they are measured in $R_{\rm ws}$ units. The grid step size is $dh = 0.1R_{\rm ws}$, the vortex is $L = 200R_{\rm ws}$ and the capture radius is $r_c = 0.204R_{\rm ws}$ (region 3 with $\beta = 1$). Note that the simple geometry leads to several disjoint maxima that spread over several steps, given that for a small grid step dh the energy of the configuration does not change until the vortex has been moved by one capture radius away from the aligned nuclei.

pinned. We see that in any given zone (fixed $E_{\rm eff}$ and r_c) the unpinning energy depends on the vortex orientation only through $\Delta N(\theta,\phi) = N_{\rm free}(\theta,\phi) - N_{\rm bound}(\theta,\phi)$, the change in the number of captured nuclei between the two configurations. In fig. 3.7 we plot the quantity $|\Delta N(\theta,\phi)|/\widetilde{L}$ as a function of (θ,ϕ), where $\widetilde{L} = L/R_{\rm ws}$ is the (adimensional) vortex length in units of $R_{\rm ws}$; the plot corresponds to region 3 (NP regime), so that actually $\Delta N(\theta,\phi) < 0$. Notice that the aligned configuration of fig. 3.5 would correspond to $\Delta N(0,0)/\widetilde{L} = -0.5$, since $N_{\rm free}(0,0) = 0$ and $N_{\rm bound}(0,0) = L/(2R_{\rm ws})$ (the captured nuclei are a distance $s = 2R_{\rm ws}$ apart). It is evident from the figure that most orientations have $|\Delta N(\theta,\phi)| \ll 0.5$.

The force required to move the vortex away from the bound configuration can be easily calculated using the following expression:

$$F(\theta,\phi) = \frac{\Delta E(\theta,\phi)}{D(\theta,\phi)} \tag{3.17}$$

where $D(\theta,\phi)$ identifies the average distance required to reach the free configuration from the pinned one. We estimate this quantity by counting in the density plot the

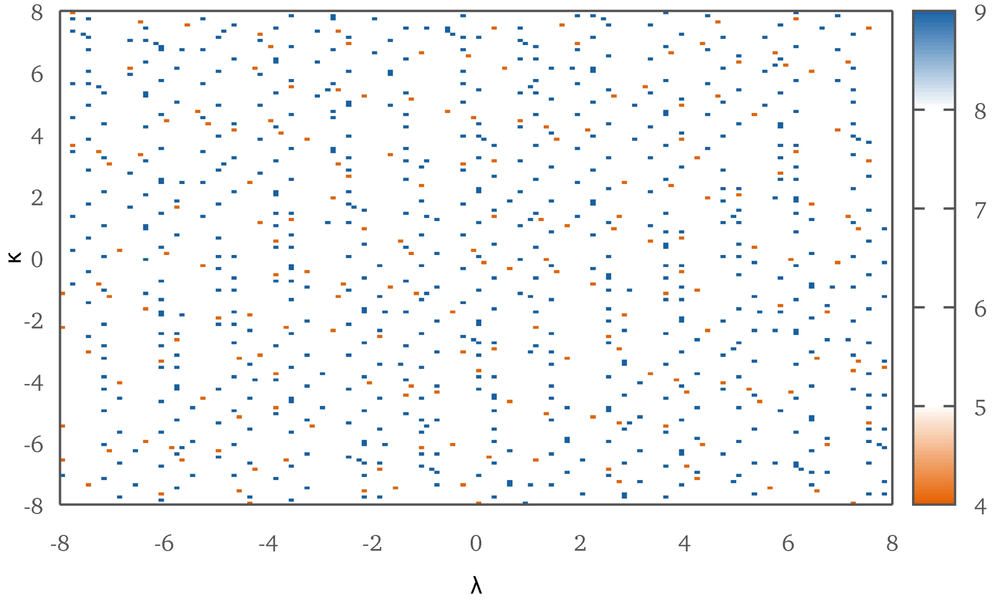

Figure 3.6: Number of captured pinning sites $N(\lambda,\kappa)$ when the vortex is *non–aligned* with the lattice (we selected a random orientation). The color codes are described in the sidebar. For details on the parameters used to produce this plot see fig. 3.5.

number $n_{N_{\text{bound}}}$ of disjoint positions where $N(\lambda,\kappa) = N_{\text{bound}}$ (we sometimes omit the angular dependence for notational simplicity). In other words, $n_{N_{\text{bound}}}$ represents the number of distinct extremal configurations (maxima in the NP regime, minima in the IP regime) found in the sampling square region. For a uniform distribution of these extremal points (square array of step $2D$) we would have $n_{N_{\text{bound}}}\pi D^2 \simeq l^2$, where l is the side of the square region tested by parallel–transporting the vortex. We thus take as a reasonable definition for the average distance in the general case:

$$D(\theta,\phi) = \frac{l}{\sqrt{\pi n_{N_{\text{bound}}}(\theta,\phi)}} \tag{3.18}$$

Finally, the force per unit length is

$$f_L(\theta,\phi) = \frac{F(\theta,\phi)}{L} \tag{3.19}$$

For the procedure described above it is clearly necessary to unambiguously count $n_{N_{\text{bound}}}(\theta,\phi)$. With the parallel–transport operation, we explore a portion of the plane that is perpendicular to the vortex axis. This region is a square region of side l that is sampled with a grid of step dh. This means that we have to look for the position of maxima/minima analyzing a set of points $(\lambda,\kappa)_{ij} = (-l/2+i\,dh, -l/2+j\,dh)$. If we merely

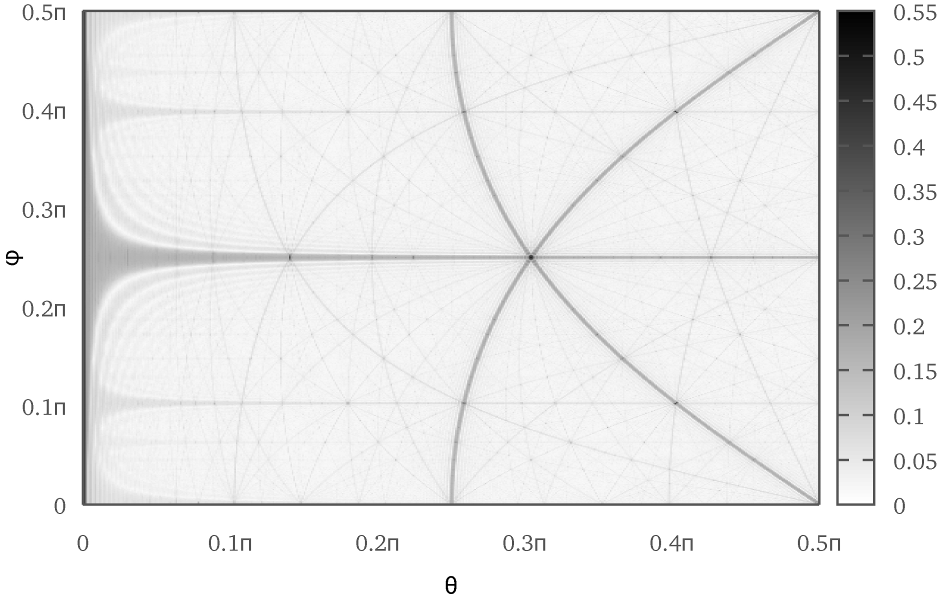

Figure 3.7: Difference between the number of pinning sites of the free and bound configurations as a function of the vortex orientation (θ, ϕ). Here we plot $|\Delta N(\theta, \phi)|/\widetilde{L}$, where $\widetilde{L}$ is the (adimensional) vortex length in units of the Wigner-Seitz radius. The color codes are described in the sidebar. The figure has been obtained considering a vortex of length $L = 200R_{\text{ws}}$ and capture radius $r_c = 0.204R_{\text{ws}}$ (region 3 with $\beta = 1$).

count the number of points for which $N_{ij} = N(\lambda, \kappa)_{ij}$ reaches its maximum/minimum value, this result would be strongly conditioned by the choice of the dh parameter. In fact, for small values of dh, it is obvious that a single “maximum/minimum position” will be split over several points $(\lambda, \kappa)_{ij}$, altering the final result.

One possible solution is to take into account only *disjoint* maxima/minima: this means that two extremal points count as one if they are “first–neighbors”. This approach requires a second–pass analysis over the values N_{ij} to identify the clusters in the density map, and it allows us to correctly evaluate a configuration such as the one in fig. 3.5, in which the alignment of the vortex with the symmetry axis of the crystal leads, for small grid steps, to several neighboring equivalent configurations. Without considering clustering, we would have counted $n_{N_{\text{bound}}} = 1745$ for this particular case ($dh = 0.1R_{\text{ws}}$). Counting only *disjoint* extremal points, instead, gives the correct answer of $n_{N_{\text{bound}}} = 145$, and this result does not change if we explore the square region with a smaller step size.

In this work the method just described has been slightly generalized to treat extremal points that are topologically disjoint but “very close” and thence physically equivalent. As described previously, the actual vortex radius (ξ) and the site radius (R_N) are encoded together in the single parameter r_c because this is the only relevant quantity (from the geometrical point of view) in the evaluation of the number of vortex–lattice interactions for a given configuration. However, the site radius in this picture has still a physical meaning: in order for a nucleus to *actually* enter or exit the vortex core and thus change the vortex-lattice energy, the vortex axis must move by at least $2R_N$. Therefore, if two extremal points are less than $2R_N$ apart there is no actual change in energy for the vortex to move from one to the other and therefore they must be counted together as a single pinning site. In other words we choose to count two extremal points as one if their distance is less than a quantity $\eta \sim 2R_N$.

In conclusion, the number $n_{N_{\text{bound}}}(\theta, \phi)$ appearing in eq. (3.18) is corrected to take into account the "clusters" of extremal points as determined by the parameter η: it corresponds to the number of *disjoint* clusters, each representing a physically distinct pinning site. For the five zones in table 3.1, the quantity $2R_N$ is always in the range $(0.25 \div 0.75)R_{\text{ws}}$. In order to make the calculations affordable, we fix $\eta = 0.5R_{\text{ws}}$ for every zone, after testing that there is no significant difference in the final results for the pinning force (below 10% and anyways well within the error bars) under variations of η in the previous range. Altogether, it is evident that the main uncertainty in the calculation of the pinning force comes from the determination of $n_{N_{\text{bound}}}(\theta, \phi)$: in order to have some measure of this and since we are dealing with a counting measurement, we will associate to $n_{N_{\text{bound}}}$ the standard error $\pm\sqrt{n_{N_{\text{bound}}}}$.

To obtain the final value f_L for the mesoscopic pinning force, we must repeat the above calculations for each value of (θ, ϕ), and then take the angular average:

$$f_L = \langle f_L(\theta, \phi) \rangle = \frac{1}{4\pi} \int f_L(\theta, \phi)\, d\Omega \tag{3.20}$$

An estimate of the error $\pm\sigma_{f_L}$ on f_L can also be obtained, by propagating the error on $n_{N_{\text{bound}}}(\theta, \phi)$ in eqs. (3.17) and (3.20).

We also checked that our results are reasonably independent from the choice of the parameters l and dh used in the parallel-transport sampling procedure. In figs. 3.8 and 3.9 we show an example of the convergence of the calculated f_L for different values of l and dh. In the following we will fix $l = 16\,R_{\text{ws}}$ and $dh = 0.005\,R_{\text{ws}}$, which provide an acceptable accuracy (well within the error bars $\pm\sigma_{f_L}$) while allowing for a not too long computational runtime.

3.4 Results of the model

The results of our calculations are summarized in table 3.3. We have applied the algorithm described in the previous sections to different choices of the parameter L, starting from a short vortex with length equal to $100R_{\text{ws}}$ up to a configuration with $L = 5000R_{\text{ws}}$. For each value of L and for each zone of table 3.1 we have calculated the pinning force per unit length f_L and the estimated error σ_{f_L} for two values of the polarization correction factor, $\beta = 1$ (i.e. the case of a bare interaction) and $\beta = 3$, which is close to the value obtained in realistic Montecarlo simulations of neutron

Table 3.3: Results of the calculations for vortexes with length L up to $5000R_{\text{ws}}$. The parameters of table 3.2 were used as inputs for the counting procedure. The quantities $\langle D \rangle$, $\langle \Delta N \rangle / \widetilde{L}$ and $\langle \Delta E \rangle / L$ are the angular averages of $D(\theta, \phi)$, $\Delta N(\theta, \phi)/\widetilde{L}$ and $\Delta E(\theta, \phi)/L$ respectively. The last two columns show the force per unit length and its uncertainty.

L $[R_{ws}]$	β	#	r_c $[R_{ws}]$	$\langle D \rangle$ $[R_{ws}]$	$\langle \Delta N \rangle / \tilde{L}$ $[10^{-2}]$	$\langle \Delta E \rangle / L$ $[10^4$ erg/cm$]$	f_L $[10^{15}$ dyn/cm$]$	σ_{f_L} $[10^{15}$ dyn/cm$]$
100	1	1	0.289	1.320	4.185	0.549	1.222	0.086
		2	0.313	1.356	4.466	1.290	3.404	0.250
		3	0.204	1.270	-3.687	5.689	22.970	1.453
		4	0.531	2.064	-5.994	17.127	61.521	5.689
		5	2.514	3.893	-13.779	5.439	12.578	2.501
	3	1	0.591	2.072	6.730	0.417	0.630	0.069
		2	0.555	2.005	6.496	0.704	1.362	0.143
		3	0.504	2.060	-5.866	7.240	18.459	1.751
		4	1.490	3.396	-9.725	5.542	10.904	1.698
		5	8.080	4.634	-23.797	0.553	0.994	0.256
500	1	1	0.289	2.066	1.940	0.254	0.367	0.058
		2	0.313	2.142	2.031	0.587	1.015	0.167
		3	0.204	1.732	-1.504	2.321	7.190	0.833
		4	0.531	2.880	-2.342	6.693	17.690	3.028
		5	2.514	4.348	-5.184	2.046	4.349	1.277
	3	1	0.591	3.092	2.900	0.179	0.191	0.046
		2	0.555	2.970	2.809	0.304	0.416	0.095
		3	0.504	2.804	-2.305	2.845	5.418	0.946
		4	1.490	3.915	-3.541	2.018	3.529	0.726
		5	8.080	4.842	-8.812	0.205	0.375	0.130
1000	1	1	0.289	2.407	1.431	0.188	0.238	0.053
		2	0.313	2.467	1.491	0.431	0.651	0.152
		3	0.204	2.049	-1.086	1.676	4.388	0.744
		4	0.531	3.210	-1.615	4.616	11.033	2.587
		5	2.514	4.467	-3.575	1.411	3.024	1.090
	3	1	0.591	3.358	2.113	0.131	0.133	0.042
		2	0.555	3.283	2.044	0.221	0.286	0.088
		3	0.504	3.129	-1.606	1.982	3.403	0.816
		4	1.490	4.131	-2.362	1.346	2.350	0.566
		5	8.080	4.938	-6.037	0.140	0.267	0.112
2500	1	1	0.289	2.845	1.031	0.135	0.149	0.050
		2	0.313	2.900	1.067	0.308	0.420	0.143
		3	0.204	2.533	-0.756	1.167	2.462	0.688
		4	0.531	3.544	-1.062	3.034	6.777	2.324
		5	2.514	4.648	-2.355	0.930	2.184	0.981
	3	1	0.591	3.663	1.513	0.094	0.096	0.040
		2	0.555	3.530	1.455	0.158	0.207	0.083
		3	0.504	3.468	-1.074	1.325	2.205	0.740
		4	1.490	4.294	-1.463	0.833	1.506	0.466
		5	8.080	4.992	-3.941	0.092	0.190	0.101
5000	1	1	0.289	3.067	0.852	0.112	0.123	0.049
		2	0.313	3.147	0.884	0.255	0.339	0.140
		3	0.204	2.783	-0.603	0.930	1.828	0.656
		4	0.531	3.731	-0.828	2.366	5.317	2.233
		5	2.514	4.681	-1.834	0.724	1.801	0.936
	3	1	0.591	3.799	1.223	0.076	0.080	0.039
		2	0.555	3.714	1.183	0.128	0.171	0.080
		3	0.504	3.632	-0.844	1.042	1.677	0.713
		4	1.490	4.482	-1.085	0.618	1.133	0.433
		5	8.080	5.044	-2.996	0.070	0.153	0.096

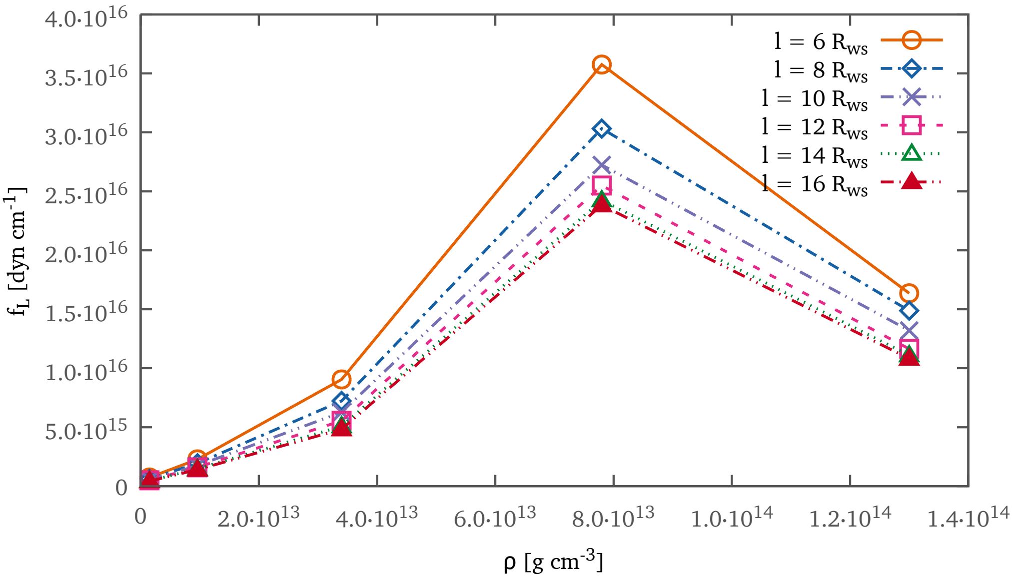

Figure 3.8: Convergence test for the l parameter used in our calculation. In this figure we can see the pinning force per unit length for the five zones of the inner crust, obtained with different choices of the parameter: *increasing* the value of l the curves become closer, showing the convergence of the model. This picture corresponds to a vortex of length $L = 200R_{\rm ws}$.

matter (Gandolfi et al., 2008). The results for the pinning force per unit length are also plotted in fig. 3.10 for $\beta = 1$ and in fig. 3.11 for $\beta = 3$. In the table we also show the results for $\langle D \rangle$, for $\langle \Delta N \rangle / \widetilde{L}$ and for $\langle \Delta E \rangle / L$, which are the angular averages of $D(\theta, \phi)$, $\Delta N(\theta, \phi)/\widetilde{L}$, and $\Delta E(\theta, \phi)/L$ respectively. We notice that $|\langle \Delta N \rangle| / \widetilde{L} \ll 0.5$ when $\widetilde{L} \sim 10^3$, which confirms the inadequacy of using symmetric vortex-lattice configurations when evaluating the mesoscopic pinning force (Jones, 1990b).

From these results it is possible to see that there is a strong dependence of the pinning force per unit length on the parameter L: increasing the length of the vortex a consistent decrease in the mesoscopic pinning force can be observed. This behavior was indeed expected, following the argument by Jones (1991b) that the difference in energy between adjacent configurations becomes vanishingly small for infinite vortex rigidity ($L \to \infty$). However, using a realistic vortex length of order $\sim 10^3 R_{\rm ws}$, as discussed in section 3.2.3, the pinning force is still not negligible.

The other important parameter of the model is the polarization factor β. The results show that f_L doesn't depend very strongly on the choice of this parameter in the three lower density regions, while the effect is more important in the two high density regions, where the mesoscopic pinning force is significantly larger in the strong pairing scenario ($\beta = 1$) than in the weak one ($\beta = 3$). It's also worth noting that changing the polarization factor from $\beta = 1$ to $\beta = 3$, results in a shift to lower densities of the

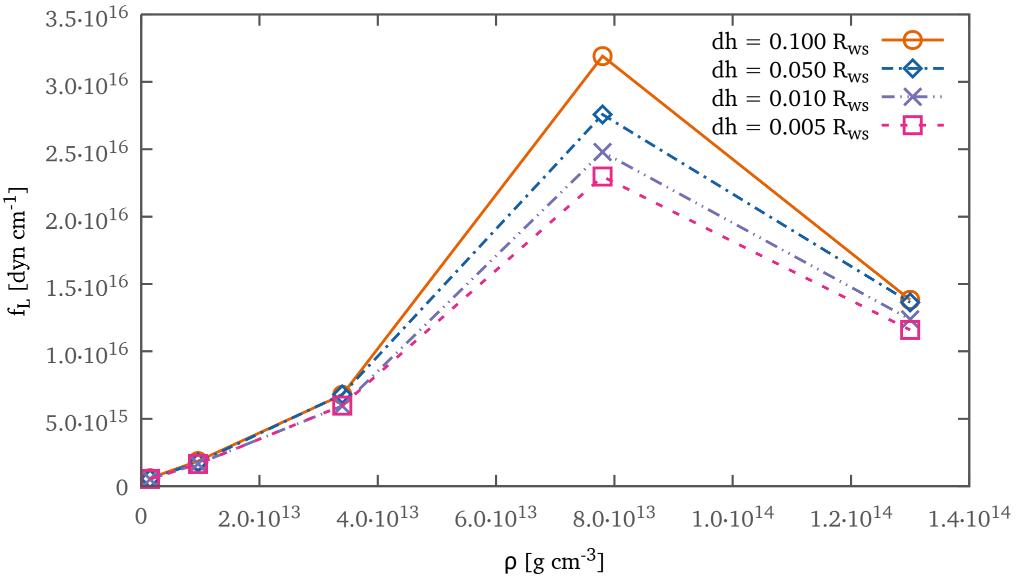

Figure 3.9: Convergence test for the dh parameter used in our calculation. As in fig. 3.8 we can see that *decreasing* the value of dh the curves become closer, showing the convergence of the model also for this parameter. This picture corresponds to a vortex of length $L = 200R_{\mathrm{ws}}$.

maximum of the pinning profile. The position in density of the maximum pinning force can be relevant to determine the angular momentum accumulated in the crust between pulsar glitches, as discussed in Pizzochero (2011).

A comparison between our results and those found in the literature shows that the maximum pinning forces per unit length obtained in this work are at least two orders of magnitude smaller than those found for an aligned vortex (Alpar et al., 1984a; Anderson et al., 1982) and which have been commonly used in the study of pulsar glitches. As we shall discuss in the following, however, they are still large enough to account for the large glitches observed in the Vela pulsar.

3.4.1 Analytic approximations

The results presented up to now refer to the calculation of the mesoscopic pinning force corresponding to the fiducial parameters R_{ws}, R_N, ξ and E_p in table 3.1. However, existing or future calculations of the inner crust nuclear structure, of the neutron superfluid pairing properties and of the microscopic vortex-nucleus interaction may provide alternative sets of parameters to those used in the present work. It is possible to generalize our approach and obtain a simple analytic expression which allows to calculate the pinning force per unit length f_L for different choices of the input parameters.

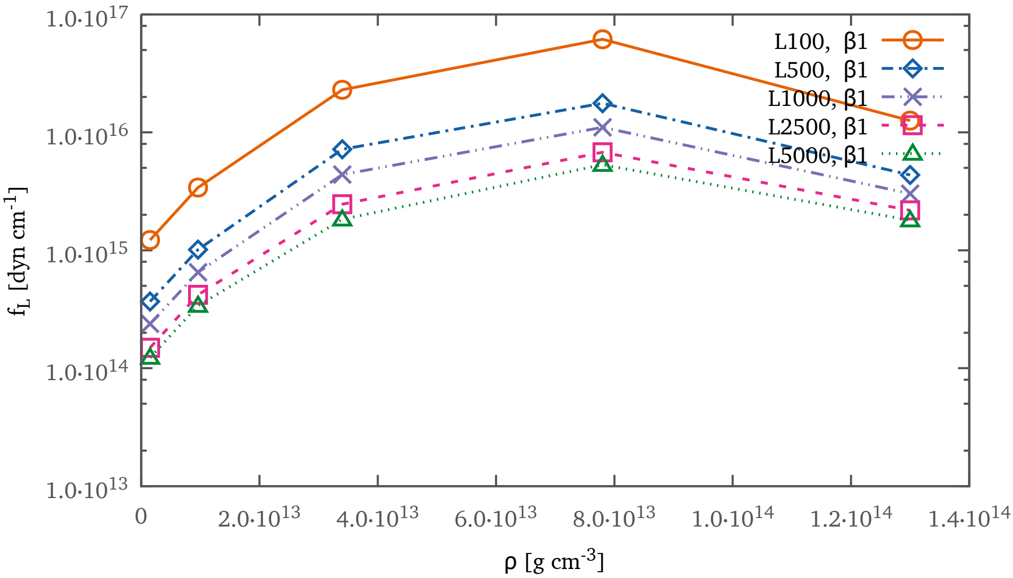

Figure 3.10: The pinning force per unit length for the $\beta = 1$ case. The mesoscopic pinning force is plotted as a function of the baryonic density of matter for the five zones considered and for different vortex lengths.

In eq. (3.20), the quantity E_{eff} can be factorized. We can also express all the lengths in R_{ws} units and then define an adimensional quantity $\widetilde{f}_{\widetilde{L}}(\widetilde{r}_c)$ that depends *only* on the adimensional capture radius $\widetilde{r}_c = r_c/R_{\text{ws}}$ and the adimensional vortex length $\widetilde{L} = L/R_{\text{ws}}$. The quantity $\widetilde{f}_{\widetilde{L}}(\widetilde{r}_c)$ is purely geometrical and it contains all the information obtained from the counting procedure described in the preceding sections. The force per unit length f_L (in dyn/cm) can then be obtained as

$$f_L = \frac{E_{\text{eff}}}{R_{\text{ws}}^2} \widetilde{f}_{\widetilde{L}} \left(\frac{r_c}{R_{\text{ws}}} \right) \tag{3.21}$$

where E_{eff} must be expressed in MeV and the radius of the Wigner–Seitz cell in cm.

We have calculated $\widetilde{f}_{\widetilde{L}}(\widetilde{r}_c)$ for different choices of $\widetilde{r}_c$ (in the realistic range $0 \div 8$) and for different vortex lengths (of order $\widetilde{L} \sim 10^3$) for both the NP and IP regimes We then fitted a non-linear function $f^*(x)$ to the calculated values of $\widetilde{f}_{\widetilde{L}}$: we used a function of the form

$$f^* = Ax + B\left[\log(1+x)\right]^W + C \tag{3.22}$$

where A, B, C and W are the parameters to be fitted. In fig. 3.12 we show the results for the $\widetilde{L} = 5000$ case; the error bars have also been added, as obtained from the propagation of the error on $n_{N_{\text{bound}}}(\theta, \phi)$. We see that the calculated points can be fitted reasonably (within the error bars) with the choice of parameterization in eq. (3.22). In table 3.4 we give the parameters obtained from the fitting procedure.

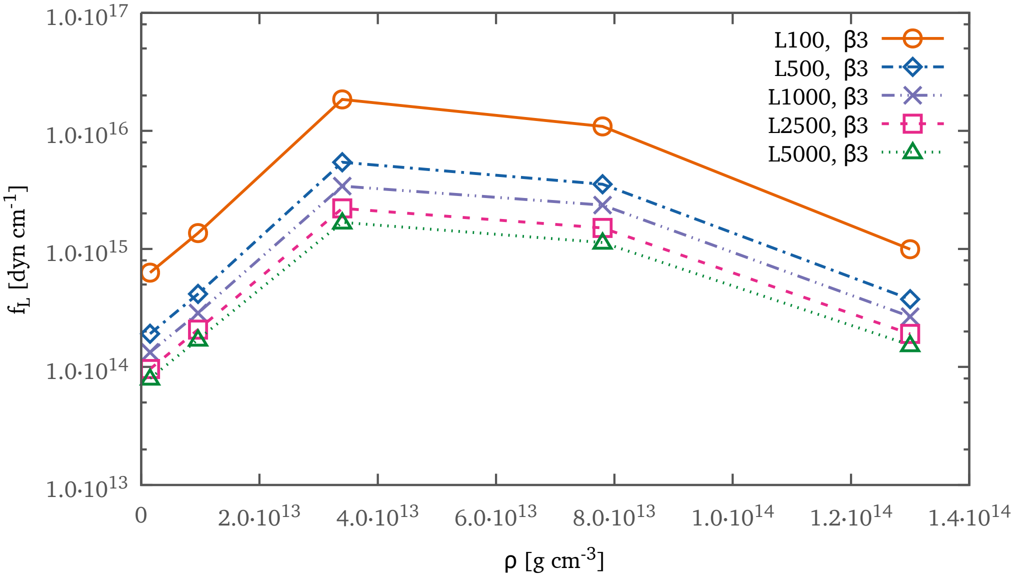

Figure 3.11: The pinning force per unit length for the $\beta = 3$ case. The pinning force per unit length for the $\beta = 1$ case. The mesoscopic pinning force is plotted as a function of the baryonic density of matter for the five zones considered and for different vortex lengths.

Table 3.4: Fit parameters for the function $f^* = Ax + B\,[\log(1+x)]^W + C$. Three different vortex lengths L are considered for both the NP and IP regimes.

		A $[10^{-10}]$	B $[10^{-9}]$	W	C $[10^{-8}]$
$L = 1000\,R_{\rm ws}$	NP	- 5.04	-2.08	1.974	-1.169
	IP	-33.63	14.49	1.586	1.155
$L = 2500\,R_{\rm ws}$	NP	-12.10	1.80	-0.366	-0.995
	IP	- 5.99	12.31	0.997	0.490
$L = 5000\,R_{\rm ws}$	NP	-10.35	0.75	-0.643	-0.726
	IP	-12.36	12.24	1.114	0.389

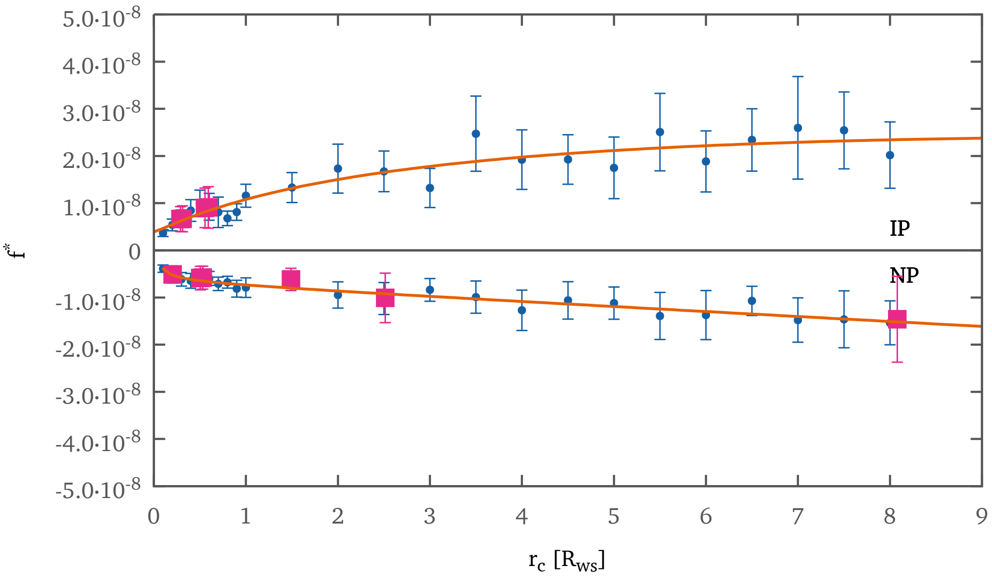

Figure 3.12: Plot of the calculated values of $\widetilde{f}_{\widetilde{L}}$ (for $\widetilde{L} = 5000$) as a function of the capture radius r_c (in units of R_{ws}). The error bars for the estimated errors on $\widetilde{f}_{\widetilde{L}}$ are also shown. The squares are the values of $\widetilde{f}_{\widetilde{L}}$ corresponding to the ten values of r_c in table 3.2. The fitting curves f^* for both the interstitial (above) and nuclear (below) pinning regimes are also shown (see table 3.4).

We notice that, within the uncertainty given by the quite large error bars, there is no significant difference in the magnitude of $\widetilde{f}_{\widetilde{L}}(\widetilde{r}_c)$ between the *nuclear* and the *interstitial* regime. This means that the force per unit length, for given $\widetilde{r}_c$ and E_{eff}, remains roughly the same if we take the microscopic vortex-nucleus force to be attractive or repulsive. The fact that attractive and repulsive vortex-nucleus interactions are equivalent for the pinning of vortexes to the lattice was already noted by Link (2009).

3.5 Conclusions

In this chapter we have presented a realistic calculation of the pinning force per unit length acting on a vortex in a neutron star crust. We have calculated the mesoscopic pinning force at different densities for straight vortexes that cross the star inner crust, and averaged over all the possible orientations of the crustal lattice with respect to the vortex. Our results confirm the expectations of (Jones, 1991b), that the averaging procedure over different orientations tends to smooth out energy differences between different configurations, leading to weaker pinning forces. In the limit of infinitely long vortexes the pinning force would vanish; for realistic values of the vortex tension the force per unit length is, however, still sizable and in the range $f_L \approx 10^{14} - 10^{15}$ erg/cm depending on the position in the crust. We find that the mesoscopic pinning force depends very little on whether the pinning force is attractive (nuclear pinning) or repulsive (interstitial pinning) in a given region of the star, but it can be quite sensitive to in-medium polarization effects, which can shift the position of the maximum and thus alter the angular momentum distribution in the crust of a neutron star.

In the following chapter we will apply the calculated forces to the problem of pulsar glitches in order to understand if these results can explain large glitches in the Vela pulsar, within the framework of the “snowplow” model (Pizzochero, 2011). More generally the forces that we have calculated can be used to generate realistic pinning profiles for glitch models (Haskell et al., 2012c; Haskell and Antonopoulou, 2013), simulations of vortex dynamics in neutron stars (Warszawski and Melatos, 2008) or mode calculations (Glampedakis and Andersson, 2009; Link, 2012a).

CHAPTER 4

Core pinning

The pinning interaction in the core of a neutron star is a much less explored problem than the crustal pinning one faced in chapter 3. In the NS interiors, matter is not organized in lattice because it's in superfluid and superconductive state: an hypothetical pinning force can't be related to vortex–lattice interaction. Instead it's possible, under certain circumstances, an interaction of the vortex with the magnetic flux carried by the superconductive protons. Currently it's yet unclear if protons in the core form a type I superconductor, in which the magnetic field is contained in regions of normal protons (Sedrakian, 2005) and therefore pinning effects are excluded (Jones, 2006), or they make a transition to a type II superconductivity state (Migdal, 1959; Baym et al., 1969). In this latter case the magnetic flux is confined to flux tubes and a pinning interaction between vortexes and flux tubes is possible. The transition from type II to type I occurs above a critical density that is expected to be bigger than the nuclear saturation density but it's still unknown, due to the uncertainties in the nucleon–nucleon potentials (Link, 2003).

In the following chapters we will face the problem from a macroscopic point of view: we will test the "snowplow" model firstly without any form of pinning in the neutron star interiors, and after, in chapter 6, considering that a fraction of the vorticity in the core is completely blocked by entanglement with the flux tubes. Conversely in this chapter we want to adopt a mesoscopic approach, applying the same conceptual ideas of chapter 3 to estimate the pinning force per unit length in the core of a neutron star. We will show that the core pinning (if the star is actually in type II state) is two orders of magnitude lower than the crustal one, and this means that, according to the results of chapter 6, it can be safely neglected in our macroscopic glitch model.

4.1 A simple approach

In type II superconductor core of a neutron star, the magnetic flux is confined inside tubes that have a core of normal protons; the radius of this region can be taken equals to the proton coherence length $\xi_p \approx 10\,\mathrm{fm}$. On the other side the coherence length for neutrons, and therefore the radius of the vortex, is $\xi_n \approx 25\,\mathrm{fm}$ (Link, 2003). The coupling between the two condensates is due to the induced proton current around the vortexes that magnetizes them (Alpar et al., 1984c; Chau et al., 1992; Harvey et al., 1986): this kind of entrainment generate the pinning force because a magnetized neutron vortex interact with the flux confined in the tubes. Outside the flux tube, the magnetic field falls off exponentially over a distance equal to the London length. We identify this quantity with Λ_p that is approximately equals to 80 fm, and in the same way we call $\Lambda_n \approx 10\,\mathrm{fm}$ the length scale over which the magnetic field of the vortex decays. Results of Ruderman et al. (1998); Link (2003, 2012a) indicate that the energy increase per single interaction between a vortex approaching a flux tube is $E_p \approx 5\,\mathrm{MeV}$, over the length range Λ_p.

To calculate the pinning force per unit length in the core we can use a very simple model, as done by Link (2003). We can consider a straight vortex immersed in an array of flux tubes. These tubes form a two dimensional quadratic array in the xy plane and they extend in the z direction. The vortex lies in the xy plane, aligned with a versor of the lattice and therefore perpendicular to the flux tubes. Given that the force per single interaction is $F_p = E_p/\Lambda_p$, the force per unit length can be easily evaluated as

$$f = \frac{F_p}{l_\phi} = \frac{E_p}{\Lambda_p\, l_\phi}, \tag{4.1}$$

where l_ϕ is the average spacing between flux tubes. This quantity depends on the magnetic field B of the star because $l_\phi = 1/\sqrt{n_\phi}$, where $n_\phi = B/\Phi_0$ ($\Phi_0 = \pi\hbar c/e$ is the flux quantum). We can express B in unit of 10^{12} G (we identify this quantity as B_{12}, and we will use the realistic value of ≈ 1 in the following; for a magnetar $B_{12} \approx 100 \div 1000$, as we'll discuss) obtaining the benchmark $l_\phi \approx 3000/\sqrt{B_{12}}$fm. As a conclusion, the approach here described gives as result an order of magnitude for the core pinning force per unit length of 10^{15} dyn/cm (see Link (2003)).

4.2 The realistic mesoscopic model

The naive calculation just described here gives as result the maximum pinning force because it considers only the aligned configuration. Qualitatively this is the same approach of the first works about the crustal pinning, that were focused on the force per single interaction F_p; then the force per unit length was simply found by dividing this quantity by the spacing between pinning site. In chapter 3 we overcome this schema, justifying the need to consider and average all possible orientations between vortex and the lattice. Here we are focusing on the core pinning due to the vortex–fluxtube interaction that is quite different under some physical points of view, but we can apply the same conceptual approach (that we review here) of the previous chapter to correctly estimate the force per unit length f_p. In fact the vortex has a finite rigidity and this means that can be considered straight only on a length scale L; on larger scale the interaction with fluxtubes will bend the vortex, changing its orientation

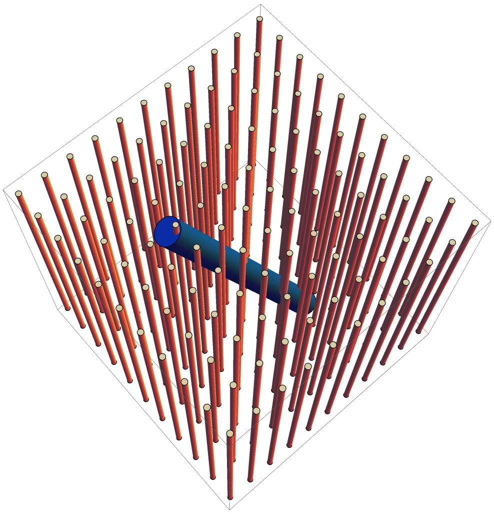

Figure 4.1: Schematic representation of a vortex immersed in a regular lattice of flux–tubes, all oriented in the same direction.

with the lattice. Moreover, unlike the vortexes that are expected to be approximately parallel to the rotational axis of the star (except for bending), the flux tube array has a complicated structure because the tubes are twisted and therefore entangle the vortexes. The geometric configuration that we take into account is described in fig. 4.1. We consider a vortex of finite length immersed in a lattice of straight fluxtubes with a generic casual orientation. The tubes extend parallel over the z direction and are infinitely long; in the xy plane they are equally spaced on a regular grid. The Wigner–Seitz radius of the lattice cell is R_{ws} and of course the distance between two consecutive tubes in the grid is $2R_{\mathrm{ws}}$. As discussed before, $R_{\mathrm{ws}} = l_\phi/2$ and therefore its value depends on the magnetic field of the star by the following relation:

$$R_{\mathrm{ws}} = \frac{1500}{\sqrt{B_{12}}}\mathrm{fm}. \tag{4.2}$$

It's important to note that here, by the moment, we don't take into account the twisted structure of the fluxtubes (for the entanglement effect), as this aspect will be covered later. To estimate the length L on which the vortex can be considered rigid, we can use the same technique of section 3.2.3: the eq. (3.15) indicates that L, in units of R_{ws}, scales as $\sim 2TR_{\mathrm{ws}}/E_p$ where T is the tension of the vortex. Even if we use the same tension used in section 3.2.3 for crustal pinning, the results in this case will be different because R_{ws}, that control the scale of the problem, is bigger. In fact, following the prescription used by Link (2003), $R_{\mathrm{ws}} \approx 1500\,\mathrm{fm}$ (in the crustal pinning this parameter is $\sim 30\,\mathrm{fm}$), and this lead certainly to $L \sim 10^4 R_{\mathrm{ws}}$. As we will show later, a longer vortex will results, as expected, in a lower pinning force per unit length f. We'll see that even just taking $L = 1000R_{\mathrm{ws}}$, f will be at least two orders of magnitude lower that the crustal pinning case (enough to justifying the neglect in the snowplow model). Iin order to maintain the computational time affordable, we will perform our calculations here with these four different choices of L: $1000R_{\mathrm{ws}}$, $2500R_{\mathrm{ws}}$, $5000R_{\mathrm{ws}}$ and $10\,000R_{\mathrm{ws}}$.

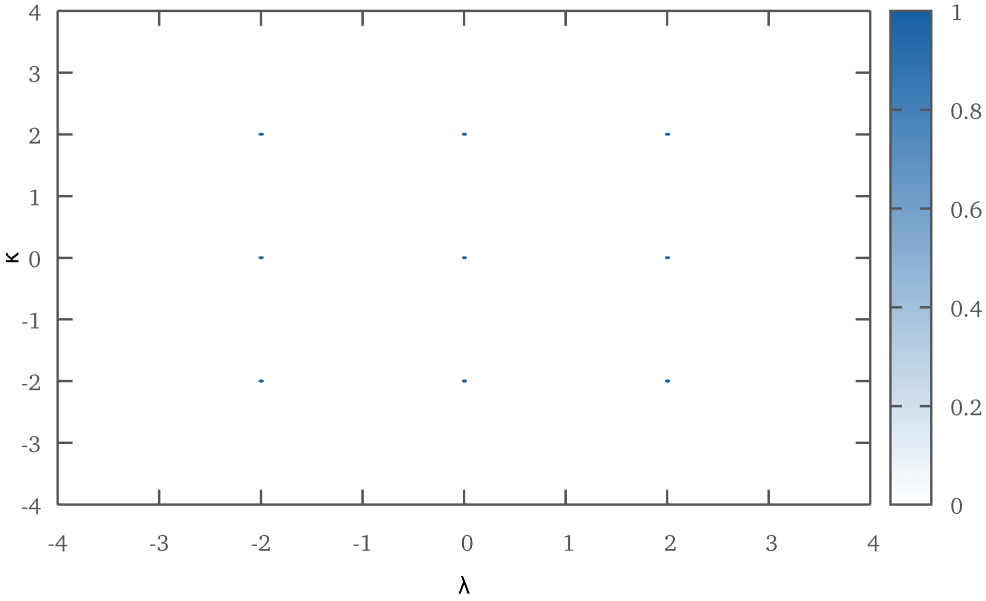

Figure 4.2: Number of captured pinning sites $N(\lambda, \kappa)$ when the vortex is aligned with the lattice. The color codes are described in the sidebar. The axes κ and λ represent the translation of the vortex with respect to the initial position, and they are measured in R_{ws} units. The grid step size is $dh = 0.01 R_{\text{ws}}$, the vortex length is $L = 500 R_{\text{ws}}$ and the capture radius is $r_c = 0.027 R_{\text{ws}}$. The lattice is the one represented in fig. 4.1

To explain the algorithm used, let's start with a vortex with a random orientation with respect the fluxtubes array. The orientation is identified using standard polar coordinates, therefore with the angles θ and ϕ that the vortex form with the lattice. For a given choice of (θ, ϕ), we perform a counting procedure by moving the vortex parallel to itself, covering a square region with side l, with steps of an amount dh. We identify the displacement of the vortex from the initial position with (λ, κ), and for each new position we count the number of intersections $N(\lambda, \kappa)$ that the vortex has with the tubes.

This problem becomes simpler (and is geometrically equivalent) if we consider the fluxtube as a line without dimension, while the vortex is a cylinder with a capture radius $r_c = \xi_p + \xi_n$. This means that every time a "flux–line" falls into the cylinder that represent the neutron vortex we must increment our counter. The fig. 4.2 shows with color codes the number of interaction as a function of the position (λ, κ). This plots represents the extreme case when the vortex is perfectly aligned with the fluxtubes array, namely $\theta = \phi = 0$: as expected a single interaction is recorded only at correspondence of a tube, creating a regular simple pattern. The coordinates λ and κ are given in R_{ws}units and the dark dots are so small because the capture radius is tiny compared to the spacing between tubes: the benchmarks by Link (2003) in fact indicate that

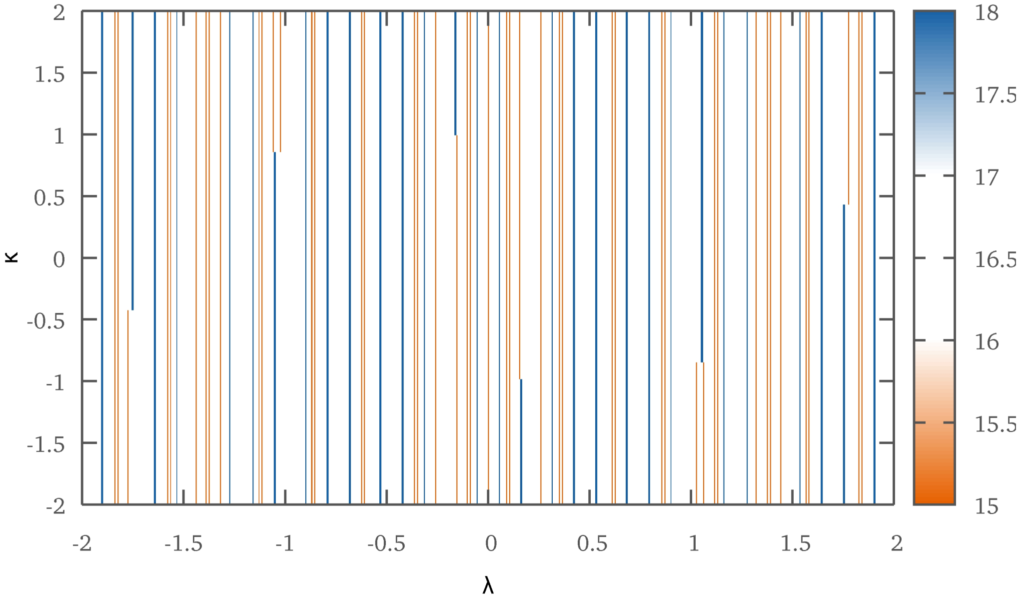

Figure 4.3: Number of captured pinning sites $N(\lambda,\kappa)$ when the vortex is non–aligned with the lattice (we selected a random orientation). The color codes are described in the sidebar. For details on the parameters used to produce this plot see fig. 4.2

$r_c \sim 0.025 R_{\mathrm{ws}}$. On the other hand, fig. 4.3 shows a more general situation, in which the vortex is randomly aligned with the lattice: we can see an alternation of light and dark lines that represent zones where the number of interactions reaches its minimum and maximum value respectively.

The single vortex–fluxtube interaction can be repulsive (R) or attractive (A) depending on whether the magnetic fields are aligned or antialigned: this fact reflects in a different sign of the quantity E_p that can be positive (R case) or negative (A case). We must cover these two cases separately, in order to correctly evaluate the pinning force per unit length. In the attractive regime, we identify the *bound* positions with the displacements (λ,κ) of the vortex for which the number of interactions is maximal, i.e. $N(\lambda,\kappa) = N_{\mathrm{bound}} = \max(N(\lambda,\kappa))$. On the contrary, the repulsive situation focuses on the minimum number of interaction (this defines the *bound* positions), and this means that $N_{\mathrm{bound}} = \min(N(\lambda,\kappa))$.

Once we have dealt this distinction, we can properly calculate the force with a generalized approach that covers both cases. In fact the change in energy obtained by moving the vortex away from its bound configuration will be:

$$\Delta E(\theta,\phi) = E_p(N_{\mathrm{free}}(\theta,\phi) - N_{\mathrm{bound}}(\theta,\phi)) \tag{4.3}$$

where we take N_{free} as the average number of interactions counted in all visited displacements: $N_{\mathrm{free}}(\theta,\phi) = \langle N(\lambda,\kappa)\rangle$. The force (per unit length) required to move away the vortex from the bound position is therefore easily calculated as

$$f_L(\theta,\phi)=\frac{\Delta E(\theta,\phi)}{L\,D(\theta,\phi)}, \tag{4.4}$$

where $D(\theta,\phi)$ is the average distance between the bound and free configuration.

Until now, the procedure described is the same one that has been applied also for the pinning in the inner crust of the neutron star. The calculation of the mean distance $D(\theta,\phi)$ is however a little different. In chapter 3 we have used the surface density of the bound configurations, but here the pattern showed in fig. 4.3 suggests another approach. The degeneration of the lattice in the z direction reflects in density plot with alternating "vertical" stripes of positions with equal energy. The fact that these stripes are oriented vertically depends on our choice of the reference system for (λ,κ); with a different choice the stripes would be oblique, but the model remains valid and consistent. Therefore we count the number $n_{N_{\mathrm{bound}}}$ of disjoint line–like regions for which the number of intersection is N_{bound} and use the linear density of these, i.e:

$$D(\theta,\phi)=\frac{l}{n_{N_{\mathrm{bound}}}(\theta,\phi)}, \tag{4.5}$$

where l is the side of the square region covered with the parallel transport procedure. The last step of our algorithm is averaging over all possible orientation, thus performing an integration over the whole solid angle $d\Omega=\sin\theta\,d\theta\,d\phi$.

As described before, a single interaction affects the energy of the configuration by a fixed amount E_p, no matter at what angle, between vortex and fluxtube, the intersection occurs. A better approach could be considering the intersecting volume, but unfortunately this picture would be computationally intractable. A reasonable solution can be found by following the idea that this intersecting volume leads to a factor $1/\sin\theta$ that must be included in the calculations. We can therefore define a new quantity E_{eff} which is the effective energy per interaction and has the following expression:

$$E_{\mathrm{eff}}=E_p\frac{|\cos\theta|}{\sin\theta} \tag{4.6}$$

The factor $|\cos\theta|$ in this equation cames from the expression of the magnetic energy between two dipole. The final equation for the pinning force per unit length is then:

$$f_L=\frac{1}{4\pi}E_p\int\frac{N_{\mathrm{free}}(\theta,\phi)-N_{\mathrm{bound}}(\theta,\phi)}{L\,D(\theta,\phi)}\frac{|\cos\theta|}{\sin\theta}\,d\Omega. \tag{4.7}$$

4.2.1 Flux–tubes entanglement

Until now we have considered straight flux tubes that are parallel to the z axis and therefore they form a regular oriented array. Anyway, as pointed out by Ruderman et al. (1998); Link (2003) this array has likely a much more complicated structure because the flux tubes are twisted and entangled. Of course this effect can impact

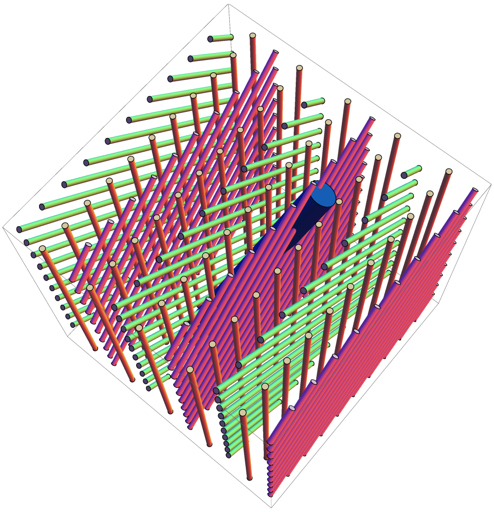

Figure 4.4: Schematic representation of a vortex immersed in the lattice used to model the entanglement. We can see the different planes of parallel fluxtubes.

over the results of our model and we want now to take into account this aspect. In order to accomplish this requirement, we change the lattice structure by considering alternating planes of tubes perpendicular to the y direction. Each plane contains parallel tubes oriented with an angle α relative to the z direction. The sequence of the angles α is $\{0, -\pi/4, 0, \pi/4, 0, -\pi/4, \dots\}$. This configuration, showed in fig. 4.4, permits us to model the entanglement, maintaining a net magnetic field oriented as the z direction. The spacing between these planes is the same of the spacing between the flux–tubes in one plane, i.e. $2R_{\text{ws}}$: this guarantees that the distance between two tubes is always greater than this value.

With this new configuration we can apply the same counting procedure, by moving a randomly oriented vortex with a parallel transport operation. The typical density plot is different from the case without entanglement, because the alternate planes of tubes brake the degeneracy showed in fig. 4.3. The plot of fig. 4.5 represent the situation of a randomly oriented vortex when the entanglement is taken into account. The details of the model described until now remains valid except for eq. (4.5) which specifies our definition of the average distance between the *bound* configuration, and must be corrected. We adopt the same approach used for the crustal pinning (see eq. (3.18) in chapter 3), as the typical patterns in the density plots are similar. The number $n_{N_{\text{bound}}}$, in this case, is therefore the number of *disjoint* regions for which the number of intersection between the vortex and the flux–tubes is N_{bound}. In this context we consider two points spaced by less that $\eta = 2\xi_p$ as belonging to the same *disjoint* region, for the reasons treated in chapter 3 (we will discuss mode deeply about the parameter η in the following section). The average spacing between extremal conditions is

$$D(\theta,\phi) = \frac{l}{\sqrt{\pi n_{N_{\text{bound}}}(\theta,\phi)}} \tag{4.8}$$

as they are uniformly distributed in the (λ,κ) plane. The expression for the force per

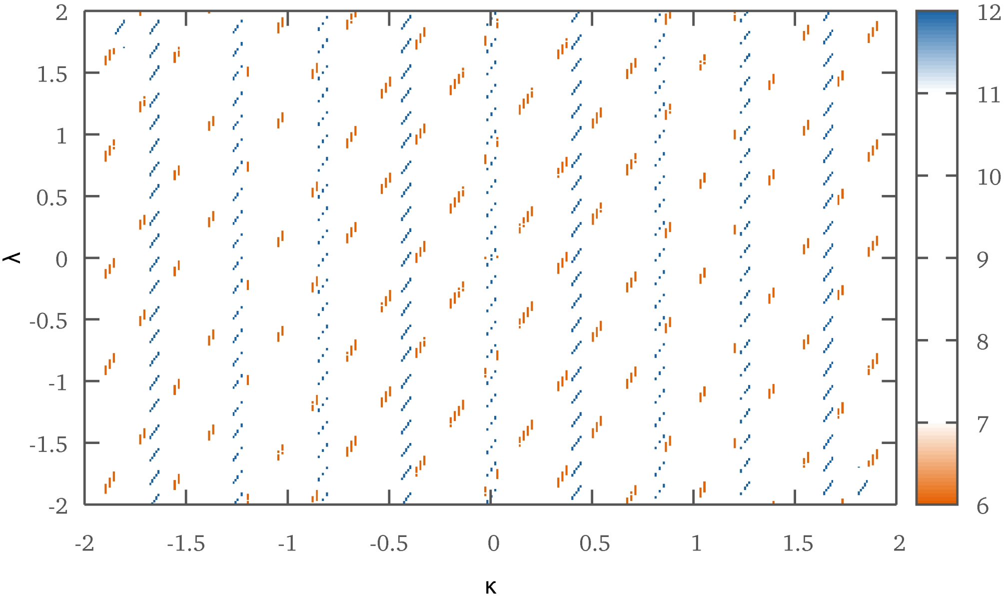

Figure 4.5: Number of captured pinning sites $N(\lambda, \kappa)$ when the vortex is non–aligned with the lattice (we selected a random orientation) when the entanglement is considered. The color codes are described in the sidebar. For details on the other parameters used to produce this plot see fig. 4.2.

unit length of a single orientation remain identical to eq. (4.4), and the average over the whole solid angle leads to the final result:

$$f_L = \frac{1}{4\pi} E_p \int \frac{N_{\text{free}}(\theta, \phi) - N_{\text{bound}}(\theta, \phi)}{L\, D(\theta, \phi)} \frac{|\cos\theta|}{\sin\theta}\, d\Omega. \tag{4.9}$$

4.3 Results

In eq. (4.7) we can see that E_p is factorized and, from the discussion of the previous section, we know that all the counted quantities depend only on the capture radius r_c. A specific discussion must be done for the *disjoint* parameter η because this quantity apparently doesn't depends on r_c, as we take it to be $\eta = 2\xi_p$. Anyway it's easy to show that this is not true. In fact, the neutron and proton coherence lengths can be expressed in the following way (Mendell, 1991):

$$\xi_p \approx 16\, x_p^{1/3} \rho_{14}^{1/3} \Delta_p(\text{MeV})^{-1}\text{fm} \tag{4.10}$$

$$\xi_n \approx 16\, x_n^{1/3} \rho_{14}^{1/3} \Delta_n(\text{MeV})^{-1}\text{fm} \tag{4.11}$$

where we have neglected the entrainment in the core; moreover x_p and x_n represent respectively the proton and neutron fraction over the total density and ρ_{14} is the density expressed in $10^{14}\,\mathrm{g\,cm^{-3}}$ units. By taking the realistic benchmarks $\Delta_n = \Delta_p = 1\,\mathrm{MeV}$, $x_n = 0.95$, $x_p = 0.05$ and $\rho_{14} = 2.8$ we obtain $\xi_p \approx 8.5\,\mathrm{fm}$ and $\xi_n \approx 22\,\mathrm{fm}$. The expressions provided indicate also that $(\xi_p/\xi_n) \simeq \left(x_p/x_n\right)^{1/3}$ and therefore we can express the capture radius as

$$r_c = \xi_p + \xi_n = \left[1 + \left(\frac{x_n}{x_p}\right)^{1/3}\right]\xi_p \tag{4.12}$$

and then, as we take $\eta = 2\xi_p$, we have

$$\eta = \frac{2}{1 + \left(\frac{x_n}{x_p}\right)^{1/3}} r_c \tag{4.13}$$

With realistic values for the proton and neutron fractions in the core of a neutron star we obtain $\eta \simeq 0.55 r_c$. We can thus express all the lengths in R_{ws}units (for this purpose we will write $\widetilde{L}$ to indicate L/R_{ws}) and define a new quantity $\widetilde{f_{\widetilde{L}}}$ that depends only on the parameter $\widetilde{r_c} = r_c/R_{\mathrm{ws}}$. Then the force per unit length f_L (in dyn cm^{-1}) can be obtained as $f_L = \widetilde{f_{\widetilde{L}}}(\widetilde{r_c}) E_p / R_{\mathrm{ws}}^2$, where E_p must be expressed in MeV and the radius of the Wigner–Seitz cell in cm.

In the following, the pinning force per unit length will be given thus as $\widetilde{f_{\widetilde{L}}}$ because this generalized version gives the possibility of calculating the result for specific values of E_p and R_{ws}. Of course the dependence of $\widetilde{f_{\widetilde{L}}}$ on the vortex length L can't be removed, therefore the four cases indicated will be explored, namely $1000\,R_{\mathrm{ws}}$, $2500\,R_{\mathrm{ws}}$, $5000\,R_{\mathrm{ws}}$ and $10\,000\,R_{\mathrm{ws}}$. The calculations rely on the appropriate choice of the parameter l (side of the square region considered during the parallel–transport operation) and of the grid step dh. In fig. 4.6 we show the convergence of our results for l and dh. The first parameter affects the calculation of the factor D because increasing l reflects in a more accurate evaluation of the density of maximal position: covering a square region of side $l = 16 R_{\mathrm{ws}}$ (as done in the following) is enough to count a good value of bound sites, from the statistical point of view. In the meanwhile a tiny grid step $dh = 0.005\,R_{\mathrm{ws}}$ is required to resolve all the bound positions, for the smallness of the capture radii used. A further reduction of this parameter wouldn't change the result thanks to the fact that we consider only the disjoint regions, regardless of how densely they are sampled.

The figs. 4.7 to 4.9 show our calculations with the parameters indicated, for different vortex lengths. We cover both the attractive case (A, negative values of the force) and the repulsive one (R) by evaluating the pinning force per unit length $\widetilde{f_{\widetilde{L}}}$ as a function of the capture radius r_c: the dots in the plots correspond to the configurations considered. Every case is explored with the two lattice types, to cover both the non–entangled and the entangled condition. The confidence levels of $1\,\sigma$ are also plotted: given that we are dealing with a counting procedure, we can simply

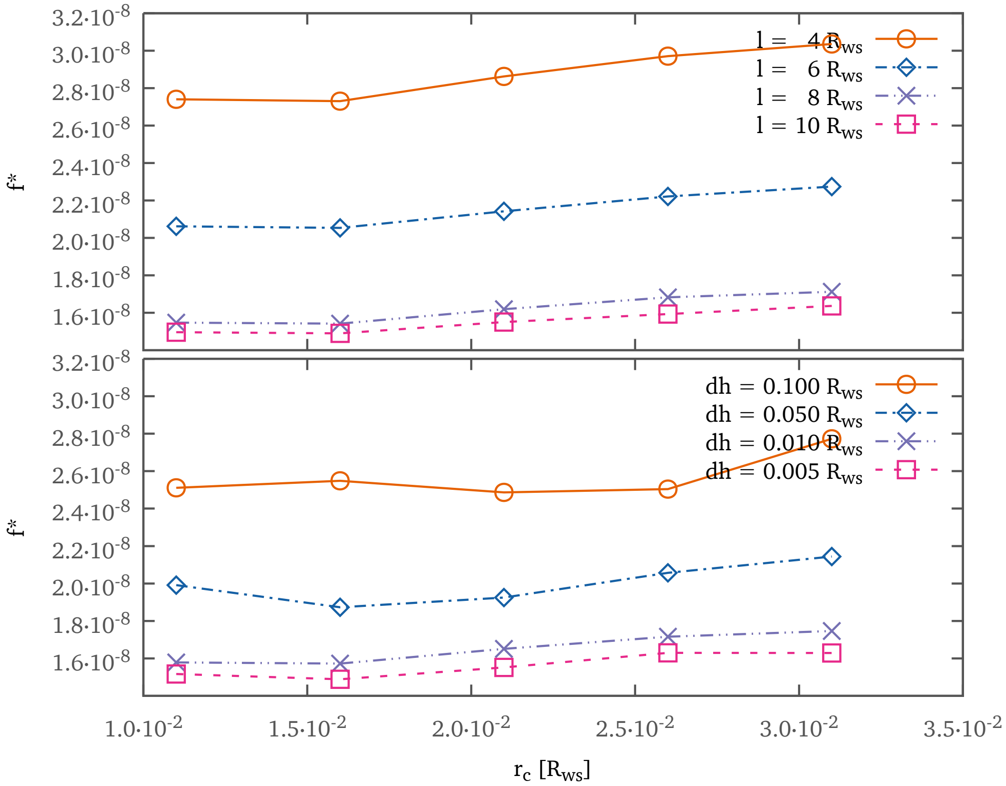

Figure 4.6: Convergence test for the parameters l and dh used in our calculation. In this figure we can see the pinning force per unit length $f_{\widetilde{L}}$ for different values of the capture radius r_c: increasing the value of l the curves become closer, showing the convergence of the model. An analogous effect is obtained by reducing the step size dh in the parallel transport operation. These pictures correspond to a vortex of length $L = 5000\,R_{\rm ws}$.

assume that the result of our integration for a single orientation is $n_{N_{\rm bound}} \pm \sqrt{n_{N_{\rm bound}}}$. We can then propagate this error in eqs. (4.4) and (4.7) to obtain the required result $\widetilde{f_L} \pm \sigma_{\widetilde{f_L}}$. The explored range for the capture radius is $(5 \times 10^{-3} \div 0.7)\,R_{\rm ws}$: this choice is driven to the fact that for a magnetar $r_c/R_{\rm ws}$ is much bigger than in a normal pulsar. In this work we consider $r_c = 30\,\text{fm}$ for both cases, but of course the magnetic field in eq. (4.2) change significantly from $B_{12} = 1$ for a pulsar (and therefore $r_c = 0.02\,R_{\rm ws}$) to $B_{12} = 1000$ (which corresponds to $r_c = 0.6\,R_{\rm ws}$) for a magnetar.

The curves in these plots are the results of a fitting procedure that provides an analytic expression for the quantity $\widetilde{f_L}(r_c)$. We fit a non-linear function $f(x)$ to the calculated values of $f_{\widetilde{L}}$ for different choices of $r_c/R_{\rm ws}$: the function used is

$$f^* = Ax + B\,[\log(1+x)]^W + C \tag{4.14}$$

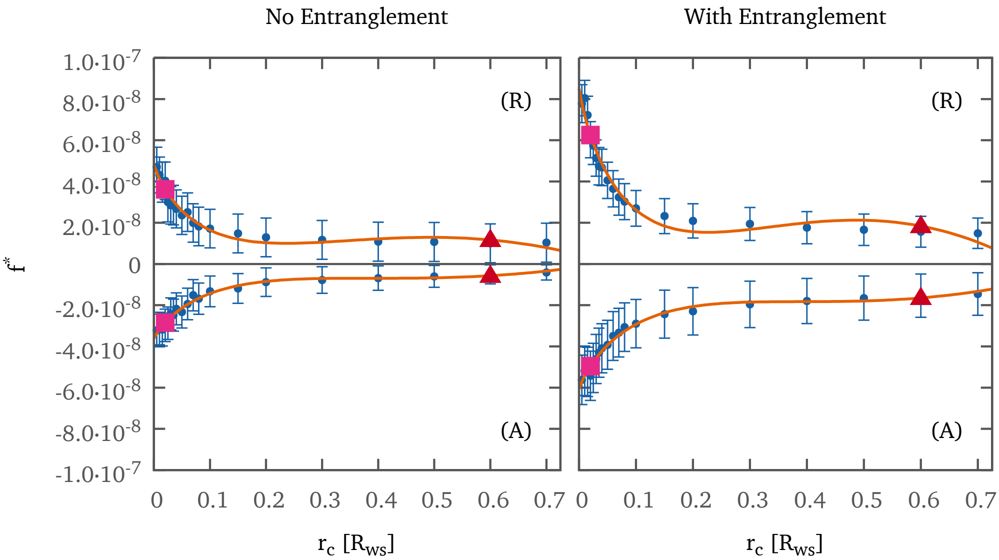

Figure 4.7: Plot of the calculated values of $\widetilde{f}_{\widetilde{L}}$ (for $\widetilde{L} = 1000$) as a function of the capture radius r_c (in units of R_{ws}). The error bars for the estimated errors on $\widetilde{f}_{\widetilde{L}}$ are also shown. The left picture refers to the simple regular lattice of flux–tubes, while on the right we have taken into account also the entanglement by using the described lattice. The fitting curves f^* for both the repulsive (above) and attractive (below) regimes are also shown (see table 4.1). The squares indicate the inferred values for a typical neutron star, while the triangles are referred to the capture radius for a magnetar (see text for details).

where A, B, C and W are the parameters of the fit and x is the fit variable, which describes the capture radius in R_{ws} units. The table 4.1 reports the obtained values which describe the curves. All the curves are finally plotted together in fig. 4.11 for the non–entangled case, and in fig. 4.12 for the entangled one. As expected, a longer vortex is related to a smaller pinning force per unit length. It's also worth noting that there is no significant difference in the order of magnitude of the result from the attractive configuration to the repulsive one. This means that the force per unit length, for a given capture radius, remain roughly the same if we consider the single site interaction attractive or repulsive. Moreover we note that there is no significant difference in the order of magnitude between the two lattice configurations (with or without the entanglement) taken into account: the following considerations about the impact of these result on pulsar glitch models are valid for both cases.

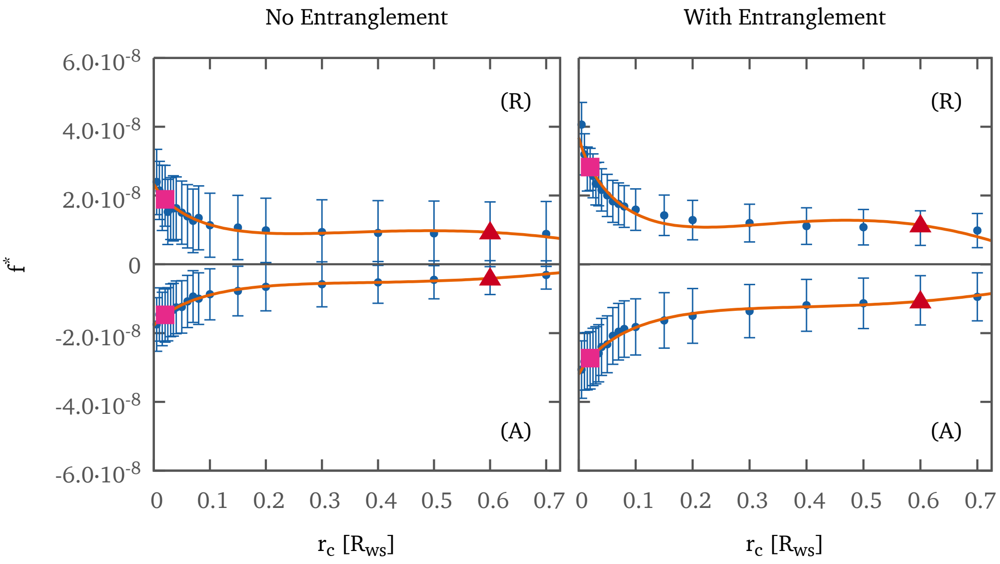

Figure 4.8: Plot of the calculated values of $f_{\widetilde{L}}$ (for $\widetilde{L} = 2500$) as a function of the capture radius r_c (in units of R_{ws}). See fig. 4.7 for other details.

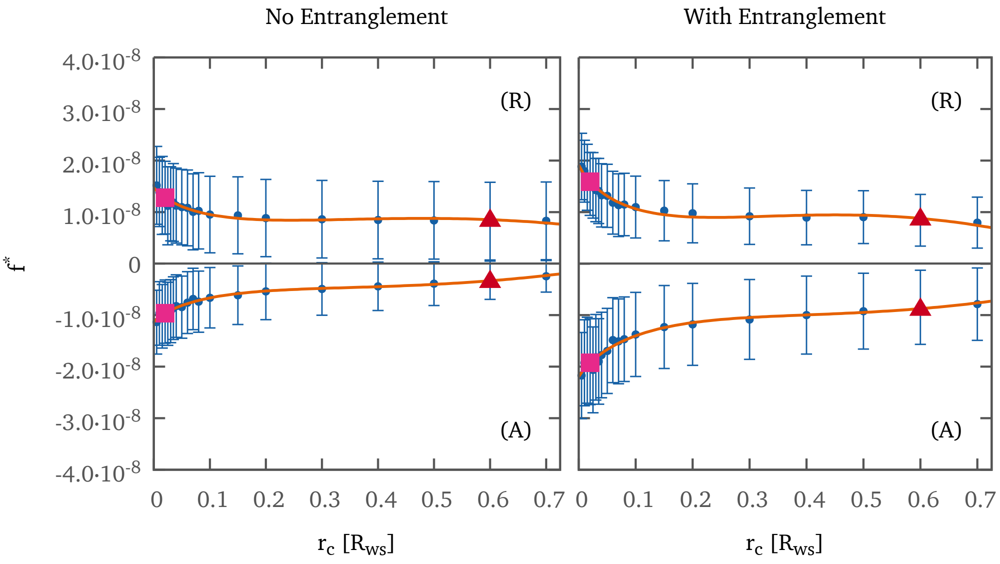

Figure 4.9: Plot of the calculated values of $f_{\widetilde{L}}$ (for $\widetilde{L} = 5000$) as a function of the capture radius r_c (in units of R_{ws}). See fig. 4.7 for other details.

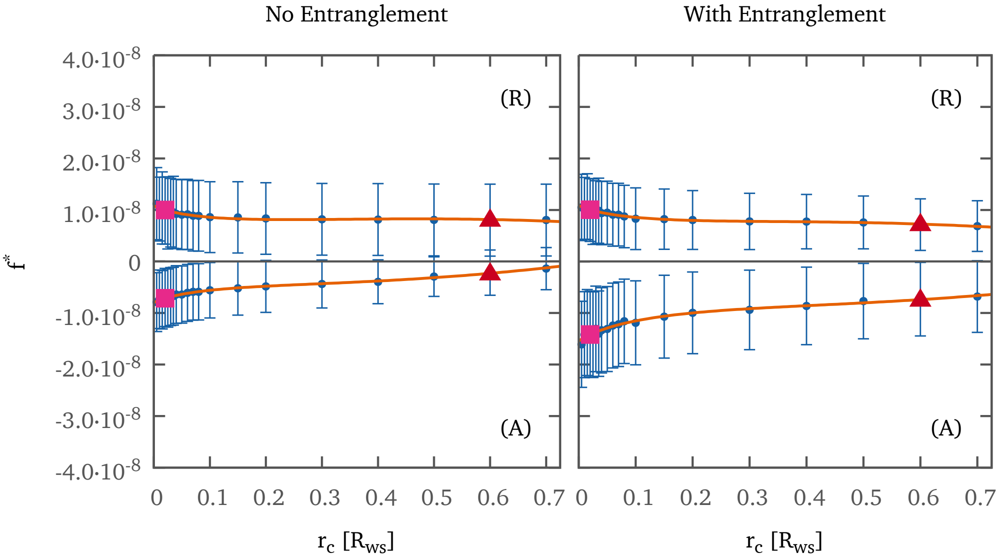

Figure 4.10: Plot of the calculated values of $\widetilde{f}_{\widetilde{L}}$ (for $\widetilde{L} = 10000$) as a function of the capture radius r_c (in units of R_{ws}). See fig. 4.7 for other details.

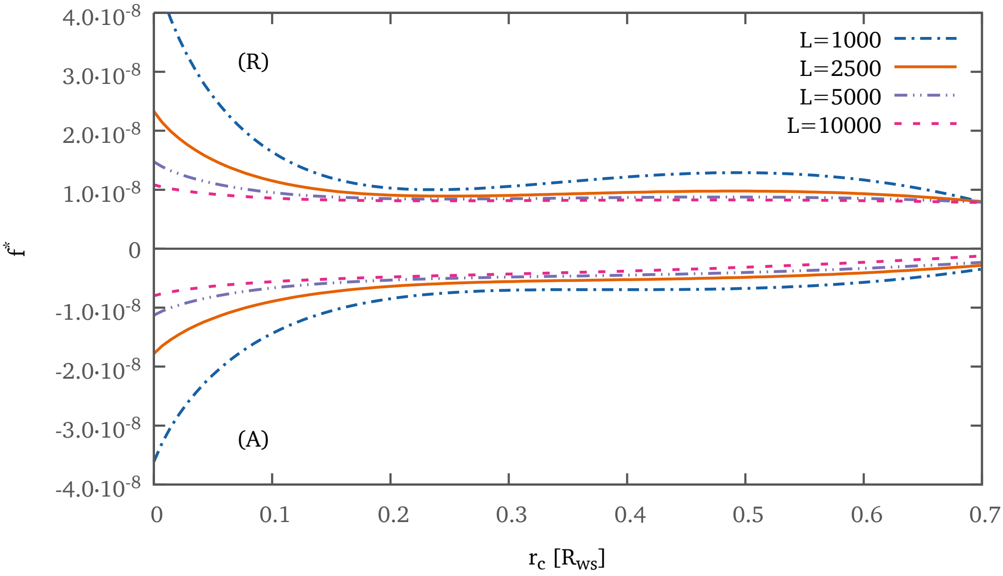

Figure 4.11: Plot of the fitting curves of table 4.1 obtained with the simple lattice without considering the entanglement effect.

Table 4.1: Fit parameters for the function $f^* = Ax + B\,[\log(1+x)]^W + C$. Four different vortex lengths L are considered for both the attractive (A) and repulsive (R) regimes. We give the results also for the entangled configurations.

			A $[10^{-7}]$	B $[10^{-6}]$	W	C $[10^{-8}]$
No Entanglement	$L = 1000 R_{\mathrm{ws}}$	A	6.546	−0.986	1.325	−3.610
		R	−11.230	1.695	1.296	4.814
	$L = 2500 R_{\mathrm{ws}}$	A	2.667	−0.396	1.319	−1.778
		R	−4.044	0.611	1.301	2.328
	$L = 5000 R_{\mathrm{ws}}$	A	1.496	−0.218	1.297	−1.128
		R	−1.818	0.274	1.297	1.473
	$L = 10\,000 R_{\mathrm{ws}}$	A	0.865	−0.119	1.252	−0.798
		R	−0.803	0.121	1.293	1.083
With Entanglement	$L = 1000 R_{\mathrm{ws}}$	A	9.315	−1.403	1.328	−6.051
		R	−21.590	3.253	1.289	8.503
	$L = 2500 R_{\mathrm{ws}}$	A	3.924	−0.585	1.330	−3.198
		R	−8.319	1.249	1.284	3.681
	$L = 5000 R_{\mathrm{ws}}$	A	2.214	−0.328	1.335	−2.194
		R	−3.137	0.470	1.285	1.912
	$L = 10\,000 R_{\mathrm{ws}}$	A	0.981	−0.141	1.348	−1.542
		R	−0.770	0.113	1.295	1.087

4.4 Conclusions

The results presented here are given in such way that they don't depend on the particular value of the Wigner–Sietz cell radius and of the single interaction energy: they are valid over a large range for the capture radius r_c and can be specialized when needed. However it's interesting to estimate the force, using the benchmarks presented previously (see also Link (2003)) that are so far the most realistic indication for the values of E_p, R_{ws} and r_c in the core of a neutron star. These results are reported in the upper part of table 4.2. Similarly we evaluate the same quantities for a magnetar (lower part of the table), for which we take a different capture radius, as described before. With regard to the values related to the *pulsar* case, they are significantly lower (more than two orders of magnitude) that the ones obtained with analogue technique of the crustal pinning (see chapter 3): this justify the assumption used in the snowplow model (see chapter 5) where we consider that the part of a vortex which threads the core of the neutron star is not subjected to a pinning–like interaction.

Anyway, a comparison of these results with the ones obtained for the crust can reveal an interesting aspect of the mesoscopic pinning force. In both cases we have seen that the *geometric* factor $\widetilde{f}_{\tilde{L}}$ (which depends only on the structure of the lattice

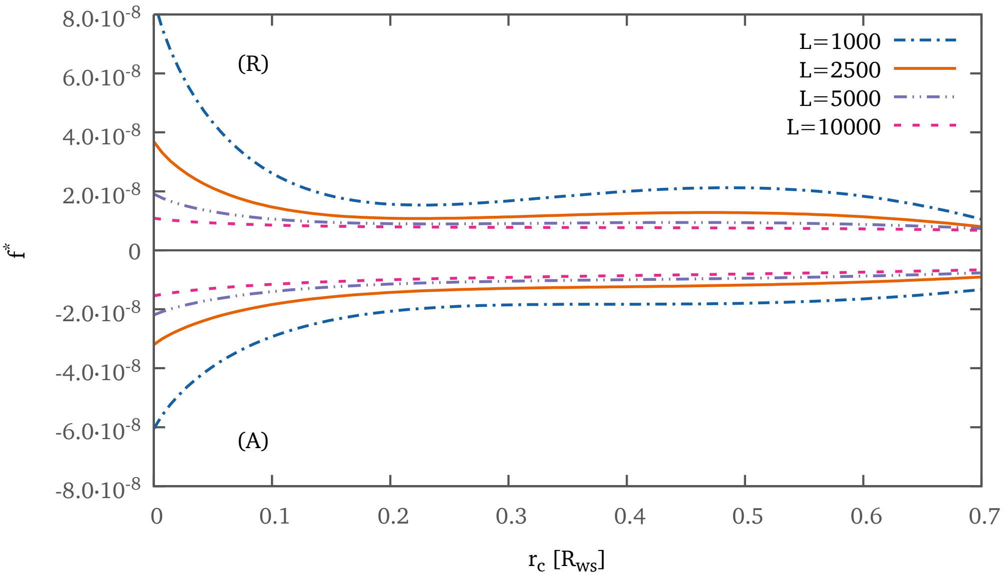

Figure 4.12: Plot of the fitting curves of table 4.1 obtained with the lattice constructed to take into account the entanglement effect.

and doesn't contain any scale parameter) has always the same order of magnitude of $\approx 10^{-8}$ dyn cm MeV$^{-1} \approx 0.006$, regardless of the type of lattice used. This means that the pinning force per unit length is overall dependent on the term $E_p/R_{\rm ws}^2$; in other words, as the pinning energy per site E_p is nearly the same in all configurations, the differences in the final results for the pinning in the crust and core (both with and without entanglement) must be addressed to the different scale factor $R_{\rm ws}$ which describes the spacing between the lattice sites.

Table 4.2: In this table we specialize the results of the fitting procedure of table 4.1 for the typical benchmarks of a pulsar and a magnetar.

	r_c [fm]	E_p [MeV]	R_{ws} [fm]	A/R	L [R_{ws}]	f_L [10^{12} dyn/cm] **No Ent.**	f_L [10^{12} dyn/cm] **With Ent.**
Pulsar	30	5	1500	A	1000	6.323	11.015
					2500	3.263	6.068
					5000	2.142	4.279
					10000	1.583	3.149
	30	5	1500	R	1000	8.043	13.901
					2500	4.200	6.288
					5000	2.840	3.529
					10000	2.219	2.229
Magnetar	30	5	50	A	1000	1139.737	3294.471
					2500	818.247	2152.945
					5000	666.678	1747.798
					10000	459.340	1479.343
	30	5	50	R	1000	2330.755	3674.238
					2500	1863.837	2274.851
					5000	1705.225	1754.075
					10000	1628.853	1452.359

PART II

THE SNOWPLOW MODEL

CHAPTER 5

The "snowplow" model

In this chapter we present the snowplow model, a fully consistent model that can explain the large glitches ($\Delta\nu/\nu \approx 10^{-6} - 10^{-5}$) recorded in a subset of pulsars known as giant glitchers. This model has been proposed by Pizzochero (2011) and applied analytically to describe the average properties of giant glitchers such as the inter-glitch waiting time, the step in frequency and that in frequency derivative. The model has been initially developed in Newtonian gravity and for a polytropic equation of state, but here we want to we extend the model to realistic backgrounds, obtained by integrating the relativistic equations of stellar structure and using physically motivated equations of state to describe matter in the neutron star. Especially the pinning forces used is of the orders of magnitude suggested by the calculations shown in the previous chapters, i.e. $\sim 10^{15}$ dyn cm^{-1}.

We find that this more detailed treatment still reproduces the main features of giant glitches in the Vela pulsar and allows us to set constraints on the equation of state. In particular we find that stiffer equations of state are favoured and that it is unlikely that the Vela pulsar has a high mass (larger than $M \approx 1.5\,\mathrm{M}_\odot$).

5.1 Pinning and vorticity

One of the most important ingredients of the model is clearly $f_{\mathrm{pin}}(\rho)$, the pinning force per unit length that acts on the vortex line as a result of its interaction with the lattice (in the inner crust). As shown in the previous chapters, although the pinning force per pinning site can readily be evaluated from the knowledge of the pinning energy (Alpar, 1977; Epstein and Baym, 1992; Donati and Pizzochero, 2003, 2004, 2006), the force per unit length of a vortex, which is the quantity that must be equated to the Magnus force in order to understand whether a vortex is pinned or free, is much more complex to evaluate, as it depends on the rigidity of a vortex and on its orientation with respect to the crustal lattice. In chapter 3 we have have performed numerical simulations to evaluate this quantity, taking into account different orientation of the bcc lattice. We have found that the order of magnitude of the maximum pinning force

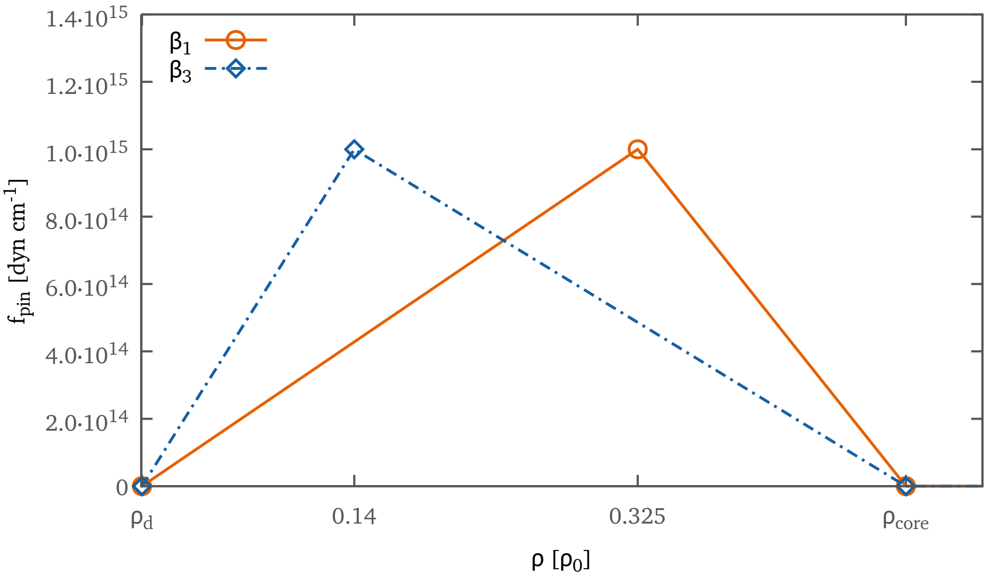

Figure 5.1: The profile of the pinning force $f_{\text{pin}}(\rho)$ for the two cases $\beta = 1$ and $\beta = 3$, with a choice for the maximum of $f_{\text{PM}} = 10^{15}$ dyn cm^{-1}.

f_{PM} is approximately 10^{15} dyn cm^{-1} and that there is no significant difference for the pinning force per unit length in considering vortex–nucleus interaction attractive or repulsive in different regions. Another interesting result found regards the position of the maximum f_{PM} that is dependent on the pairing gap profile used. It is known that the polarization effects of the neutron medium reduce the paring gap, but there is yet no agreement on how strong this suppression will be, although it seems reasonable to divide the $\Delta(\rho)$ by a factor β between 2 and 3. Here we consider here the case $\beta = 1$ and $\beta = 3$, as we have done also previously. The results in chapter 3 suggest that for the two corresponding profiles $f_{\text{pin}}(\rho)$ the maximum is shifted at different densities, even if the parameter β is, of course, only a scaling factor on the same pairing gap profile. The precise height of the maximum thus depends on the vortex tension (and thus “rigidity length”) used in the model (although the order of magnitude remains 10^{15} dyn cm^{-1}) and does not affect the location of the maximum (once β is fixed).

In this work we therefore constrain the exact value of the maximum amplitude of the pinning force by fitting the average waiting time between giant glitches in the Vela pulsar, as will be explained in the next sections. In fig. 5.1 we show the two pinning profiles $f_{\text{pin}}(\rho)$ used in this work for $\beta = 1$ and $\beta = 3$ (plotted here with the choice of $f_{\text{PM}} = 10^{15}$ dyn cm^{-1}). The case β_1 has a maximum at $\rho \approx 0.325\rho_0$, while in the β_3 case the maximum is at $\rho \approx 0.14\rho_0$. In both configurations we take the pinning force to vanish at ρ_{core} and ρ_d, due to the fact that the lattice exists only in the crust

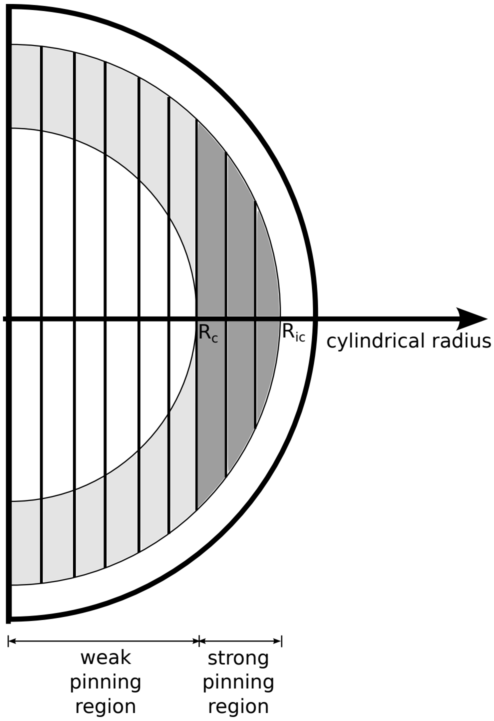

Figure 5.2: A schematic representation of the geometry of our problem (out of scale). The whole shaded area represents the inner crust of the NS, where vortexes are pinned to the lattice. The darker part indicates the strong pinning region, where the vortexes are subjected to pinning for their whole length. The star is threaded by straight continuous vortexes.

and that in the outer crust there are no free neutrons to produce vortexes. In this chapter we neglect any kind of pinning interaction in the core of the neutron stars: the results in chapter 4 supports this approach; anyway we will discuss this possibility in the following chapter.

A single vortex line will be described parallel to the rotational axis and distant from this axis by a distance x, that represent the cylindrical radius. We consider also the vortex line to be continuous throughout the core: there is, in fact, no theoretical evidence for the existence of an interface of normal matter between the core and the inner crust, that can justify the hypothesis of a core with vorticity separated from the crust (Zhou et al., 2004). Naturally the vortexes may not be straight and parallel to the rotational axis, as turbulence may develop in the stellar interior, especially in the presence of strong pinning (Link, 2012a,b). We will not consider this possibility here, but will discuss some of its likely consequences in the following.

With the above hypothesis, we can identify two (cylindrical) pinning regions based on the strength of the pinning interaction. The *strong* pinning region is defined by $x > R_c$ and corresponds to the part of the star in which the vortexes lie entirely in the inner crust region, and are therefore subject to pinning for their whole length. On the other hand, in the *weak* pinning region ($x < R_c$), a vortex line is pinned only at its extremities that are immersed in the crust, while there is no pinning interaction in the core (see fig. 5.2).

5.2 The model

Thanks to the axial symmetry of the problem, we can describe the macroscopic quantities of the rotating superfluid in terms of the variable $n(x)$ that represents the number of vortexes per unit area, at a distance x from the rotational axis of the star. The angular velocity $\Omega_s(x)$ of the superfluid component of the star is in fact proportional to the number $N(x)$ of vortexes enclosed in a cylindrical region of cylindrical radius x, and can be expressed as:

$$\Omega_s(x) = \frac{\kappa}{2\pi} \frac{N(x)}{x^2} = \frac{\kappa}{2\pi x^2} \int_x n(x')\, da' \tag{5.1}$$

where the integration is performed on the area enclosed by the radius x. This result follows from the quantization of the circulation per vortex line that is encoded in the constant $\kappa = \pi\hbar/m_N$.

Once a star has been fixed by the choice of an EoS and the integration of the TOV equations, the model requires, as a first step, the evaluation of the pinning force for the whole length of a generic vortex line. This can be obtained starting from the function $f_{\text{pin}}(\rho)$ discussed previously. Let us imagine a vortex line parallel to the rotational axis of the star and distant x: the total pinning acting on it is given by the integration of $f_{\text{pin}}(\rho)$ over its length:

$$F_{\text{pin}}(x) = 2 \int_0^{\ell(x)/2} f_{\text{pin}}\left[\rho\left(\sqrt{x^2+z^2}\right)\right] dz \tag{5.2}$$

where $\ell(x) = 2\sqrt{R_{\text{ic}}^2 - x^2}$ is the length of the vortex line, obtained considering that the vortex line ends at the inner–outer crust surface. To understand better the role of the pinning force, we choose a neutron star of $1.4\,\mathrm{M}_\odot$ with SLy equation of state and we plot the function $F_{\text{pin}}(x)$ for x from 0 to R_{ic} (fig. 5.3, corresponding to $\beta = 1$ and $f_{\text{PM}} = 10^{15}$ dyn cm^{-1}).

The pinning interaction is not the only force that acts on a vortex line. As shown in Ruderman and Sutherland (1974), pinning prevents the vortex line from moving with the local superfluid velocity because the vortex line is compelled to have the velocity of the normal matter component (the normal component rotates as a rigid body with angular velocity Ω_c). This fact give rise to a Magnus force:

$$\mathbf{f}_m = \kappa \rho_s\, \mathbf{e}_z \times (\mathbf{v}_v - \mathbf{v}_s) \tag{5.3}$$

where $\mathbf{v}_v$ is the velocity of the vortex line and $\mathbf{v}_s$ is the superfluid velocity; here $\mathbf{f}_m$ must be intended as force per unit length.

In this expression ρ_s is the density of the superfluid fraction of the star. In fact the whole star can be divided in two components: the normal one (which includes also the protons in the core as they are coupled with the crust by the magnetic field) and the superfluid one, on which the Magnus force will act. It thus follows that

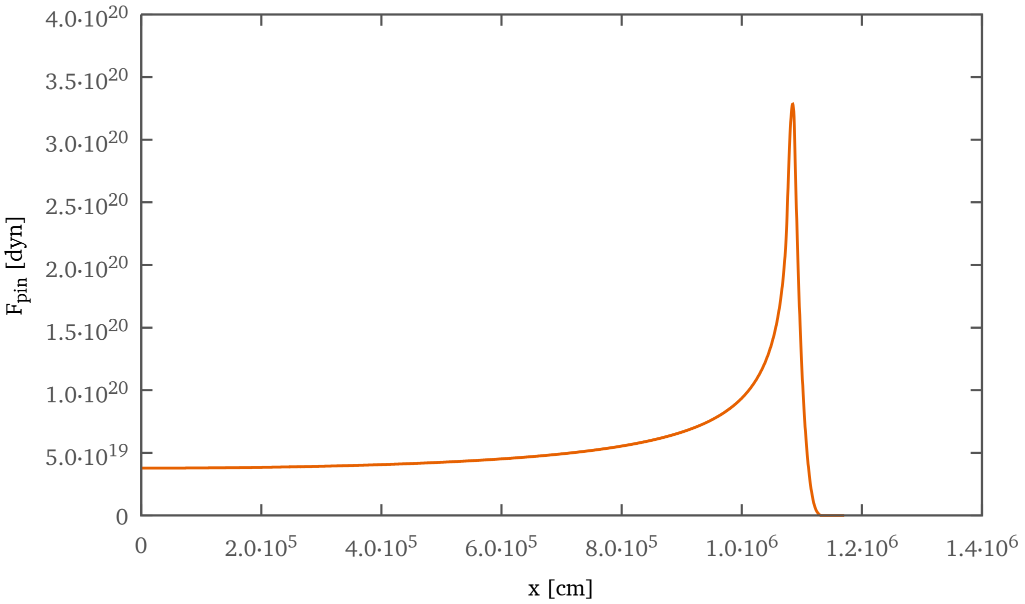

Figure 5.3: The total pinning force $F_{\text{pin}}(x)$ integrated on the whole length of a vortex line distant x from the rotational axis of the star. This plot is obtained taking a star of $1.4\,\mathrm{M}_{\odot}$ and SLy EoS. The pinning profile used is the $\beta = 1$ case plotted in fig. 5.1.

$\rho_s = (1 - x_p)\rho$ where x_p is the proton fraction at a given density. Of course this quantity is a microphysical property of matter and for this reason is strictly dependent on the EoS used. As this information is not provided with the EoSs used, we use the results of Zuo et al. (2004) who give the proton fraction $x_p(\rho)$ as a function of the total density in the case of two–body interactions and also in the case of three-body forces. We use both the $x_p(\rho)$ relations of Zuo et al. (2004) but we consider also a third case where the proton fraction is a constant that does not depend on the total density. We also introduce the parameter Q that represent the superfluid fraction of the star. It is defined for the general case as:

$$Q = I_s/I_{\text{tot}} = \frac{\int_0^R r^4(1 - x_p(\rho))\rho(r)\,dr}{\int_0^R r^4\rho(r)\,dr} \tag{5.4}$$

where we have used eq. (2.12); I_{tot} is the total moment of inertia and I_s is the moment of inertia of the superfluid component. In the case of a constant proton fraction it then follows that $Q = 1 - x_p$. The average value is $Q \approx 0.95$ and therefore we shall test our model also with this prescription.

The Magnus force in eq. (5.3) has only one component in the radial direction ($\mathbf{v}_v$ and $\mathbf{v}_s$ are, in fact, directed along $\mathbf{e}_\theta$, so the cross product is directed along $\mathbf{e}_x$) and therefore can be rewritten as:

$$\mathbf{f}_m(x,z) = f_m(x,z)\,\mathbf{e}_x = -\kappa\rho_s(x,z)x\Delta\Omega(x)\,\mathbf{e}_x \tag{5.5}$$

where the difference of the two velocities is written as:

$$\Delta v(x) = x\Delta\Omega(x) = x\left[\Omega_c - \Omega_s(x)\right]$$

and depends only on the coordinate x, as described by eq. (5.1). This quantity is negative between two glitches because the normal component spins slower that the superfluid one; indeed the Magnus force is a hydrodynamical lift that pushes the vortex outward from the rotational axis. The key point here is the fact that the normal component spins down as a consequence of the loss of energy by electromagnetic radiation of the star: the result is an increase of $f_m(x,z)$ in the time interval between glitches.

The same integration performed with f_{pin} over the length of the vortex can be done with the Magnus force. We can consider the total Magnus force acting on a vortex line distant x from the rotational axis:

$$\begin{aligned} F_m(x) &= 2\int_0^{\ell(x)/2} f_m(x,z)\,dz \\ &= 2\kappa x\Delta\Omega(x)\int_0^{\ell(x)/2} \rho_s\left(\sqrt{x^2+z^2}\right)dz. \end{aligned} \tag{5.6}$$

The basic idea here is to compare the pinning force and the Magnus force to find the critical lag $\Delta\Omega_{\text{cr}}(x)$ that represents the depinning condition: when the actual lag between the two components of the stars reaches the value $\Delta\Omega_{\text{cr}}$ at some point with cylindrical radius x, the vortexes here are unbound from the lattice, as the Magnus force now exceeds the pinning interaction that held the vortexes in place:

$$F_{\text{pin}}(x) = F_m(x) = \Delta\Omega_{\text{cr}}(x)F_m^*(x) \tag{5.7}$$

Here $F_m^*(x) = F_m(x)/\Delta\Omega_{\text{cr}}(x)$ and it is plotted in fig. 5.4 using the same reference star as in fig. 5.3. The important quantity is therefore the critical lag that can be easily evaluated as:

$$\Delta\Omega_{\text{cr}}(x) = \frac{\int_0^{\ell(x)/2} f_{\text{pin}}\left[\rho\left(\sqrt{x^2+z^2}\right)\right]dz}{\kappa x\int_0^{\ell(x)/2} \rho_s\left(\sqrt{x^2+z^2}\right)dz}. \tag{5.8}$$

In fig. 5.5 we plot the critical lag for sample stars from table 2.2.

It is important to point out that the lag shows a peak $\Delta\Omega_{\text{crmax}} = \Delta\Omega_{\text{cr}}(x_{\text{max}})$ in a region that corresponds to the inner crust, that is the region where the pinning is stronger. In this region our estimate of $\Delta\Omega_{\text{cr}}(x)$ is reasonable since pinning is continuous along the whole single vortex. This is not the case for the critical lag in the core, because here pinning acts on vortexes only at their extremities: as explained

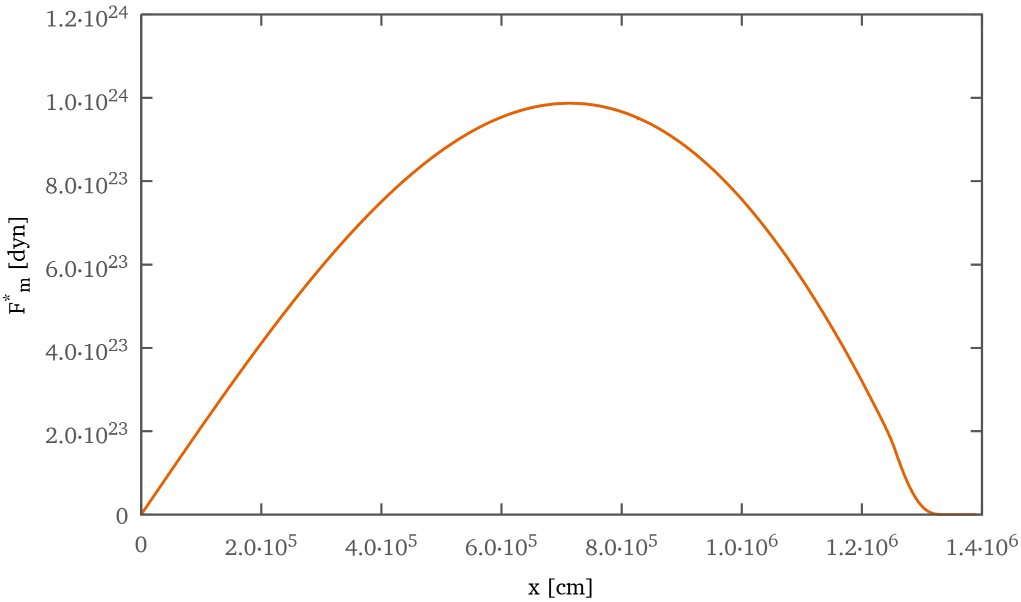

Figure 5.4: Plot of the expression $F_m^*(x) = F_m(x)/\Delta\Omega(x)$ as a function of the cylindrical radius x. This plot is obtained taking a star of $1.4\,\mathrm{M}_\odot$ and SLy EoS.

by Pizzochero (2011) this fact is responsible of the *weak* pinning in this region, even though we can assume that the system maintains axial symmetry due to the collective rigidity of vortex bundles(Ruderman and Sutherland, 1974).

As the star slows down, the depinning condition $\Delta\Omega(x) \geq \Delta\Omega_{\rm cr}(x)$ is first reached in the *core*: as shown by Link (2009), in this region repinning is dynamically possible if the lag falls below a critical value (smaller than the one for depinning). This suggest the following interpretation: in the *core*, as the star slows down, the vortexes are continuously depinned and repinned, establishing a dynamical creep that removes the excess vorticity on short timescales. Furthermore the Magnus force in the interior is likely to overcome the tension of vortexes and depin them long before the unpinning condition in the crust is met (Adams et al., 1985; Haskell et al., 2012a). The conclusion is thus that vortexes in the core can essentially be considered free. In this region the scattering of electrons off magnetised vortex cores is mainly responsible for the drag forces and for the short relaxation timescale $\tau_c \sim 1-10\,\mathrm{s}$ (Alpar et al., 1984c; Andersson et al., 2006): this means that we can consider the normal and the superfluid components in the core as coupled with a lag of order $|\dot{\Omega}|\tau_c$.

In the time between glitches, the depinning region becomes larger, involving also the crust: in the inner crust the excess vorticity is repinned and creates a thin vortex sheet that moves toward the peak: this sheet is pushed outward by the increasing Magnus force and it stores angular momentum. When the peak is reached, there is no more pinning interaction that can block the excess vorticity: this vorticity is suddenly

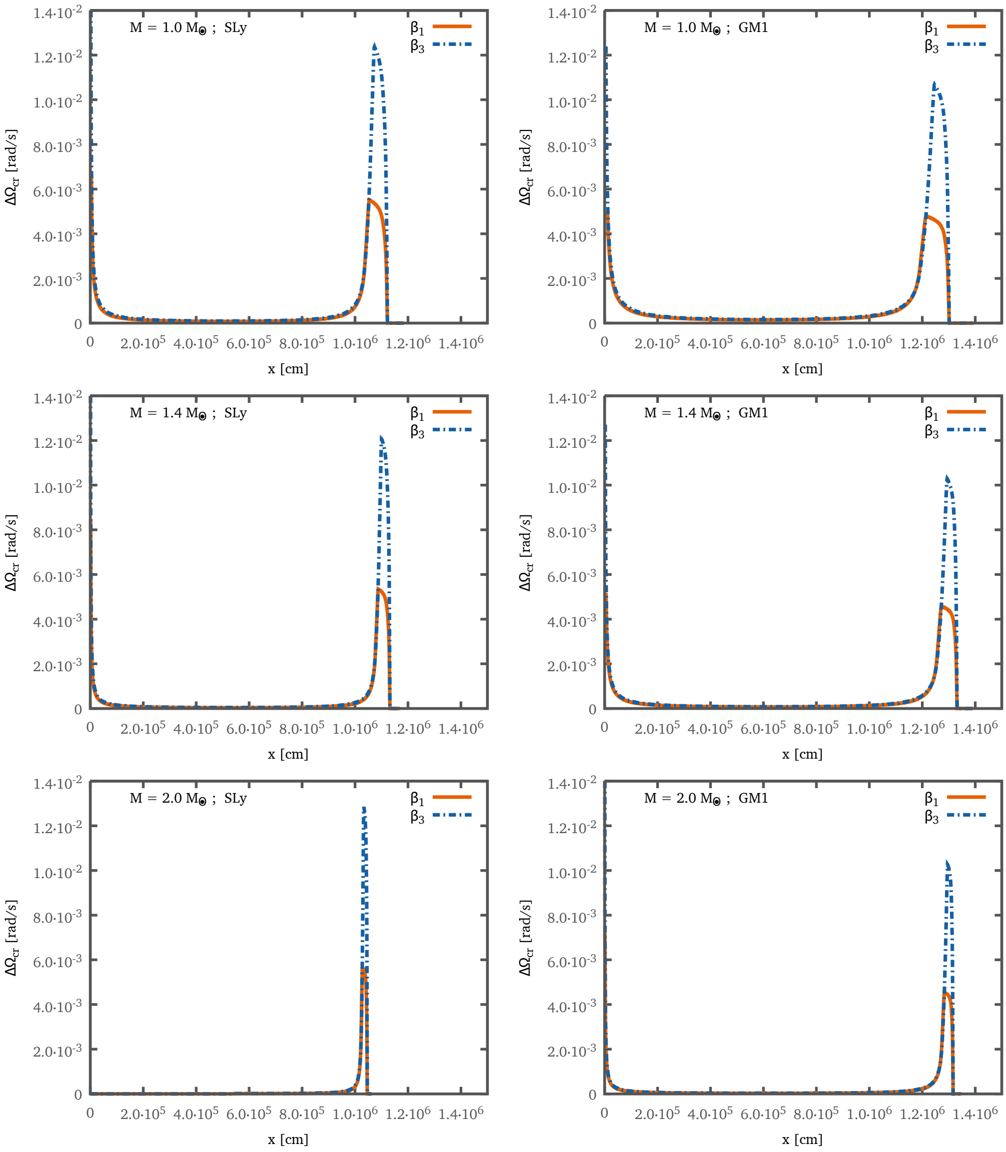

Figure 5.5: Plot of the critical lag $\Delta\Omega_{cr}(x)$ for different stellar models, with varying mass and equations of state. The pinning profiles used are plotted in fig. 5.1 and we consider both the case $\beta = 1$ and the case $\beta = 3$. Note that in both cases ($\beta = 1$ and $\beta = 3$) the maximum amplitude of the pinning force is the same, so the difference in the maximum lag for the two cases is now entirely due to the different position in density of the maximum in the pinning force profile.

released and reaches the outer crust. At this moment the angular momentum stored by vortexes is transferred to the normal component of the star, and this causes the glitch.

It is straightforward now to evaluate the time interval between two glitches; this is given by the time needed to create a lag $\Delta\Omega_{\mathrm{crmax}}$:

$$\Delta t_{\mathrm{gl}} = \frac{\Delta\Omega_{\mathrm{crmax}}}{|\dot{\Omega}|} \tag{5.9}$$

where $\dot{\Omega}$ is the deceleration of the normal component referred to the pre-glitch steady-state condition.

The above arguments indicates that, immediately before a glitch, a lag of $\Delta\Omega_{\mathrm{crmax}}$ will have been created for $x = x_{\mathrm{max}}$. This means that we can use eq. (5.1) to express the number of vortexes stored at the peak in the sheet just before a glitch:

$$N_{\mathrm{v}} = \frac{2\pi}{\kappa} x_{\mathrm{max}}^2 \Delta\Omega_{\mathrm{crmax}}. \tag{5.10}$$

Due to the particular shape of the critical lag in fig. 5.5, we can assume that in this moment the excess vorticity in the region $x > x_{\mathrm{max}}$ has been entirely removed by the Magnus force, and therefore the N_{v} vortexes are the only ones responsible for the transfer of angular momentum to the normal component of the star. To evaluate the angular momentum transfer we start from the definition $dL = \Omega_s(x)\, dI_s$. As we are interested in the angular momentum stored by N_{v} vortexes at the peak of the pinning potential, we use the relation in eq. (5.10) and perform the integration on the cylindrical region $x_{\mathrm{max}} < x < R_c$ to obtain the requested quantity (the integration on the coordinate x stops at R_c due to the fact that in the outer crust there is no superfluid component):

$$\Delta L_{\mathrm{gl}} = 2\kappa N_{\mathrm{v}} \int_{x_{\mathrm{max}}}^{R_c} x\, dx \int_0^{\ell(x)} \rho_s(\sqrt{x^2+z^2})\, dz. \tag{5.11}$$

Following the arguments above, at the moment of a glitch only a fraction of the core superfluidity is coupled to the normal component of the star: in fact, the rise time of a glitch (τ_{gl}) is very short and only the instantaneously depinned fraction of vorticity in the core can respond to the variation of the angular velocity of the crust. We introduce the parameter Y_{gl} to encode this fractional quantity. In fact the best observational upper limit is of $\tau_{\mathrm{gl}} < 40\,\mathrm{s}$ for the Vela 2000 glitch (Dodson et al., 2002), while an interesting lower limit of $\tau_{\mathrm{gl}} > 10^{-4}\,\mathrm{ms}$ can be set by the non–detection of gravitational waves from the Vela 2006 glitch (Warszawski and Melatos, 2012a). Theoretical estimates suggest that $\tau_{\mathrm{gl}} \approx 1 - 10\,\mathrm{s}$ (Haskell et al., 2012c).

In the pre–glitch steady–state condition, due to the long timescales involved, we can assume $Y_{\infty} = 1$; but during a glitch this quantity cannot be calculated with the snowplow model as it depends on the detailed short–time dynamics of the vortexes, and must thus be determined with other approaches. As this is beyond the scope of the current work, the quantity $Y_{\rm gl}$ is taken as a parameter of this model, and must be inferred from the observational data as shown in the next section.

The value $Y_{\rm gl}$ is needed for the evaluation of $\Delta\Omega_{\rm gl}$, the jump in angular velocity of the normal component of the star due to a glitch. This corresponds to the ratio between the angular momentum transfer $\Delta L_{\rm gl}$ and the effective moment of inertia $I_{\rm eff}$ of the coupled fraction of matter during the glitch. One thus has that $I_{\rm eff} = (1-Q)I_{\rm tot} + QY_{\rm gl}I_{\rm tot}$ and the requested quantity is therefore:

$$\Delta\Omega_{\rm gl} = \frac{\Delta L_{\rm gl}}{I_{\rm tot}\left[1-Q\left(1-Y_{\rm gl}\right)\right]}. \tag{5.12}$$

A further parameter of the glitch that can be calculated is the relative acceleration of the crust. As illustrated in Pizzochero (2011) the desired relation follows from variation at the glitch of the Euler equation for the normal component and angular momentum conservation:

$$\frac{\Delta\dot{\Omega}_{\rm gl}}{\dot{\Omega}_\infty} = \frac{Q(1-Y_{\rm gl})}{1-Q(1-Y_{\rm gl})}. \tag{5.13}$$

5.3 Results and observations

In this section we test the model proposed here against observations. As the model has been developed for giant glitches we shall compare our results to observations of giant glitches in the Vela pulsar. The Vela (PSR B0833-45 or PSR J0835-4510) has a spin frequency $\nu \approx 11.19$ Hz and spin-down rate $\dot{\nu} \approx -1.55 \times 10^{-11}$ Hz s^{-1}; from relation in eq. (5.9) this value correspond to a maximum critical lag of $\Delta\Omega_{\rm crmax} = 8.6 \times 10^{-3}\ \mathrm{rad\,s^{-1}}$, where we have considered that the average time between glitches for this pulsar is 2.8 years. The glitch is usually described in terms of permanent steps in the frequency and frequency derivative and a series of transient terms that decay exponentially. It is well known that at least three transient terms are required, with decay timescales that range from months to hours (Flanagan, 1996). Recent observations of the 2000 and 2004 glitch have shown that an additional term is required on short timescales, with a decay time of approximately a minute. Given that the detection in 2004 was only barely above the noise we shall refer to the January 2000 glitch. In this case the jump in angular velocity was of $\Delta\Omega_{\rm gl} = 2.2 \times 10^{-4}$ rad/s (Dodson et al., 2002, 2007). This is a fairly typical value for giant glitches in the Vela, and we take it as our reference value. The relative step in frequency derivative corresponding to the transient term with the shortest decay timescale (1 minute) for this glitch is $\Delta\dot{\Omega}_{\rm gl}/\dot{\Omega}_\infty \approx 18 \pm 6$ (1σ error), and we assume that this is a good approximation to the *instantaneous* step in frequency derivative at the time of the glitch.

As explained in the previous section, the model has two free parameters that are the maximum value of the pinning force value $f_{\rm PM}$ and $Y_{\rm gl}$: this means that, once a

Table 5.1: This table gives the fitting parameters $f_{\rm PM}$ (maximum of the pinning force per unit length) and $Y_{\rm gl}$ (fraction of coupled vorticity at the glitch) for all the considered configurations. $x_{\rm max}$ is the position (cylindrical radius) of the maximum critical lag. These values refer to a constant proton fraction $x_p(\rho) = 0.05$ (the corresponding fraction of moment of inertia due to the superfluid component of the star is $Q = 0.95$). Unphysical (negative) values for $Y_{\rm gl}$ are not reported (see text for details). Since the angular momentum transferred to the crust during a glitch is strongly dependant on the ratio $x_{\rm max}/R_{\rm ic}$ (see section 5.3), this quantity is also reported in table.

		$\beta = 1$				$\beta = 3$			
EoS	M ($\mathrm{M}_\odot$)	$x_{\rm max}$ (km)	$x_{\rm max}/R_{\rm ic}$	$f_{\rm PM}/10^{15}$ ($\mathrm{dyn\,cm^{-1}}$)	$Y_{\rm gl}$	$x_{\rm max}$ (km)	$x_{\rm max}/R_{\rm ic}$	$f_{\rm PM}/10^{15}$ ($\mathrm{dyn\,cm^{-1}}$)	$Y_{\rm gl}$
SLy	1.0	10.530	0.938	1.562	0.203	10.724	0.955	0.697	0.027
	1.1	10.654	0.945	1.581	0.148	10.829	0.960	0.704	0.009
	1.2	10.753	0.951	1.595	0.106	10.910	0.965	0.709	–
	1.3	10.827	0.956	1.606	0.074	10.968	0.968	0.713	–
	1.4	10.875	0.961	1.613	0.048	11.001	0.972	0.715	–
	1.5	10.897	0.965	1.616	0.027	11.010	0.975	0.716	–
	1.6	10.889	0.969	1.615	0.011	10.990	0.977	0.715	–
	1.7	10.847	0.972	1.609	–	10.937	0.980	0.711	–
	1.8	10.759	0.975	1.596	–	10.838	0.982	0.705	–
	1.9	10.600	0.979	1.572	–	10.667	0.985	0.694	–
	2.0	10.279	0.982	1.525	–	10.332	0.987	0.672	–
GM1	1.0	12.129	0.932	1.798	0.493	12.447	0.956	0.809	0.078
	1.1	12.315	0.939	1.825	0.389	12.604	0.961	0.819	0.051
	1.2	12.473	0.945	1.849	0.307	12.737	0.965	0.827	0.031
	1.3	12.604	0.950	1.868	0.242	12.844	0.968	0.834	0.015
	1.4	12.710	0.955	1.884	0.190	12.929	0.971	0.840	0.003
	1.5	12.792	0.959	1.896	0.148	12.992	0.974	0.844	–
	1.6	12.852	0.962	1.905	0.113	13.034	0.976	0.847	–
	1.7	12.890	0.966	1.910	0.083	13.055	0.978	0.848	–
	1.8	12.901	0.969	1.912	0.060	13.052	0.980	0.848	–
	1.9	12.885	0.972	1.910	0.040	13.022	0.982	0.846	–
	2.0	12.836	0.974	1.902	0.023	12.960	0.984	0.842	–
	2.1	12.744	0.977	1.889	0.007	12.854	0.985	0.835	–
	2.2	12.586	0.980	1.865	–	12.683	0.987	0.824	–
	2.3	12.287	0.982	1.821	–	12.367	0.989	0.803	–

Table 5.2: The fitting parameters given here (defined in table 5.1) refer to the proton fraction $x_p(\rho)$ proposed by Zuo et al. (2004), obtained with two–body forces.

		$\beta = 1$				$\beta = 3$			
EoS	M (M$_\odot$)	$x_{\rm max}$ (km)	$x_{\rm max}/R_{\rm ic}$	$f_{\rm PM}/10^{15}$ (dyn cm^{-1})	$Y_{\rm gl}$	$x_{\rm max}$ (km)	$x_{\rm max}/R_{\rm ic}$	$f_{\rm PM}/10^{15}$ (dyn cm^{-1})	$Y_{\rm gl}$
SLy	1.0	10.530	0.938	1.618	0.212	10.724	0.955	0.727	0.029
	1.1	10.654	0.945	1.637	0.152	10.829	0.960	0.735	0.007
	1.2	10.753	0.951	1.652	0.105	10.910	0.965	0.740	–
	1.3	10.827	0.956	1.663	0.067	10.968	0.968	0.744	–
	1.4	10.875	0.961	1.671	0.036	11.001	0.972	0.746	–
	1.5	10.897	0.965	1.674	0.010	11.010	0.975	0.747	–
	1.6	10.889	0.969	1.673	–	10.990	0.977	0.745	–
	1.7	10.847	0.972	1.666	–	10.937	0.980	0.742	–
	1.8	10.759	0.975	1.653	–	10.837	0.982	0.735	–
	1.9	10.600	0.979	1.628	–	10.666	0.985	0.723	–
	2.0	10.279	0.982	1.579	–	10.332	0.987	0.701	–
GM1	1.0	12.129	0.932	1.861	0.522	12.446	0.956	0.843	0.099
	1.1	12.315	0.939	1.890	0.415	12.605	0.961	0.854	0.070
	1.2	12.473	0.945	1.914	0.330	12.736	0.965	0.863	0.048
	1.3	12.604	0.950	1.934	0.262	12.844	0.968	0.870	0.029
	1.4	12.710	0.955	1.951	0.207	12.929	0.971	0.876	0.014
	1.5	12.792	0.959	1.963	0.162	12.992	0.974	0.880	0.002
	1.6	12.852	0.962	1.972	0.124	13.034	0.976	0.883	–
	1.7	12.888	0.966	1.978	0.092	13.055	0.978	0.884	–
	1.8	12.900	0.969	1.980	0.064	13.052	0.980	0.884	–
	1.9	12.885	0.972	1.977	0.039	13.022	0.982	0.882	–
	2.0	12.836	0.974	1.970	0.018	12.960	0.984	0.878	–
	2.1	12.744	0.977	1.956	–	12.854	0.985	0.871	–
	2.2	12.586	0.980	1.931	–	12.683	0.987	0.859	–
	2.3	12.286	0.982	1.885	–	12.367	0.989	0.838	–

star has been fixed (by choosing the EoS, the mass M, and the superfluid fraction relation) we can use two observational quantities to constrain the parameters of the model and compare further observables to the quantities predicted by calculations. In particular, for each fixed star, we rescale the maximum of the pinning force in order to produce the maximum critical lag $\Delta\Omega_{\rm crmax}$ required to reproduce the average waiting time between glitches in the Vela. This allows us to calculate directly and univocally the angular momentum $\Delta L_{\rm gl}$ from eq. (5.11). As we want to reproduce a glitch of amplitude $\Delta\Omega_{\rm gl} = 2.2 \times 10^{-4}$ rad/s, eq. (5.12) can be rewritten in the following form:

$$Y_{\rm gl} = \frac{1}{Q}\left[\frac{\Delta L_{\rm gl}}{I_{\rm tot}\Delta\Omega_{\rm gl}} + Q - 1\right], \tag{5.14}$$

and therefore can be used to fix the coupled fraction of matter during the glitch. Tables 5.1 to 5.3 give the fitting parameters for all the configurations tested. We can see that the value of the maximum pinning force $f_{\rm PM}$ does not change significantly

Table 5.3: This table is analogous to tables 5.1 and 5.2: here the proton fraction used is that calculated by Zuo et al. (2004) with three–body forces.

		$\beta = 1$				$\beta = 3$			
EoS	M ($\mathrm{M}_\odot$)	$x_{\max}$ (km)	$x_{\max}/R_{\mathrm{ic}}$	$f_{\mathrm{PM}}/10^{15}$ ($\mathrm{dyn\,cm^{-1}}$)	Y_{gl}	$x_{\max}$ (km)	$x_{\max}/R_{\mathrm{ic}}$	$f_{\mathrm{PM}}/10^{15}$ ($\mathrm{dyn\,cm^{-1}}$)	Y_{gl}
SLy	1.0	10.530	0.938	1.619	0.197	10.724	0.955	0.728	0.011
	1.1	10.654	0.945	1.638	0.133	10.829	0.960	0.735	–
	1.2	10.753	0.951	1.653	0.080	10.910	0.965	0.740	–
	1.3	10.827	0.956	1.664	0.036	10.968	0.968	0.744	–
	1.4	10.875	0.961	1.672	–	11.001	0.972	0.746	–
	1.5	10.897	0.965	1.675	–	11.010	0.975	0.747	–
	1.6	10.889	0.969	1.674	–	10.990	0.977	0.746	–
	1.7	10.847	0.972	1.667	–	10.937	0.980	0.742	–
	1.8	10.759	0.975	1.654	–	10.837	0.982	0.735	–
	1.9	10.600	0.979	1.629	–	10.666	0.985	0.724	–
	2.0	10.279	0.982	1.580	–	10.332	0.987	0.701	–
GM1	1.0	12.129	0.932	1.862	0.521	12.446	0.956	0.843	0.095
	1.1	12.315	0.939	1.891	0.413	12.605	0.961	0.854	0.065
	1.2	12.473	0.945	1.915	0.326	12.736	0.965	0.863	0.042
	1.3	12.604	0.950	1.935	0.257	12.844	0.968	0.870	0.022
	1.4	12.710	0.955	1.952	0.200	12.929	0.971	0.876	0.006
	1.5	12.792	0.959	1.964	0.153	12.992	0.974	0.880	–
	1.6	12.852	0.962	1.973	0.112	13.034	0.976	0.883	–
	1.7	12.888	0.966	1.979	0.077	13.055	0.978	0.885	–
	1.8	12.900	0.969	1.981	0.046	13.052	0.980	0.884	–
	1.9	12.885	0.972	1.978	0.017	13.022	0.982	0.882	–
	2.0	12.836	0.974	1.971	–	12.960	0.984	0.878	–
	2.1	12.744	0.977	1.957	–	12.854	0.985	0.871	–
	2.2	12.586	0.980	1.932	–	12.683	0.987	0.859	–
	2.3	12.286	0.982	1.886	–	12.367	0.989	0.838	–

with the total mass of the star. In these tables negative values of Y_{gl} are not given as they would not be physically acceptable: a negative value would mean that there is not enough angular momentum to produce the required jump in angular velocity, even if we consider the core vorticity completely decoupled from the normal component of the star at the time of the glitch.

The remaining tables, numbered 5.4, 5.5 and 5.6, show the physical quantities that the “snowplow” model permits to evaluate. These are of course the angular momentum ΔL_{gl} transferred to the crust during the glitch and the relative step in frequency derivative. We can see that the order of magnitude for ΔL_{gl} is 10^{40} erg s, that is compatible with the upper limits on the glitch energy obtained from observations of the power wind nebula surrounding Vela (Helfand et al., 2001) and with the results found in Pizzochero (2011), where the same model is applied analytically with a polytropic EoS in Newtonian gravity. From these tables one can see that, for a particular choice of EoS and proton fraction, the angular momentum ΔL_{gl} stored

Table 5.4: This table shows, for the considered configurations, the physical quantities that the “snowplow” model permits to evaluate: the number N_v of vortexes stored at the peak in critical lag just before the glitch, the angular momentum transferred to the crust ΔL_gl, and the step in frequency derivative on short timescales $\Delta\dot{\Omega}_\mathrm{gl}/\dot{\Omega}_\infty$. Like table 5.1 (that gives the fitting parameters used), this one refers to a constant proton fraction that gives $Q = 0.95$.

			$\beta = 1$			$\beta = 3$		
EoS	M ($\mathrm{M}_\odot$)	R (km)	N_v (10^{13})	ΔL_gl (10^{40} erg s)	$\Delta\dot{\Omega}_\mathrm{gl}/\dot{\Omega}_\infty$	N_v (10^{13})	ΔL_gl (10^{40} erg s)	$\Delta\dot{\Omega}_\mathrm{gl}/\dot{\Omega}_\infty$
SLy	1.0	11.855	3.041	3.889	3.124	3.154	1.216	12.184
	1.1	11.830	3.113	3.425	4.242	3.216	1.059	15.950
	1.2	11.797	3.171	2.996	5.622	3.265	0.919	–
	1.3	11.758	3.215	2.601	7.331	3.299	0.792	–
	1.4	11.705	3.244	2.235	9.476	3.319	0.677	–
	1.5	11.635	3.257	1.903	12.166	3.325	0.570	–
	1.6	11.545	3.252	1.595	15.629	3.313	0.477	–
	1.7	11.422	3.227	1.304	–	3.280	0.387	–
	1.8	11.260	3.175	1.033	–	3.221	0.304	–
	1.9	11.025	3.082	0.771	–	3.121	0.226	–
	2.0	10.620	2.898	0.498	–	2.928	0.147	–
GM1	1.0	13.940	4.034	11.480	0.931	4.249	2.741	7.086
	1.1	13.943	4.159	10.433	1.384	4.357	2.456	9.128
	1.2	13.940	4.267	9.429	1.927	4.449	2.180	11.657
	1.3	13.930	4.357	8.481	2.570	4.524	1.958	14.462
	1.4	13.913	4.430	7.599	3.330	4.584	1.743	17.882
	1.5	13.885	4.488	6.764	4.242	4.629	1.542	–
	1.6	13.845	4.530	5.977	5.344	4.660	1.355	–
	1.7	13.788	4.557	5.198	6.744	4.674	1.184	–
	1.8	13.715	4.565	4.543	8.336	4.672	1.020	–
	1.9	13.620	4.553	3.895	10.385	4.651	0.869	–
	2.0	13.495	4.519	3.284	12.999	4.606	0.727	–
	2.1	13.330	4.455	2.688	16.541	4.532	0.593	–
	2.2	13.095	4.345	2.104	–	4.411	0.460	–
	2.3	12.713	4.140	1.481	–	4.195	0.327	–

by vortexes decreases with the total mass of the star. This behaviour can be easily explained, as shown by Pizzochero (2011), in terms of the quantity $x_\mathrm{max}/R_\mathrm{ic}$ shown in the tables: ΔL_gl is obviously related to the number N_v of vortexes stored at the peak (in tables 5.4 to 5.6; see also eq. (5.11)) – that however doesn’t change significantly with the mass – but it depends strongly on the ratio $x_\mathrm{max}/R_\mathrm{ic}$ which increases at higher masses. In Pizzochero (2011) (fig. 4) it is clearly shown that the angular momentum stored by the vortexes at the peak decreases rapidly moving the position of the peak towards the outer crust. The quantity ΔL_gl also depends on the equation of state used (a stiffer EoS produces higher values of ΔL_gl) and on the pinning profile: the $\beta = 3$ condition, when other variables are fixed, gives lower values for the angular momentum, accordingly to the fact that the relative position of the peak with respect to the inner crust radius is higher.

Table 5.5: The quantities $\Delta L_{\rm gl}$ and $\Delta\dot{\Omega}_{\rm gl}/\dot{\Omega}_\infty$ here reported follows from calculation based on the proton fraction proposed by Zuo et al. (2004) with two–body interactions. The corresponding fitting parameters are shown in table 5.2. $Q = I_s/I_{\rm tot}$ is the global superfluid fraction of moment of inertia.

				$\beta = 1$			$\beta = 3$		
EoS	M ($\mathrm{M}_\odot$)	R (km)	Q	$N_{\rm v}$ (10^{13})	$\Delta L_{\rm gl}$ (10^{40} erg s)	$\Delta\dot{\Omega}_{\rm gl}/\dot{\Omega}_\infty$	$N_{\rm v}$ (10^{13})	$\Delta L_{\rm gl}$ (10^{40} erg s)	$\Delta\dot{\Omega}_{\rm gl}/\dot{\Omega}_\infty$
SLy	1.0	11.855	0.948	3.041	4.048	2.962	3.154	1.272	11.609
	1.1	11.830	0.945	3.113	3.565	4.036	3.216	1.108	15.210
	1.2	11.797	0.942	3.171	3.119	5.362	3.265	0.961	–
	1.3	11.758	0.938	3.215	2.708	7.005	3.299	0.828	–
	1.4	11.705	0.934	3.244	2.327	9.065	3.319	0.708	–
	1.5	11.635	0.930	3.257	1.981	11.650	3.325	0.596	–
	1.6	11.545	0.925	3.252	1.660	–	3.313	0.499	–
	1.7	11.422	0.920	3.227	1.357	–	3.280	0.405	–
	1.8	11.260	0.913	3.175	1.076	–	3.221	0.321	–
	1.9	11.025	0.905	3.082	0.803	–	3.120	0.239	–
	2.0	10.620	0.890	2.898	0.518	–	2.928	0.153	–
GM1	1.0	13.940	0.966	4.034	11.939	0.856	4.248	2.874	6.713
	1.1	13.943	0.964	4.159	10.850	1.292	4.357	2.559	8.719
	1.2	13.940	0.962	4.267	9.805	1.814	4.448	2.303	10.982
	1.3	13.930	0.961	4.357	8.820	2.433	4.524	2.047	13.792
	1.4	13.913	0.959	4.430	7.903	3.164	4.584	1.822	17.063
	1.5	13.885	0.956	4.488	7.034	4.041	4.629	1.612	20.994
	1.6	13.845	0.954	4.530	6.216	5.101	4.660	1.416	–
	1.7	13.788	0.952	4.556	5.463	6.367	4.674	1.237	–
	1.8	13.715	0.949	4.564	4.743	7.943	4.672	1.066	–
	1.9	13.620	0.946	4.553	4.051	9.948	4.651	0.909	–
	2.0	13.495	0.942	4.519	3.415	12.463	4.606	0.760	–
	2.1	13.330	0.938	4.455	2.796	–	4.532	0.620	–
	2.2	13.095	0.933	4.345	2.188	–	4.411	0.481	–
	2.3	12.713	0.925	4.140	1.552	–	4.195	0.342	–

The “snowplow” model permits to calculate also the step in spin–down rate immediately after a glitch, and this quantity is given in our tables as $\Delta\dot{\Omega}_{\rm gl}/\dot{\Omega}_\infty$. It has been calculated only for acceptable values of $Y_{\rm gl}$, and must be compared with the reference value of $\Delta\dot{\Omega}_{\rm gl}/\dot{\Omega}_\infty = 18 \pm 6$, taken from the Vela 2000 glitch (Gandolfi et al., 2008). These values suggest that the $\beta = 3$ configurations are preferred and this can be considered in reasonable agreement with the microscopic results found by Gandolfi et al. (2008): they find that a realistic suppression factor for the pairing gap $\Delta(\rho)$ is $\beta \approx 1.5$ but, crucially, also that the maximum for $\Delta(\rho)$ is shifted at lower densities. This leads to a profile close to what we obtain for $\beta = 3$ in our model.

Finally let us remark that the results in tables 5.4 to 5.6, for the (microscopically favoured) case $\beta = 3$, seem to indicate that a stiffer equation of state (GM1) is preferred as is a lower mass (possibly in the region of $1.4\,\mathrm{M}_\odot$) for the Vela pulsar. Naturally such a quantitative conclusion is difficult to make on the basis of one observation and

Table 5.6: The proton fraction used for this table is the three–body forces model of Zuo et al. (2004). The corresponding fitting parameters are shown in table 5.3.

				$\beta = 1$			$\beta = 3$		
EoS	M ($\mathrm{M}_\odot$)	R (km)	Q	N_v (10^{13})	ΔL_gl (10^{40} erg s)	$\Delta\dot{\Omega}_\mathrm{gl}/\dot{\Omega}_\infty$	N_v (10^{13})	ΔL_gl (10^{40} erg s)	$\Delta\dot{\Omega}_\mathrm{gl}/\dot{\Omega}_\infty$
SLy	1.0	11.855	0.931	3.041	4.049	2.960	3.154	1.272	11.607
	1.1	11.830	0.924	3.113	3.567	4.034	3.216	1.108	–
	1.2	11.797	0.916	3.171	3.120	5.360	3.265	0.961	–
	1.3	11.758	0.908	3.215	2.708	7.002	3.299	0.828	–
	1.4	11.705	0.899	3.244	2.328	–	3.319	0.708	–
	1.5	11.635	0.888	3.257	1.981	–	3.325	0.597	–
	1.6	11.545	0.876	3.252	1.661	–	3.313	0.499	–
	1.7	11.422	0.862	3.227	1.358	–	3.280	0.405	–
	1.8	11.260	0.844	3.175	1.076	–	3.221	0.321	–
	1.9	11.025	0.820	3.082	0.803	–	3.120	0.239	–
	2.0	10.620	0.779	2.898	0.518	–	2.928	0.153	–
GM1	1.0	13.940	0.962	4.034	11.944	0.856	4.248	2.874	6.712
	1.1	13.943	0.959	4.159	10.854	1.292	4.357	2.559	8.718
	1.2	13.940	0.957	4.267	9.809	1.813	4.448	2.303	10.981
	1.3	13.930	0.953	4.357	8.824	2.432	4.524	2.047	13.791
	1.4	13.913	0.950	4.430	7.906	3.163	4.584	1.822	17.061
	1.5	13.885	0.946	4.488	7.037	4.039	4.629	1.612	–
	1.6	13.845	0.942	4.530	6.218	5.099	4.660	1.416	–
	1.7	13.788	0.937	4.556	5.465	6.365	4.674	1.237	–
	1.8	13.715	0.931	4.564	4.744	7.939	4.672	1.066	–
	1.9	13.620	0.925	4.553	4.052	9.944	4.651	0.909	–
	2.0	13.495	0.917	4.519	3.416	–	4.606	0.760	–
	2.1	13.330	0.907	4.455	2.797	–	4.532	0.620	–
	2.2	13.095	0.894	4.345	2.188	–	4.411	0.481	–
	2.3	12.713	0.873	4.140	1.553	–	4.195	0.342	–

it would be highly desirable to have information on the short-timescale post-glitch behaviour not only of other Vela giant glitches, but also of other glitching pulsars. Note that short term components of the relaxation have not been measured for other giant glitchers, however the “snowplow” model can be used to predict waiting times, obtaining results which are consistent with observations (Haskell et al., 2012c).

5.4 Conclusions

In this chapter we have extended the “snowplow” model for giant pulsar glitches of Pizzochero (2011) to incorporate relativistic background stellar models and realistic equations of state. In particular we have tested the model for the SLy and GM1 equations of state. Unfortunately these equations of state do not include information on beta equilibrium, so we use the proton fractions calculated by Zuo et al. (2004). It would of course be highly desirable to use proton fractions that are consistent with the individual equations of state in future work, in order to set stringent constraints. Furthermore we have used, for the first time, the realistic profiles for the pinning forces per unit length calculated in chapter 3, in order to evaluate the amount of angular momentum that can be transferred to the crust during a glitch.

The model contains three free parameters, the mass of the star M, the fraction of superfluid that is coupled to the crust during a glitch Y_{gl}, and the maximum amplitude of the pinning force, f_{PM}. Note in fact that while the location of the maximum is precisely determined by the microphysical calculations of chapter 3, the actual value of the maximum can vary by factors of order unity or more as it depends on the poorly constrained value of the vortex tension. We thus treat it as a normalization and determine its value by requiring that the waiting time between glitches is of 2.8 years, as is approximately the case for Vela glitches. We then fit the size of the glitch to an average Vela glitch to obtain the value of Y_{gl}. In particular we take the value of the Vela 2000 glitch, $\Delta\Omega = 2.2 \times 10^{-4}$ rad/s (Dodson et al., 2002).

Having determined the free parameters in our model, except for the mass of the NS which is free, we compare our results to the post glitch step in frequency derivative. Unfortunately the changes in $\dot{\nu}$ on short time scales after a glitch are observationally challenging to detect and it has been possible to fit for transient steps in frequency and frequency derivative on timescales of minutes after a glitch only for the Vela 2000 and 2004 glitch (Dodson et al., 2002, 2007). Given that the detection is only barely above the noise for the 2004 glitch (Dodson et al., 2007) we fit to the values obtained for the 2000 glitch, which we assume to be a good approximation of the instantaneous post glitch behaviour. This justifies our choice of also fitting to the value of the jump in frequency of the Vela 2000 glitch.

The comparison of the model to the observational constraints first of all highlights that the general results of the analytic model of Pizzochero (2011) remain valid even in our more physically realistic approach and the results are in general consistent for both equations of state for a reasonable range of neutron star masses. The glitch model presented here thus appears robust and compatible with the observations of giant glitches in the Vela and is, as shown in Haskell et al. (2012c), compatible with the average waiting time between giant glitches in other pulsars. This further reinforces the hypothesis that giant glitches are approximately periodic phenomena that occur close to the maximum lag that the pinning force can support in the crust, while smaller glitches may be triggered by random events such as crust quakes (Ruderman, 1976; Ruderman et al., 1998) or vortex avalanches (Warszawski and Melatos, 2008; Melatos and Warszawski, 2009; Warszawski and Melatos, 2011, 2012a). Furthermore our results favour lower masses for the Vela pulsar (smaller than $1.5\,\mathrm{M}_{\odot}$) and stiffer equations of state. Note however that such a quantitative conclusion is difficult to draw as not only are we comparing to a single observation but dynamical simulations have also shown that superfluid mutual friction will contribute significantly to the short term post-glitch spindown as may friction at the crust/core interface (these aspects will be discussed in chapters 8 and 9).

CHAPTER 6

Investigating superconductivity with the snowplow model

The high density interior of a neutron star is expected to contain superconducting protons and superfluid neutrons. Theoretical estimates suggest that the protons could form a type II superconductor in which the stellar magnetic field is carried by flux tubes. The strong interaction between the flux tubes and the neutron rotational vortexes leads, in this case, to strong pinning, i.e. vortex motion could be impeded. This has important implications especially for pulsar glitch models as it would lead to a large part of the vorticity of the star being decoupled from the “normal” component, to which the electromagnetic emission is locked.

In the chapter 4 we have seen that the this pinning interaction seems very low and therefore negligible. In this regard, in the previous chapter the snowplow model has been developed and applied without considering any kind of pinning force in the core of the neutron star. Anyway, we can explore the consequences of strong pinning in the core on the “snowplow” model, making use of same realistic equations of state and relativistic background models (as done in the previous chapter) for the neutron star. We find that in general a large fraction of pinned vorticity in the core is not compatible with observations of giant glitches in the Vela pulsar. The conclusion is thus that either most of the core is in a type I superconducting state or that the interaction between vortexes and flux tubes is weaker than previously assumed (in agreement with the results of chapter 4).

6.1 Introduction

Neutron stars allow us to probe the state of matter in some of the most extreme conditions in the universe. Not only can the density in the interior of these very compact objects exceed nuclear saturation density, but NSs also host some of the strongest magnetic fields in nature, with intensities of up to $\approx 10^{15}$ G for magnetars.

Not surprisingly, modelling such complex objects requires the use of some poorly understood physics.

In particular the star will rapidly cool below the critical temperature for the neutrons to be superfluid and the protons to be superconducting. The protons of the outer core are predicted to form a type II superconductor (Migdal, 1959; Baym et al., 1969), in which the magnetic flux is confined to flux tubes, inside which the magnetic field strength is of the order of the lower critical field for superconductivity, $B_c \approx 10^{15}$ G. However, above a critical density of approximately $\rho_c \approx 3 \times 10^{14}\,\mathrm{g/cm^3}$, one expects a transition to type I superconductivity, in which the formation of fluxtubes is no longer favourable but rather the magnetic field is contained in regions of normal protons (Sedrakian, 2005). Given that the critical density for this transition is easily reached in NS interiors it is possible that a sizeable portion of the star may in fact be in a type I superconducting state (Jones, 2006): this is the case that has been discussed in chapter 5, where the pinning phenomena was only considered in the inner crust of the neutron star.

An important issue to address is, however, whether vortexes will only pin to the crustal lattice or whether they are pinned to flux tubes if the outer core is in a type II superconducting state (Link, 2003), thus effectively decoupling a large fraction of the stellar moment of inertia from the crust. Furthermore if vortexes are pinned in the core this is likely to lead to the onset of turbulence and may play an important role in pulsar ’timing noise’ (Link, 2012a). The interaction between flux tubes and vortexes can also have a strong impact on the gravitational wave driven r-mode instability (Ho et al., 2011; Haskell et al., 2012a) and on NS precession (Link, 2003).

Here we investigate the effect of vortex pinning in the core on the “snowplow” glitch model by considering a fraction of the core vorticity blocked. We implement the model with realistic equations of state and relativistic stellar models, as in chapter 5, and show that, in general, one cannot fit the size and postglitch jumps in frequency derivative of Vela giant glitches if a large portion of the core vortexes are pinned. This points towards the fact that most of the core could in fact be in a type I superconducting state, or that the vortex/flux tube interaction is weaker than previously assumed, as showed in chapter 4 and as some microphysical estimates suggest (Babaev, 2009).

Furthermore Glampedakis and Andersson (2011) recently showed that vortex pinning in the core is likely to be a short lived phenomenon that may only be relevant in a short period of a NS’s life and in magnetars, and in their hydrodynamical model of giant pulsar glitches Haskell et al. (2012c) also find that vortex pinning in the core is inconsistent with the observed post-glitch relaxation timescales in the Vela.

6.2 The model

The starting point of our investigation will be the “snowplow” model for glitches of Pizzochero (2011), which we have explored int he previous chapter and which we briefly review here. We take the NS to be a two component system, where one of the components, the so-called "normal" component, is given by the crust and all charged components tightly coupled to it by the magnetic field. The other, the "superfluid", is given by the superfluid neutrons in the core and crust. The superfluid rotates by forming an array of quantized vortexes which carry the circulation and mediate an interaction between the two components known as Mutual Friction, which in the core can couple the two fluids on timescales of seconds (Andersson et al., 2006). Vortexes can, however, also be *pinned* to ions in the crust or flux-tubes in the core (Anderson and Itoh, 1975; Alpar, 1977; Pines et al., 1980; Alpar et al., 1981; Anderson et al., 1982; Ruderman et al., 1998; Link, 2003). As a consequence vortex motion is impeded and the superfluid cannot spin-down, effectively decoupling it from the normal component which is spinning down due to electromagnetic emission. If a lag builds up between the superfluid and the normal component this will, however, give rise to a Magnus force acting on the vortexes, which takes the form $\mathbf{f}_m = \kappa\rho_s\hat{\mathbf{\Omega}} \times (\mathbf{v}_v - \mathbf{v}_s)$, where $\mathbf{f}_m$ is the force *per unit length*, $\kappa = 1.99 \times 10^{-3}\,\mathrm{cm}^2/\mathrm{s}$ is the quantum of circulation, ρ_s is the superfluid density, $\hat{\mathbf{\Omega}}$ is the unit vector pointing along the rotation axis, $\mathbf{v}_v$ is the velocity of the vortex lines and $\mathbf{v}_s$ is the velocity of the superfluid. We assume that the neutrons are superfluid throughout the star and take $\rho_s = (1 - x_p)\rho$, with x_p the proton fraction calculated by Zuo et al. (2004). Once the Magnus force integrated over a vortex exceeds the pinning force, the vortex will unpin and be free to move out.

We follow the procedure of chapter 5 and integrate the relativistic equations of stellar structure for two realistic equations of state, SLy (Douchin and Haensel, 2001) and GM1 (Glendenning and Moszkowski, 1991). We assume straight vortexes that cross through the core (Zhou et al., 2004) and for the pinning force per unit length $\mathbf{f}_p$ we use the realistic estimates of chapter 3 with the profile of fig. 5.1. Balancing the pinning force to the Magnus force and integrating over the vortex length allows us to calculate the lag at which the vortexes will unpin in different regions. The normalization of $\mathbf{f}_p$ is chosen in such a way as to give an inter-glitch waiting time $T_g = \Delta\Omega_{\mathrm{max}}/|\dot{\Omega}|$ of approximately 2.8 yr for the Vela pulsar, where $\Delta\Omega_{\mathrm{max}}$ is the maximum of the critical unpinning lag.

If there is no pinning in the core vortexes will unpin and move out toward the crust, where they encounter a steeply increasing pinning potential and repin. This leads to the creation of a thin vortex sheet that moves towards the peak of the potential, the so-called "snowplow" effect. Once the maximum of the critical lag has been reached the vortexes can no longer be held in place and the excess vorticity is released catastrophically, exchanging angular momentum with the normal component and giving rise to a glitch (Pizzochero, 2011). We assume that this is the mechanism that gives rise to giant glitches, i.e. glitches with steps in the spin rate $\Delta\Omega_{gl} \approx 10^{-4}\,\mathrm{rad/s}$ that are observed in the Vela and other pulsars (Espinoza et al., 2011). Smaller glitches are likely to be triggered by crust quakes or random vortex avalanches (Warszawski and Melatos, 2008; Melatos and Warszawski, 2009; Warszawski and Melatos, 2011).

We can easily calculate the number of vortexes in the vortex sheet once it has reached the peak of the potential as $N_v = \frac{2\pi}{\kappa} r_{\mathrm{max}}^2 \Delta\Omega_{\mathrm{max}}$, where r_{max} is the cylindrical radius at which the maximum of the critical lag is located and $\Delta\Omega_{\mathrm{max}}$ the value of said maximum. The angular momentum exchanged as the vortexes move out and annihilate is then given by:

$$\Delta L_{\text{gl}} = 2\kappa Q N_v \int_{r_{\max}}^{R_c} x\,dx \int_0^{l(x)/2} \rho(\sqrt{x^2+z^2})dz \tag{6.1}$$

where $Q = I_s/I_{\text{tot}}$ is the superfluid fraction of the moment of inertia, R_c is the radius of the inner crust where the vortexes annihilate (taken at neutron drip density), $l(x)$ is the length of a vortex at a given cylindrical radius x and ρ is the density. The glitch observables can then be derived as

$$\Delta\Omega_{\text{gl}} = \Delta L/I_{\text{tot}}[1-Q(1-Y_{\text{gl}})] \tag{6.2}$$

and

$$\Delta\dot{\Omega}_{\text{gl}}/\dot{\Omega}_\infty = [Q(1-Y_{\text{gl}})]/[1-Q(1-Y_{\text{gl}})], \tag{6.3}$$

where $\Delta\Omega_{\text{gl}}$ is the step in angular velocity due to the glitch and $\Delta\dot{\Omega}_{\text{gl}}/\dot{\Omega}_\infty$ is the *instantaneous* step in the spin-down rate immediately after the glitch, relative to the steady state pre-glitch spindown rate $\dot{\Omega}_\infty$. We have also introduced the parameter Y_{gl} which represents the fraction of superfluid moment of inertia which is coupled to the crust during the glitch. Given that the rise time τ_r is very short (less than a minute (Dodson et al., 2002)) it is likely that only a small fraction of the core will be coupled to the crust on this short timescale, with the rest of the star recoupling gradually on longer timescales and giving rise to the observed exponential post-glitch relaxation (see Haskell et al. (2012c) for a detailed discussion of this issue). The best observational upper limits on the rise time are $\tau_r < 40\,\text{s}$ (Dodson et al., 2002) from the Vela 2000 glitch, while an interesting lower limit of $\tau > 10^{-4}$ ms can be derived from the non detection of a GW signal from the Vela 2006 glitch (Warszawski and Melatos, 2012a). Theoretical estimates, on the other hand, give $\tau_r \approx 1-10\,\text{s}$ (Haskell et al., 2012a), which thus easily allow for the angular momentum in eq. (6.1) to be exchanged during the short rise times observed in radio pulsars.

Let us now consider the motion of a vortex if the NS core is a type II superconductor. As a vortex approaches a flux tube its magnetic energy will increase if they are alligned or decrease if they are antialigned reasulting in an energy per intersection of approximately $E_p \approx 5\,\text{MeV}$ (Ruderman et al., 1998). Note that we have neglected the contribution associated with the reduction of the condensation energy cost if a vortex and a flux tube overlap. This leads to an energy cost per interesection slightly smaller than that estimated above (of the order $E_p \approx 0.1-1\,\text{MeV}$) (Ruderman et al., 1998; Sidery and Alpar, 2009). Vortex motion is thus impeded by the flux tubes, that provide an effective pinning barrier unless the vortexes have enough energy to cut through them. The corresponing pinning force per unit length of a vortex has been estimated to be $f_p \approx 3\times10^{15}B_{12}^{1/2}\text{dyn cm}^{-1}$ (Link, 2003), and is balanced by the Magnus force for a critical relative velocity of $w_c \approx 5\times10^3 B_{12}^{1/2}\text{cm s}^{-1}$. This leads to a critical lag (at a radius of 10 km) $\Delta\Omega_c \approx 5\times10^{-3}B_{12}^{1/2}\text{rad/s}$, where we have assumed an average density for the core of $\rho = 3 \times 10^{14}$ g cm^{-3}. Given the large value of the critical lag, comparable to what could be built up in-between Vela glitches, a substantial part of the vorticity in the core could be pinned.

To account for this effect we shall assume that a fraction of the vorticity in the core is pinned and does not contribute to the angular momentum stored in the vortex sheet. This is equivalent to assuming that all the vorticity within a radius $R_v = \eta R_b$ is frozen, with R_b the radius of the base of the crust and η a free parameter. We thus define a fraction of pinned vorticity in the core as $\xi = R_v^2/r_{\rm max}^2$. The total number of vortexes in the vortex sheet before the glitch scales accordingly:

$$N_v = (1-\xi)\frac{2\pi}{\kappa} r_{\rm max}^2 \Delta\Omega_{\rm max} \tag{6.4}$$

By using eq. (6.4) in eq. (6.1) we can obtain the angular momentum exchanged during the glitch and by fitting the size of a glitch, $\Delta\Omega_{\rm gl}$, we can derive the coupled fraction of superfluid

$$Y_{\rm gl} = \frac{1}{Q(1-\xi)}\left[\frac{\Delta L}{\Delta\Omega_{\rm gl} I_{\rm tot}} + Q - 1\right]. \tag{6.5}$$

The instantaneous step in the frequency derivative then follows from

$$\frac{\Delta\dot{\Omega}_{\rm gl}}{\dot{\Omega}_\infty} = \frac{Q(1-\xi)(1-Y_{\rm gl})}{1-Q[1-(1-\xi)Y_{\rm gl}]} \tag{6.6}$$

6.3 Results

In order to compare our results with observations we consider the case of the Vela pulsar. The Vela (PSR B0833-45 or PSR J0835-4510) has a spin frequency $\nu \approx 11.19$ Hz and spin-down rate $\dot{\nu} \approx -1.55 \times 10^{-11}$ Hz s^{-1}. Giant glitches are observed roughly every thousand days and have relative frequency jumps of the order $\Delta\Omega/\Omega \approx 10^{-6}$. The spin-up is instantaneous to the accuracy of the data, with upper limits of 40 s for the rise time obtained from the 2000 glitch (Dodson et al., 2002) and of 30 s for the 2004 glitch, although this limit was less significant (Dodson et al., 2007)). The glitch is usually fitted to a model consisting of permanent steps in the frequency and frequency derivative and a series of transient terms. It is well known that to fit the data at least three are required, with decay timescales that range from months to hours (Flanagan, 1996). Recent observations of the 2000 and 2004 glitch have shown that an additional term is required on short timescales, with a decay time of approximately a minute. Given that the Vela 2000 glitch provides the most robust observational results, we shall compare the expression in eq. (6.6) to the step in frequency derivative associated with the short timescale (1 minute) after the Vela 2000 glitch, which we assume is a reasonable approximation to the instantaneous post-glitch step in the spin down rate. The parameter $Y_{\rm gl}$ is obtained from eq. (6.5) by fitting to the Vela 2000 glitch size of $\Delta\Omega/\Omega = 2.2 \times 10^{-6}$ (Dodson et al., 2002).

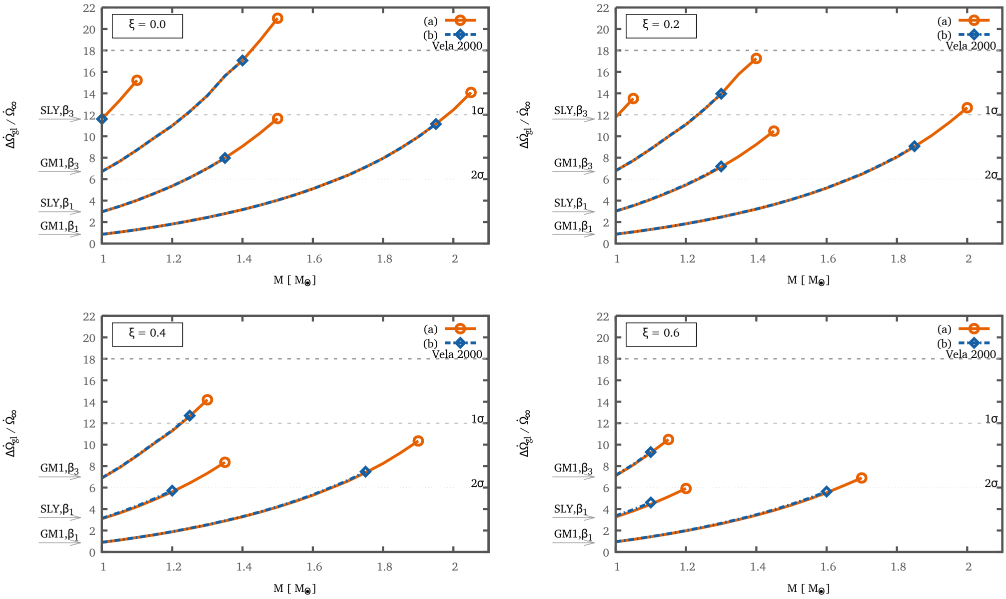

Figure 6.1: We plot the value of the fractional step in frequency derivative $\Delta\dot{\Omega}/\dot{\Omega}$ for varying values of the fraction of pinned vorticity in the core, ξ for SLy and GM1. The parameter β encodes in-medium polarization effects, as described in the text. For x_p we use the results of Zuo et al. (2004), both those obtained with two-body interactions (case a) and with three-body forces (case b). The end of the curves in these two cases corresponds to the point after which we can no longer find a reasonable physical solution. The horizontal line represents the measured value for the Vela 2000 glitch, and the thin lines are respectively 1σ and 2σ deviations. It is clear that in general both EOSs and models for the proton fraction are compatible with free vorticity in the core. As we increase the pinned fraction however it becomes increasingly more difficult to fit the data, and for $\xi > 0.5$ no solution can be found at the 1σ level.

In fig. 6.1 we show the results for varying values of ξ, for both SLy and GM1. The parameter β encodes the reduction of the pairing gap due to polarization effects in the neutron medium. Recent calculations suggest that polarization reduces the gap and shifts the maximum to lower densities (Gandolfi et al., 2009), an effect which in our setting corresponds to the value $\beta \approx 3$, while $\beta = 1$ corresponds to a bare particle approximation. The horizontal lines show the region that is allowed by the measurements of the step in frequency derivative of the Vela 2000 glitch. It is obvious that most equations of state and proton fractions can match this value if all vorticity in the core is free, as was also found in the previous chapter and by Haskell et al. (2012c), although we note that for the more realistic case of $\beta = 3$ and three body cases included in the calculation of x_p, the stiffer equation of state is clearly favored. We now compare this to the case in which part of the core is in a type II superconducting state and part of the vorticity is pinned. As we can see from fig. 6.1, as the parameter

ξ increases it becomes increasingly harder to fit the observed values of $\Delta\dot{\Omega}$ and in most cases this is only possible for a very restricted interval of masses. In general one cannot obtain a physically reasonable fit if more than half of the vorticity in the core is pinned. This points to the conclusion that the vortex/flux tube interaction is weaker than previously assumed and that most of the vorticity in the core is, in fact, free. This conclusion is compatible with that of Haskell et al. (2012c), who found that a weak coupling between the superfluid and normal component in the core (as would be the case if most of the vortexes in the core are pinned) does not allow to fit the shorter post-glitch relaxation timescales of the Vela. Note that the conclusions of this Letter and those of Haskell et al. (2012c) are derived in different methods (in this case calculating the exchange of angular momentum in a static model, in the case of Haskell et al. (2012c) by fitting the post-glitch relaxation with a dynamical multifluid model) and are thus independent, save for the use of the pinning forces calculated in Grill (2011); Grill and Pizzochero (2012).

6.4 Conclusions

In this chapter we have extended the "snowplow" model Pizzochero (2011) discussed in the previous chapter, to account for the possibility that part of the vorticity in the core may be pinned due to the interaction between vortexes and flux tubes. We fit the step in frequency and in frequency derivative of the Vela 2000 glitch to obtain constraints on the pinned fraction of vortexes in the core and in general find that both quantities cannot be fitted for reasonable physical parameters if the pinned fraction is larger than 50%. Although we do not deal with the microphysical details of the vortex dynamics in the core, our conclusions are quite general. The only quantity that is needed to evaluate the angular momentum that is exchanged during a glitch is, in fact, the number of vortexes that are stored close to the peak of the pinning potential in the crust. As long as the excess vorticity of the core can be transferred to the equatorial strong pinning region in-between glitches the details of the vortex motion are not influential.

The general conclusion is that either most of the core is in a type I superconducting state (and the vortex pinning is negligible (Sedrakian, 2005)), or that the vortex/flux tube interaction is weaker than previously thought. This is the same conclusion that Haskell et al. (2012c) come to after fitting the post-glitch short-term relaxation of Vela glitches with a hydrodynamical model. If such an conclusion is confirmed it would have serious implications also for NS precession (Link, 2003) and for GW emission (Haskell et al., 2008; Lander et al., 2012; Ho et al., 2011; Haskell et al., 2012a). Note that on a microphysical level it is very likely that the interaction between vortexes and flux tubes is weaker than the previous estimates presented here. These estimates are upper limits on the strength of the pinning force, as they do not account for the finite rigidity of vortexes, which could lead to a reduction of a factor 100-1000, as theoretical estimates in chapter 4 also confirm. Furthermore recent calculations (Babaev, 2009) suggest that in the presence of strong entrainment or gapped Σ^- hyperons in the crust the interaction between flux tubes and vortexes will be significantly weaker, and even in the presence of pinning the superfluid may be coupled to the crust on short timescales (Sidery and Alpar, 2009).

CHAPTER 7

Measuring neutron star masses with pulsar glitches

In this chapter we want to extend the snowplow model described previously in order to overcome its limitations. The paradigm proposed till now use the two component approach together with a realistic macroscopic scenario (spherical geometry, density profile from TOV equilibrium with realistic EOSs, density-dependent pinning and Magnus forces) and with the assumption (microscopically better justified) of continuous vortexes across the core and the crust. The strength of this perspective is its simplicity, with at the same time the ability of identify a storing mechanism for the angular momentum of neutron vortexes that it suddenly released to the crust at the glitch. The angular momentum reservoir is created by the existence of clear peak in the critical lag profile, obtained by equating the pinning force acting on a vortex with the Magnus force that tends to push it outward. The plots of fig. 5.5 clearly show this peak: the strong pinning barrier in the crust and the flat profile in the core (consequence of the assumption of continuous vortexes) suggest the snowplow mechanism. In the time between two glitches the actual lags builds up and the depinning region becomes larger, pushing a thin vortex sheet (that actually store the angular momentum exchanged during the glitch) toward the maximum of the critical lag. When this maximum is reached we have a glitch because there is no more strong pinning region that can stop the vortexes from reaching the crust: the vortexes in the thin sheet unpin simultaneously and a vortex avalanche starts down the peak. The glitch event relaxes the two components of the star, reducing the lag and allowing the vorticity in the core to be repinned: this is important because in this way the process can repeat itself.

Following this approach it's possible to calculate the number of vortexes stored and their angular momentum (see eq. (5.11)) and consequently the jump size $\Delta\Omega_{\rm gl}$ of the glitch. The model relay on two free parameters: the maximum value pinning force $f_{\rm PM}$ and the fraction of vorticity coupled to the normal crust during the glitch, $Y_{\rm gl}$. In chapter 5 we proceeded by fixing the value of $f_{\rm PM}$ in order to reproduce the average waiting time between glitches observed for the Vela pulsar, while the recorded jump in $\dot{\Omega}$ was used to infer the value of $Y_{\rm gl}$ (referred to the Vela 2000 glitch, see (Dodson et al., 2002)).

The snowplow model is a consistent mechanism for vortex accumulation and thence a realistic description of the angular momentum reservoir, which is needed to explain the glitch phenomenon. However, it is not a plausible description of the actual trigger mechanism, since it predicts a constant period between glitches and therefore it cannot reproduce the wide distribution of intervals between glitches observed in reality. Moreover, the statistical studies of Melatos and Warszawski (2009) indicate that the distribution of glitch sizes and times are compatible with the behavior of critical systems and that several glitch triggers appear as possible (vortex knock–on, acoustic waves, etc). Therefore, in this revised version of the snowplow model proposed here, we leave the trigger as a unknown mechanism, whose origin and timing properties are still to be determined. We use the snowplow scenario of vortex accumulation in an outward moving sheet to evaluate the angular momentum stored in the crust as a function of the time passed from the previous glitch. This yields the maximum value of a glitch if all the excess vorticity removed from the core and accumulated at the sheet was released at that time and its angular momentum was transferred instantaneously to the crust.

The main feature of the snowplow model that remains valid here is the vortex sheet, namely a thin cylindrical shell of more–than–average vortex density, dynamically out of equilibrium and moving outwards against the pinning potential, driven by the increasing lag associated to the crust secular spin-down. On one hand, it provides for the first time a realistic mechanism to store the angular momentum which is necessary to justify the occurrence of a glitch. On the other hand, the presence of the vortex sheet may be crucial in the trigger mechanism; indeed, triggering the catastrophic and simultaneous unpinning of the accumulated excess vorticity appears simpler when this is concentrated in a thin cylindrical shell, rather than being diffused all across the crust.

7.1 The entrainment in the snowplow paradigm

In chapter 5 we used a simple profile for the pinning force per unit length that was scaled in order to obtain the corrected waiting time. Here we leave the trigger as an unknown mechanism that cause a glitch at a arbitrary time t after the previous one: there is no prescription to perform a fitting on the pinning force and therefore we will use here the realistic profiles obtained in chapter 3 for the configuration $L = 5000, \beta = 3$, that is microscopically favoured (see also considerations in chapter 5 and (Gandolfi et al., 2008)). The values used are reported in fig. 3.11 and in table 3.3.

An important aspect that was neglected in the original model is superfluid entrainment. As showed by Andersson et al. (2012) the presence of this non–dissipative coupling between the neutron fluid and the proton one can't be neglected and it is important to explain observational data. The effect of entrainment can be represented

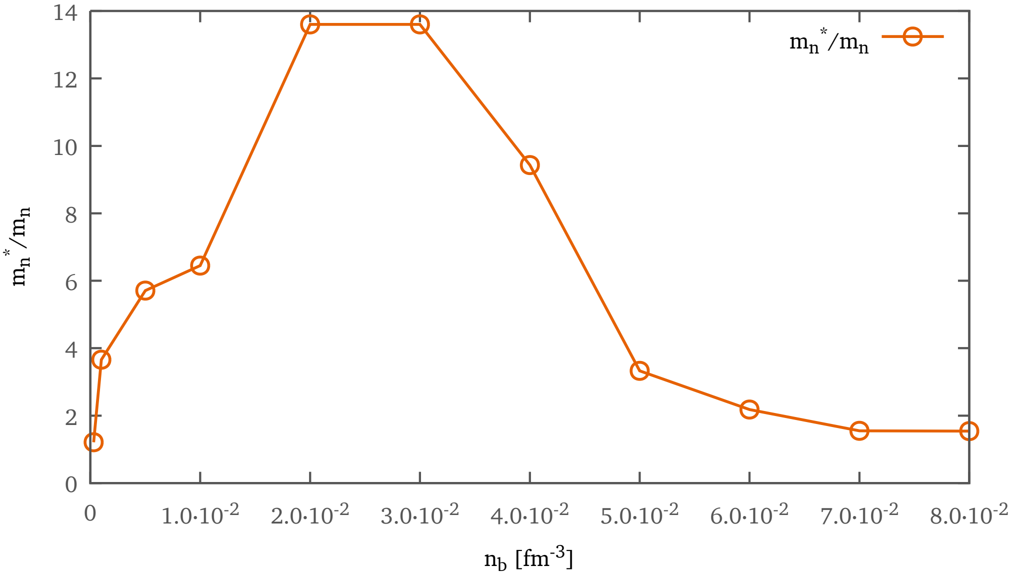

Figure 7.1: Plot of the entrainment effective neutron mass m_n^*/m_n as a function of the barion density n_b (Chamel, 2006). These values will be used here and in the following to model the entrainment effect in a neutron star crust.

by a neutron effective mass, $m_n^*(\rho)$, and we introduce it in the snowplow model in the standard way, by reducing locally the neutron-proton velocity lag for pinned vorticity. We will use for $m_n^*(\rho)$ the recent values calculated by Chamel (2012) for the crust of neutron stars. The values of m_n^* are given by the author as a function of the barion density n_b (see fig. 7.1 for a plot of the ratio m_n^*/m_n versus n_b). The barion density can be related to the density ρ following the considerations suggested by Haensel and Potekhin (2004) for a thermodynamically consistent EOS that lead to the this equation:

$$n_b(r) = \frac{1}{m_n}\left[\rho(r) + \frac{P(r)}{c^2}\right] e^{\Phi(r)-\Phi(R)} \tag{7.1}$$

where $\Phi(r) = \sqrt{1-2GM/(Rc^2)}$. As done in previous chapters, we obtain a realistic star by integrating the TOV equations with SLy and GM1 as equations of state, than the eq. (7.1) lets us assign a value to the effective neutron mass m_n^* for every radius r.

The range of density covered by Chamel (2012) is the typical one of the inner crust of a neutron star. Recent calculations by the same author (Chamel, 2006) suggest that the proton effective mass is slightly lower than the bare mass in the core but can be larger in the crust. This means that the entrainment parameters will vanish close to the base of the crust (Carter et al., 2006): we can therefore consider the $m_n^* = m_n$ in the core of the star.

In a simple global two fluid model, the entrainment affects the dynamics with a nondissipative coupling between the fluids that can be modeled with the following equations (see also Andersson et al. (2012)):

$$(I_p - \varepsilon_n I_n)\dot{\Omega}_p + \varepsilon_n I_n \dot{\Omega}_n = -a\Omega_p^3 - \Psi(r) \tag{7.2}$$

$$(I_n - \varepsilon_n I_n)\dot{\Omega}_n + \varepsilon_n I_n \dot{\Omega}_p = \Psi(r) \tag{7.3}$$

where Ψ encodes pinning, drag forces and eventually other dissipative interactions. It's clear from these equations that a fraction of the neutron component behaves as the proton one; the coefficient of this coupling is ε_n that is strictly related to the effective neutron mass:

$$\varepsilon_n = 1 - \widetilde{m_n^*} \tag{7.4}$$

where $\widetilde{m_n^*} = \frac{m_n^*}{m_n}$. In case of perfect pinning, the left side of eq. (7.3) vanishes (it's easy to verify that in case $\varepsilon_p = 0$ the standard condition used in the snowplow model is reproduced, see chapter 5). This means that even if the vortexes are pinned to the crust, the macroscopic angular velocity of the neutron fluid decrease as a consequence of the coupling with the protons. This is the main effect of the entrainment:

$$\dot{\Omega}_n = -\frac{\varepsilon_n}{1-\varepsilon_n}\dot{\Omega}_p \tag{7.5}$$

From this equation it's possible to calculate the actual lag developed in the star interiors for a time t after a glitch: we call ω the raw lag expressed as $\omega = |\dot{\Omega}_p|t$ and correct it to take into account the entrainment:

$$\Delta\Omega(t) = (\dot{\Omega}_n - \dot{\Omega}_p)t = \left(-\frac{\varepsilon_n}{1-\varepsilon_n} - 1\right)\dot{\Omega}_p t = \frac{\omega}{\widetilde{m_n^*}} \tag{7.6}$$

As described before, we consider an unspecified trigger for the glitch that happens at a time t after the previous one. At this time, the lag $\Delta\Omega(t)$ built by the star has depinned the inner region of the star, before the vortex sheet that is placed at the position $x^*(t)$, as explained by the fig. 7.2. In order to estimate the glitch size, we consider that the angular momentum transferred to the crust is that of the shaded region in the plot: this represent the excess of vorticity after the vortex sheet that is completely removed by the catastrophic avalanche. From eq. (2.21) eq. (2.22) we can express this quantity in the following way:

$$\Delta L_{\mathrm{gl}}(t) = \int \min(\omega(t)/\widetilde{m_n^*}, \Delta\Omega_{\mathrm{cr}})\, x^2 \rho_n(x,z)\, dV \tag{7.7}$$

where the integration must be done in the cylindrical region outside the vortex sheet position x^*. With the usual cylindrical coordinates this becomes

$$\Delta L_{\mathrm{gl}}(t) = 2\pi \int_{x^*}^{R_{\mathrm{ic}}} x^3\, dx \int_0^{\ell(x)} \min(|\dot{\Omega}_p|t, \widetilde{m_n^*}(x,z)\Delta\Omega_{\mathrm{cr}}(x))\, \frac{\rho_n(x,z)}{\widetilde{m_n^*}(x,z)} dz. \tag{7.8}$$

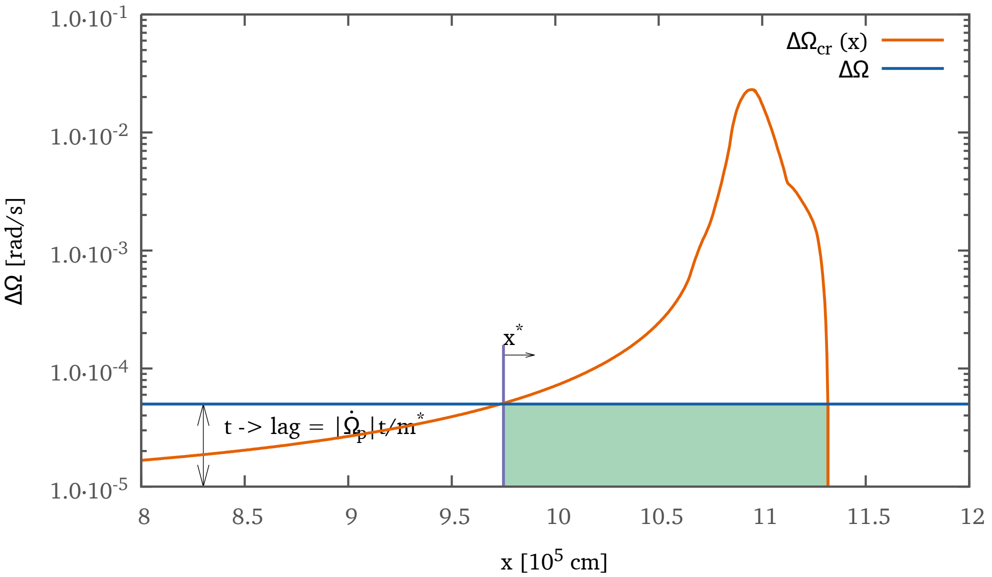

Figure 7.2: This plot shows the critical lag profile of a $1.4\,M_\odot$ GM1 star, as a function of the cylindrical radius x. The shaded region indicates the vorticity involved in the calculation of the angular momentum $\Delta L_{\rm gl}(t)$ transferred to the crust at the glitch (t represent the interglitch time).

Now it's easy to calculate the jump in angular velocity at the glitch, as in chapter 5: $\Delta\Omega_{\rm gl}(t) = \Delta L_{\rm gl}(t)/I_{\rm eff}$, where again the effective momentum of inertia used is

$$I_{\rm eff} = (1-Q)I_{\rm tot} + QY_{\rm gl}I_{\rm tot}. \tag{7.9}$$

This approach leaves us with only one free parameter: after choosing the EOS and the mass of the neutron star, the remaining free quantity is the coupled vorticity $Y_{\rm gl}$.

The result of this revised snowplow model is a function $\Delta\Omega_{\rm gl}(t)$ representing the maximum possible glitch size as a function of the time passed since the previous glitch. All actual glitches must lie below this curve, since vortex avalanches are rarely maximal, as discussed by Espinoza et al. (2011). The vorticity accumulated at the sheet is released simultaneously by the trigger and initiates a global avalanche while the vortex sheet is disrupted, but the avalanche itself may develop in different ways. The snowplow model only provides an upper bound for the glitch size, while the triggering and the dynamics of vortex avalanches are probably better studied by statistical methods suitable for critical systems.

In the fig. 7.3 is plotted the curves $\Delta\Omega_{\rm gl}(t)$ for different choices of the free parameter $Y_{\rm gl}$. We choose to plot the quantity against the raw lag $\omega = |\dot{\Omega}_p|t$, instead the simple interval t between glitches, in order to easily compare the results obtained for a star with the ones obtained for a neutron star with different slowdown. As explained

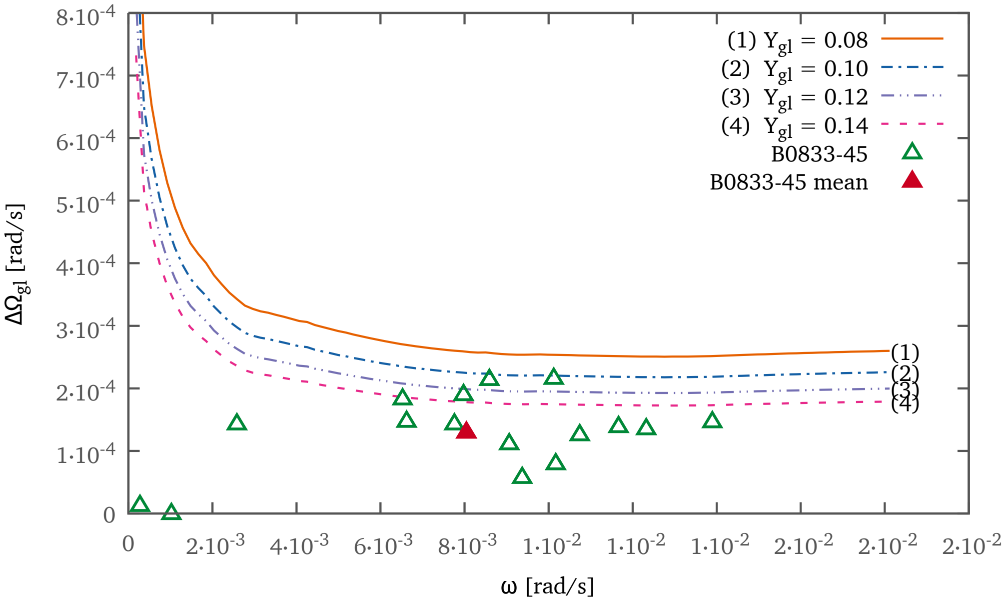

Figure 7.3: Plot of the curves $\Delta\Omega_{gl}(t)$ obtained with different values of the parameter Y_{gl}. All these results are referred to the same $1.3\,M_\odot$ GM1 star. The dots represent the observed glitches of the Vela pulsar.

before, this is not the actual lag developed, due to the presence of the entrainment. In this plot we report, together with the calculated curves, also the observational data of the Vela Pulsar B0833–45: every point represents a recorded glitch, with its jump size in ordinate and the interglitch time multiplied by $|\dot{\Omega}_p|$ on the x axis (for this pulsar the average slowdown is $\dot{\Omega}_p = -9.843\,24 \times 10^{-11}\,\mathrm{rad/s^2}$, see Manchester et al. (2005)). To obtain these curves, we have fixed the mass of the star to be $M = 1.3\,M_\odot$. An analogous approach has been used to test the effect of the parameter M: in fig. 7.4 we change the value of the mass of the star, keeping fixed the fraction of coupled vorticity $Y_{gl} = 0.10$.

From the plots it's clear that both parameters control the value of the jump size for a given waiting time. Increasing the fraction of coupled vorticity lowers the curve in the plot discussed previously, i.e. reduce $\Delta\Omega_{gl}$ consistently for every time t. The effect of the mass is pretty much the same: a massive star will show smaller glitches for every waiting time considered, due to the fact that the shape of the curve remains nearly the same.

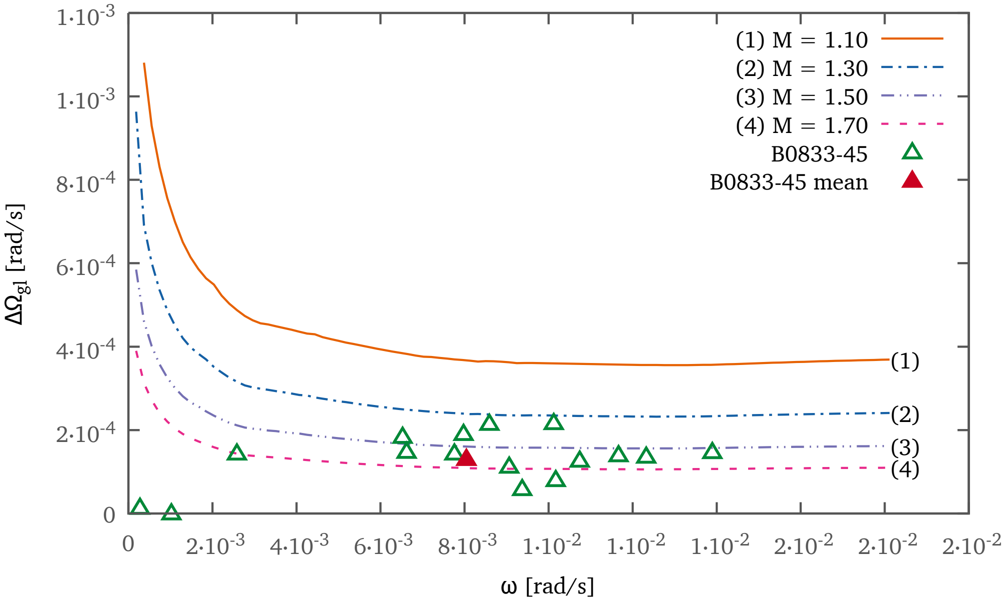

Figure 7.4: Plot of the curves $\Delta\Omega_{\text{gl}}(t)$ obtained with different values of the total mass M of the star. All these results are calculated keeping fixed $Y_{\text{gl}} = 0.10$ and all other parameters. The dots represent the observed glitches of the Vela pulsar.

7.2 Fitting of NS masses with the snowplow model

The considerations exposed in the previous section can be used now to infer the mass of a neutron star in the following way. For this purpose we consider the 15 youngest neutron stars among the set of the *frequent glitchers* (we define with this term the pulsars with at least 5 observed glitches) detailed in table 7.2. These pulsars are the first 15 rows of the table (the column τ reports the age of the pulsar). As explained before, we use a fixed pinning profile obtained from the realistic mesoscopic calculations done in chapter 3 ($L = 5000\,R_{\text{ws}}$, $\beta = 3$), and therefore, once we have fixed the equation of state, we have only two free parameters, namely the mass M and the fraction of coupled vorticity Y_{gl}. For the EoS we will adopt, as usually, the stiff GM1 or the softer SLy. From the results in chapter 2 we can see that the first one admits a larger maximum mass $M_{\text{max}} = 2.36\,\text{M}_\odot$, while for the other $M_{\text{max}} = 2.05\,\text{M}_\odot$.

For each of the 15 younger glitchers, we can plot the observed $\Delta\Omega_i$ vs $\omega_i = |\dot{\Omega}|\tau_i$, where τ_i is the time elapsed from the previous glitch, as well as the curve $\Delta\Omega_{\text{gl}}(\omega)$. As explained, the observed glitches cannot lie above the theoretical upper limit represented by the curve; then we proceed as follows to remove the degeneracy related to the two free parameters:

1. we set the mass of Vela at some value M_{Vela}; then we vary Y_{gl} until the calculated

curve $\Delta\Omega_{gl}(\omega)$ is tangent to the largest observed glitch in Vela.

2. we fix Y_{gl} at the value found for Vela; then, for each of the other 14 objects, we vary the mass M until the curve is tangent to the largest observed glitch in each object.

The procedure is shown in fig. 7.5 and fig. 7.6 where we have used SLy as EOS; and in fig. 7.7 and fig. 7.8 for the stiffer equation of state GM1. In both cases we have set the mass of Vela to be $M_{Vela} = 1.3\,M_{\odot}$, and the mass fitting was made with a discrete step of $0.01\,M_{\odot}$. In the figures we also plot the position of the vortex sheet, $X(t)$ (scale on the right ordinate axis), as a function of the lag; two gray horizontal lines indicate the inner and outer radius of the inner crust. Repeating this for all the 15 glitchers and testing both EOSs, we find that:

- most glitchers can be fitted with a mass smaller than M_{max}. The only exceptions are B1758 and B1737, for which all the observed glitches are well below the curve $\Delta\Omega_{gl}(\omega)$ corresponding to M_{max};
- in the stronger glitchers, the events are triggered when the vortex sheet is completely immersed in the crust (curve $X(t)$ between the two horizontal lines); in the weaker objects, the glitches are triggered when the vortex sheet is mostly immersed in the core, with only the vortex extremities pinned in the crust. Due to the strong entrainment and the realistic values for the pinning force we can conclude that these glitches are always triggered well before reaching the maximum of the pinning potential.

The inferred values of the masses of the considered pulsars are summarized in table 7.1. Since we are fitting the maximal glitches, which are absolute lower limits, the masses we obtain are absolute upper limits: any future larger glitch can only reduce the value obtained here. We have chosen initially to set the mass for Vela at $M_{Vela} = 1.3\,M_{\odot}$. Nevertheless, we have also tested the model by fixing $M_{Vela} = 1.2\,M_{\odot}$: we have observed that this produce a coherent shift by $0.1\,M_{\odot}$ on all the other calculated masses, and therefore the considerations exposed in the next section remain valid: here we will discuss these results in connection with the other observable quantities of the pulsars (see table 7.2). The results presented here are obtained with $Y_{gl} = 0.02$ for SLy and $Y_{gl} = 0.10$ for the GM1 equation of state, values that are reasonable and in perfect agreement with the results of chapter 5.

We want to highlight here the role of the entrainment in the model. In fig. 7.9 we see the curve $\Delta\Omega_{gl}(t)$ in two cases: with the entrainment and without the entrainment. The result is immediately clear: in the configuration without the entrainment there is no chance of fitting all the observational data, because the curve in the plot is “too short”. Changing the free parameters of the model, M and Y_{gl} would not help much, because they only shift vertically the curve. The value of ω_{end} where the curve stops is of course strictly related to the value of the peak of the critical unpinning lag of the star: when the built lag reaches the peak of the critical lag, the star must exhibit its

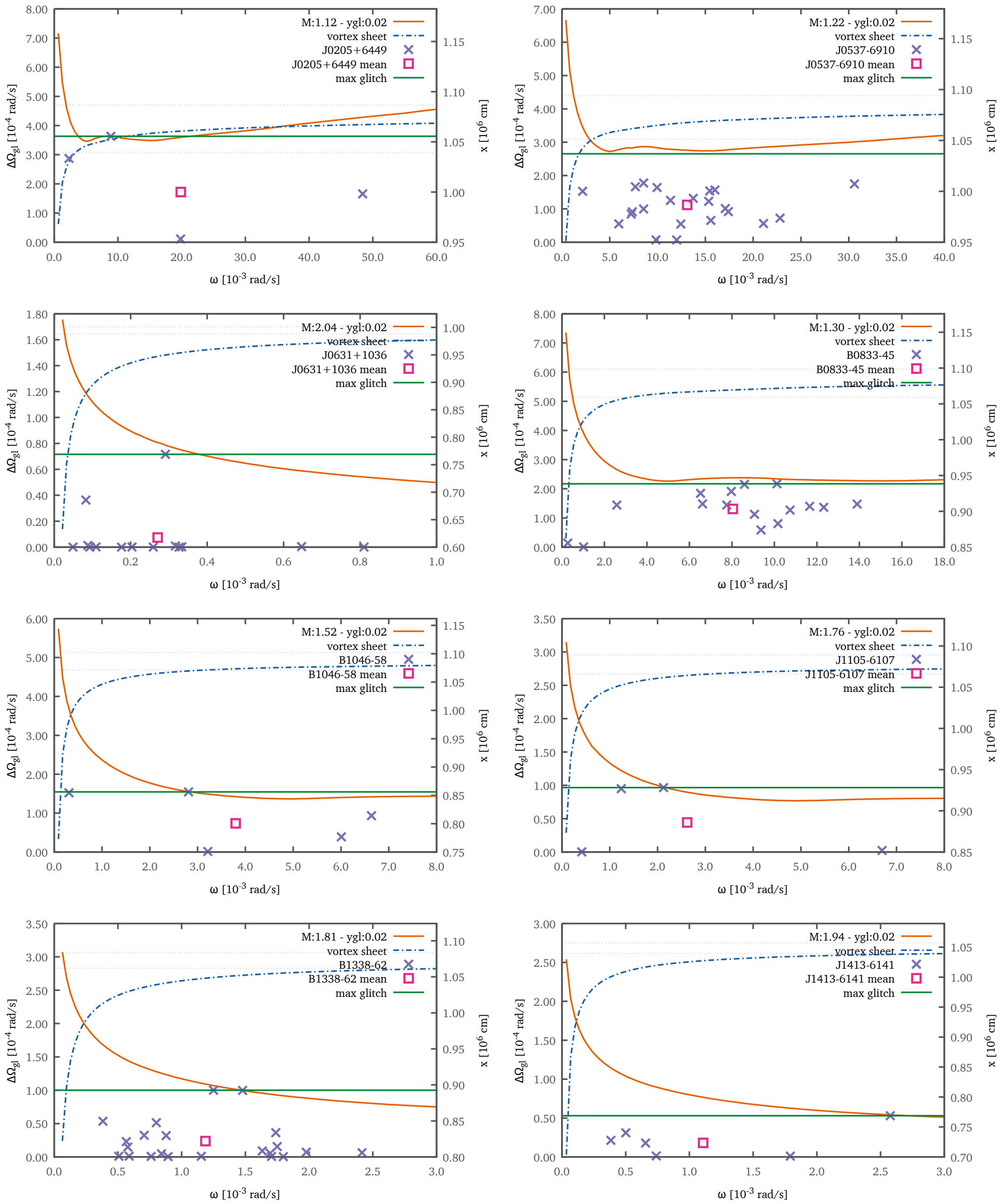

Figure 7.5: These plots show the results of the fitting procedure (with SLy EoS) for the frequent glitchers taken into account (first 8 pulsars, continues in fig. 7.6). For each case we plot the calculated profile $\Delta\Omega_{\rm gl}(t)$ together with the observed values (with dots, see table 2.2 for details). The square corresponds to the average value of the measured glitches. We plot also the position $x^*(\omega)$ of the depinnig front at the moment of the glitch (to be read on the right y axis). The green horizontal line corresponds to the maximum observed $\Delta\Omega_{\rm gl}$, while the other two dotted horizontal lines indicates the inner crust region of the star (on the right y axis).

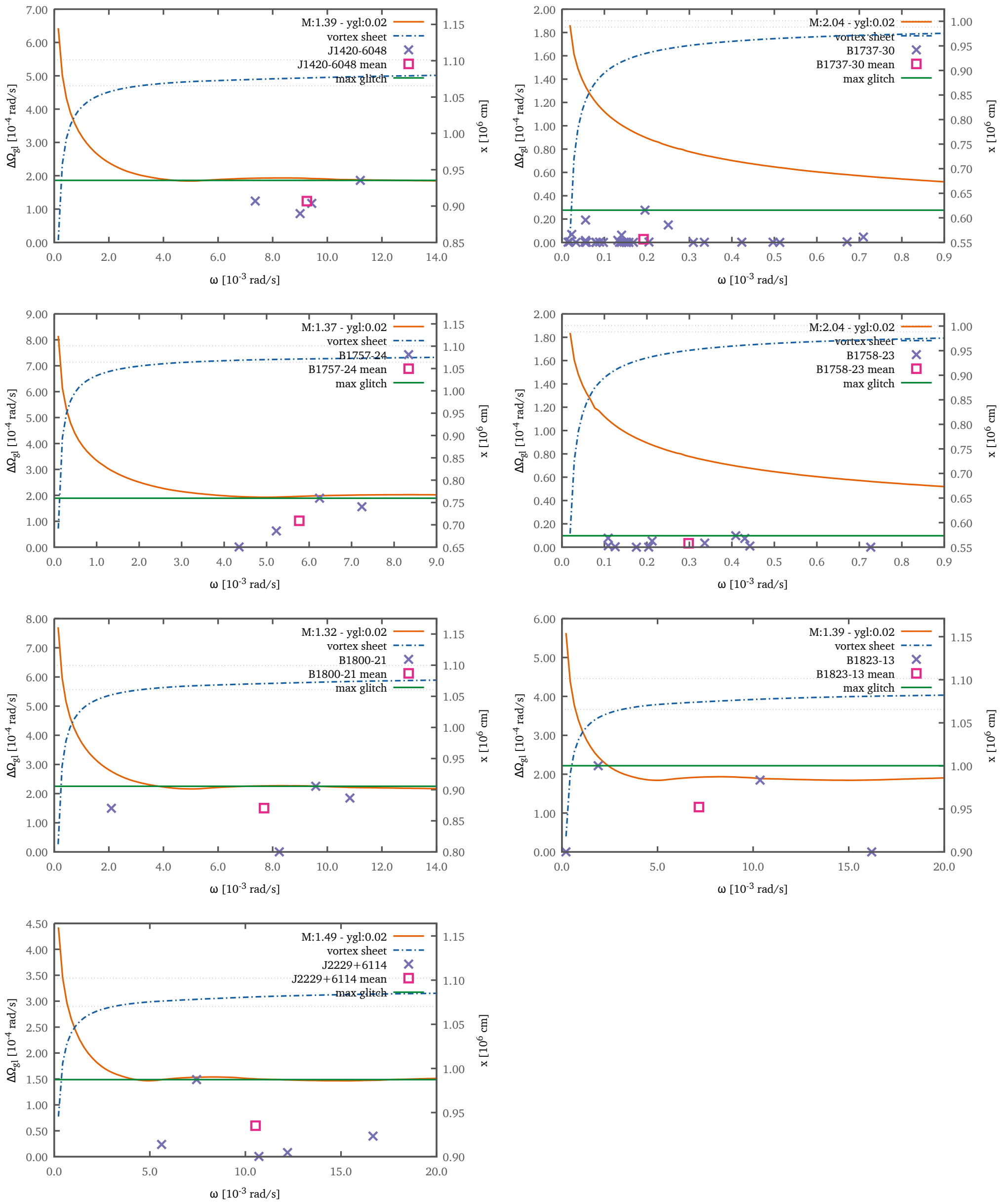

Figure 7.6: These plots complete the results of fig. 7.5 and therefore they are referred to the SLy equation of state. See fig. 7.5 for details.

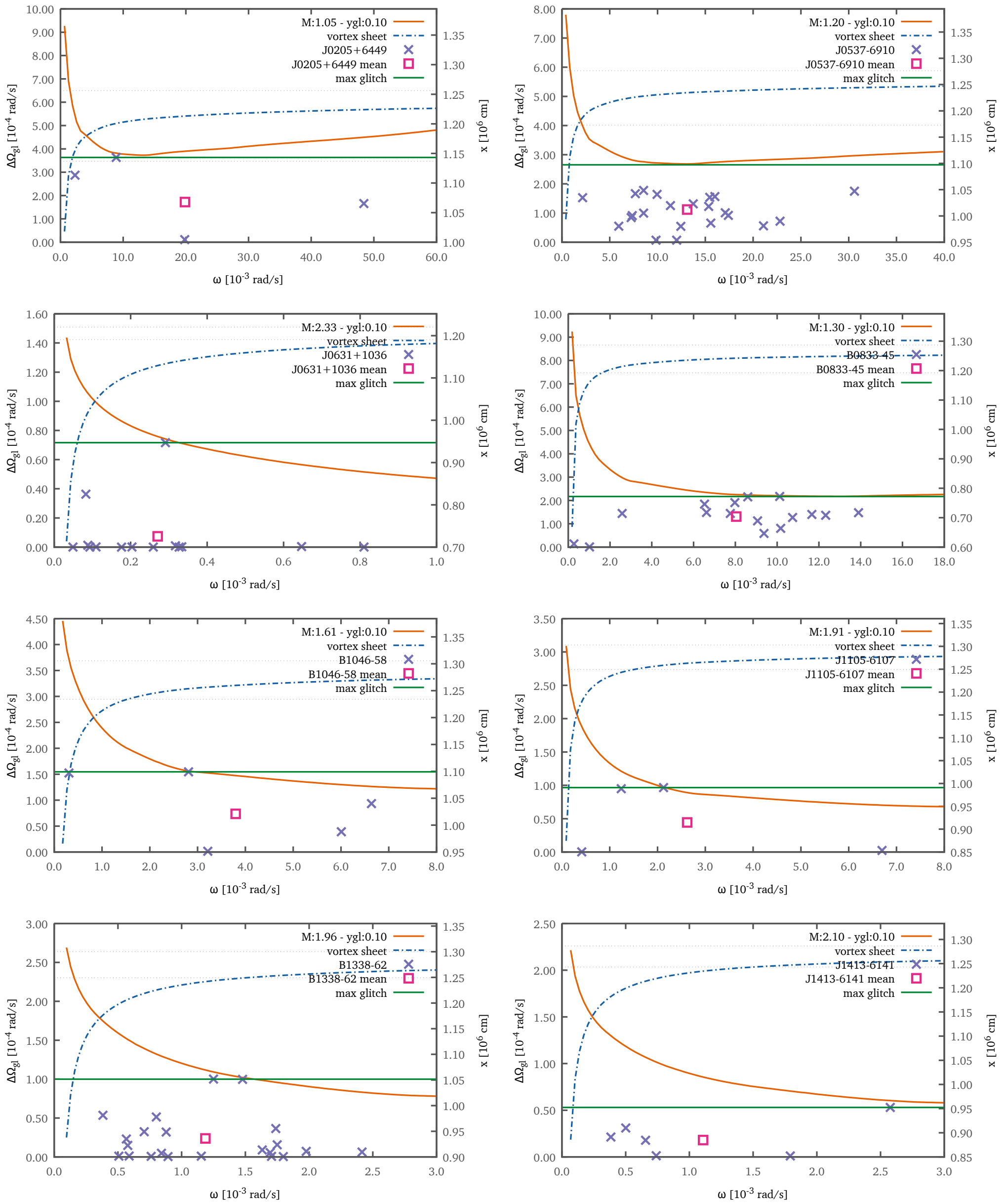

Figure 7.7: These plots show the results of the fitting procedure (with GM1 EoS) for the frequent glitchers taken into account (first 8 pulsars, continues in fig. 7.8). For each case we plot the calculated profile $\Delta\Omega_{\mathrm{gl}}(t)$ together with the observed values (with dots, see table 2.2 for details). The square corresponds to the average value of the measured glitches. We plot also the position $x^*(\omega)$ of the depinnig front at the moment of the glitch (to be read on the right y axis). The green horizontal line corresponds to the maximum observed $\Delta\Omega_{\mathrm{gl}}$, while the other two dotted horizontal lines indicates the inner crust region of the star (on the right y axis).

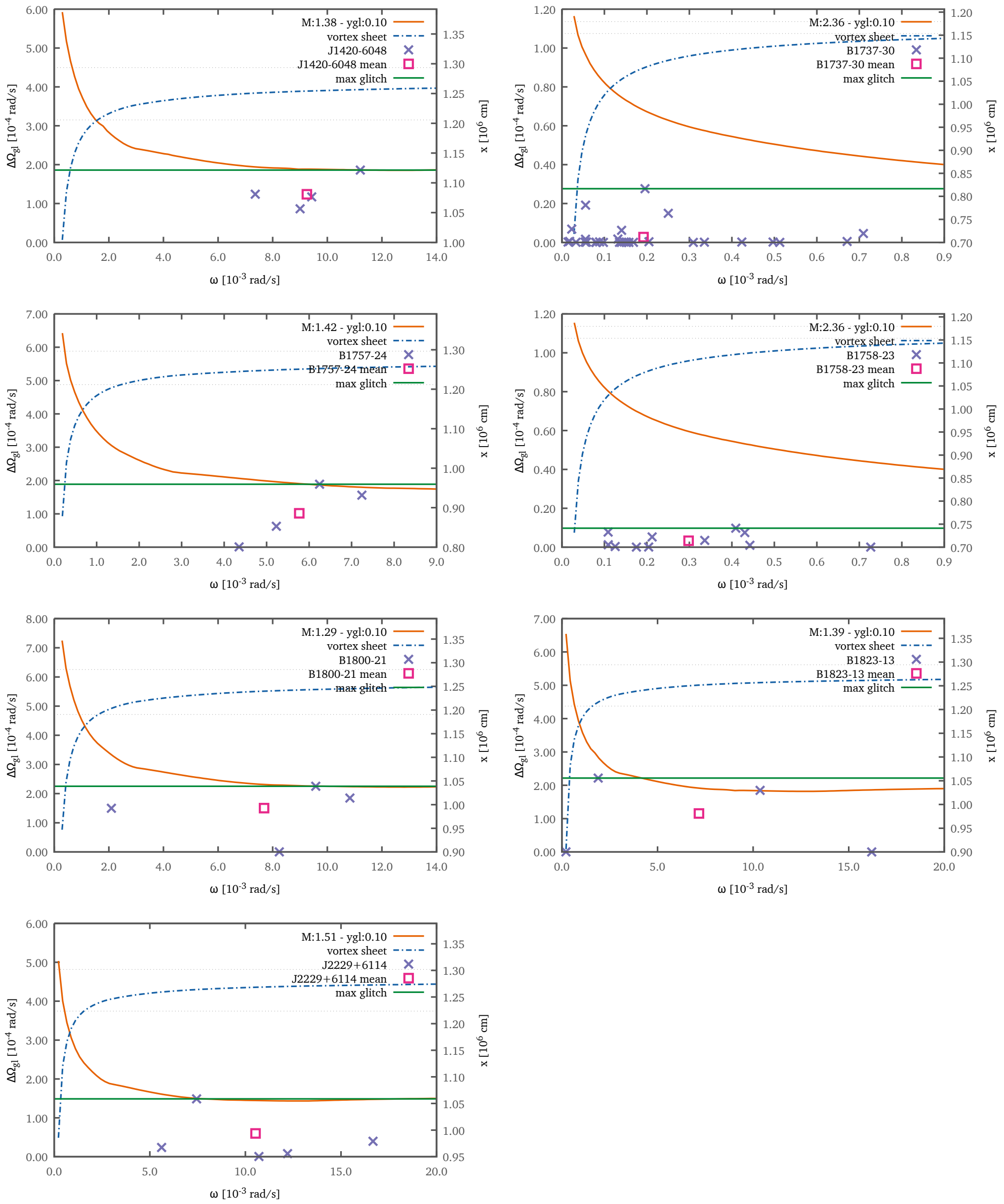

Figure 7.8: These plots complete the results of fig. 7.7 and therefore they are referred to the GM1 equation of state. See fig. 7.7 for details.

Table 7.1: This table summarizes the results of the fitting procedure for both SLy and GM1 (see figs. 7.5 to 7.8 for graphical representation). For each pulsar, the reported mass M is the value of this parameter which fits better the observational data.

Pulsar name	**SLy mass** [$\mathrm{M}_\odot$]	**GM1 mass** [$\mathrm{M}_\odot$]
J0205+6449	1.12	1.05
J0537-6910	1.22	1.20
J0631+1036	2.04	2.33
B0833-45	1.30	1.30
B1046-58	1.52	1.61
J1105-6107	1.76	1.91
B1338-62	1.81	1.96
J1413-6141	1.94	2.10
J1420-6048	1.39	1.38
B1737-30	2.04	2.36
B1757-24	1.37	1.42
B1758-23	2.04	2.36
B1800-21	1.32	1.29
B1823-13	1.39	1.39
J2229+6114	1.49	1.51

maximum glitch. As explained before, the rate at which this lag is built is controlled by the parameter $1/\widetilde{m_n^*}$: the entrainment slows down the entire process, allowing to encompass observational data related to glitches with big waiting time, as in fig. 7.9. This is another important argument in support of the need to include the entrainment in our models: as explained by fig. 7.1, the entrainment is not a small correction to the behavior of the neutron stars, but it is a crucial aspect both for the microscopic and macroscopic points of view.

7.3 A new analysis of the observational data

Existing statistical studies of glitching pulsars as presented by astronomers try to classify them in different classes, related to particular features of the jump parameters: for example, the slow glitchers of Zuo et al. (2004) interpreted as manifestation of two-state magnetospheric switching, or the large glitchers of Espinoza et al. (2011) interpreted as manifestation of large, global avalanches of previously pinned superfluid vortexes, namely the superfluid-glitch paradigm of Anderson and Itoh. The snowplow model, as described before, is a quantitative and realistic implementation of this approach, focused on the large glitchers, and therefore it can explain these events. However, if the large glitches can be explained in terms of superfluid–glitches, the question remains of why only certain pulsars behave in such a way and, conversely,

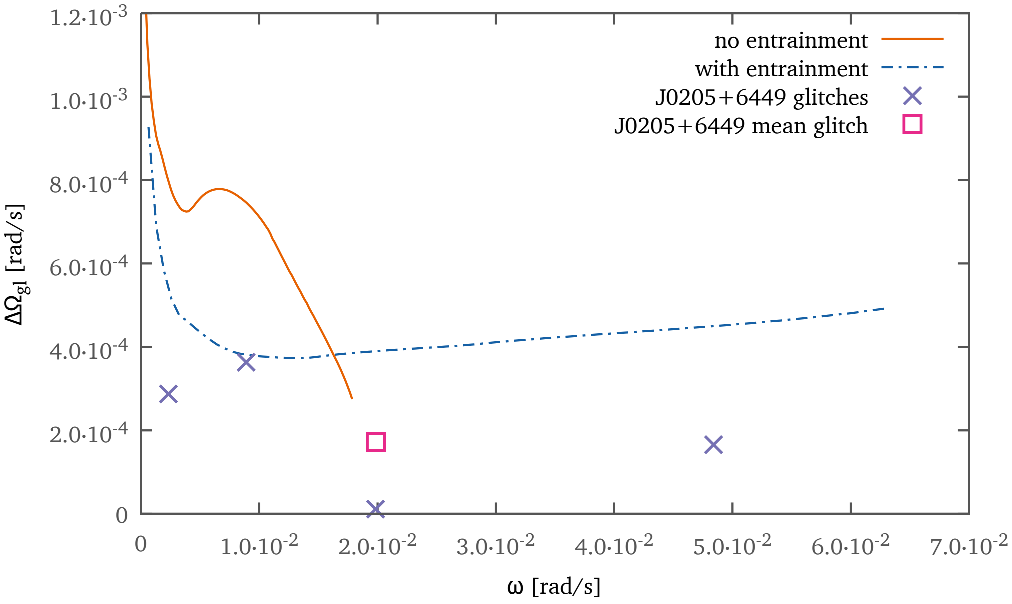

Figure 7.9: This plots shows the effect of the entrainment. The two curves are obtained with the same parameters (GM1, $M = 1.05$ and $Y_{\text{gl}} = 0.10$) except for the fact that $\varepsilon_n = 0$ in one case. We can see that without the entrainment is not possible to fit all the measured values even if we change the mass M or the fraction of coupled vorticity Y_{gl}.

of what is the effect of vortex avalanches in the other (non-large) glitchers. In order to answer this, firstly we need to analyze the existing data in a new way, which can reveal gradually changing features among different glitchers rather than focus on their differences. Then we will merge this analysis with the fitted masses obtained in the previous section, to see if this parameter plays an important role in the dynamics of a glitch and affect the observed quantities.

For statistical significance, we only consider the 25 pulsars for which at least five glitches have been observed. In table table 7.2 we have reported these NS with all the quantities relevant for this analysis: rotational parameters (pulsation, Ω, and spin-down, $|\dot{\Omega}|$), observational parameters (number of glitches, N_{gl}, and observational time between the first and last glitch observed, $T_{\text{obs}} = t_{\text{last}} - t_{\text{first}}$) and glitching parameters (size of largest observed glitch, $\Delta\Omega_{\text{gl}_{\text{max}}}$, average glitch size, $\langle \Delta\Omega_{\text{gl}} \rangle$, and average waiting-time between glitches, $\langle t_{\text{gl}} \rangle = T_{\text{obs}}/(N_{\text{gl}} - 1)$).

For the moment we do not include Crab, whose anomalous behavior may be correlated to its very young age. In order to better identify and understand the behavior of these NS, we subdivide the remaining 24 objects in two groups:

- *frequent glitchers*: we identify with this term the 17 stars with $5 \le N_{\text{gl}} \le 7$. In the following plot, these NS are marked by triangles.

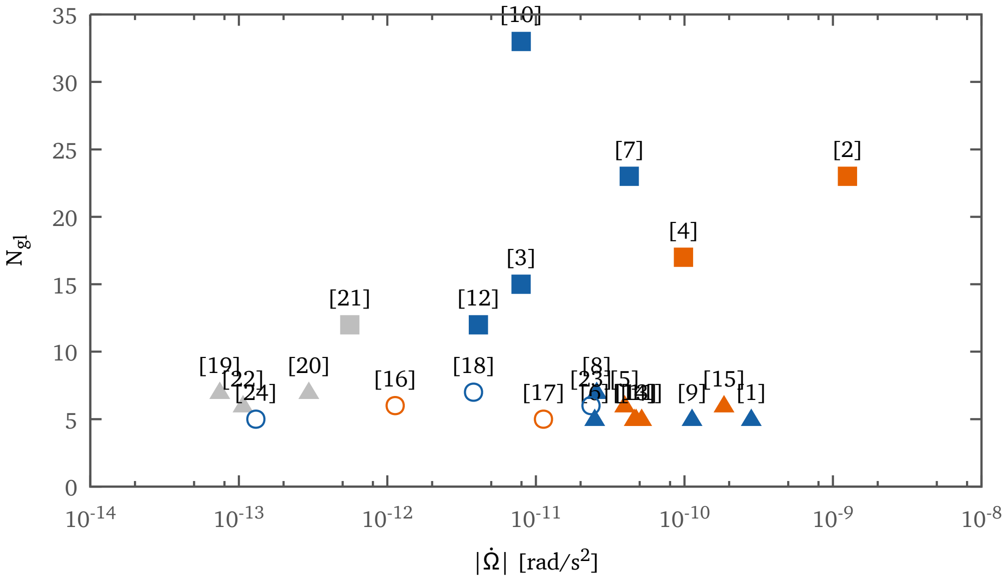

Figure 7.10: For each pulsar of table 7.2 we plot here the number of recorded glitches N_{gl} versus the spin–down $|\dot{\Omega}|$. The convention for colors and symbols (valid also for the following plots) is detailed in the text.

- *very frequent glitches*: the other 7 glitchers with $N_{gl} \geq 12$, identified by squares in plots.

In fig. 7.10 we show N_{gl} plotted versus $|\dot{\Omega}|$, using this convention for the symbols. We further indicate by empty circle the group of *single glitchers*, namely those 5 frequent objects which in the observation time have shown a single glitch orders of magnitude larger than the $N_{gl} - 1$ remaining ones. For later discussion, we also use a color code: gray for the older glitchers (defined here by their slow spin-down $|\dot{\Omega}| < 10^{-12}$ rad/s^2), orange for the large glitchers of Espinoza et al. (2011), and blue for the remaining objects. Consistently, we may call younger glitchers those with large spin-down $|\dot{\Omega}| > 10^{-12}$ rad/s^2. In the following, we will treat the 5 single glitchers as a class by its own; therefore, only the 19 remaining non-single glitchers will be classified as older (4) and younger (15) objects: this last group is the one used in the previous section for the mass fitting.

7.3.1 The *strength* of a glitcher

An important aspect of a NS for this analysis is its *strength*. With this concept we want to characterize the star with the size of its glitches. For this purpose, a choice can be taking into account the size of its largest (maximal) glitch, although limited by the

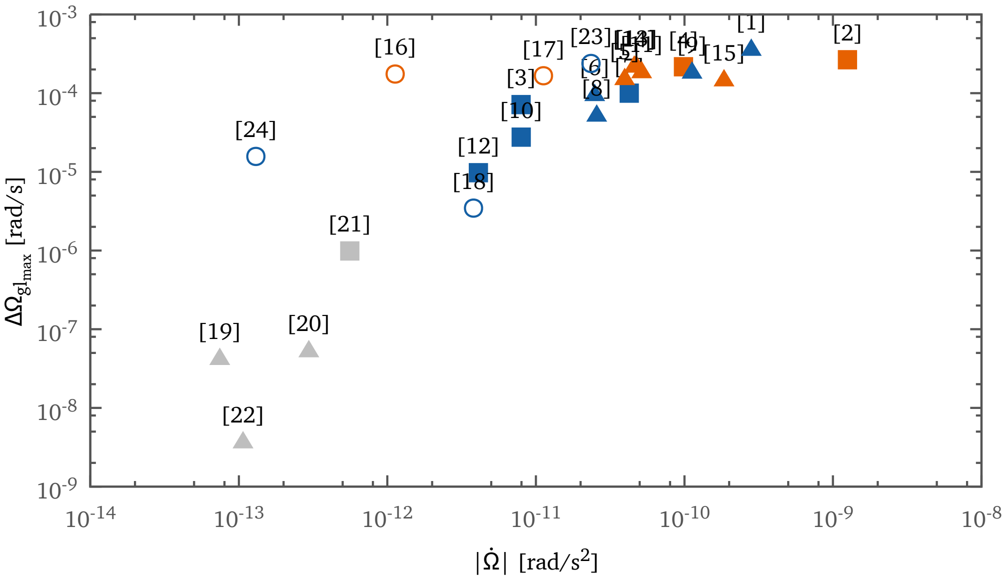

Figure 7.11: Maximal glitch jump $\Delta\Omega_{\mathrm{gl}_{\max}}$ versus the spin–down parameter $|\dot{\Omega}|$ for pulsars in table 7.2.

low event statistics (obviously, less so for the very–frequent glitchers): $\Delta\Omega_{\mathrm{gl}_{\max}}$ is of course an absolute lower limit for each pulsar, which can only be raised by future observations. The plot in fig. 7.11 shows this quantities plotted against the slow-down $|\dot{\Omega}|$ of the star. The plot reveals some interesting facts:

- the sizes of the maximal glitches extend for five orders of magnitude, with $\Delta\Omega_{\mathrm{gl}_{\max}}$ in the range $(3 \times 10^{-9} \div 3 \times 10^{-4})$ rad/s. All the older glitchers have small strengths, with $\Delta\Omega_{\mathrm{gl}_{\max}} \leq 10^{-6}$ rad/s, while the younger objects have significantly larger strengths, with $\Delta\Omega_{\mathrm{gl}_{\max}} \geq 10^{-5}$ rad/s. The single glitchers, whose only large glitch is also the maximal one, all have $\Delta\Omega_{\mathrm{gl}_{\max}} > 10^{-6}$ rad/s;

- the 9 large glitchers of Espinoza et al. (2011) (2 of which are single glitchers), all with $\Delta\Omega_{\mathrm{gl}_{\max}} > 10^{-4}$ rad/s, do not seem to stand out as a special class: there are several other pulsars with similar or larger strengths (5 objects, 3 of which are single glitchers);

- if we exclude the (weak) older glitchers and we only consider the (stronger) younger and single glitchers, we see that their strengths span the range 3×10^{-6} rad/s$\div 3 \times 10^{-4}$ rad/s with continuity, without indication of subdivision in distinct classes;

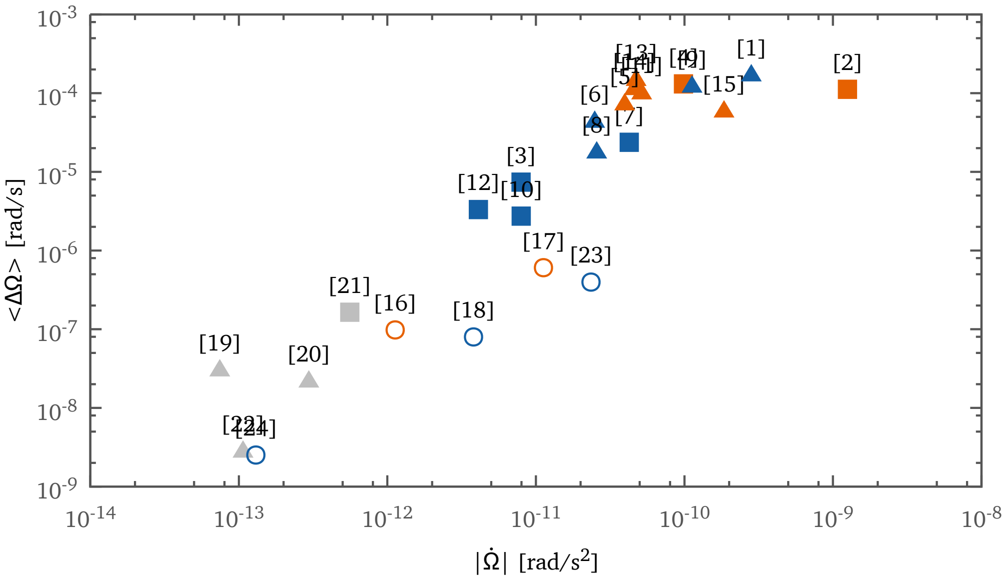

Figure 7.12: Average glitch jump $\langle \Delta\Omega_{\rm gl} \rangle$ versus the spin–down parameter $|\dot{\Omega}|$ for pulsars in table 7.2.

- there is no evident correlation between $\Delta\Omega_{{\rm gl}_{\rm max}}$ and $|\dot{\Omega}|$. There are pulsars with very different spin-downs showing similar glitch strength, while pulsars with comparable spin-downs can glitch differently (see in particular the two very-frequent glitchers at $|\dot{\Omega}| = 8 \times 10^{-12}\,{\rm rad/s^2}$).

The choice of taking $\Delta\Omega_{{\rm gl}_{\rm max}}$ to characterize the *strength* of a glitcher is not obviously the single one. We can consider for this purpose also the average jump size of the neutron star, $\langle \Delta\Omega_{\rm gl} \rangle$, calculated with the $N_{\rm gl}$ recorder events. Of course this quantity is affected by an error (e.g., the standard deviation $\sigma_{\Delta\Omega_{\rm gl}}$, that quantifies the dispersion of the glitch values around their mean) that can be also quite large: this fact indicates that $\langle \Delta\Omega_{\rm gl} \rangle$ is probably a poorer indicator of a glitcher strength than its maximal value, which is an absolute lower limit. Anyway the fig. 7.12 shows the relation between $\langle \Delta\Omega_{\rm gl} \rangle$ and $|\dot{\Omega}|$ revealing other interesting properties (here, for the single glitchers, the average is calculated omitting the single large glitch, and thus it refers only to the $N_{\rm gl} - 1$ remaining tiny glitches):

- the single glitchers have very small average strengths, comparable to those of the older glitchers, namely $\langle \Delta\Omega_{\rm gl} \rangle < 5 \times 10^{-7}\,{\rm rad/s}$. Conversely, the younger glitchers have much larger average strengths, with $\langle \Delta\Omega_{\rm gl} \rangle$ in the range $(2 \times 10^{-6} \div 2 \times 10^{-4})\,{\rm rad/s}$

- in the single glitchers, the size of the maximal glitch is more than two orders of magnitude larger than the average size of the remaining tiny events.

These considerations leads to a remarkable interpretation of the single–glitchers class: the single large event and the remaining small ones appear as a manifestation of two quite different phenomena, quantitatively if not qualitatively. Since three of the five single glitchers are also large glitchers (here defined only by $\Delta\Omega_{\mathrm{gl}_{\max}} > 10^{-4}\,\mathrm{rad/s}$, with no conditions on the spin-down jump), we naturally interpret the single events as superfluid glitches, namely large, global avalanches of superfluid vortexes. Then, the tiny events must represent much weaker phenomena, which may be explained with several plausible, not mutually–excluding, sometimes interrelated scenarios: failed or localized vortex avalanches, seismic activity, fluid or magnetic instabilities, etc.

We can now characterize the three classes by their glitch activity: on one side we found the younger glitchers, that are pulsars which frequently display superfluid–glitches, although tiny events can also take place. With opposite behavior there are the older glitchers which have not shown any superfluid–glitch in the observation time, displaying (so far) only tiny events. Single glitchers bridge these two classes, showing a single superfluid–glitch in the observation time. The different glitching behavior must be somehow related to the different spin-down, but not only (e.g., the two very-frequent glitchers at $|\dot{\Omega}| = 8 \times 10^{-12}\,\mathrm{rad/s^2}$). Since we want to study superfluid–glitches, from now on we concentrate on the 15 younger objects, that are the same object considered in the previous section about the mass–fitting procedure with the snowplow model.

7.3.2 Waiting–times and frequency of events

Another interesting parameter of the glitching activity is the average waiting–time between two consecutive events, $\langle t_{\mathrm{gl}} \rangle$. In fig. 7.13 we show $\langle t_{\mathrm{gl}} \rangle$ vs $|\dot{\Omega}|$ for the 15 younger glitchers; we also indicate lines of constant ω, where, as before, $\omega = |\dot{\Omega}|\,\langle t_{\mathrm{gl}} \rangle$ is the average raw lag built by the star between glitches (without considering the entrainment). We notice immediately the remarkable correlation $\omega \sim 0.01\,\mathrm{rad/s}$ for the large glitchers of Espinoza et al. (2011), as well as other possible correlations for objects with $\omega \sim 10^{-3}\,\mathrm{rad/s}$ and $\omega \sim 10^{-4}\,\mathrm{rad/s}$. The snowplow paradigm clearly suggests that the average lag between glitches is the correct variable when comparing the timing properties of different glitchers, since it corrects for their differences in spin–down: pulsars with larger spin–down reach the same lag in shorter times. Physically, ω represents the average slow–down of the observable crust before critical conditions are reached and a new glitch is triggered. With these considerations it's possible to compare directly the glitching parameters of different pulsars. Each glitcher is characterized by the size of its glitches, $\Delta\Omega_{\mathrm{gl}_i}$, and by their time of occurrence, T_i (with $i = 1, .., N_{\mathrm{gl}}$); the time intervals between glitches are then obtained as $t_i = T_i - T_{i-1}$ and the corresponding critical lags are defined as $\omega_i = |\dot{\Omega}| t_i$ (with $i = 2, .., N_{\mathrm{gl}}$); thence ω is the average value of the critical lag. In fig. 7.14 we show $\Delta\Omega_{\mathrm{gl}_i}$ vs ω_i for the

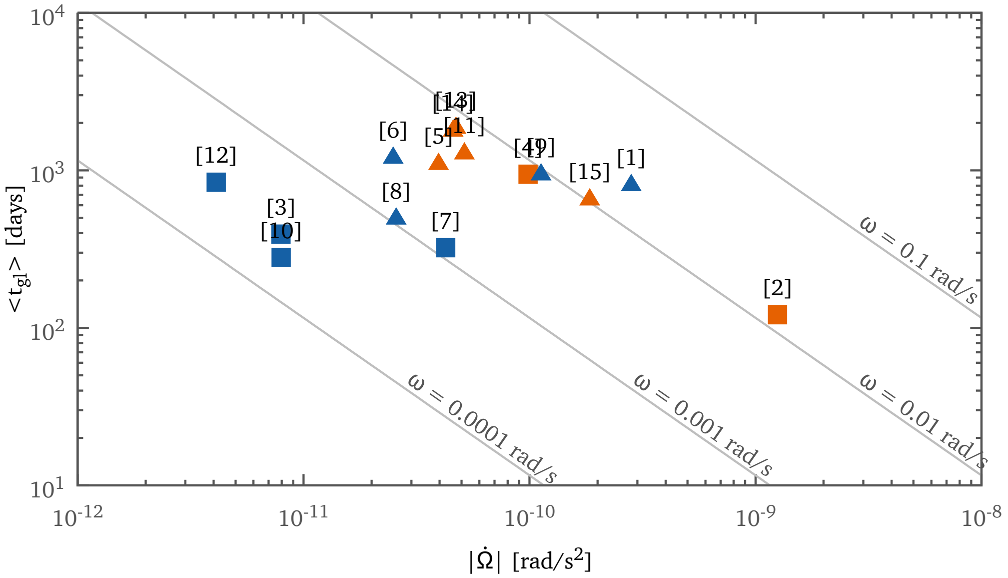

Figure 7.13: Average waiting time $\langle t_{\mathrm{gl}} \rangle$ between two consecutive glitches versus the spin–down parameter $|\dot{\Omega}|$ for pulsars in table 7.2.

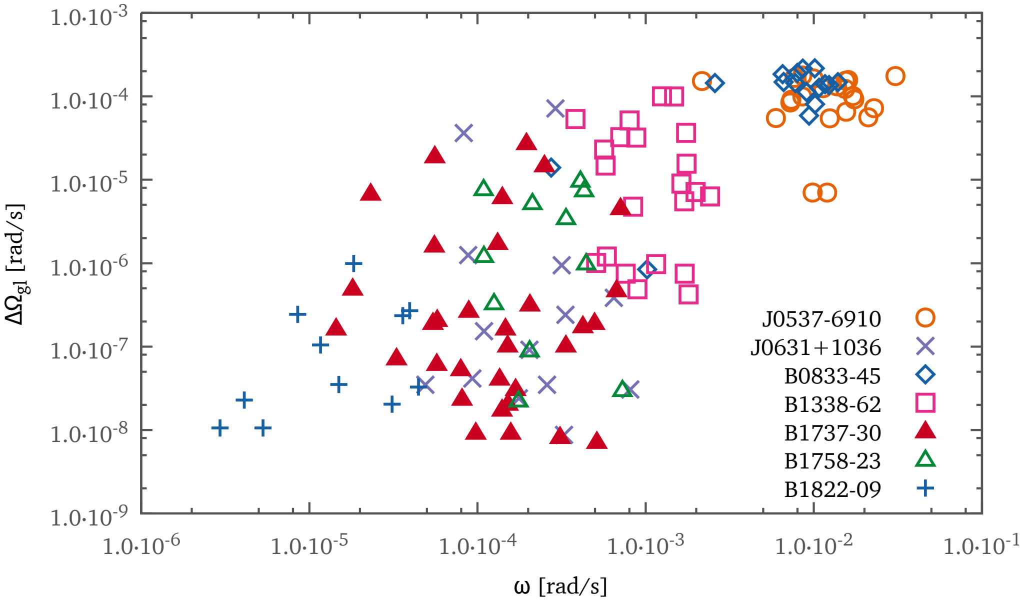

Figure 7.14: For each of the *very frequent glitchers* of table 7.2 we plot all the recorded events with different symbols: the jump size $\Delta\Omega_{\mathrm{gl}_i}$ is plotted against the lag $\omega = |\dot{\Omega}| t_i$

very–frequent glitchers, which are statistically more relevant. We notice the following features:

- B0833–45 (Vela) and J0537–6910, both classified as large glitchers by Espinoza et al. (2011), have a similar activity with large glitches ($\Delta\Omega_{\mathrm{gl}_i} \sim 10^{-4}\,\mathrm{rad/s}$) occurring at large critical lags ($\omega_i \sim 10^{-2}\,\mathrm{rad/s}$). The distribution of glitches is relatively narrow, both in size and critical lag, with only a few events significantly smaller in size than the rest.

- B1338–62 presents maximal glitches only a factor 2-3 smaller than those in the previous pulsars; however its glitching activity occurs at much smaller critical lags ($\omega_i \sim 10^{-3}\,\mathrm{rad/s}$), and the glitch sizes are distributed over more than two orders of magnitudes. Notice that its two maximal glitches, a factor two larger than the two next-to-maximal events, happened only after 18 years of observation: namely large events are not frequent.

- J0631+1036 and B1758–23 are similar, with critical lags of order $10^{-4}\,\mathrm{rad/s}$ and glitch sizes distributed over four orders of magnitude, with large events rare as compared to smaller ones. While J0631+1036 presents maximal glitches only 30% smaller than those in B1338–62, the pulsar B1758–23 has not yet undergone similar large events, possibly due to its spin-down smaller by a factor of two, with a consequent slower evolution, and to the rarity of large events for these glitchers.

- B1737–30 has the same spin-down as J0631+1036, but its maximal glitch is about a factor of two smaller; moreover, its glitching activity occurs over a wider range of critical lags (extending down to $10^{-5}\,\mathrm{rad/s}$), and the glitch distribution is even more dominated by very small events.

- B1822–09 is the only older object among the very-frequent glitchers. Its glitches are always smaller than $10^{-6}\,\mathrm{rad/s}$, comparable to the small events of the previous younger objects.

7.3.3 The role of the critical lag

Altogether, there is indication of a (so far unnoticed) correlation between strength of the glitcher and critical lag at which its glitches are triggered; moreover, the distribution of glitch sizes changes with strength as well: the weaker the glitcher the more scattered its glitch sizes, with small events gradually outnumbering large ones. To make this statement more quantitative, we can characterize the glitchers by the average values of their parameters; in fig. 7.15 we show $\Delta\Omega_{\mathrm{gl}_{\max}}$ and $\langle\Delta\Omega_{\mathrm{gl}}\rangle$ vs ω for each of the 15 younger glitchers, and the numerical values are given in table 7.2. The dispersion (standard deviation) of the glitch sizes around their average values are also indicated,

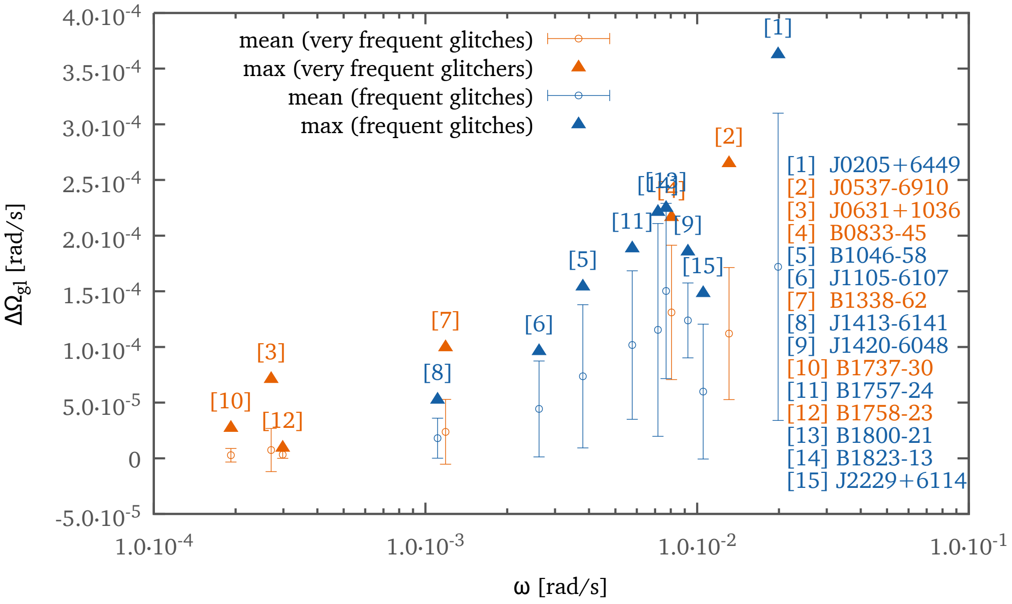

Figure 7.15: Maximum glitch jump $\Delta\Omega_{\rm gl}$ (triangles) and average value (circles, with standard deviation) versus the lag $\omega = \langle|\dot{\Omega}|\tau_i\rangle$ for pulsars in table 7.2.

as error bars; a different color is used to distinguish between frequent and very–frequent glitchers. We observe the following features, which are the main results of the present analysis:

- considering the maximal lag of the very–frequent glitchers, we see a net correlation between $\Delta\Omega_{\rm gl_{max}}$ vs ω, as expected from the previous discussion. Only object [12] is below the value expected from object [3] but, as seen before, this can be explained by the rarity of large events in this group of pulsars and the slow evolution of B1758–23, namely as an observational selection effect.

- considering the maximal lag of the frequent glitchers, we see that the previous correlation is confirmed and extended to a much larger range of values. Only objects [8],[6],[9] and [15] are below the value expected from interpolation of the other objects, but this can be explained by the low statistics of frequent glitchers. The crucial fact is that the maximal glitch is only an observational lower limit that can only be raised in the future, so that values of $\Delta\Omega_{\rm gl_{max}}$ below the interpolating line are acceptable when testing the correlation, while values above the line would spoil it.

- considering the average lag, a correlation between $\langle\Delta\Omega_{\rm gl}\rangle$ vs ω is still present, but less stringent than before, particularly for the stronger glitchers. The fact is that average values are associated to large error bars, while maximal values are

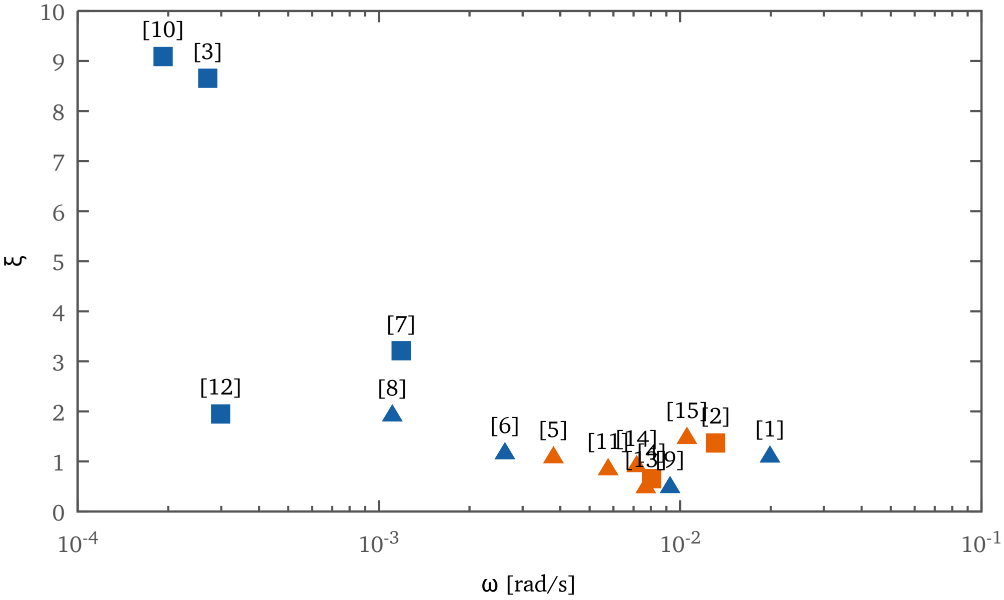

Figure 7.16: Plot of the dispersion parameter ξ versus the average lag ω for pulsars in table 7.2.

absolute lower limits and thence they are better indicators of the strength of a glitcher.

Average values, however, are useful to illustrate the difference in the distribution of glitch sizes discussed previously; in fig. 7.16 we show ξ vs ω, where

$$\xi = (\Delta\Omega_{\mathrm{gl}_{\mathrm{max}}} - \langle\Delta\Omega_{\mathrm{gl}}\rangle) / \langle\Delta\Omega_{\mathrm{gl}}\rangle \,. \tag{7.10}$$

The weak and intermediate strength glitchers have $\xi \gg 1$, while strong glitchers correspond to $\xi \sim 1$, thus quantifying the difference in distribution between small and large events observed in fig. 7.14. The anomaly of objects [12] and [8] reflects the small value of their maximal events, discussed before.

Finally, in fig. 7.17 we show the total observational lag $\omega_{\mathrm{obs}} = |\dot{\Omega}| T_{\mathrm{obs}}$ vs $|\dot{\Omega}|$ for each of the 24 glitchers of table 7.2. In the older objects, ω_{obs} has not yet even reached the minimal critical value associated to the weakest glitchers. During the observation time, they simply had no time to reach the critical conditions for triggering a global superfluid–glitch. The ω_{obs} of single glitchers is smaller than 10^{-2} rad/s, so that they are strong glitchers which did non have enough time to undergo a second large glitch. Therefore, the behavior of older and single glitchers is consistent with that of the younger objects, the difference being related to observational selection effects.

In conclusion, our analysis of observations has revealed an unknown strong correlation between the strength of a glitcher, as measured by its maximal event, and

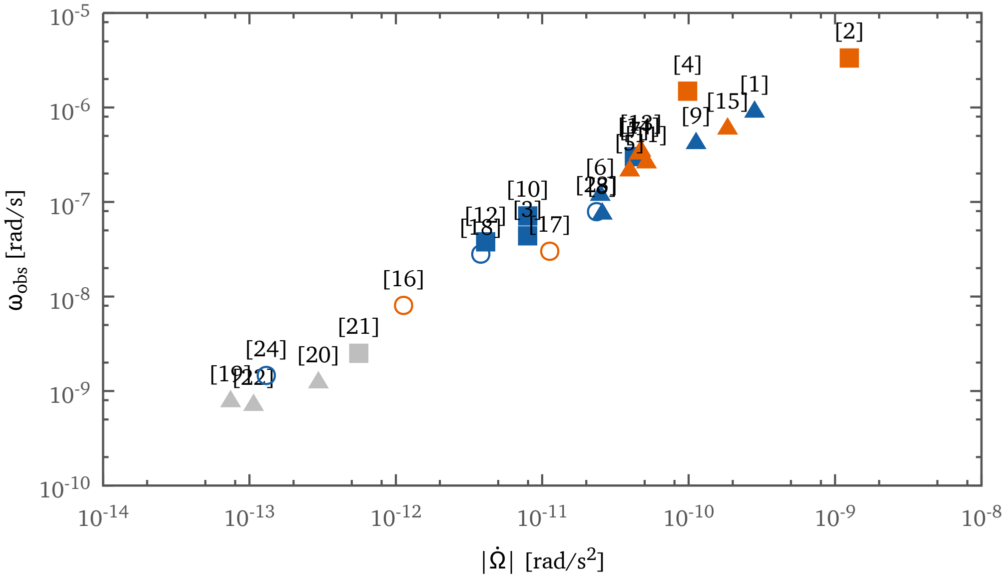

Figure 7.17: Total observational lag $\omega_{\rm obs} = |\dot{\Omega}| T_{\rm obs}$ versus the spin–down parameter $|\dot{\Omega}|$ for pulsars in table 7.2.

the average critical lag at which its glitches are triggered. Actually, the critical lag is a better indicator of the strength than the maximal glitch size, since it seems less affected by statistical effects. We thus see that observationally there is a unified way to describe all the glitchers with $N_{\rm gl} = 5$, in terms of the average lag between glitches. Theoretically, this suggests the presence of a common mechanism: superfluid-glitches are a natural candidate. Moreover, the distribution of strengths could be related to physical differences among the glitchers: mass is the natural candidate, since less massive stars have thicker inner crusts with larger moments of inertia and thus are able to store more angular momentum.

7.4 Observational data and the snowplow model

The considerations above indicate that the average lag ω it's an important parameter that controls the glitching behavior of a neutron star. The natural conclusion of this analysis is then linking this observative quantity to the mass that we have inferred in section 7.2 with the snowplow model and the fitting procedure described. This is shown in fig. 7.18 for SLy and in fig. 7.19 for GM1, where the mass M is plotted against the lag ω. We observe the following general features:

- the very–frequent glitchers show a strong correlation between M and ω; as the average lag spans the range $(10^{-4} \div 10^{-2})$ rad/s, the mass varies between $\sim 1\,{\rm M}_\odot$

and $M_{\max}$. Only objects [10] and [12] are not fitted even by the maximum mass allowed by the EoS (in the plots, they are marked at $M_{\max}$); we already discussed the case of B1758, in terms of observational selection effects (slow evolution and rarity of large events in weaker glitchers). Similar arguments may apply to B1737, which is the weakest in our sample of 15 objects; a future glitch twice the size of the existing maximal event would be consistent with the trend in fig. 7.15, and would be fitted by a mass $M \sim M_{\max}$

- the frequent glitchers confirm the correlation and extends it to intermediate values, showing a theoretical distribution of masses that could be checked against observations. Objects [8],[6],[9] and [15] are above the trend expected from interpolation, corresponding to their behavior in fig. 7.15 and related to the low statistics; conversely, no object is below the expected trend. This is consistent with the fact that the masses determined here are upper limits: any larger event observed in the future for a glitcher can only lower its mass value

- the previous results are quite robust. As seen in figs. 7.18 and 7.19, they do not depend strongly on the choice of the still unknown EoS for dense matter. Moreover, we checked that changing the pinning force profile within its theoretical error bars, or decreasing the strong entrainment of Chamel (2012) by up to a factor two can be absorbed by a small change in the parameter $Y_{\rm gl}$, leaving the mass profile basically unchanged. It is also worth remarking that with no entrainment it is not possible to fit consistently all the glitchers, as covered deeply before

- the choice $M_{\rm Vela} = 1.3\,{\rm M}_\odot$ allows all the glitchers to lie in the mass range $M > 1\,{\rm M}_\odot$. We checked, however, that changing the value for Vela by δM simply shifts all the other masses by about the same amount

In conclusion, assuming the snowplow mechanism we are able to give a unified explanation of the glitch phenomenon, by showing quantitatively that strong glitchers correspond to low-mass neutron stars and weak objects to more massive stars; the behavior of older and single glitchers is also accounted for in the present scenario, in terms of observational selection effects. The correlation between mass and glitching strength found in the snowplow model suggests some further qualitative remarks, that are consistent with the observed phenomenology. Indeed, low-mass neutron stars have much thicker inner crusts than high-mass objects (up to a factor of four between $1\,{\rm M}_\odot$ and $M_{\max}$). Thence one expects that crust fractures (starquakes), generated either by the spin–down of the normal rigid crust or by the strain exerted on the nuclear lattice by the sheet of accumulated vorticity, are induced much more easily in high-mass than in low-mass pulsars. We may thus speculate that such starquakes can also trigger vortex avalanches, by destabilizing the vortex sheet (e.g., unpinning large portions of it); this would naturally explain the fact that glitches in strong (low-mass) objects are triggered at critical lags that are much larger than those observed in weak (high-mass)

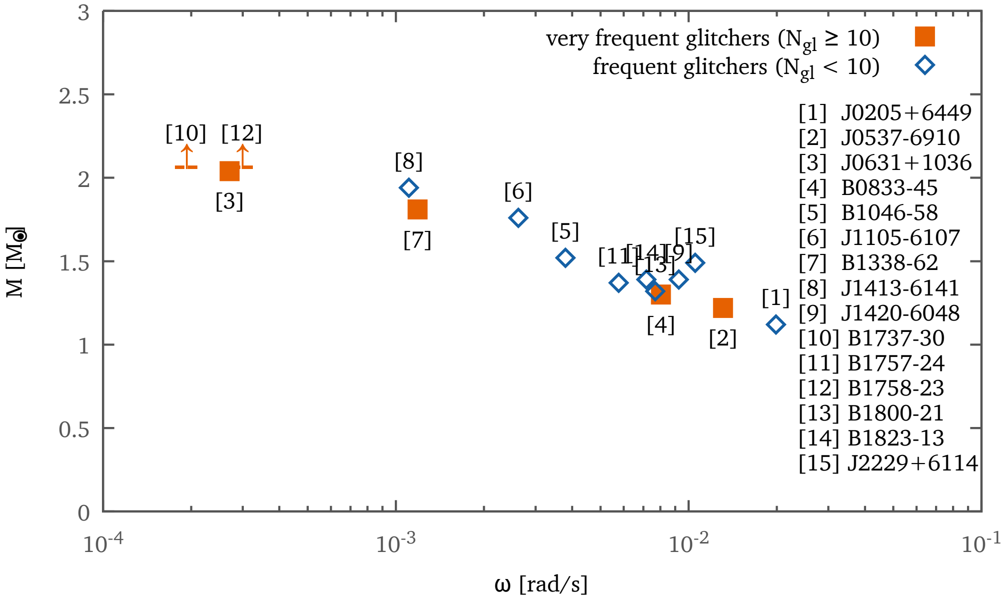

Figure 7.18: We plot here the inferred mass M (with SLy, obtained with the fitting procedure described) of the frequent glitchers versus the average lag ω.

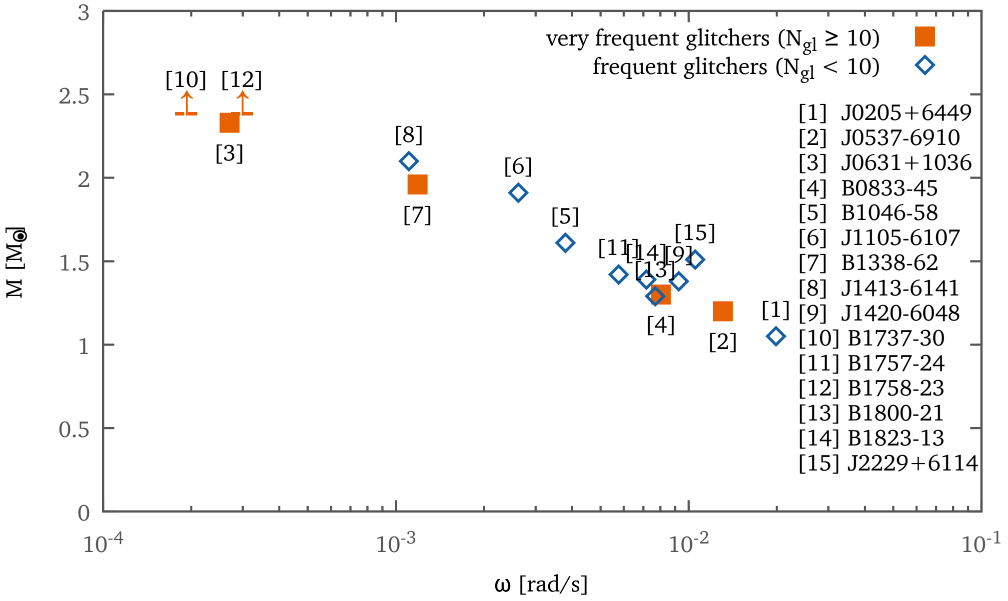

Figure 7.19: We plot here the inferred mass M (with GM1, obtained with the fitting procedure described) of the frequent glitchers versus the average lag ω.

glitchers. Moreover, the difference in critical lags implies that glitches are triggered when the vortex sheet is located in different positions with respect to the core–crust interface, as noticed before. Again we may speculate that avalanches triggered in a strong sheet closer to the equator are more likely to propagate without losing their momentum, thus explaining the fact that in strong glitchers most events are large and comparable; conversely, avalanches triggered in a weak sheet further away from the equator are easily damped, which could account for the rarity of large events observed in weak glitchers.

Table 7.2: Observational values for the pulsars considered in this chapter. We report the rotational parameters Ω and $\dot{\Omega}$ together with the number of glitches $N_{\rm gl}$, the average waiting time $\langle t_{\rm gl} \rangle$ (and its standard deviation), the maximal jump size $\Delta\Omega_{\rm gl_{max}}$ and the corresponding mean value (and associated error). We report also the whole observational time $T_{\rm obs}$ and the age of the pulsar τ (see appendix A). Data are taken from `http://www.atnf.csiro.au/research/pulsar/psrcat/` (Manchester et al., 2005) and `http://www.jb.man.ac.uk/pulsar/glitches.html` (Espinoza et al., 2011)

	Pulsar	$N_{\rm gl}$	Ω [rad/s]	$\dot{\Omega}$ [rad/s^2] 10^{-11}	τ [years] 10^3	$\langle t_{\rm gl} \rangle$ [days]	$\sigma_{t_{\rm gl}}$ [days]	ω [rad/s] 10^{-4}	σ_ω [rad/s] 10^{-4}	$\Delta\Omega_{\rm gl_{max}}$ [rad/s] 10^{-5}	$\langle \Delta\Omega_{\rm gl} \rangle$ [rad/s] 10^{-5}	$\sigma_{\Delta\Omega_{\rm gl}}$ [rad/s] 10^{-5}	$T_{\rm obs}$ [days]
[1]	J0205+6449	5	95.611	−28.193	5	815	723.6	198.58	176.26	36.332	17.199	13.805	3261
[2]	J0537-6910	23	389.722	−125.161	5	121	57.8	131.00	62.48	26.540	11.207	5.932	2665
[3]	J0631+1036	15	21.832	−0.794	44	394	309.4	2.70	2.12	7.161	0.742	1.936	5519
[4]	B0833-45	17	70.338	−9.846	11	946	444.6	80.44	37.82	21.704	13.098	6.032	15 129
[5]	B1046-58	6	50.806	−3.957	20	1110	672.7	37.96	23.00	15.461	7.364	6.435	5551
[6]	J1105-6107	5	99.429	−2.490	63	1218	1129.8	26.20	24.31	9.661	4.436	4.308	4871
[7]	B1338-62	23	32.498	−4.254	12	323	153.8	11.86	5.65	10.004	2.374	2.912	7099
[8]	J1413-6141	7	21.998	−2.568	14	499	361.3	11.08	8.02	5.301	1.806	1.799	2996
[9]	J1420-6048	5	92.156	−11.241	13	953	140.9	92.51	13.69	18.606	12.383	3.363	3810
[10]	B1737-30	33	10.353	−0.795	21	280	264.4	1.92	1.82	2.762	0.274	0.613	8945
[11]	B1757-24	5	50.296	−5.150	15	1296	243.6	57.67	10.84	18.890	10.169	6.669	5185
[12]	B1758-23	12	15.110	−0.410	58	841	516.3	2.98	1.83	0.977	0.331	0.334	9251
[13]	B1800-21	5	47.006	−4.725	16	1883	821.8	76.85	33.55	22.530	15.031	7.874	7530
[14]	B1823-13	5	61.911	−4.590	21	1808	1634.5	71.69	64.83	22.170	11.534	9.558	7230
[15]	J2229+6114	6	121.712	−18.454	10	661	241.7	105.31	38.54	14.873	5.992	6.058	3303
[16]	B0355+54	6	40.178	−0.113	564	1425	1909.4	1.39	1.86	17.542	0.010	7.161	7127
[17]	J0729-1448	5	24.967	−1.124	35	669	946.3	6.50	9.19	16.668	0.061	7.454	2677
[18]	B0740-28	7	37.677	−0.380	157	1233	1075.8	4.05	3.53	0.347	0.008	0.131	7395
[19]	B1642-03	7	16.207	−0.007	3451	1779	538.0	0.11	0.03	0.004	0.003	0.001	10 675
[20]	J1814-1744	7	1.580	−0.030	85	709	321.2	0.18	0.08	0.005	0.002	0.001	4255
[21]	B1822-09	12	8.171	−0.056	232	409	303.1	0.20	0.15	0.099	0.016	0.027	4500
[22]	B1900+06	6	9.329	−0.011	1385	1357	885.1	0.13	0.08	$< 10^{-8}$	$< 10^{-8}$	$< 10^{-9}$	6786
[23]	B1951+32	6	158.942	−2.350	107	672	311.3	13.65	6.32	23.841	0.040	9.733	3361
[24]	B2224+65	5	9.206	−0.013	1120	2799	3487.0	0.32	0.39	1.571	0.000	0.703	11 194

Part III

A dynamical model

CHAPTER 8

The hydrodynamical model

The static “snowplow” model presented in the previous chapters relies on a small set of realistic assumptions and therefore provides a precise insight on the storing mechanism of angular momentum that is responsible of a glitch. This phenomenon is well described not only on the qualitative point of view, but also quantitatively: in fact, using the pinning force calculated in chapter 3, we can make predictions about the typical observables of a glitch, namely the jump size $\Delta\Omega_{\rm gl}$ and the average waiting time $t_{\rm gl}$. We found that the paradigm explains well the giant glitches of a Vela–like low–mass pulsar, and also the small ones of a big NS, if we include the entrainment effects in our description, as done in chapter 7. Conversely, this approach cannot provide any indication about the timescales of the event, such as the rise interval of the jump and the recovery phase. In this chapter we want to overcome this limitation and we present the required formalism to construct a dynamical model of a glitch, that can follow its whole evolution. A such kind of model will be implemented realistically in the following chapter and the predictions obtained will be compared to the observative data currently available. Having a good dynamical simulation of a glitch will be more and more important in the near future because the next generations of radio telescopes are expected to provide a more precise description of the phenomenon that must be compared to the theoretical estimate.

8.1 Introduction

The snowplow model of chapter 5 describes qualitatively how a glitch happens. Essentially, in the time between two events, the superfluid component of the star is decoupled from the charged one (protons and normal matter) and the excess of vorticity (which carries angular momentum) is stored as a sheet in the inner crust, thanks to the typical profile of the critical lag. The reason for this decoupling is addressed to the pinning force that acts in the inner crust of the star. Just before the glitch, the pinning barrier is no longer strong enough to prevent the vortexes from reaching the crust: this collective motion produce the jump in angular velocity. In other words, this phenomenon can be seen as a fast recoupling of the two component of the star that transfers angular momentum from the superfluid part to the normal one. Currently it's unclear which is the right timescale of this recoupling, even if we know that it is almost instantaneous: the observational data provide an upper bound for the rise time of 40 s (for the Vela pulsar, see Dodson et al. (2002, 2007)). The data indicate also a recovery phase after the jump, in which the rotational velocity decrease with a slope greater than the steady–state spindown; at the end of this phase the regular electromagnetic spindown continues but the star has gained a net step in velocity compared to the pre–glitch condition. This behaviour can be easily modeled with the two component approach that is a simple way to describe the recovery after the glitch. In this picture, the two dynamical variables are the angular velocities of the components: Ω_c for the charged one and Ω_s for the superfluid. The differential equations can be written as:

$$I_c\dot{\Omega}_c = -\alpha - \frac{I_c(\Omega_c - \Omega_s)}{\tau_c} \tag{8.1}$$

$$I_s\dot{\Omega}_s = \frac{I_c(\Omega_c - \Omega_s)}{\tau_c}, \tag{8.2}$$

where, of course, I_c and I_s are the respective moment of inertia. The term α encodes the electromagnetic spin–down, while τ_c is the timescale of the recovery recoupling. This approach provides the following solution (more details in appendix B):

$$\Omega_c(t) - \Omega_0(t) = \Delta\Omega_{\rm gl}\left[Qe^{-t/\tau} + 1 - Q\right]. \tag{8.3}$$

in which the glitch happens at $t = 0$ ($\Omega_0(t)$ is the electromagnetic spindown): the instantaneous jump is $\Delta\Omega_{\rm gl}$ and then for $t \to +\infty$ we have that $\Omega_c - \Omega_0 = \Delta\Omega_{\rm gl}(1-Q)$. This means that its possible to fit the recovery behavior by changing these parameters: this framework, in fact, has been the starting point of many seminal works about pulsar glitches.

It's important to note that the quantity $\Delta\Omega_{\rm gl}$ is an input parameter of the model: there is no way, in this picture, to obtain theoretically an order of magnitude for the jump size and the raise timescale. In order to follow the whole evolution we must slightly improve the approach: we cannot consider anymore the superfluid component described only by a single "rigid–body" rotational velocity. In fact the glitch is due to the motion of vortexes inside the star and this mean that we have to follow in some way this phenomenon. We will use the hydrodynamic formalism for NS developed by Prix (2004) and Andersson and Comer (2006): every component of the star is modeled as a fluid and thus we will not follow the dynamics of vortexes, but rather the evolution of the differential rotational velocities $\Omega_X(x)$. Anyway, vortexes keep on playing an important role because they are responsible for the interaction between the components that will be encoded in the pinning and mutual friction terms.

8.2 The multifluids formalism and neutron stars

We briefly review here the application of the multifluid formalism to the neutron stars, as proposed by Prix (2004) and Andersson and Comer (2006). A full derivation of the formalism and of the equations of motion is detailed in appendix C.

The general lagrangian considered here, which describes the Newtonian hydrodynamics, can be written in the following form:

$$\mathcal{L}(n_X, n^i_X) = \sum_X m^X \frac{g_{ij} n^i_X n^j_X}{2n_X} - \mathcal{E}(\rho), \tag{8.4}$$

where g_{ij} is the metric tensor (flat in our case, $g_{ij} = \delta_{ij}$) and the subscript X refer to each component included in the model. This means that n_X indicates the particle density of a component, while n^i_X is defined as a vector component of the flux of particles, i.e.: $n^i_X = n_X v^i_X$. In this picture, $\mathcal{E}(\rho)$ is the internal energy of the system. If we want our description to be invariant under a Galileian boost, the term $\mathcal{E}$ must be in the following form, as shown by Prix (2004):

$$\mathcal{E}(n_X, n^i_X) = \mathcal{E}(n_X, \Delta^i_{XY}) \tag{8.5}$$

where Δ^i_{XY} is the relative velocity between the fluids, i.e. $\Delta^i_{XY} = v^i_X - v^i_Y = \frac{n^i_X}{n_X} - \frac{n^i_Y}{n_Y}$ The requirement of isotropy constrains again the form of $\mathcal{E}$ to be $\mathcal{E} = \mathcal{E}(n_X, \Delta^2_{XY})$ which leads to the following total differential for the internal energy:

$$d\mathcal{E} = \sum_X \mu^X dn_X + \frac{1}{2} \sum_{X,Y} \alpha^{XY} d\Delta^2_{XY}, \tag{8.6}$$

where μ^X is the chemical potential for the X constituent.

The lagrangian in eq. (8.4) permits also to define the momentum variables: if we differentiate $\mathcal{L}$, which is a function of n_X and n^i_X, we find that

$$d\mathcal{L} = \sum_X \left[\frac{\partial \mathcal{L}}{\partial n_X} dn_X + \sum_i \frac{\partial \mathcal{L}}{\partial n^i_X} dn^i_X \right] = \sum_X \left[p^0_X dn_X + \sum_i p^i_X dn^i_X \right]. \tag{8.7}$$

As a consequence, if we consider also the expression for the term $\mathcal{E}$, the momenta are:

$$p^X_i = m^X g_{ij} v^j_X - \sum_Y \frac{2\alpha^{XY}}{n_X} \Delta^j_{XY} \tag{8.8}$$

$$-p^X_0 = \mu^X - m_X \frac{v^2_X}{2} + v^i_X p^X_i \tag{8.9}$$

Of course, for the properties of the internal energy $\mathcal{E}$, the term α^{XY} is a symmetric matrix that is also called the *entrainment* matrix, because it encodes the non dissipative interactions between the fluids. The expression above shows that in general the momenta are not aligned with the respective velocities, and this is the entrainment effect; it can be null only if the matrix α^{XY} is null, or if all constituents move together ($\Delta^i_{XY} = 0$). The eq. (2.17), that is strictly linked to the irrotational property of a superfluid, must be changed therefore to take into account also the entrainment: the velocity–circulation is generally not conserved, contrary to the conservation of momentum–circulation. The correct equation, which always holds, is

$$\oint \mathbf{p} \cdot d\mathbf{l} = \kappa m_n N(x). \tag{8.10}$$

Following the considerations exposed in appendix C it's possible to derive the equation of motion for this system:

$$f_i^X = n_X(\partial_t + v_x^j \nabla_j) p_i^X + n_X \nabla_i (\Phi + \mu^X) - \sum_Y 2\alpha^{XY} \Delta^j_{XY} \nabla_i v_j^X \tag{8.11}$$

where Φ is the gravitational potential and the force f_i^X on the left side encodes all other interactions, including dissipative terms (like the mutual friction between the components) and all external forces.

The picture just presented can be easily adapted to the case of a neutron star, with the following consideration. In a NS core, we can identify four fluids: neutrons, protons, electrons and entropy. In this model p, e, s are considered comovent and are identified by the label c, while n identify the neutrons. To make the model consistent, we must impose charge conservation which implies $\Gamma_e = \Gamma_p$ (where Γ_X is the particle creation rate) and local charge neutrality that can be written as $n_e = n_p$. Another constraint required is baryon conservation $\Gamma_n + \Gamma_p = 0$ and mass conservation:

$$m \equiv m_n = m_p + m_e \tag{8.12}$$

This means that we can write the density of the two fluids as $\rho_n = m n_n$ and $\rho_c = m n_p$. Moreover, the internal energy of the system is

$$\begin{aligned} d\mathcal{E} &= T ds + \mu^n dn_n + \mu^e dn_e + \mu^p dn_p + \alpha^{en} dw^2_{en} + \alpha^{pn} dw^2_{pn} + \alpha^{sn} dw^2_{sn} && (8.13) \\ &= T ds + \mu^n dn_n + \mu^e dn_e + \mu^p dn_p + \alpha dw^2 && (8.14) \end{aligned}$$

where we have used the fact that exists only one independent relative velocity

$$w^i \equiv v_c^i - v_n^i = w^i_{en} = w^i_{pn} = w^i_{sn} \tag{8.15}$$

and therefore we can define the total entrainment consequently $\alpha \equiv \alpha^{en} + \alpha^{pn} + \alpha^{sn}$.

The equations of motion become simpler if we absorb the gravitational term in the extended forces $\tilde{f}_i^X = f_i^X + \rho_X \nabla_i \Phi$ which satisfy the relation $\tilde{f}_i^n + \tilde{f}_i^c = 0$. We can refer to this force as the *mutual friction* ($f^{\mathrm{mut}} \equiv \tilde{f}^n$) because it encodes all the interactions between the two components, except the entrainment that has been treated separately. The eq. (8.11) is therefore rewritten as the system

$$\frac{f^{\text{mut}}{}_i}{\rho_n} = \left(\partial_t + v_n^j \nabla_j\right)\left(v_i^n + \varepsilon_n w_i\right) + \nabla_i \tilde{\mu}_n + \varepsilon_n w_j \nabla_i v_n^j \tag{8.16}$$

$$\frac{-f^{\text{mut}}{}_i}{\rho_p} = \left(\partial_t + v_p^j \nabla_j\right)\left(v_i^p + \varepsilon_p w_i\right) + \nabla_i \tilde{\mu}_p + \varepsilon_p w_j \nabla_i v_p^j \tag{8.17}$$

where we have replaced the constituent index c with p for consistency with other works about this subject; in other words we will consider two fluid, namely the superfluid neutrons n and the "protons" p with which we indicate all other comoving constituents. In the previous system we have also used the following definitions:

$$\varepsilon_X = \frac{2\alpha}{\rho_X} \qquad\qquad \tilde{\mu}_X = \frac{\mu_X}{m} \tag{8.18}$$

From now on, the entrainment will be encoded in the model with the terms ε_X, as done also in chapter 7; moreover, this parameter is linked to the effective mass in the usual way: $\varepsilon_X = 1 - m_X^*/m_X$. The equation below clearly indicate the consistency relation that will be useful in the following:

$$\varepsilon_n \rho_n = \varepsilon_p \rho_p. \tag{8.19}$$

Defining the proton fraction x_p as $x_p = \rho_p/(\rho_p + \rho_n)$, the following equations hold:

$$\varepsilon_p = \frac{\varepsilon_n \rho_n}{\rho_p} = \frac{\varepsilon_n(1 - x_p)}{x_p} \tag{8.20}$$

$$\varepsilon_n + \varepsilon_p = \varepsilon_n \left(1 + \frac{1 - x_p}{x_p}\right) = \frac{\varepsilon_p}{1 - x_p} \tag{8.21}$$

8.3 Mutual friction and equations of motion

The equations presented in the previous section contain a fundamental term for our model, the *mutual friction*. We must now understand how we can encode the dissipative interaction between the two constituents of the star, the neutrons (superfluid) and the protons (all other charged comoving components). To accomplish this task, we can consider that this is not the only force that acts on a superfluid vortex: as presented in section 2.3, the Magnus force pushes the vortexes in the radial (cylindrical) direction. This is an hydrodynamic lift that is adaptive: in other words it arises when a drag effect acts on a vortex, i.e. $\mathbf{f}_M + \mathbf{f}_d = 0$ (this condition is valid in our assumption of a massless vortex). In this work we will consider drag forces $\mathbf{f}_d$ of the form $\mathbf{f}_d = \gamma(\mathbf{v}_L - \mathbf{v}_p)$, where $\mathbf{v}_L$ is the velocity of the vortex line. Starting from this point we can follow some consideration about the dynamics of vortexes to derive in another, but simpler, way the equations of motion presented previously, equations that will be used in the following (see also Antonelli (2014)). The final result will not contains any reference to the vortexes, but it will use the angular velocities of the constituent Ω_n and Ω_p as dynamic variables: this last variable is the principal observable parameter of a glitch and therefore it will be easy for us to compare the results with real data.

As explained in the previous section, the entrainment effect reflects in the fact that the momentum vector and the respective velocity are not aligned, i.e. $\mathbf{v}_n \neq \mathbf{p}_n/m_n$. For future convenience we can define the new variable $\mathbf{v}_\nu$ as $\mathbf{v}_\nu \equiv \mathbf{p}_n/m_n$; this means that the relation between all these quantities is (see also section 2.4)

$$\mathbf{p}_n = m_n\mathbf{v}_\nu = m_n(\mathbf{v}_n + \varepsilon_n(\mathbf{v}_p - \mathbf{v}_n)) \qquad\qquad \mathbf{v}_n = \frac{\mathbf{p}_n/m_n - \varepsilon_n\mathbf{v}_p}{1-\varepsilon_n} \tag{8.22}$$

Moreover, it's easy to verify that the circulation relation in eq. (8.10) can be written in local form as:

$$\frac{1}{x}\frac{\partial}{\partial x}\left(x^2\Omega_\nu\right) = \kappa n(x) \tag{8.23}$$

where of course Ω_ν is defined as $\Omega_\nu = v_\nu^\theta/x$.

The condition explained before that involves the Magnus force and the drag one, can be expanded with these relations in the following way:

$$\begin{aligned}
&\mathbf{f}_M + \mathbf{f}_d = 0\\
&\kappa\rho_n\mathbf{e}_z \times (\mathbf{v}_L - \mathbf{v}_n) = \eta(\mathbf{v}_L - \mathbf{v}_p)\\
&\kappa\rho_n\mathbf{e}_z \times \left(v_L^\theta\mathbf{e}_\theta + v_L^x\mathbf{e}_x - \frac{p_n/m_n - \varepsilon_n v_p}{1-\varepsilon_n}\mathbf{e}_\theta\right) = \gamma\left(v_L^\theta\mathbf{e}_\theta + v_L^x\mathbf{e}_x - v_p\mathbf{e}_\theta\right)
\end{aligned} \tag{8.24}$$

where we have used the fact that the azimuthal symmetry for the superfluid makes $\mathbf{v}_n$ and $\mathbf{v}_p$ to be directed as $\mathbf{e}_\theta$; as done also in the static models of the part II, here we work in cylindrical coordinate system, where x indicates the cylindrical radius. We can separate the vector components of the forces and we have:

$$\begin{cases}
-\rho_n v_L^\theta + \dfrac{\rho_n}{1-\varepsilon_n}p_n/m_n - \dfrac{\rho_n\varepsilon_n}{1-\varepsilon_n}v_p = \dfrac{\gamma}{\kappa}v_L^x & (\mathbf{e}_x)\\
\rho_n v_L^x = \dfrac{\gamma}{\kappa}v_L^\theta - \dfrac{\gamma}{\kappa}v_p & (\mathbf{e}_\theta)
\end{cases} \tag{8.25}$$

The quantities ρ_X and ε_X that appear in these equations depend generally on the spherical radius, or anyway on coordinates x and z. In order to preserve the cylindrical symmetry of the system, we integrate the relations above over the vortex length: this will let us remove the dependency on z, making the final equations tractable with numerical computational methods. Therefore we obtain

$$\begin{cases}
-Av_L^\theta + B\dfrac{p_n}{m_n} - Cv_p = Dv_L^x\\
Av_L^x = Dv_L^\theta - Dv_p
\end{cases}
\implies
\begin{cases}
v_L^\theta = \dfrac{\mathcal{R}^2 - C/A}{\mathcal{R}^2+1}v_p + \dfrac{1}{\mathcal{R}^2+1}\dfrac{B}{A}v_\nu\\
v_L^x = \tilde{\mathcal{B}}(v_\nu - v_p)
\end{cases} \tag{8.26}$$

where the following definitions hold

$$
\begin{aligned}
&A=\int \rho_n dz \qquad B=\int \frac{\rho_n}{1-\varepsilon_n}dz \qquad C=\int \frac{\rho_n\varepsilon_n}{1-\varepsilon_n}dz \\
&D=\int \frac{\gamma}{k}dz \qquad \mathcal{R}=D/A \qquad \widetilde{\mathcal{B}}=\frac{\mathcal{R}}{\mathcal{R}^2+1}\frac{B}{A}
\end{aligned}
\tag{8.27}
$$

The results just found indicate how a vortex moves under the action of the Magnus and drag forces, because give the velocity $\mathbf{v}_L$ of the vortex line as a function of the drag parameters $\mathcal{R}$ and $\widetilde{\mathcal{B}}$. The condition of a vortex pinned to the crustal lattice can be thought as a vortex subjected to a infinite dynamic drag force that therefore acts as a static friction; in other words when $\gamma \to +\infty$, which implies that $D \to +\infty$, we find that the vortex line is comovent with the proton fluid because $v_L^\theta = v_p$ and has null component in the radial direction, $v_L^x = 0$. This is precisely what we expect in the "perfect" pinning condition.

We can now consider the continuity equation for the number of vortexes $N(x)$ inside a circle of radius x. This equation can be written, in integral form, as:

$$
\frac{d}{dt}N(x) = -\int_\Sigma n\mathbf{v}_L \cdot d\mathbf{S} = -\oint n v_L^x dl \tag{8.28}
$$

where n represent the vortexes surface density. For the circulation property of a superfluid (see eq. (8.10)) the above relation becomes

$$
\frac{d}{dt}N(x) = \frac{d}{dt}\left(\frac{1}{\kappa}\frac{2\pi x p_n}{m_n}\right) = \frac{2\pi}{\kappa}x\dot{\Omega}_v = -n v_L^x 2\pi x \tag{8.29}
$$

Now, using eqs. (8.23) and (8.26) we obtain:

$$
\dot{\Omega}_v = -\frac{1}{x}\frac{\partial}{\partial x}\left(x^2\Omega_v\right)\widetilde{\mathcal{B}}(\Omega_v-\Omega_p) = -\left[2\Omega_v + x\frac{\partial}{\partial x}\Omega_v\right]\widetilde{\mathcal{B}}(\Omega_v-\Omega_p) \tag{8.30}
$$

The second equation of motion, needed to complete the system, can be found by considering the conservation on angular momentum. This let us to directly encode also the electromagnetic spin–down (with the variable $\mathbf{T}_{\text{ext}}$) which is an important aspect of the rotational properties of neutron stars, and which is not explicitly inserted in eq. (8.16):

$$
\frac{d}{dt}\mathbf{L} = -\mathbf{T}_{\text{ext}} \tag{8.31}
$$

Thanks to the consistency relation eq. (8.19) between the entrainment coefficients, and for the definition of $\mathbf{v}_v$, the infinitesimal angular momentum can be expressed in the following way:

$$
\begin{aligned}
d\mathbf{l} &= \mathbf{x}\times(\rho_p\mathbf{v}_p + \rho_n\mathbf{v}_n)dV \\
&= \mathbf{x}\times\left[\rho_p(\mathbf{v}_p+\varepsilon_p(\mathbf{v}_n-\mathbf{v}_p)) + \rho_n(\mathbf{v}_n+\varepsilon_n(\mathbf{v}_p-\mathbf{v}_n))\right]dV \\
&= x^2\left\{\left[\rho_p(\Omega_p+\varepsilon_p(\Omega_n-\Omega_p))\right] + \rho_n\Omega_v\right\}dV\mathbf{e}_z
\end{aligned}
\tag{8.32}
$$

Putting all the pieces together, we can write now the final system in local form:

$$\begin{cases} (\rho_p - \varepsilon_p \rho_p)\dot{\Omega}_p + \varepsilon_n \rho_n \dot{\Omega}_n & = -t_{\text{ext}}(r) - \Psi(r) \\ (\rho_n - \varepsilon_n \rho_n)\dot{\Omega}_n + \varepsilon_p \rho_p \dot{\Omega}_p & = \Psi(r) \end{cases} \tag{8.33}$$

where $\Psi(r)$ is the mutual friction term and therefore it's defined with the eq. (8.30) as $\Psi(r) = \rho_n \dot{\Omega}_v$. The factor $t_{\text{ext}}(r)$ encodes the spin–down torque due to the electromagnetic emission of the star. We want to adapt here the dipole model of appendix B and therefore we impose that $t_{\text{ext}}(r) = \beta \rho_p(r) \Omega_p^3$. The first equation of the system, taken in absence of entrainment and mutual friction, can be integrated with the factor $\int x^2 \, dV$ to obtain:

$$I_p \dot{\Omega}_p = -\beta I_p \Omega_p^3 \tag{8.34}$$

Comparing this equations with the one obtained with the standard magnetic dipole one can find that

$$t_{\text{ext}}(r) = \beta \rho_p(r) \Omega_p^3 = \frac{1}{I_p} \frac{R^6 B_{\text{mag}}^2}{6c^3} \rho_p(r) \Omega_p^3. \tag{8.35}$$

Considering the local relation $\varepsilon_n \rho_n = \varepsilon_p \rho_p$, we can solve the initial system for $\dot{\Omega}_p$ and $\dot{\Omega}_n$:

$$\begin{cases} \dot{\Omega}_p & = -\dfrac{\Psi(r) + (1-\varepsilon_n) t_{\text{ext}}(r)}{(1-\varepsilon_n - \varepsilon_p)\rho_p} \\ \dot{\Omega}_n & = +\dfrac{\Psi(r) + \varepsilon_p t_{\text{ext}}(r)}{(1-\varepsilon_n - \varepsilon_p)\rho_n} \end{cases} \tag{8.36}$$

In our simulations we will not consider the differential rotation of the proton fluid; instead we will consider the "protons" (i.e. all the charged components) as a rigid body. This assumption is justified by the short timescale (less than few seconds) on which the ions in the crust are anchored by the superconductive protons in the core: as we want to follow the dynamics of the neutron star with time steps grater than this coupling, our model remains consistent and can produce realistic results. We therefore integrate the first equation of the system, multiplying both terms by the factor $\rho_p x^2 \, dV$:

$$\dot{\Omega}_p = -\frac{1}{I_p} \int \frac{\Psi(x,z)}{1-\varepsilon_n - \varepsilon_p} x^2 \, dV + \mathcal{A} \Omega_p^3 \tag{8.37}$$

where

$$\mathcal{A} = -\frac{R^6 B_{\text{mag}}^2}{6c^3 I_p^2} \int \frac{1-\varepsilon_n}{1-\varepsilon_n - \varepsilon_p} \rho_p x^2 \, dV \tag{8.38}$$

The dynamical equation for the neutron superfluid must be kept in local form, in order to follow the movement of the vorticity and therefore the exchange of angular momentum between the two fluids. As done before, in order to guarantee that the angular velocity Ω_n depends only on the cylindrical radius x and not on the coordinate z, we perform a weighted average over the vortex length for the entrainment coefficients:

$$\overline{\varepsilon_X}(x) = \frac{\int \varepsilon_X \rho_X \, dz}{\int \rho_X \, dz} \tag{8.39}$$

In order to simplify the notation, we define also the following quantities:

$$\mathcal{H}(x) = \frac{1}{1 - \overline{\varepsilon_n} - \overline{\varepsilon_p}} \tag{8.40}$$

$$\mathcal{F}(x) = \frac{\overline{\varepsilon_n}}{1 - \overline{\varepsilon_n} - \overline{\varepsilon_p}} \tag{8.41}$$

$$\mathcal{B}(x) = \widetilde{\mathcal{B}}(1 - \overline{\varepsilon_n}) \tag{8.42}$$

$$\mathcal{Q}(x) = \frac{1}{x}\frac{\partial}{\partial x}\left[x^2\left(\Omega_n + \overline{\varepsilon_n}\left(\Omega_p - \Omega_n\right)\right)\right]\mathcal{B}(x)\left(\Omega_p - \Omega_n\right)\mathcal{H}(x) \tag{8.43}$$

We can now write the final system of equations that we will use in the following simulations:

$$\begin{cases} \dot{\Omega}_p & = -\dfrac{2\pi}{I_p}\displaystyle\int_0^R \mathcal{Q}(x)x^3\left(\int_{-\ell(x)}^{+\ell(x)} \rho_n \, dz\right) dx + \mathcal{A}\Omega_p^3 \\ \dot{\Omega}_n(x) & = \mathcal{Q}(x) + \beta\mathcal{F}(x)\Omega_p^3 \end{cases} \tag{8.44}$$

In case of null entrainment, $\varepsilon_n = \varepsilon_p = 0$ and $\widetilde{\mathcal{B}} = \mathcal{B} = \mathcal{R}/(1+\mathcal{R}^2)$ because $B = A$ in eq. (8.27). Moreover $\mathcal{F} = 0$ and $\mathcal{H} = 1$: the dynamics simplifies in $\dot{\Omega}_n(x) = \mathcal{Q}(x)$ and $\dot{\Omega}_p = -\left(\int \mathcal{Q}(x)x^2 dV\right)/I_p - \beta\Omega_p^3$.

8.4 Physical inputs of the model

As our goal is to apply the model just described to simulate a glitch in realistic conditions, we must implement the equations using reasonable physical inputs and define the validity range of all the parameters. The starting point is of course a neutron star density profile obtained by integrating the TOV equations (see eq. (2.11)) with an equation of state. As done in the previous chapters we will use GM1 and SLy as EoS: by changing the boundary condition of the integration, this approach let us to construct a star with specified mass M (and consequently a defined radius R) of which we know the density profile $\rho(r)$, as detailed in section 2.2.2. In a fully consistent model, the proton fraction $x_p(r) = \rho_p(r)/\rho(r)$ and the entrainment coefficients could be obtained directly from the equation of state, because this quantity is a microphysical property of matter. unfortunately, this information is not provided with many of the EoS that can be found in literature (and with the EoS used in this work), so we will consider the simplified case in which the proton fraction is constant and therefore doesn't depend on the radius r. We introduce the variable Q defined as $Q = I_n/I_{\rm tot}$: this approach leads to $x_p = 1-Q$ and therefore $\rho_n(r) = Q\rho(r)$ and $\rho_p = (1-Q)\rho(r)$. As discussed in section 5.2, the results of Zuo et al. (2004) about the proton fraction indicate that Q lies in the range $(0.85 \div 0.95)$.

Also the entrainment coefficients are not provided with the EoSs; however, they have been calculated recently using different models for the core and the crust of a NS. In particular, Chamel (2012) applied the band theory approach to estimate the values of the neutron effective mass m_n^* for the typical density range of the inner crust. In the following we will use these values, as we have done in chapter 7 (see fig. 7.1 for a plot of the effective mass versus the barion density, which can be expressed as a function of the radius r with eq. (7.1)). It's important to note that the entrainment is a substantial effect, as indicated by the ratio $m_n^*/m_n \approx 10$, and not only a small correction: as suggested by the static snowplow model, the vorticity is stored and released in the crust and therefore this is the part of the star that plays the most important role. In other words the presence of the entrainment must be carefully considered because it can affect significantly the dynamics of the system. Regarding the core, Chamel (2006) suggests that the proton effective mass is slightly lower than the bare mass in the core while we have seen that it's larger in the crust. This means that the entrainment parameters will vanish close to the base of the crust and therefore we will consider the $m_n^* = m_n$ in the core. The effective mass is related to the ε_n coefficient by the equation $\varepsilon_n = 1 - m_n^*/m_n$; moreover $\varepsilon_p = \varepsilon_n \rho_n/\rho_p$, as discussed previously.

8.4.1 Pinning interaction and critical lag

As pointed out in part II, one of the fundamental ingredients of the snowplow model is the existence of the pinning interaction between the crustal lattice and the neutron vortexes. The model has been developed starting from the ideas of the seminal works by Alpar et al. (1981) and Anderson et al. (1982), where the authors suggested that this kind of interaction can be responsible of a storing mechanism for the superfluid angular momentum; the glitch is therefore a sudden exchange of this angular momentum from the superfluid component to the normal one.

In chapter 3 we have presented a mesoscopic approach that has allowed us to move from the pinning force per single interaction to the pinning force per unit length: as we are considering glitch models, the interaction per unit length plays a crucial role because it links the microphysics of the vortex–nucleus system to the macroscopic point of view required to understand global dynamics. Moreover, our results indicate that the correct order of magnitude for this last quantity should be 10^{15} dyn/cm, two order of magnitude lower that the forces previously considered. Then, in chapter 5, we have calculated the critical unpinning lag profile $\Delta\Omega_{\rm cr}(x)$, obtained by equating the pinning interaction and the Magnus force (after integration on the vortex length): the fig. 5.5 shows some examples of $\Delta\Omega_{\rm cr}(x)$ for different configurations. The shape of this profile, which presents an evident peak located in the crustal region of the star, suggests the storing mechanism for the angular momentum: vortexes are depleted in the central region of the star (where $\Delta\Omega_{\text{cr}}$ is low) and packed in a thin sheet just before the peak; when the actual lag overcomes the critical value $\Delta\Omega_{\text{cr}_{\max}}$ also the last barrier is depinned and the recoupling is sudden.

Given its importance, we need to include the pinning also in our hydrodynamical simulations. As pointed out previously, we can think of pinning as a static friction, whereas drag is a dynamical one. If we consider the parameter γ in eq. (8.27) and take $\gamma \to +\infty$, we obtain $\mathcal{B} = 0$. This means that the pinning condition can be easily modeled by taking $\mathcal{Q}(x) = 0$ in the stellar regions where vortexes are anchored to the lattice. Of course we discriminate between the two opposite configurations with the critical lag profile: this means that generally when the actual lag $\Delta\Omega(x)$ is less than $\Delta\Omega_{\text{cr}}(x)$ we are in the *pinned* condition, while the *unpinned* condition is given by the relation $\Delta\Omega(x) \geq \Delta\Omega_{\text{cr}}(x)$. A different prescription will be used when a glitch starts, as we will discuss later. The term $\mathcal{Q}(x)$ in the differential equations must be corrected in the following way:

$$\mathcal{Q}(x) = \begin{cases} 0 & \textit{pinned} \\ \dfrac{1}{x}\dfrac{\partial}{\partial x}\left[x^2\left(\Omega_n + \overline{\varepsilon_n}\left(\Omega_p - \Omega_n\right)\right)\right]\mathcal{B}(x)\left(\Omega_p - \Omega_n\right)\mathcal{H}(x) & \textit{unpinned} \end{cases} \tag{8.45}$$

The critical lag $\Delta\Omega_{\text{cr}}(x)$ is calculated using the same equations of chapter 5 and with the same hypothesis: we consider that the vortexes are straight and thread the whole star, and, for the results of chapter 4, we neglect any kind of pinning interaction in the core. The pinning profile used is the $L = 5000, \beta = 3$ case of fig. 3.11.

Generally we will start our simulations with corotating components, which means that $\Omega_n(x) = \Omega_p$ for every cylindrical radius x. This condition resembles the ideal situation of the star after a glitch that has completely recoupled the two fluids; moreover in this way we can follow the entire build up of the lag and evaluate the interglitch time. In the initial condition, of course, vortexes are *pinned* everywhere; while $\Delta\Omega(x)$ increase (this is due to the fact that $\mathcal{Q}(x) = 0$ and Ω_p is subjected to the electromagnetic torque) the inner region of the star switch to the *unpinned* condition because the lag excesses the critical values and therefore the components recouple thanks to the term $\mathcal{Q}(x) \neq 0$. These considerations can be useful to understand qualitatively the role of the entrainment. If $\varepsilon_p = \varepsilon_n = 0$, it follows that $\mathcal{F}(x) = 0$ and $\mathcal{H}(x) = 1$ everywhere and therefore the *pinned* case is equivalent to $\dot{\Omega}_n = 0$. In other words the external torque affects only the proton fluid. This is not true when the entrainment is not null: in this situation, even if $\mathcal{Q}(x) = 0$ (*pinned* condition), Ω_n decreases because the external spindown acts partially also on the neutron fluid. This is the same effect discussed in section 7.1 and the obvious consequence is that the time needed to build up a certain lag is greater than the null entrainment case.

Initially we will not consider any kind of *repinning* and therefore an *unpinned* region remains so until the end of the glitch/simulation. We will discuss later for alternative approaches about this aspect.

8.4.2 Drag coefficients

As showed by eq. (8.44), all the physical information about the nature of the mutual friction is encoded in the parameter $\mathcal{B}$ that must be discussed carefully. The expressions in eq. (8.27) indicate that this quantity is a function of the dimensionless term $\mathcal{R}$, which, in turn, is related to the usual drag parameter γ used in other works about this subject:

$$\mathcal{B} = \frac{\mathcal{R}}{1+\mathcal{R}^2}, \qquad \mathcal{R} = \frac{\gamma}{k\rho_n}. \tag{8.46}$$

It's clear from this expression that in principle, the parameter $\mathcal{B}$, that is relevant for us, depends on the position inside the star. As discussed previously, we remove the dependency on the coordinate z by performing an average over that direction (following the vortex–line), but anyway we must handle the dependency on the cylindrical radius because the mutual friction is due to different physical phenomena for each region of the star. Therefore we need to identify a realistic validity range for the value of $\mathcal{B}$ in the core and in the inner crust of the star, and also to understand what happens during a glitch. As we will cover deeply in the next chapter, the interplay of these different parameter plays a fundamental role in the dynamics of a glitch, determining the rise time of the event and also the recovery phase: in fact, comparing the system in eq. (8.44) with the dynamical equations of the simple global two component description in eq. (8.1), it's easy to understand that in our model the timescale τ of the evolution is linked to $\mathcal{B}$ as:

$$\tau \approx \frac{1-\varepsilon_n}{2\Omega_n \mathcal{B}} \tag{8.47}$$

NS Core

In the core of a neutron star, the interaction between the two fluids is due to the scattering of electrons (which are part of the proton fluid) off the neutron superfluid vortexes. From the results of Andersson et al. (2006), this effect couples the components with a very short timescale (≈ 10 rotational periods, that for the Vela pulsar means less that a second). The authors suggest the following expression for the drag coefficient $\mathcal{B}_c$ (the subscript c indicate that this equation is valid in the core region):

$$\mathcal{B}_c = 4\times 10^{-4}\left(\frac{m_p^*}{m_p}-1\right)^2\left(\frac{m_p}{m_p^*}\right)^{1/2}\left(\frac{x_p}{0.05}\right)^{7/6}{\rho_{14}}^{1/6} \tag{8.48}$$

where ρ_{14} is the total density expressed in units of $10^{14}\,\mathrm{g\,cm^{-3}}$, x_p is the proton fraction (that we consider as a constant) and m_p^* is the proton effective mass that is estimated to be in the range $m_p^*/m_p \approx 0.5 \div 0.7$. The above expression is valid in the case of a superconductor of type I, but anyway, as pointed out by Sidery and Alpar (2009), the possibility that a fraction of the core is in type II superconducting state must also be discussed, as this aspect is still unclear. In this case the coupling timescale between the two components could be even smaller for the vortex–fluxtube dissipative interaction, even if the presence of a pinning effect can significantly change this picture because it decouples the two fluid. The results of chapter 4 suggest that the pinning force per unit length is small if compared to the crustal pinning and therefore we can neglect this aspect. In this work we will not consider the possibility of a type II superconducting state, even if this is an interesting issue, and, following the same prescription used by Haskell et al. (2012c), we will adopt the eq. (8.48) to estimate a realistic range for the drag parameter $\mathcal{B}_c$. Equation (8.48) depends weakly on the density, which furthermore doesn't change rapidly in the core of a neutron star: we can therefore remove this dependency and consider $\mathcal{B}_c \approx 1 \times 10^{-4}$ as a constant for the whole region. Our simulations will use values for this parameter in the range $10^{-5} \div 5 \times 10^{-4}$.

Inner crust

In the inner crust, two different physical processes can be responsible of a mutual friction between the components, each one with a particular coupling timescale. As pointed out by Jones (1992), the vortexes can interact with the sound waves in the lattice: this effect dominates the dissipation when the relative velocity between the vortex line and the lattice is small ($v_L \leq 10^2\,\mathrm{cm\,s^{-1}}$). The calculation of the drag coefficient for this process is highly uncertain because it involves a mesoscopic averaging procedure over the vortex length (similar to the approach used in chapters 3 and 4): this lead to a reduction factor of the order of $\approx 10^{-4}$. Haskell et al. (2012c) used, for the glitch simulations, a constant parameter $\mathcal{B}_p \approx 10^{-10}$ to indicate the coupling due to the lattice phonon oscillations in the inner crust of the star. When the relative velocity between a vortex and a lattice is high, another kind of dissipation could arise. In this case, for the excitation of Kelvin waves in the vortex, it interacts with the lattice with much shorter timescale respect to the typical one involved in the phononic mutual friction. The results of Epstein and Baym (1992) suggest a value of $\mathcal{B}_k \approx 10^{-3}$ for the strong drag parameter related to the Kelvin excitations.

To model the dependency of the effective drag on the relative velocity, we construct a profile $\mathcal{B}_{\mathrm{crust}}$ that is a function of the local actual lag ω. We want also to explore the effect of a strong *viscous* drag which entangle and block the vortex (it's therefore a pinning–like effect) when the relative velocity with respect to the normal component falls below a threshold. In other words we consider a very high value of the drag parameter in order to encode this effect. Thanks to the relation between $\mathcal{B}$ and $\mathcal{R}$, i.e. $\mathcal{B} = \mathcal{R}/(1+\mathcal{R}^2)$ we can operate in the regime $\mathcal{R} > 1$ and consider a parameter γ_v such that the corresponding $\mathcal{B}$ value equals $\mathcal{B}_p$. The net effect on the dynamical model is therefore the same of a phononic drag, but this approach makes easy to construct a transition function between γ_v and γ_k (which correspond to $\mathcal{B}_k$) as a function of the local lag $\omega(x)$. In this work we consider

$$\mathcal{R}_{\mathrm{crust}}(x) = \frac{\gamma_v}{\kappa\,\langle \rho_n(x) \rangle} \exp\left\{ \frac{\ln(\gamma_k/\gamma_v)}{1 + \exp[-q(\omega(x) - \eta\,|\Delta\Omega_{\mathrm{cr}}(x)|)]} \right\} \tag{8.49}$$

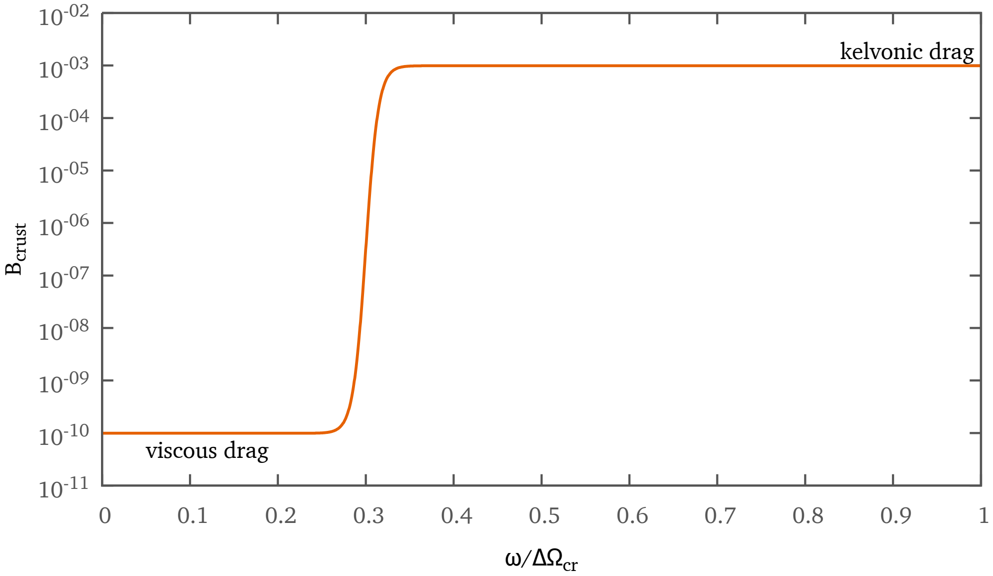

Figure 8.1: In this figure we plot the dependency of the crustal drag parameter $\mathcal{B}_{\rm crust}$ over the lag ω between the two components of the star. For this plot we used eq. (8.49) with $\gamma_k = 10^{14}\,\mathrm{g\,cm^{-1}\,s^{-1}}$, $\gamma_\nu = 10^{21}\,\mathrm{g\,cm^{-1}\,s^{-1}}$ and $\langle\rho\rangle = 5\times10^{13}\,\mathrm{g\,cm^{-3}}$. The parameter η is fixed here to be $\eta = 0.3$.

where

$$q = \frac{1}{S}\ln\left[\ln(\gamma_\nu/\gamma_k) - 1\right] \tag{8.50}$$

and $\langle\rho_n\rangle$ is the average of the neutron fluid density over the vortex length. This expression let us to introduce a smooth transition between the two values of the γ parameter which are different for several order of magnitude. The width of the transition region is S and we fix this value to be 10^{-4} rad/s, while the transition value is defined as a fraction η of the local critical lag $\Delta\Omega_{\rm cr}(x)$ and in the following chapter we will test also the effect of the parameter η in glitch simulations. From eq. (8.49) we can easily obtain the resulting $\mathcal{B}_{\rm crust}$: the fig. 8.1 shows an example of the dependency of $\mathcal{B}_{\rm crust}$ over the lag ω between the two components of the neutron star.

The considerations detailed here define the values of the drag parameter for each region of the star. As our model works in cylindrical symmetry, and thanks to the fact that only in the equatorial region the vortexes are full immersed in the crust, we can consider $\mathcal{B}(x) = \mathcal{B}_{\rm crust}(x)$ for $x > R_{\rm core}$. In the region $x < R_{\rm core}$, the vortexes thread the core but are also partially immersed in the crust of the star at their extremities; therefore we need to perform an average procedure. Following the expressions in eq. (8.27), we average $\mathcal{R}_{\rm crust}$ and the corresponding value $\mathcal{R}_c$ for the core over the vortex length; then we can calculate with eq. (8.46) the final effective drag $\mathcal{B}(x)$ that we use in the simulation (see eq. (8.44)).

8.4.3 Triggering a glitch and post–glitch phase

The snowplow model of chapter 5 naturally identifies a trigger mechanism for the glitch: when the actual lag reaches the maximum value of the critical lag profile $\Delta\Omega_{\mathrm{crmax}}$, all pinning barriers are broken and the vortexes can reach the crust to which they transfer their angular momentum. This approach leads of course to a precisely defined interglitch time, that is the interval required to build up a lag of $\Delta\Omega_{\mathrm{crmax}}$. In chapter 7 this limitation has been overcome with the adoption of a variable trigger, in other words a glitch can happen after a certain time t^* (or equivalently after a actual lag ω^*) from the previous event. Even if there are many models, the physical nature of this trigger is still unclear, and it's beyond the scope of this work to investigate about these aspects. Anyway, triggering a glitch at different lags let us to study the evolution and the resulting observables when the angular momentum available for the glitch changes: for this hydrodynamic model therefore we will adopt the same prescription, also to compare the results with the ones of chapter 7. Of course, the quantity $\varphi = \omega^*/\Delta\Omega_{\mathrm{crmax}}$ that parameterize the trigger can vary in the range $0\div1$, because $\Delta\Omega_{\mathrm{crmax}}$ represent the maximum lag that can be built up by the star.

When the lag reaches the value $\varphi\Delta\Omega_{\mathrm{crmax}}$, a glitch is triggered by considering *unpinned* all the vortexes in the crust (the part of the crust where the critical lag is below the threshold and the whole core are likely to be already depinned) and we change the drag profile in order to let the two components begin to recouple fast. This effect is achieved only acting on the value $\mathcal{R}_{\mathrm{crust}}(x)$ of eq. (8.49): we only lower the threshold which determines the shifting between the kelvonic drag and the viscous one, in other words the parameter η is replaced with a new smaller value η_g. The change $\eta \to \eta_g$ implies that the crust now evolves under the effect of a kelvonic drag $\mathcal{B}_{\mathrm{crust}} \approx B_k \approx 10^{-3}$ which is associated to a timescale small enough to produce the rise of the glitch. As explained in the previous section, the recoupling reduces the lag $\omega(x)$: when its value reaches the threshold $\eta_g\Delta\Omega_{\mathrm{cr}}(x)$, $\mathcal{B}_{\mathrm{crust}} \approx B_p \approx 10^{-10}$ which means that the vortexes are entangled and their motion is now decoupled from the crust, as expected when the vortexes are pinned. In other words our approach permits us to implement in a simple way the repinning phenomenon after the glitch: the timescales now are so long that we can consider the vorticity attached to the lattice and therefore the star is ready to build up the lag required for another glitch.

CHAPTER 9

Results of the dynamical simulations

The model detailed in chapter 8 has been implemented in a full consistent computer code that can solve the system of differential equations under different physical condition. One important aspect of the code is in fact the possibility of changing easily the inputs of the simulations, allowing us to investigate the influence of a single parameter on the resulting glitch. We have therefore explored the dependency of the observable data of this phenomenon with respect to the various drag parameters (in order to better understand the rise time and the recovery phase) and to the proton fraction of the star. Moreover we have tested different pinning/repinning conditions, together with a parameterized trigger mechanism based on the same prescription adopted in chapter 7, in order to reproduce the same results with a dynamical approach.

All the simulations has been built with realistic physical background, starting from the density profile of the star: the first step is always the integration of the TOV equations (see eq. (2.11)) with a valid EoS. As the density in the crust of a neutron star changes very rapidly (see fig. 2.5), we need to construct a fairly dense spatial grid (with steps $dx \approx 10^2$ cm of the cylindrical radius, in order to maintain the computations feasible). Furthermore the typical timestep suggested by the values of the drag parameters is very small if compared to the interval required to build up the lag that stores the angular momentum. Taking the Vela Pulsar as example, this interval is ≈ 2.8 yr: this means that use must follow the evolution for about 3 year with a timestep of the order of ≈ 10 s (estimated with $\mathcal{B}_c = 5 \times 10^{-4}$). All these considerations indicate that we are facing a really challenging task from the computational point of view: we have therefore developed a highly parallelized and optimized code that runs in reasonable time and still allows to easily test different physical inputs.

The diagram in fig. 9.1 illustrate the scheme of execution of a simulation. Before the true evolution code, in the *startup* block all the physical inputs are correctly evaluated: we prepare the star (obtained by TOV integration) and setup the spatial grids with

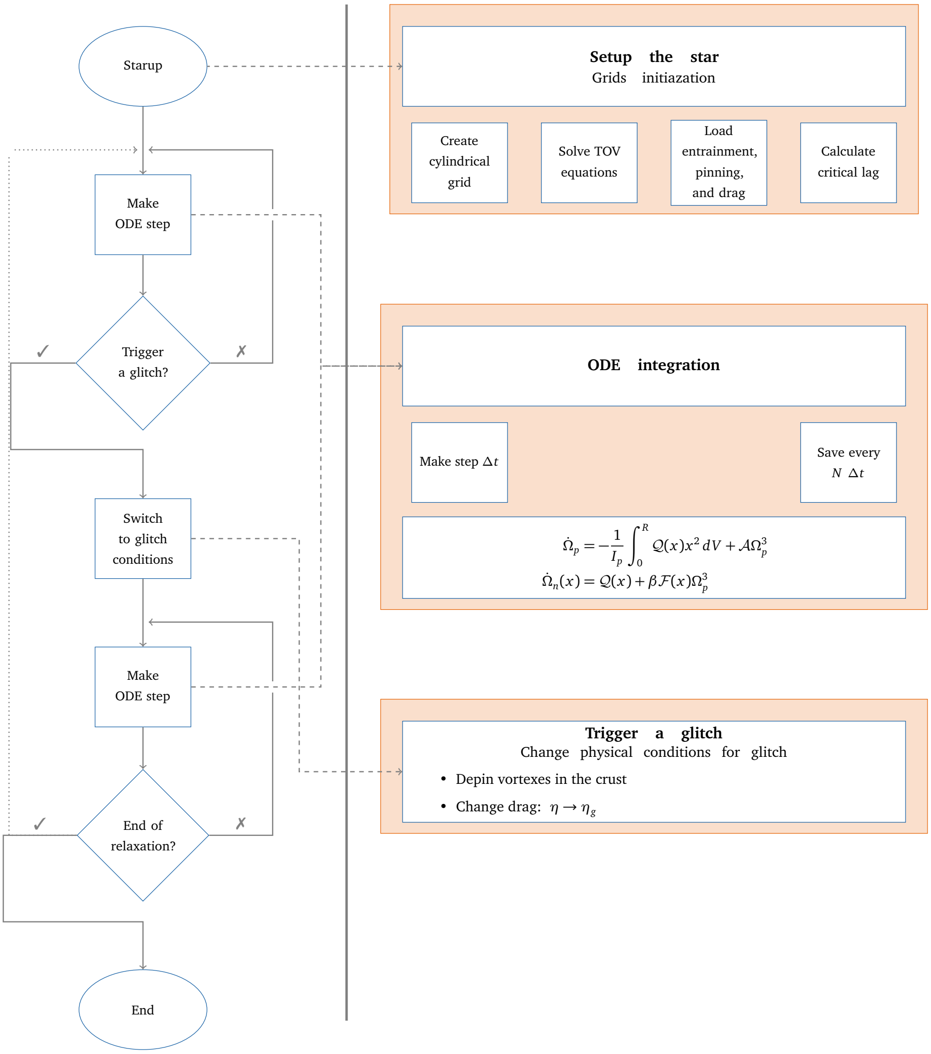

Figure 9.1: This diagram represents the execution flow implemented in the computer code which simulates the glitch following the hydrodynamical model described in the previous chapter.

precalculated static values, like pinning forces, critical unpinning lag, entrainment coefficients and the effective drag profile for the pre–glitch phase. Generally we begin with corotating components, which means that $\Omega_i \equiv \Omega_n(x) = \Omega_p$ for every cylindrical radius x. After these steps we star integrating the differential equations of eq. (8.44): we use the Runge–Kutta 4th order method with a timestep Δt to calculate how our dynamical variables change over time. As described in the previous chapter, we need to consider a set of values for the neutron angular velocity (the star must develop differential rotation in order to produce a glitch), i.e. $\Omega_{n_i} = \Omega_n(x_i)$, where the x_i points are spaced on the grid by an amount $dx \approx 10^2\,\mathrm{cm}$. On the contrary, for the charged fluid, we perform an integration at every timestep, in order to consider the component as rigidly rotating and to obtain an observable quantity. The timestep Δt must be chosen accordingly to the timescale τ given by the drag forces (following the eq. (8.47)) otherwise the numerical computational error is not controlled.

The pre–glitch phase ends when the glitch conditions (i.e the trigger conditions) are met. Then the event is fired by depinning the part of the crust that is still blocked and by switching to the kelvonic drag: this is obtained by simply substituting the parameter η in eq. (8.49) with a lower value η_g, as explained in section 8.4.2.

9.1 Qualitative analysis of a simulation

We propose the results of simple simulation in order to analyze qualitatively how a glitch is reproduced by our model. In this run we neglect for a moment the entrainment (we will discuss later about the consequences of this effect) and we trigger a glitch only when the actual lag ω reaches the peak of the critical lag profile $\Delta\Omega_{\mathrm{crmax}}$. As initial condition, we take the two fluids as comovent at the typical rotational velocity of the Vela pulsar, i.e. $\Omega_i = \Omega_p = \Omega_n(x) = 70\,\mathrm{rad/s}$. Moreover we fix the drag coefficient in the core as $\mathcal{B}_c = 10^{-4}$ and we set $\mathcal{B}_k = 10^{-3}$ (the star used is obtained with GM1 as EoS and it has mass of $1.3\,\mathrm{M}_\odot$). The result of the entire simulation is plotted in fig. 9.2; in this figure we have reported only the temporal evolution of the angular velocity $\Omega_p(t)$ of the charged component. The values are shifted by the quantities t_0 and Ω_0 which represent here the time at the beginning of the glitch and the respective angular velocity. We can see that the event happens after $\approx 3\,\mathrm{yr}$ from the beginning of the simulation.

In the interval before the glitch, the angular velocity decreases regularly for the effect of the electromagnetic torque (the magnetic field value is taken here to be $B_{\mathrm{mag}} = 3 \times 10^{12}\,\mathrm{G}$). Consequently the lag between the two components increases because, on the contrary, the neutron fluid is decoupled from the magnetic field. This is especially true for the inner crust region of the star where the critical lag reaches its maximum. Here the vortexes are pinned and they remain in this condition until the triggering of the glitch, thus when the lag overcome the threshold. The inner part of the star instead is involved in a progressive depinning process: starting from the inside and following the steep profile of the $\Delta\Omega_{\mathrm{cr}}(x)$ function, cylindrical shells of the

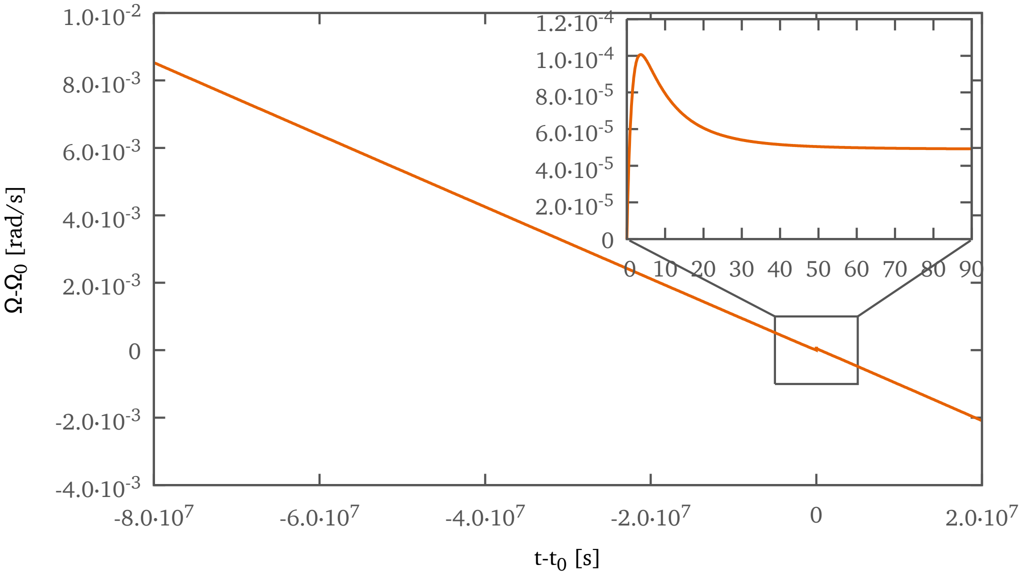

Figure 9.2: This plot shows how the rotational velocity of the crust (proton component) changes with time in the whole simulation. Points are shifted in order to place the beginning of the glitch at the origin. In the inset the first 90 seconds of the glitch are reported in detail.

neutron component fall in the *unpinned* condition and therefore begin to recouple with the charged fluid. The fig. 9.3 shows the typical situation of the star (outer core and crust) at a given time between two glitches. The shaded region indicates the part where the vorticity is still pinned to the lattice, and therefore $\mathcal{Q}(x) = 0$ here (i.e. no drag force acts here).

Where vortexes are not attached to the crust, the drag coefficients drive the evolution with the timescale given by eq. (8.47). From this expression we can easily find the equilibrium lag, that is

$$\Delta\Omega = -\dot{\Omega}\tau = -\frac{\dot{\Omega}(1-\varepsilon_n)}{2\Omega\mathcal{B}} \tag{9.1}$$

This condition is reached rapidly in the core, due to the fact that in this region the drag coefficient that acts between the two fluid is quite strong ($\mathcal{B}_c \approx 10^{-4}$) . On the other hand, in the inner crust a partial fast recoupling (where the lag decreases consistently due to the effect of $\mathcal{B}_k$) is followed by a transition to a phononic drag, for the expression eq. (8.49) used to model the effective mutual friction. This explain the fact that in fig. 9.3 the profile of the actual lag doesn't go to zero in the crust: the timescale associated with $\mathcal{B}_p$ is too long and the glitch happens before that the equilibrium condition can be reached.

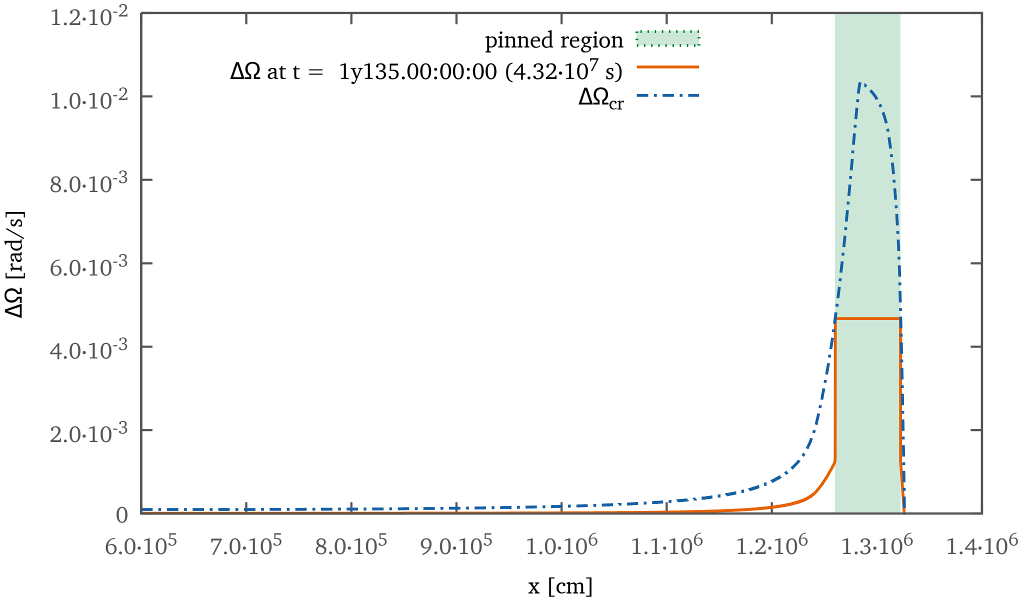

Figure 9.3: This plot shows the typical situation at a given time between two glitches. In particular we report the lag between the two components and the critical lag profile. The shaded region represents the part of the star in which vortexes are pinned (decoupled), while in the other parts the components are coupled thanks to the effect of the mutual friction.

The plot in fig. 9.4 (left part) shows how the vorticity in different zones of the star are depinned at different time. We plot, together with the value of Ω_p, also the values of Ω_n at some fixed cylindrical radius. Of course the profile of the critical lag makes it responsible of the fact that at smaller radii the depinning occurs earlier than in the external positions. This kind of plot is also useful to visualize the effect of the entrainment during the build up of the lag. The left part of the figure is referred to the simulation described until now, conducted without any form of entrainment. It's easy to see that where the vorticity is still pinned to the lattice, the corresponding value of the neutron angular velocity Ω_n doesn't change. This is not true when the coefficient ε_n and ε_p are not null. The right part of fig. 9.4 refers to a simulation in which all the parameters are the same, except for the entrainment that we take into account. Even in the *pinned* condition (i.e. before the rapid change of slope) $\dot{\Omega}_n \neq 0$ because the electromagnetic spindown partially acts also on the superfluid component (the effect is more consistent in the crust; in the core, on the other hand, we take $\varepsilon = 0$). This clarifies again the fact that the total time required by the star to build up a fixed lag is bigger when the entrainment plays a role.

When the trigger condition is met (generally when the actual lag at the peak reaches a threshold, for this simulation we take the peak $\Delta\Omega_{\mathrm{crmax}}$ itself as threshold), the glitch is fired by depinning all the vorticity in the crust and by switching the drag

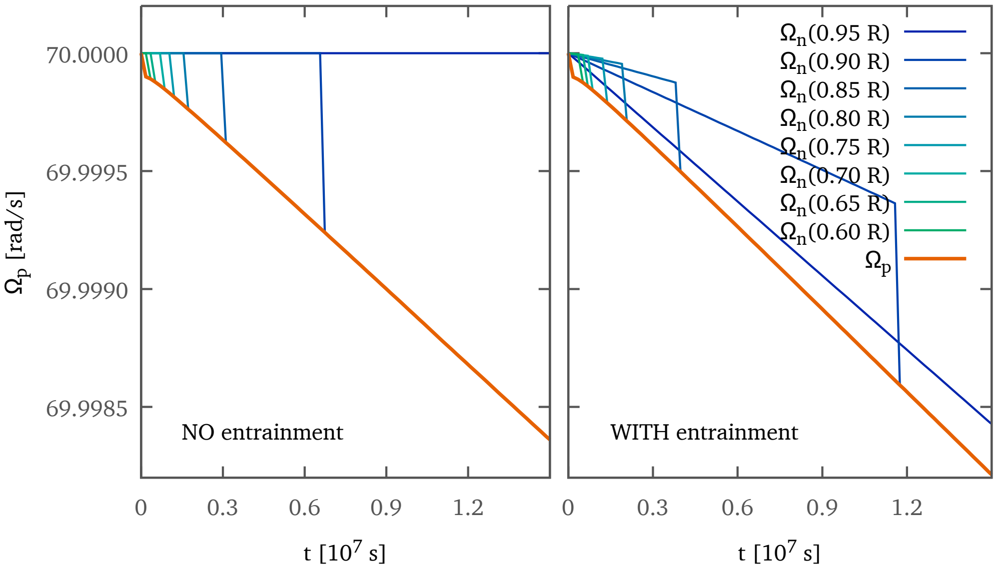

Figure 9.4: In this figure we show the effect of the entrainment in the model. We plot how Ω_p and Ω_n (for different cylindrical radii) evolve with time. In the left part (without entrainment) we can see that the Ω_n remains constant until the depinnig occurs and this quantity changes rapidly. This effect happens earlier in the core than in the crust due to the shape of the critical lag. In the right part the same quantities are plotted when the entrainment is included in the model. The considerations above remain valid, but here it's important to note that also in the pinned case, $\dot{\Omega}_n$ is not null, thanks to the presence of the entrainment.

coefficient here to the value $\mathcal{B}_k$ (i.e. to strong kelvonic mutual friction), thanks to the substitution $\eta \to \eta_g$. This means that a bulk of superfluidity stars recoupling at the same time, and with a very fast timescale. The values of $\mathcal{Q}(x)$ is strongly affected and the integral in eq. (8.44) produces a fast positive variation of Ω_p, because $\dot{\Omega}_n > 0$ (the recoupling is so strong that it overcomes the electromagnetic torque). This is the "rise" phase of the glitch (dominated by the strongest among the drag parameter, i.e. $\mathcal{B}_k$) that corresponds to the first $\approx 5\,$s in the left plot of fig. 9.5. In the same plot we can see that Ω_n decreases in the crust and this reduces the lag, bringing the system towards the condition of equilibrium.

Looking at the profile $\Omega_p(t)$, it's noteworthy that the rise of the glitch is immediately followed by a short term recovery that happens with a timescale of $\approx 50\,$s: after reaching the maximum $\Delta\Omega_{\rm gl} = \Omega_p(t_{\rm max}) - \Omega_p(0)$ (in this simulation $\Delta\Omega_{\rm gl} = 10^{-4}\,$rad/s; here and in the following we consider with $t = 0$ the beginning of the glitch), the derivative $\dot{\Omega}_p$ changes sign and therefore the proton angular velocity is reduced, until the "recovery" effect ends. This behavior is explained if we look at the critical lag in the core region. In fact, due to the rapid spin–up of the whole star and the low values

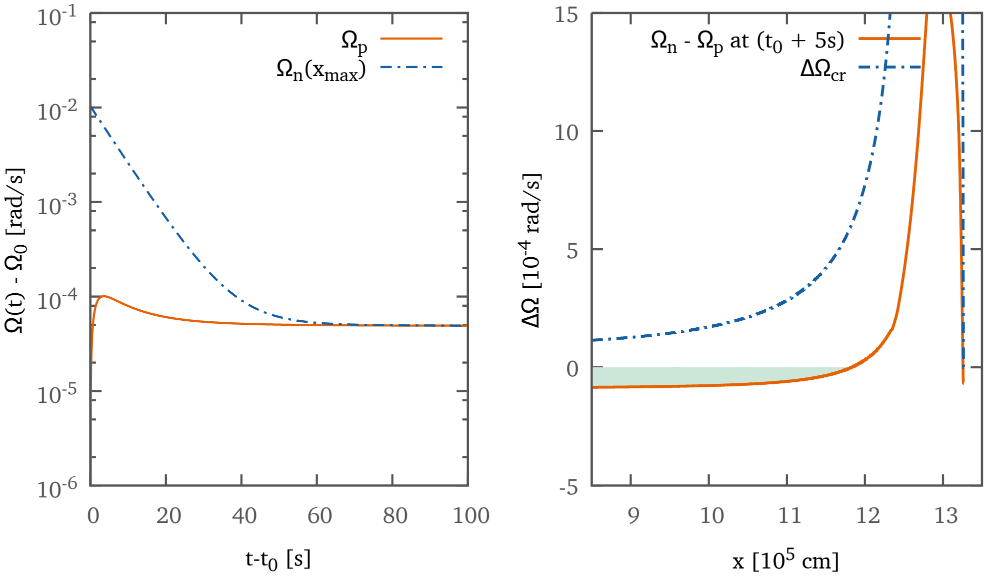

Figure 9.5: The left plot shows the first 100 s after the beginning of a glitch. We can see the initial *rise* phase (due to the effect of $\mathcal{B}_k$; it ends when $\Delta\Omega_p$ reaches its maximum) and the recovery phase in which $\dot{\Omega}_p < 0$ with absolute value granter than the pre–glitch one. In the right figure we plot the critical lag profile and the actual lag at the end of the rise. We can see that in the core the lag has changed its sign: this explains the recovery effect due to the core drag $\mathcal{B}_c$ (see eq. (8.44)).

of $\Delta\Omega_{\rm cr}$ here, the actual lag $\Omega_n - \Omega_p$ changes its sign in eq. (8.44), as we can see in fig. 9.5 (right plot, shaded region), referred to a time $t = 5\,$s after the beginning of the glitch. The flat profile of $\Delta\Omega_{\rm cr}$ for $x < R_{\rm core}$ indicates that the effect is consistent because the whole region is involved at the same time, even if the actual lag is small.

As shown, this phase is dominated by the recoupling of the core (subsequent of the rapid spin–up) and therefore the coupling parameter is $\mathcal{B}_c$ which is associated to a timescale one order of magnitude larger than the one imposed by $\mathcal{B}_k$. The interplay of these two parameters strongly affects the dynamics of the phenomenon: the kelvonic drag takes part firstly and defines mainly the maximum jump $\Delta\Omega_{\rm gl}$ of the glitch (and how long does it take to reach this value), while the mutual friction in the core of the neutron star fixes how fast $\Omega_p(t)$ reaches its final value. This value is also dependent on the value of the parameter η_g which defines when the repinnig condition is reached. The dependency of the resulting $\Omega_p(t)$ on these parameters will be explored quantitatively in the next section.

9.2 Parameter study

In the previous section we have seen, from a qualitative point of view, that the time evolution of a glitch is controlled by some parameters of our model. Here we want to explore deeply this aspect, giving some quantitative results obtained with simulations conducted with different conditions. In order to simplify the following discussion, we define now some relevant quantities. Unless otherwise specified, we consider the glitch occurring at time $t = 0$ (time when the trigger is fired), and the corresponding angular velocity of the charged component is Ω_0. The variable $t_{\rm gl}$ represents the time passed from the beginning of the simulation to the glitch itself (at the initial condition the two fluids are comovent), and corresponds roughly to the interglitch time. Generally we plot the quantity $\Delta\Omega_p(t) = (\Omega_p(t) - \Omega_0)$, which evolves with time and represent the principal observable quantity of the event. The maximum absolute value reached by $\Delta\Omega_p(t)$ is the actual jump size that we identify with the term $\Delta\Omega_{\rm gl}$; moreover this condition is reached after a time $t_{\rm max}$ (the *risetime*) from the beginning.

In all the simulations we take into account also the entrainment effect: this means that the coefficients ε_p and ε_n are not zero (the profile used is the one plotted in fig. 7.1, see eq. (8.39) for the averaging procedure over the vortex length). As discussed previously, with the entrainment the time required to build up a fixed lag is larger by a factor of the order of ε_n, i.e. ≈ 10. We have verified that our model behaves as expected about this aspect: we have done two identical simulations except for the ε_X coefficients. The glitch is always triggered when the actual lag reaches the same fraction $\varphi = 0.3$ of the critical lag: in one case we find $t_{\rm gl} = 2.4 \times 10^7$ s, while we obtain $t_{\rm gl} = 1.9 \times 10^8$ s when the entrainment is switched on (the other parameters used here are: GM1 EoS, $M = 1.3\,{\rm M}_\odot$, $Q = 0.95$, $B_{\rm mag} = 3.1 \times 10^{12}$ G, $\mathcal{B}_c = 10^{-4}$ and $\mathcal{B}_k = 10^{-3}$).

The entrainment affects significantly also the risetime of the glitch. In fact, from the eq. (8.47), we know that the timescale of the evolution is controlled, of course, by the mutual friction (with the $\mathcal{B}$ parameter), but it depends also on the ε_n coefficient, which corrects the final values. This is especially true for the crust region because here $\varepsilon_n \approx -10$ (as discussed previously, we take the entrainment null in the core): in other words, this slows down the effect of $\mathcal{B}_k$ which acts here. In particular the value of $t_{\rm max}$ increases when the entrainment is switched on by a factor $\approx \widetilde{m_n^*}$. Referring to the simulation described in the previous section (where $\varepsilon_X = 0$), we can see that a kelvonic drag $\mathcal{B}_k = 10^{-3}$ produces a risetime $t_{\rm max} \approx \tau = 7$ s; this result is in agreement with the analysis of Dodson et al. (2002, 2007) in which an upper limit for this quantity (al least for the Vela pulsar) is set to 40 s. In order to satisfy this constraint with the entrainment, we have to increase the value of the parameter $\mathcal{B}_k$ of roughly one order of magnitude, because $1 - \varepsilon_n \approx 10$. This is the first parameter that we study here, letting it vary in the range $5 \times 10^{-3} \div 5 \times 10^{-2}$, for the reasons discussed. We have taken a $1.3\,{\rm M}_\odot$ GM1 star, with $Q = 0.95$; the pinning profile is the $L = 5000, \beta = 3$ calculated in chapter 3 and we have used the prescription for the drag coefficient of section 8.4.2 ($\eta = 0.6, \eta_g = 0.2$), keeping $\mathcal{B}_c$ fixed at 10^{-4} for all runs while changing

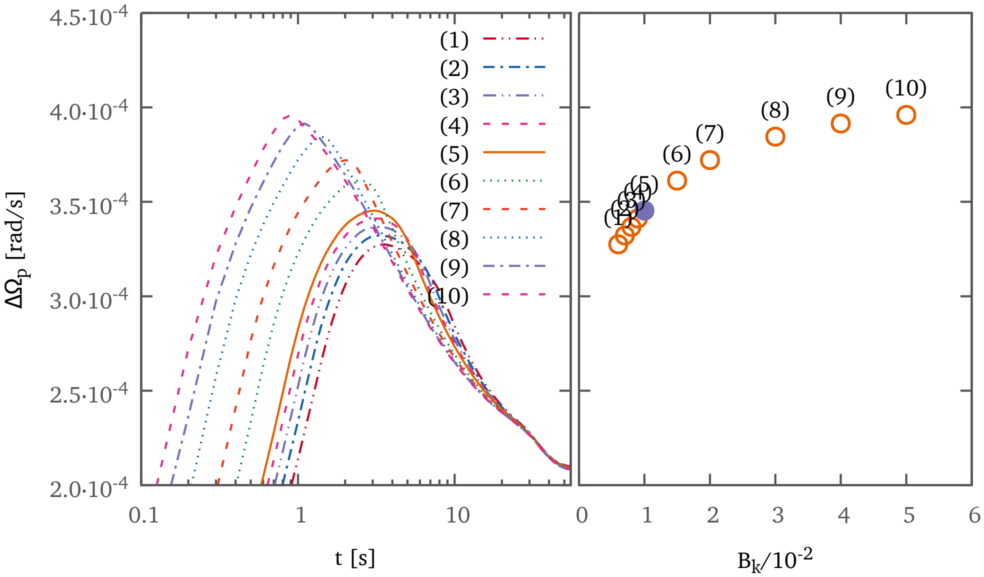

Figure 9.6: In this figure we plot the effect of the kelvonic drag parameter $\mathcal{B}_k$ over $\Delta\Omega_p(t)$. We explore the range $5\times10^{-3}\div5\times10^{-2}$ and in the right part we plot the value of $\mathcal{B}_k$ and the corresponding maximal glitch size $\Delta\Omega_{\rm gl}$. The filled dot indicates the best benchmark for this parameter: this value will be used also in the following simulations.

$\mathcal{B}_k$; the glitch is trigger when the lag $\omega = |\dot\Omega|t$ reaches the typical value for the Vela pulsar, i.e. 8.04×10^{-3} rad/s. The results of these simulations are showed in fig. 9.6. In the left part we plot how the rotational velocity of the crust changes in the first 60 seconds after the glitch, while in the right part the maximum jump size $\Delta\Omega_{\rm gl}$ is plotted against the corresponding $\mathcal{B}_k$ value. As expected, increasing $\mathcal{B}_k$ result in a reduction of the rise time $t_{\rm max}$. This means that the angular momentum stored by the superfluid is released to the crust in a shorter time and therefore the peak reached by the proton rotational velocity, i.e. $\Delta\Omega_{\rm gl}$, is bigger because a smaller fraction of the core superfluid has begun to recouple. In the range of $\mathcal{B}_k$ tested, we obtain the maximum jump of $\approx 4\times10^{-4}$ rad/s when $\mathcal{B}_k = 5\times10^{-2}$, and the corresponding rise time observed is less than 10 seconds, well below the constraint of 40 s. A high value of the kelvonic drag parameter is correlated to a more evident recovery effect: an initially larger glitch rapidly relaxes to a lower spin rate than that of a glitch involving a weaker drag parameter in which the timescales of $\mathcal{B}_k$ and $\mathcal{B}_c$ partially overlap.

In fig. 9.7 we keep $\mathcal{B}_k = 10^{-2}$ fixed and we change the drag parameter $\mathcal{B}_c$ for the core region in the range $10^{-5}\div5\times10^{-4}$ (all other parameter are the same used in fig. 9.6). The dependency of the glitch size to this parameter is inverted with respect to the kelvonic mutual friction: increasing $\mathcal{B}_c$ results in a smaller jump because the angular momentum transfer is suppressed by the strong recovery, as shown by the

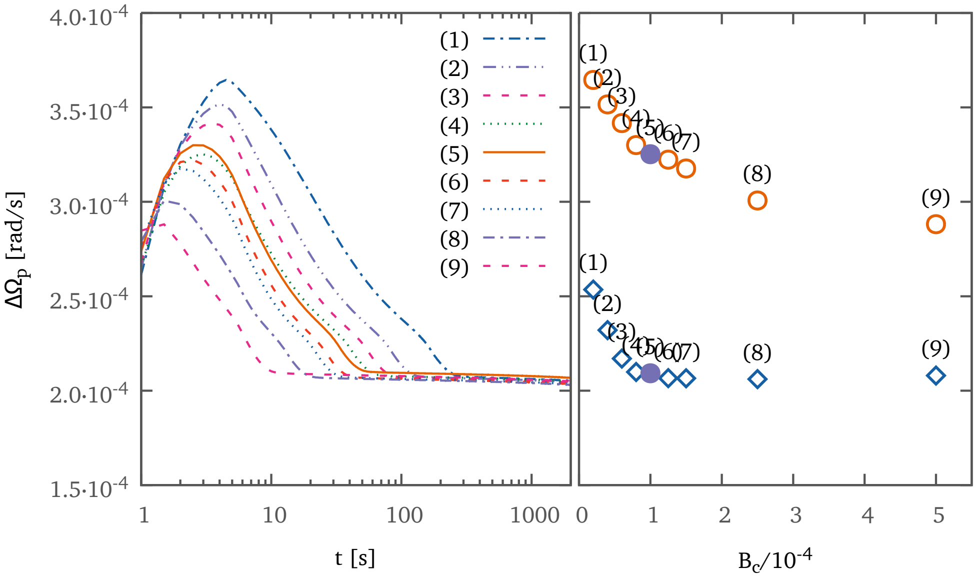

Figure 9.7: In this figure we plot the effect of the core drag parameter $\mathcal{B}_c$ over $\Delta\Omega_p(t)$. We explore the range $1 \times 10^{-5} \div 5 \times 10^{-4}$ and in the right part we plot the value of $\mathcal{B}_c$ and the corresponding maximal glitch size $\Delta\Omega_{gl}$ with circles and $\Delta\Omega_{60}$ with squares. This last quantity corresponds to the jump size extracted after 60 s form the beginning of the glitch and will be used later. The filled dots indicate the best benchmark for this parameter: this value will be used also in the following simulations.

right plot of the figure. Nevertheless we can see that the main effect of $\mathcal{B}_c$ regards the post–jump behavior in particular it determines how fast the rotational velocity of the crust reaches its “final” value, as we can see in the plot (in this context, with the term “final” value we identify the residual jump $\Delta\Omega_p$ measured when the stellar regions are fully relaxed (see eq. (9.1)) or fully repinned).

In the two sets of simulations covered until now, we have only acted on the drag parameters $\mathcal{B}_c$ and $\mathcal{B}_k$. As explained, these values control the timescales of the different phases of a glitch, but it’s clear from the derivation of the chapter 8 that they don’t affect the total angular momentum stored by the superfluid neutron vortexes before the glitch and released after to the charged component. In other words this means that the jump $\Delta\Omega_p$ observed when the crust and the core are fully relaxed (i.e when $\mathcal{B}_c$ and $\mathcal{B}_k$ have done their jobs) is the same for all runs, as we can see in the previously discussed plots. With the global two component model, covered at the beginning of chapter 8 and in appendix B, we can see that this aspect is controlled, as expected, by the parameter Q, that is the ratio between the moment of inertia of the superfluid constituent and the total moment of inertia of the star(see eq. (B.10)). We want now to test if our dynamical model shows the same behavior, i.e. the final jump is bigger

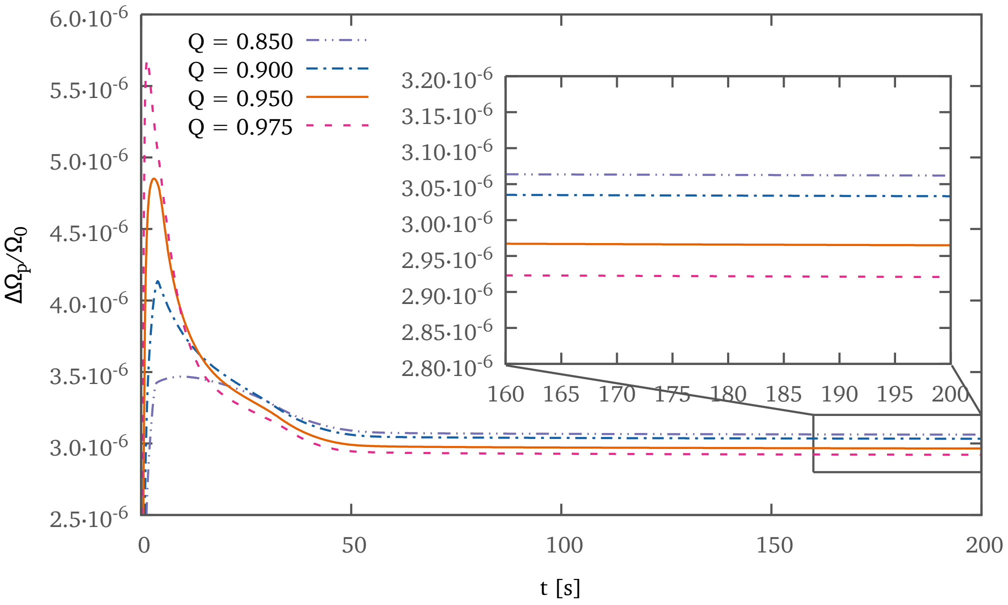

Figure 9.8: This plot shows the dependency of the glitch size on the neutron fraction value Q. This parameter affects the quantity $\Delta\Omega_{\mathrm{gl}}$ but also the residual jump size at the end of the recovery, as we can see in the small figure.

when we increase the proton fraction. The plot in fig. 9.8 reports the dependency of the residual jump with respect to the ratio $Q = I_n/I_{\mathrm{tot}}$ (see appendix B for details about the relation between the healing parameter of the global two component model and the proton fraction of the star).

In the runs reported in this section we have kept fixed $\eta_g = 0.2$. Of course this parameter affects the recovery phase of the glitch: when the lag falls below the threshold defined by η_g the vortexes behave like they are repinned to the lattice and the motion of the two components is therefore completely decoupled. This means that $\Delta\Omega_p$ doesn't change anymore (the effect given by the secular slowdown is too small to be visible on the timescales considered here), as we can see in fig. 9.9. In this plot we change the value of η_g while the other parameters are fixed at their best benchmarks used also previously ($\mathcal{B}_k = 10^{-2}$, $\mathcal{B}_c = 10^{-4}$, $Q = 0.95$, with GM1 as equation of state and $M = 1.3\,\mathrm{M}_\odot$). As expected, the flat curve condition is reached before when η_g is increased. For $\eta_g = 0.2$ we can see that the vortexes are repinned after $\approx 60\,\mathrm{s}$.

In the following we will use this value, $\eta_g = 0.2$, for the simulations. This choice is reasonable if we take into account the observative data of the Vela glitches. Dodson et al. (2002, 2007) provide a fit of the residuals for two giant glitches of this pulsar, namely the event in 2000 and the one in 2004, giving also an estimate for a very short (of the order of a minute) timescale term of the evolution (no timing analysis hasn't been yet published for the following glitches of Vela). We plot these two fits in fig. 9.10,

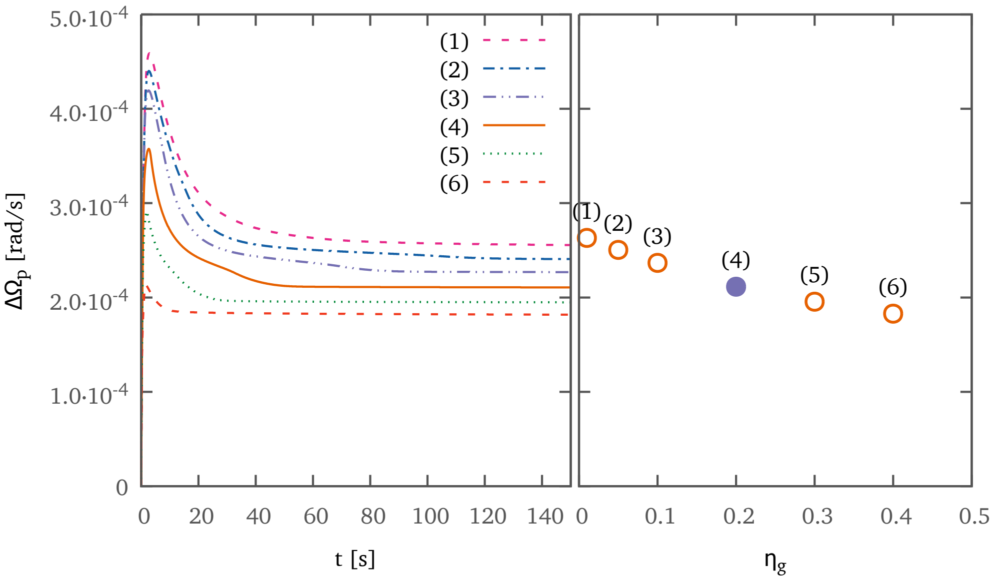

Figure 9.9: In this figure we change the value of the parameter η_g (see section 8.4.2 for details) and we plot the curves $\Delta\Omega_p(t)$ for the first 150 s form the beginning of the glitch. In the right part we plot the value of η_g and the corresponding value of $\Delta\Omega_{60}$ (glitch size after 60 s). The dot highlighted corresponds to the value of η_g that we take as benchmark for the next simulations.

together with the output of our simulation with $\eta_g = 0.2$ (as done before, $\mathcal{B}_k = 10^{-2}$, $\mathcal{B}_c = 10^{-4}$, $Q = 0.95$, with GM1 as equation of state and $M = 1.3\,\mathrm{M}_\odot$). In this figure we report the residuals, i.e. the change in rotational frequency after removing also the pre–glitch spin–down. The two events seem to be very different in the first two minutes from the beginning: in the 2000 glitch the change in ν is less than 0.1% while the situation is different for the other glitch, as we can see in fig. 9.10 (but we should take into account that the 2004 fit is less significant due to the quality of data (Dodson et al., 2007)). Anyway it's important to underline the fact that observational data don't show any *risetime* ($\dot{\Omega}_p$ is always negative) and the glitch is therefore considered as an "instantaneous" step: the upper limit for this phase is 40 s. In other words there is an unobserved window of ~ 1 min in which $\Delta\Omega_p(t)$ reaches its maximum and it's already decreasing when we begin to record data. For this reason we are interested in the quantity $\Delta\Omega_{60}$ which is the jump size extracted after 60 s from the beginning of the glitch, i.e. $\Delta\Omega_{60} = \Omega_p(t = 60\,\mathrm{s}) - \Omega_0$. In this perspective, the choice $\eta_g = 0.2$ is reasonable as it allow us to simulate an intermediate glitch between the two events of Vela considered, and to fit well the 2000 one if we shift the curve (we consider the glitch as starting at $t = -60\,\mathrm{s}$, see the fig. 9.10).

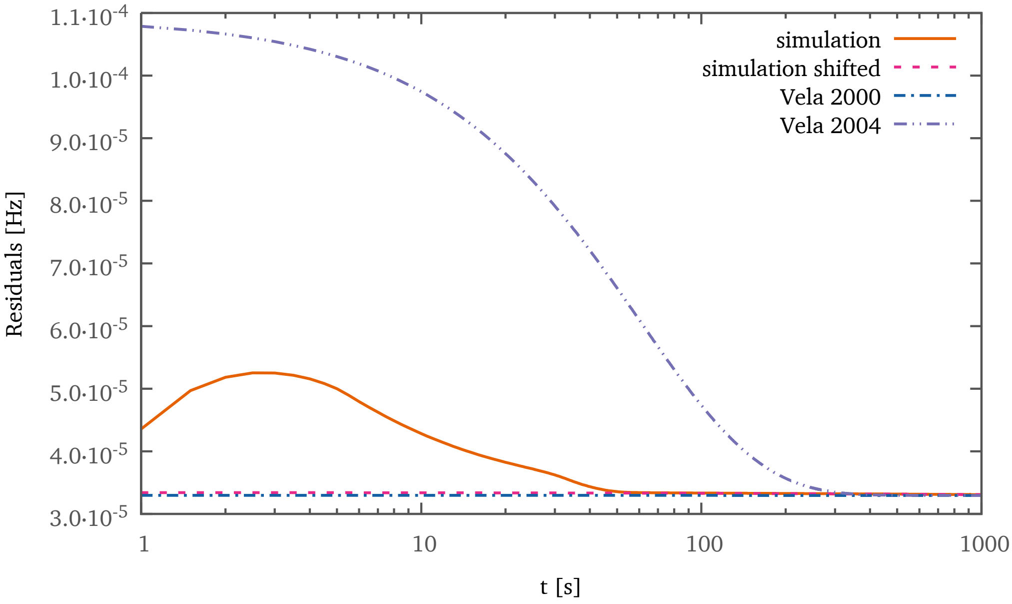

Figure 9.10: In this figure we calculate the residuals of our simulation (see text for details) and we compare the curve with those obtained from the observational data for two events of the Vela pulsar (Dodson et al., 2002, 2007). The “shifted” curve is the same of the first one, but shifted as if the glitch happens at $t = -60\,\text{s}$. As we are focusing on the recovery timescale, we have slightly scaled vertically the curves so that the glitch has decayed ot the same frequency after 1000 s.

9.3 Fit of the NS masses

One of the more interesting results of the snowplow model, discussed in chapters 5 and 7, is the possibility to infer the mass of a neutron star from the average glitch size recorded by the observations, and correlate this information with the typical waiting time of the particular object. The static model predicts in fact that a more massive star exhibits smaller glitches when compared to a neutron star of lower mass. This effect is explained by considering that an increasing the mass means also thinning the inner crust which can store less angular momentum to be transferred to the charged component during the glitch (see also the discussion at the end of chapter 5). This behavior is reproduced also by our dynamical model, as we can see in fig. 9.11. All the curves in the plot are referred to simulations conducted with the same parameters, except for the total mass M of the star that we let vary in the range $(1.2\div2.2)\,\mathrm{M}_\odot$ (here we have used GM1 as EoS, $\mathcal{B}_c = 10^{-4}$, $\mathcal{B}_k = 10^{-2}$, $\eta = 0.6$ and $\eta_g = 0.2$). The temporal evolution of the glitch is quite the same in all cases, and the curves are very similar, even if they are shifted: as we can see quantity $\Delta\Omega_{\mathrm{gl}}$ spans about one order of magnitude when the mass is changed in the range considered.

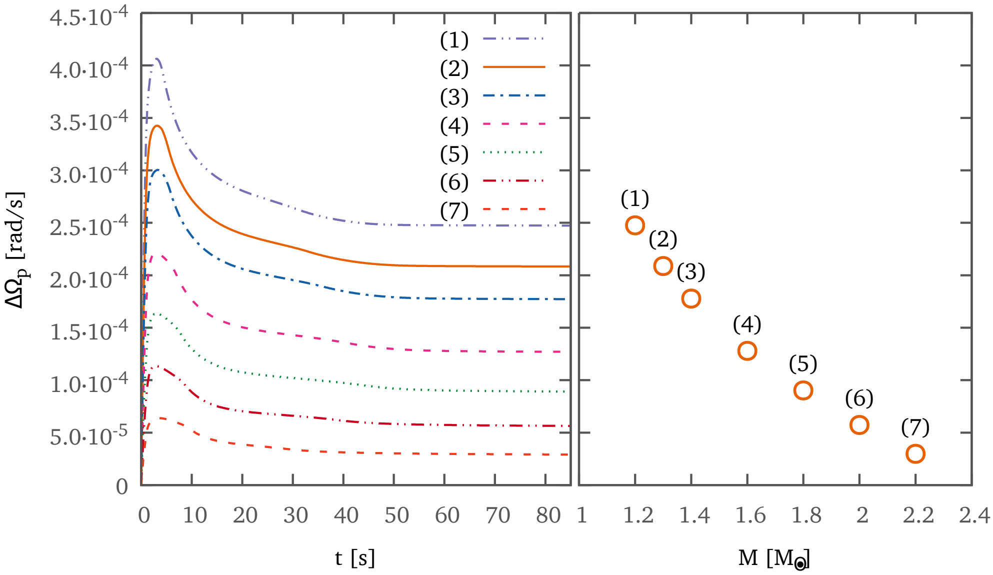

Figure 9.11: This figure shows the effect of the mass on the glitch. We simulate different glitches when all the parameters are kept fixed at their best benchmarks except for the mass M of the star. We can see that a lower mass star is associated to a bigger glitch, as expected from the results of the snowplow model of chapters 5 and 7. On the right part we plot the value of M and the corresponding $\Delta\Omega_{60}$ (glitch size after 60 s).

In the snowplow model, a similar effect on $\Delta\Omega_{gl}$ is played also by the parameter Y_{gl}, as discussed in section 7.2. This quantity encodes, in the static model, the fraction of superfluid matter coupled to the normal one at the glitch: this means that somehow Y_{gl} determines also the jump size, because in the limiting case of $Y_{gl} = 0$ all the angular momentum stored is transferred uniquely to the crust, producing the maximal glitch. The inverse dependency of these two quantities is plotted in fig. 7.3. The degeneracy of M and Y_{gl} over the glitch size has been removed in the snowplow model by fixing the parameter Y_{gl} in order to obtain a mass for the Vela pulsar of $1.3\,M_\odot$. Then we have used the same value of Y_{gl} to infer the mass of all other frequent glitchers: the calculated masses are reported in table 7.1. Moreover we have discussed about the relationship, showed by the observational data, that involves $\Delta\Omega_{gl}$ and the average lag $\omega = |\dot{\Omega}_p|\,\langle t_{gl}\rangle$ built by the star in the time between two consecutive events (see fig. 7.15).

Now we want to test if these results are also compatible with the dynamical model proposed here. We consider the six most frequent glitchers of table 2.2 and, for each case, we construct the respective star that will be used in the simulation: we use GM1 as EoS and for the mass M we take initially the total mass obtained by the fitting procedure of the snowplow model. Then we start the simulation detailed in

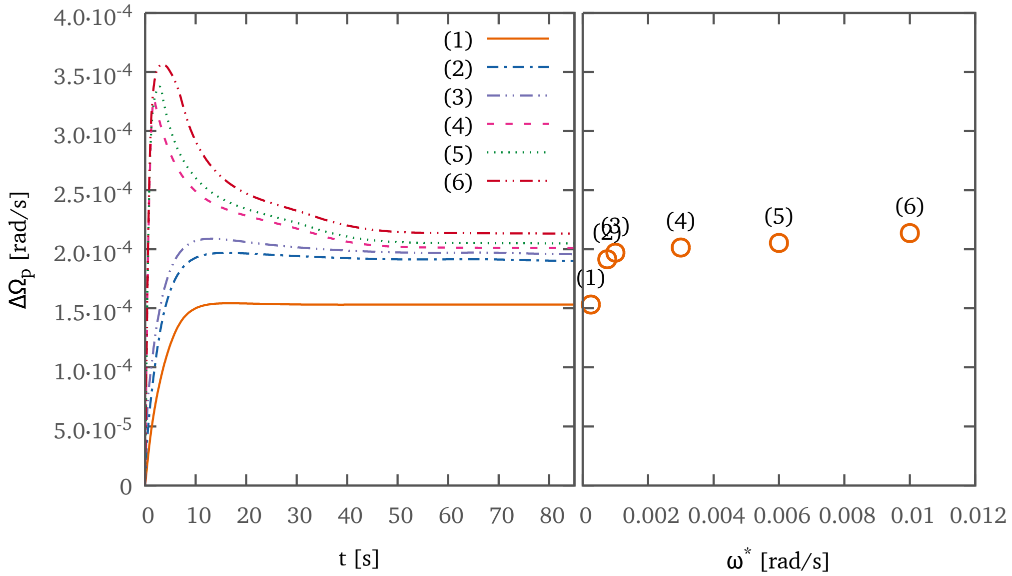

Figure 9.12: In this plot we change the value of the triggering parameter ω^*, i.e. the lag built by the two components at which the glitch is triggered when reached. All other parameters are kept fixed. This plot is analogous to those obtained with the snowplow model in chapter 7. On the right part we plot the value of ω^* and the corresponding $\Delta\Omega_{60}$ (glitch size after 60 s).

this chapter, and we use the prescription of section 8.4.3 to fire a glitch. This means that we start a glitch when the raw lag ω build by the star reaches the critical value ω^* which corresponds to the observational average lag for this particular pulsar (in fig. 9.12 we show the glitches obtained by changing the value of the triggering lag, while all other parameters are kept fixed; we can see that qualitatively the relationship between $\Delta\Omega_{\rm gl}$ and ω is in agreement with the behavior studied with the snowplow model, e.g. see figs. 7.3 and 7.4). The ultimate goal is to compare the jump size that comes from the simulation with the observational value of the extremal event.

In the dynamical approach, the parameter $Y_{\rm gl}$ doesn't exists, but its role is player here by the drag coefficients $\mathcal{B}_k$ and $\mathcal{B}_c$ because they controls the timescale, and therefore also the amount, of the coupling between the superfluid and the normal component of the star. In other words, the jump size is not affected only by the total mass, but it is also affected by these parameters, as $Y_{\rm gl}$ does in the static model. As discussed previously, the figs. 9.6 and 9.7 show quantitatively these effects. Moreover we have another source of degeneracy which comes from the parameter η of the effective drag in the crust before the glitch (η represent the fraction of the critical lag at which we have the transition to the viscous drag; see section 8.4.2). In fig. 9.13 we reports the results of the simulations performed by changing only the value of η, while keeping fixed all other parameters. We can see that the resulting effect is opposed

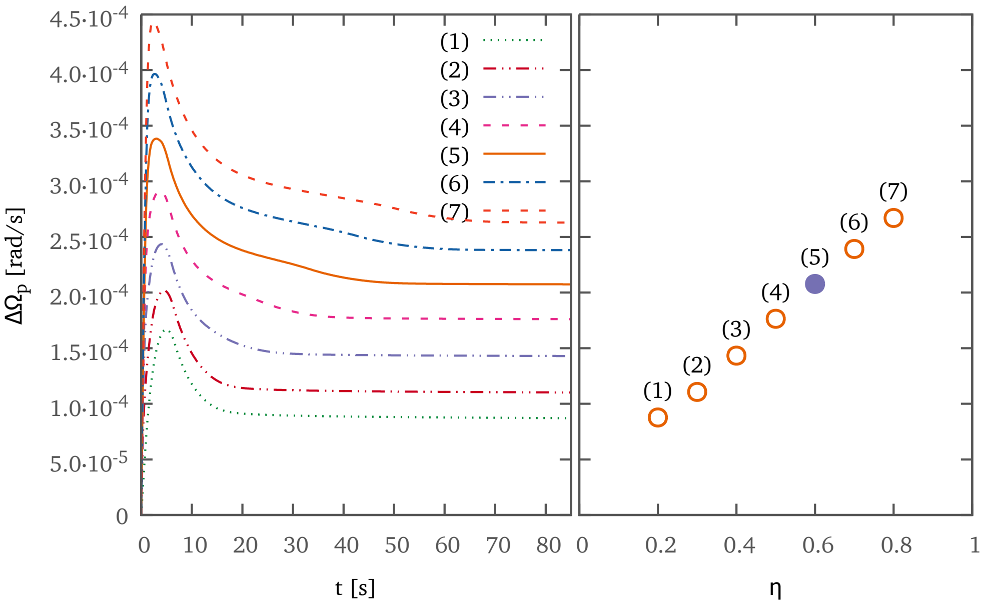

Figure 9.13: With this figure we analyze the effect of the last parameter of the model, η, which control the transition from the kelvonic drag to the viscous one in the crust. As expected a higher value of η produces a bigger glitch, as shown by the right part where η is plotted against $\Delta\Omega_{60}$.

to the one obtained by changing the mass of the star: by increasing η we increase the amount of angular momentum stored by the superfluid in vortexes between two glitches and ready to be transferred suddenly to the crust (on the other hand, the glitch size has an inverse dependency on the mass M, as showed before; this degeneracy is similar to the one discussed in the snowplow model of chapter 7 between M and Y_{gl}).

Based on the results in figs. 9.6 and 9.7 we decide to fix the kelvonic drag parameter to be $\mathcal{B}_k = 10^{-2}$, and for the core coefficient we take $\mathcal{B}_c = 10^{-4}$ as this is the best benchmark (see eq. (8.48)). This reasonable choice, together with $\eta_g = 0.2$ guarantees that the rise time of the glitches remains below the constraint of $\sim$ 40–60 s, while the recovery timescale is in agreement with the observable data for the Vela pulsar (Dodson et al., 2002, 2007). In order to fix the value for η we adopt precisely the same strategy proposed for the static model approach: we consider initially the Vela pulsar B0833–45 and we change η until we can reproduce (with the choice of the other parameters detailed above) the maximum glitch size recorded by observations ($\eta = 0.6$). With the procedure described now, all of the free parameters of the model are fixed, except for the mass M and the lag $\omega = |\dot{\Omega}|t$ at the glitch. Of course ω comes from the observational data (table 2.2, reported also in table 9.1), while for M we follow the same approach used in chapter 7. As explained before, we are focused on the quantity $\Delta\Omega_{60}$ (jump size after 60 s from the beginning of the glitch) that we

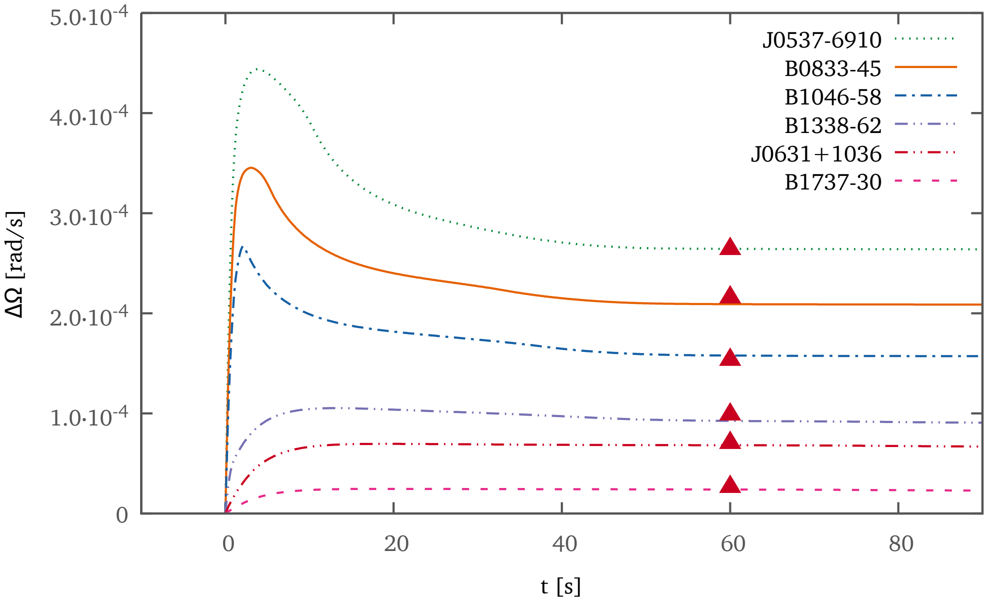

Figure 9.14: In this figure we plot the $\Delta\Omega_p(t)$ curves of our best fits for the six pulsars considered (for GM1; the corresponding plot for SLy is very similar). The triangles indicate the observational values that we fit with the procedure described (see also table 9.1).

compare with the maximum observed $\Delta\Omega_{\text{gl}}$ for each particular star: for every pulsar we slightly change the mass M until $\Delta\Omega_{60}$ matches the biggest glitch.

The inferred masses obtained with this approach are reported in table 9.1. The procedure has been applied also for the SLy equation of state, with the same choices for the pinning profile ($L = 5000$, $\beta = 3$ of chapter 3), neutron fraction ($Q = 0.95$) and drag forces: $B_c = 10^{-4}$, $\mathcal{B}_k = 10^{-2}$, $\eta_g = 0.2$. On the contrary, the parameter η has been fixed in order to reproduce $\Delta\Omega_{\text{gl}_{\max}} = 2.17 \times 10^{-4}$ rad/s, which is the Vela maximum glitch size, with a $1.3\,\text{M}_\odot$ star; the simulations indicate $\eta = 0.9$.

In figs. 9.15 and 9.16 and table 9.1 we give the results for GM1 and SLy together with the ones obtained with the snowplow model in chapter 7, for a comparison. The fig. 9.14 summarizes the simulations that are our best fits for the pulsar considered with GM1 as equation of state. The triangles represent the observational values taken as a reference for each star, positioned at 60 s as we extract the quantity $\Delta\Omega_{60}$ from the calculated curves.

In fig. 9.17 we replot the time evolution of our best fits of table 9.1 and fig. 9.14 (these are the simulations from which we extract the $\Delta\Omega_{60}$ value to be compared with the observational data), for GM1 EoS. As done before, we plot, for each pulsar, the curve $\Delta\Omega_p(t) = \Omega_p(t) - \Omega_p(0)$, and also the equivalent quantity $\Delta\Omega_n(t)$ for the neutron component. This quantity is obtained as $\Delta\Omega_n(t) = \langle\Omega_n(t)\rangle - \Omega_p(0)$, where $\langle\Omega_n\rangle$ is a weighted average of the angular velocity of neutrons. In our model we have

Table 9.1: This table summarizes the results of the fitting procedure for both SLy and GM1. For each pulsar, the reported mass M is the value of this parameter which fits better the observational data, comparing the result with the one obtained in chapter 7 with the snowplow model. We report also the average lag $\omega = |\dot{\Omega}| \langle t_{gl} \rangle$ (see table 7.2) of the particular pulsar used to trigger the glitch in the simulations and the maximum observed glitch size taken as reference to infer the mass of the pulsar.

Pulsar name	ω	$\Delta\Omega_{gl_{max}}$	**SLy**		**GM1**	
	[rad/s] 10^{-4}	[rad/s] 10^{-5}	Snowplow [M$_\odot$]	Dyn. model [M$_\odot$]	Snowplow [M$_\odot$]	Dyn. model [M$_\odot$]
J0537-6910	131.00	26.54	1.22	1.20	1.20	1.20
J0631+1036	2.70	7.16	2.04	1.80	2.33	1.85
B0833-45	80.44	21.70	1.30	1.30	1.30	1.30
B1046-58	37.96	15.46	1.52	1.45	1.61	1.45
B1338-62	11.86	10.00	1.81	1.70	1.96	1.75
B1737-30	1.92	2.76	> 2.04	2.00	> 2.36	2.30

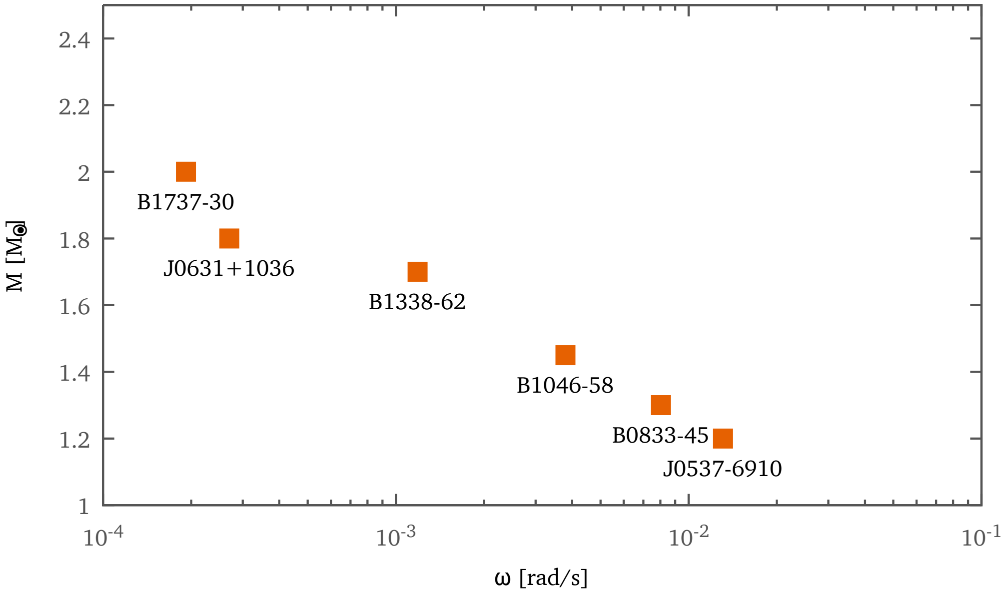

Figure 9.15: We plot here the inferred mass M (with SLy, obtained with the fitting procedure described) of the considered glitchers versus the average lag ω.

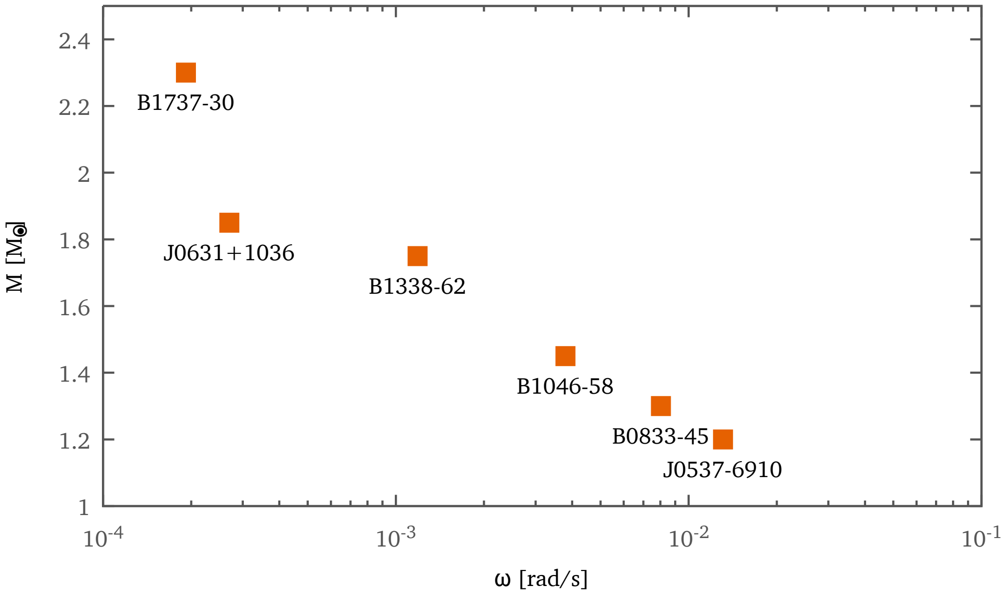

Figure 9.16: We plot here the inferred mass M (with GM1, obtained with the fitting procedure described) of the considered glitchers versus the average lag ω.

considered Ω_n as a function of the cylindrical radius, and therefore we must define a mean quantity to compare it with the angular velocity of the crust (proton fluid). The natural way to accomplish this task is to take into account the total angular momentum L_n stored by the superfluid and therefore we define

$$\langle \Omega_n(t) \rangle = \frac{L_n}{I_n} = \frac{4\pi}{I_n} \int_0^{R_{\rm ic}} x^3 \Omega_n(x,t) \left(\int_0^{\ell(x)/2} \rho_n(x,z)\, dz \right) dx \tag{9.2}$$

where $R_{\rm ic}$ is the radius of the inner/outer crust interface and $\ell(x) = 2\sqrt{R_{\rm ic}^2 - x^2}$ is the length of a vortex for which x is its distance from the rotational axis. Thanks to the definition in eq. (9.2) we obtain the “equivalent” global two component model and the plots in fig. 9.17 show an interesting point. The simulations in which the proton fluid velocity temporarily overcomes the neutron one, are also the ones that show a marked overshoot phase and therefore an evident recovery effect, indicating that these two aspects are strictly linked, as expected. This behavior is present in the first three plots of the figure, but not in the last three glitches where the rise phase is not strong enough to accelerate the proton component to a velocity bigger than $\langle \Omega_n \rangle$ and therefore there is no velocity inversion. This behavior seems again to be controlled by the lag ω built by the star between glitches (as also showed by fig. 9.12) and therefore, for our analysis, by the mass of the pulsar: this suggests that the shape of the $\Delta\Omega_p(t)$ profile could be another indicator of the parameter M.

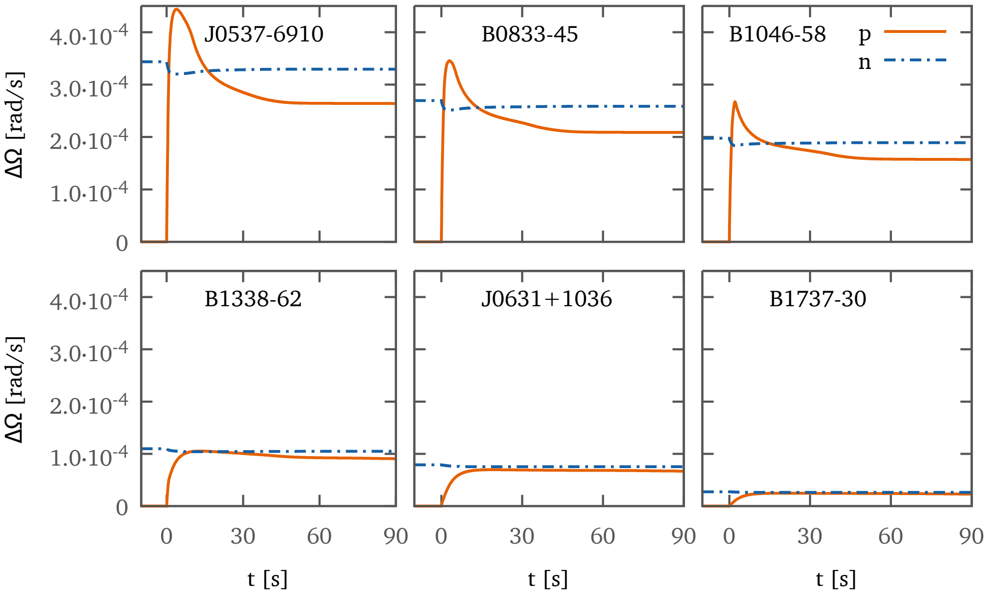

Figure 9.17: For each of the pulsar that we take into account, we plot here the time evolution of the simulation which fits better the observational data (for GM1; the corresponding plots for SLy are very similar). We plot the $\Delta\Omega_p(t)$ curve and also $\Delta\Omega_n(t)$, calculated from the weighted average of the rotational velocity of the neutron fluid, as described in eq. (9.2).

9.4 Conclusions

The results are in good agreement with those obtained with the snowplow model and thus the same considerations done at the end of chapter 7 are valid. We have found the same dependency between the mass of the pulsar and the glitching strength (fig. 9.11); moreover the strong correlation between M and ω of figs. 7.18 and 7.19 is recorded also with the dynamical model described here, as we can clearly see in figs. 9.15 and 9.16. This fact indicates that also this approach (like the static one) provides a unique explanation for both the small and the large glitchers, covering the range spanned by the observational data. As a consequence, the correlation between mass and lag can be understood by the same qualitative considerations reported in section 7.4. It's noteworthy the fact that with the dynamical approach all the NSs considered are fitted well, also the object B1737–30: the snowplow model in this case predicts a mass above the maximum allowed M_{max} for both the EoSs considered (in other words, the static model predicts jumps significantly larger than those observed). On the contrary, with the approach presented in this chapter, the glitching behavior of this star is explained consistently in the same way as for the other pulsars (in fact the inferred mass is slightly below the M_{max} limit, see table 9.1): this confirms the validity of this model in encompassing both large and non–large glitchers. Moreover we must point out that both models (static and dynamic) provide an upper bound for the mass of a NS, as they fit its maximum glitch: therefore it's always possible that in the future a new larger event lowers the inferred mass. This is especially true for B1737–30 as it spins down slower than the other stars and maybe we have not yet observed it long enough: with a slightly larger glitch and therefore a slightly lower mass required in the simulations, the data would show globally an even better correlation between M and ω.

While the results presented here are in agreement with the snowplow model, this dynamical model has many advantages over the static approach, because it allows us to study the full temporal evolution of the interglitch phase and also the rise and recovery of the jump. Moreover we have shown that it's easy to take into account all the required microphysical inputs, like pinning forces and drag interactions, and therefore building a more realistic model. In this work we have focused on the short term recovery which is due to the fast recoupling of the components of the star: in fig. 9.10 we have compared our results with the observed glitches of the Vela pulsar (2000 and 2004). Our simulation shows an intermediate behavior between the two curves taken as reference that are quite different in the first two minutes. In looking at these data we must always take into account that the upper limit for the rise of a glitch is of $\sim 60\,\mathrm{s}$. This indicates that the observational data available at the moment lack of very important information about, at least, the first minute of a glitch, which is a complex phase as it contains the rise, the true maximum $\Delta\Omega_{\mathrm{gl}}$ reached and also a fast recovery. For this reason generally we have chosen to fit the observed $\Delta\Omega_{\mathrm{gl}}$ values with the jump size extracted after $60\,\mathrm{s}$, for a more realistic comparison. We have also shown that by shifting our simulation by $60\,\mathrm{s}$ we can fit well the Vela 2000 curve (which is of better quality). It's clear now that having a precise observation of the first seconds of a glitch is really important as it would give great hints on the drag coefficients and therefore on the whole process.

Even if we have dealt with the fast recovery, of course the longer timescales suggested by the observational data can be explained by introducing other drag parameters to encode the fact that different zones of the star recouple at different times. The understanding of these aspects it's a very interesting task that we will tackle in a future work.

Conclusions and future directions

In this thesis we have faced the problem of pulsar glitches from different perspectives. This approach has been suggested by the fact that a glitch is an evident macroscopic phenomenon that is due to microscopical properties of matter at extreme densities, like superfluidity, pinning, entrainment and drag forces. All these points of view are in agreement and merge together to provide advances in our understanding of glitches.

We have focused on the mesoscopic evaluation of the pinning force per unit length, both in the inner crust of a neutron star (chapter 3, where we find $f \sim 10^{15}$ dyn/cm) and in the core (chapter 4, where the pinning interaction is very weak and negligible for our scopes, in agreement with the indications from chapter 6). Thanks to the pinning profiles obtained, we have successfully explained, with the static snowplow model and with dynamical simulations, the observational parameters of the frequent glitchers. Anyway, some aspects about the evaluation of the pinning interaction, that we have not taken into account here, can be addressed in a future work. For example we have considered the case of straight vortexes that cross the star. Although this is the natural starting point for such a calculation, in a realistic neutron star the vortex array may form a turbulent tangle, leading not only to an increased reservoir of angular momentum, but also to a modified response of the star to a glitch. Furthermore the crust of a neutron star may not form a BCC lattice but may exhibit a much more inhomogeneous structure or exhibit several kinds of "pasta" phases at the crust/core interface, altering the geometry of the nuclear clusters. We intend to explore the consequences of these effects on vortex pinning in future works.

Also in the snowplow–based calculations (chapters 5 to 7) and hydrodynamical simulations (chapters 8 and 9) we have assumed straight vortexes that cross the core of the neutron star. Although the assumption of vortexes that pass through the star appears to be justified by microphysical estimates, that do not predict an interface of normal matter between the crust and core superfluid, turbulence, which is a well known phenomenon from laboratory superfluids, may play an important role in pulsar glitches because it could couple the superfluid and the normal component on inter-glitch timescales that we have not considered here. The inclusion of turbulence in a hydrodynamical glitch simulations is, however, a complex matter as not only is the nature of the turbulence not known but also the definition of pinning force per unit length must be revisited in the presence of a turbulent tangle. Such a fundamental issue should clearly be the focus of a future work.

An important point that we want to underline here is that both the snowplow model with entrainment and the dynamical simulation code can fit well the observational data and provide a unified description of small and large glitchers. Moreover we have estimated the masses, and the results from the two approaches are in good agreement, as they suggest the same mass/glitching–strength/lag dependency. Anyway the multi–fluid model provides much more information about a glitch, as it reproduces the whole evolution of the event: we can follow the interglitch time (where the lag between the components is built), trigger a glitch and analyze the rise phase and also the recovery; all has been done with the most recent benchmarks about the physical inputs like EoS, entrainment and drag coefficients. It has been shown that the evolution of a glitch is strictly dependent on the mutual friction interaction, in particular the rise and consequently also the maximum step in frequency reached. Unfortunately, by the moment, the observational data provide only an upper bound for this crucial phase, but in the near future we hope that the next generation radio telescopes will be able to record directly the rise of a glitch and therefore put important constraints for the model.

In this work we have focused only on the short term recovery of a glitch; anyway the code can be easily modified to introduce a more precise drag force profile, following the idea that different zones of the star recouple at different times. This approach would allow to reproduce the long timescales suggested by the fit of the pulsations and therefore it’s a very interesting task.

Moreover, in this thesis we have proposed deterministic models, even if a glitch is self–organized critical event, as suggested by the observational distributions. We have not treated the nature of the trigger, which is still an unknown aspect of the problem, but it would be very interesting if we can encode it in our simulations and also merge the hydrodynamical equations together with a statistical approach (like cellular automaton), in order to reproduce the distribution of glitch sizes and waiting times.

APPENDICES

APPENDIX **A**

Rotational properties of neutron stars

The first pulsar was observed in 1967, as a astronomical source of pulsating electromagnetic waves. Their name derives indeed from the characteristic radiation registered by our telescopes. Some emit in low frequency region ($< 400\,\mathrm{MHz}$), while others in the visible or even in X or γ band; anyway, for all of them, the radiation is recorded as pulses, with a very short period ($< 10\,\mathrm{s}$).

The pulsation period is directly equivalent to the rotational period of the star, as it's clear from the fig. A.2: as a part of the emitted radiation is focused into a beam outgoing from the magnetic poles, a far detector will record a peak at the moment in which the beam intercepts, due to the rotation, the line of sight. Of course this is possible if the axis of the magnetic field is not coincident with the rotational axis of the star. The described phenomenon allows consequently to perform an extremely precise measurement of the rotational period, so precise that it's possible to record a relative change of 10^{-6} in the rotational speed, as happens in glitches.

The average period of the pulsation of all the observed pulsar is around $1.6\,\mathrm{ms}$. This is consistent, as order of magnitude, with that obtained with a simple consideration about the forces acting on the star: to ensure that the object is not destroyed under the effect of centrifugal force, this cannot exceed, in module, the gravitational one and therefore

$$\frac{GM}{R^2} = R\omega_{\max}^2 \qquad \Longrightarrow \qquad T_{\min} = \frac{2\pi}{\omega_{\max}} = 2\pi\sqrt{\frac{R^3}{GM}} \sim \frac{1}{\sqrt{G\rho}}. \tag{A.1}$$

This simple calculation allows us to understand that neutron stars, due to their very high density, are the only rotating objects that can have a period so small: if we use in eq. (A.1) the values of $M = 1\,\mathrm{M}_\odot$ and $R = 10\,\mathrm{km}$ we obtain a period $T_{\min} = 0.5\,\mathrm{ms}$, in agreement with the observed mean value (the Vela pulsar, the most studied one, has a angular velocity of $\Omega \simeq 70.6\,\mathrm{rad/s}$).

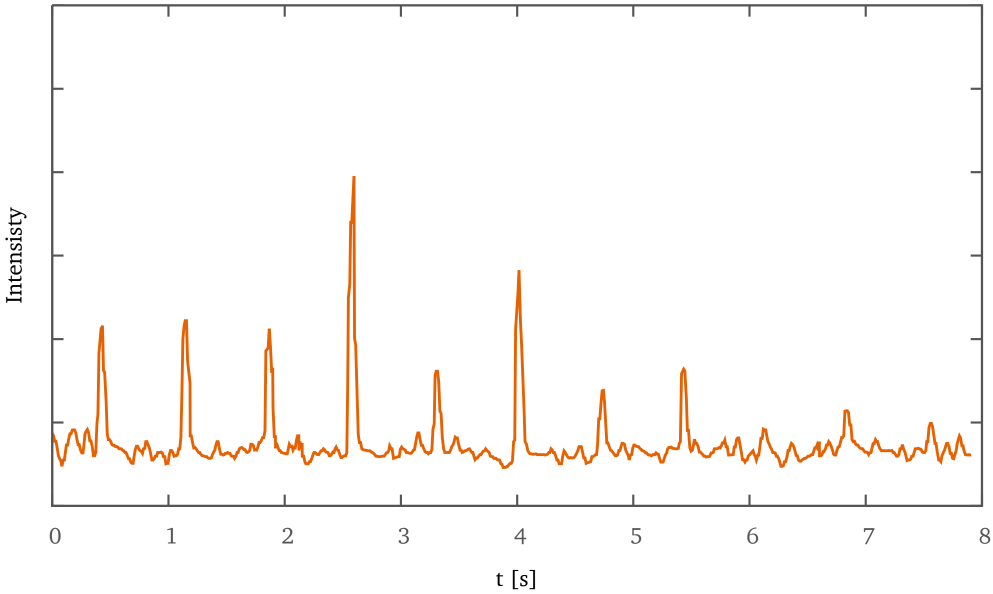

Figure A.1: Radiation intensity profile measured by a radio telescope (410 MHz) while observing the pulsar PSR 0329+54. We can see the pulsation pattern of this kind of source

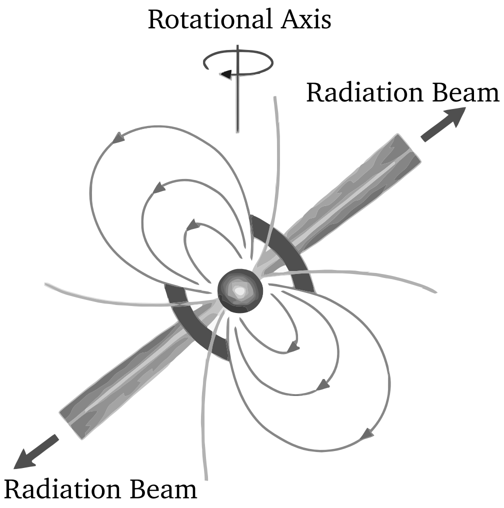

Figure A.2: Representation of the magnetic field of a pulsar with the radiation beam associated. When the axis of the field is not coincident with the rotational axis we can see the pulsations if we are on the line of sight with the star.

The glitches, however, are not the only mechanism for varying the speed of rotation of neutron stars: these in fact slow down gradually, then their period increases ($\dot{\Omega} \approx -10^{-10}\,\mathrm{rad/s^2}$). This is simply due to the fact that these stars, emitting radiation, lose energy and, given that they do not have thermonuclear reactions inside, this energy loss is manifested in the decrease of the kinetic energy of rotation. The model of *magnetic dipole*, shown below, clarifies the extent of this slowdown.

A.1 Magnetic dipole model

In this model the neutron star is treated as a magnetic dipole **m** inclined with an angle α with respect to the axis of rotation. If $m = |\mathbf{m}|$, then the field strength at the magnetic pole is $B_{\mathrm{mag}} = \frac{2m}{R}^3$, while the power of the electromagnetic emission is

$$P = -\frac{dE}{dt} = \frac{2}{3c^3}|\ddot{\mathbf{m}}|^2. \tag{A.2}$$

Projecting the vector **m** on orthonormal basis with the $\mathbf{e}_3$ versor oriented as the axis of rotation we obtain

$$\mathbf{m} = \frac{B_{\mathrm{mag}}R^3}{2}[(\sin\alpha)(\sin\omega t)\mathbf{e}_1 + (\sin\alpha)(\cos\omega t)\mathbf{e}_2 + (\cos\alpha)\mathbf{e}_3] \tag{A.3}$$

$$\ddot{\mathbf{m}} = -\frac{B_{\mathrm{mag}}R^3\omega^2\sin\alpha}{2}[(\sin\omega t)\mathbf{e}_1 + (\cos\omega t)\mathbf{e}_2] \tag{A.4}$$

$$|\ddot{\mathbf{m}}|^2 = \frac{B^2_{\mathrm{mag}}R^6\omega^4\sin^2\alpha}{4}, \tag{A.5}$$

where ω is the rotational angular velocity of the star. Substituting this result in eq. (A.2) we have

$$P = \frac{1}{6c^3}B^2_{\mathrm{mag}}R^6\omega^4\sin^2\alpha. \tag{A.6}$$

The rotational kinetic energy of the star can be written as $E = \frac{1}{2}I\omega^2$ (where I is the total momentum of inertia) and therefore its time derivative is $\dot{E} = I\omega\dot{\omega}$: we can equate this expression with eq. (A.6), in order to obtain the relation for the variation of the angular velocity

$$\dot{\omega} = -\frac{2B^2_{\mathrm{mag}}R^6\omega^3\sin^2\alpha}{3c^3I}. \tag{A.7}$$

If we use in this equation the observative data of the *Crab* pulsar, i.e. $\omega = 190\,\mathrm{rad/s}$, $\dot{\omega} = -9.7\times10^{-9}\,\mathrm{rad/s^2}$, $R = 12\,\mathrm{km}$ e $I = 1.4\times10^{45}\,\mathrm{g\ cm^2}$, we found for the magnetic field B_{mag} the value of $5.2\times10^{12}\,\mathrm{G}$. Therefore we can see that neutron stars are characterized by a very strong magnetic field, that is a consequence of the entrapment of the flux line during the compression phase from the protostar condition.

The relation expressed in eq. (A.7) for $\dot{\omega}$ doesn't take into account the fact that the NS can loss energy by gravitational radiation emission. To correct this approach we can use the following generic expression:

$$\dot{E} = -\alpha\omega^{n+1} \qquad \Longrightarrow \qquad \dot{\omega} = -\beta\omega^{n}. \tag{A.8}$$

With some algebraic manipulations we can estimate the age of a neutron star. If we evaluate the expression above "now" (indicated with the subscript $_0$) we get the value of β as $\beta = -\frac{\dot{\omega}_0}{\omega_0^n}$ and with the definition $T \equiv -\frac{\omega_0}{\dot{\omega}_0}$ we obtain

$$\dot{\omega} = -\frac{\omega^{n-1}}{T\omega_0^{n-1}}. \tag{A.9}$$

The last equation can be integrated to calculate finally the age τ of the star:

$$\int_{\omega_\tau}^{\omega_0} \frac{d\omega}{\omega^{n-1}} = -\int_0^{\tau} \frac{1}{T\omega_0^{n-1}} dt \qquad \Longrightarrow \qquad \tau = \frac{T}{n-1}\left[1 - \left(\frac{\omega_0}{\omega_\tau}\right)^{n-1}\right]. \tag{A.10}$$

In the approximation $\omega_\tau \gg \omega_0$, we find

$$\tau \sim \frac{T}{n-1}. \tag{A.11}$$

All these results can be used to add information in the $P\dot{P}$ diagram (fig. A.3). Each dot of the figure represent one NS (all the known pulsars are reported): on the x–axis we find the rotational period P of the star, while in ordinate there is its the time derivative $\dot{P}$. Thanks to the eq. (A.7) we can draw line of constant magnetic fields B, age τ and electromagnetic emission dE/dt. From the diagram we can see that the pulsars tend to fall into two main groups. There is a large group of "normal" pulsars, which are losing energy relatively quickly and spin relatively slowly; there is also a large group of pulsars that are spinning very rapidly and losing energy very slowly: these are the millisecond pulsars formed in binary systems. In this work we have taken into account mainly the very frequent glitchers that are highlighted with a square in the plot.

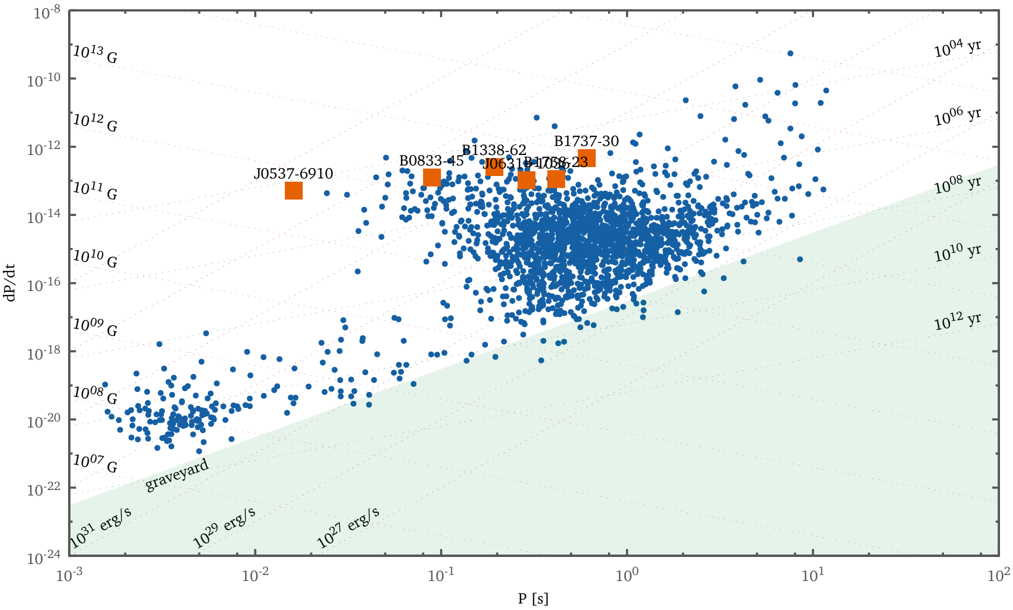

Figure A.3: In this plot each dot represents a pulsar which is plotted with its period P against the time derivative $\dot{P}$. The most frequent glitchers are highlighted as squares.

APPENDIX **B**

Global two–components model

As a neutron star is made of a superfluid component and “normal” one, we can develop a simple empirical model that describes qualitatively the post–glitch behavior of the star. The superfluid component has the features described in section 2.3; the “normal” part instead consists of the outer crust, with nuclei arranged in lattice (in the inner crust) together with all the charged matter, coupled to the crust due to the electromagnetic field. The interaction between these two components is given by the following expressions

$$I_c\dot{\Omega}_c = -\alpha - \frac{I_c(\Omega_c - \Omega_s)}{\tau_c} \tag{B.1}$$

$$I_s\dot{\Omega}_s = \frac{I_c(\Omega_c - \Omega_s)}{\tau_c}, \tag{B.2}$$

where the quantities with the subscript s refer to the superfluid, while those with c to the crust, i.e. the normal component. The parameter α is the slowdown (here considered constant) due to the emission of electromagnetic radiation, while τ_c is the time scale of the coupling between the two components, which is also taken as constant. These two equations guarantee the conservation of angular momentum, verifiable by adding one to the other. By solving the differential equations we obtain

$$I \equiv I_c + I_s \tag{B.3}$$

$$\tau \equiv \frac{\tau_c I_s}{I} \tag{B.4}$$

$$\Omega_c = \frac{\alpha}{I}t + \frac{I_s}{I}\Omega_1 e^{-t/\tau} + \Omega_2 \tag{B.5}$$

$$\Omega_s = \Omega_c - \Omega_1 e^{-t/\tau} + \frac{\alpha\tau}{I_c} \tag{B.6}$$

where Ω_1 and Ω_2 are integration constants. If we rewrite these two quantities as $\Omega_1 = \frac{\Delta\Omega_{\rm gl}QI}{I_s}$ e $\Omega_2 = \Omega_0 + \Delta\Omega_{\rm gl}(1-Q)$, and we take $t = 0$ as the time coordinate of the glitch, we can rewrite the equation that gives the angular velocity of the charged component over time in the following way:

$$\Omega_c(t) = \Omega_0(t) + \Delta\Omega_{\rm gl}\left[Qe^{-t/\tau} + 1 - Q\right]. \tag{B.7}$$

The term $\Omega_0(t)$ represents the variation of the angular velocity (slow down due to the electromagnetic torque) that is recorded in the absence of a glitch (see fig. B.1 for a graphical representation). $\Delta\Omega_{\rm gl}$ is precisely the height of the jump in speed made by the crust. The last two parameters, τ and Q, influence the post–glitch behavior and are related to the first and second order derivatives of Ω_c. More precisely, we have:

$$Q = -\tau \left.\frac{\Delta\dot{\Omega}_c}{\Delta\Omega_{\rm gl}}\right|_{t=0} \qquad\qquad \tau = -\left.\frac{\Delta\dot{\Omega}_c}{\Delta\ddot{\Omega}_c}\right|_{t=0} \tag{B.8}$$

Following the *starquake* model by Ruderman (1969) and Baym et al. (1969) it's possible to connect the healing parameter Q with structural properties of the neutron star. In particular the authors assume that a starquake, responsible of the glitch, results also in changes ΔI_s and ΔI_c on the moment of inertia of the two components. By imposing that the angular momentum of each component is separately conserved, i.e.

$$\frac{\Delta I_c}{I_c} = -\frac{\Delta\Omega_c}{\Omega_c} \qquad\qquad \frac{\Delta I_s}{I_s} = -\frac{\Delta\Omega_s}{\Omega_s}, \tag{B.9}$$

and differentiating B.1 we can find that

$$Q = \frac{I_s}{I}\left(1 - \frac{\Delta I_s}{I_s}\frac{I_c}{\Delta I_c}\frac{\Omega_s}{\Omega_c}\right). \tag{B.10}$$

In the typical case where $\Omega_s - \Omega_c << \Omega_c$, the relation can be simplified as:

$$Q \approx I_s/I. \tag{B.11}$$

This indicate that the ratio between the two components determines the "residual" jump at the end of the recovery.

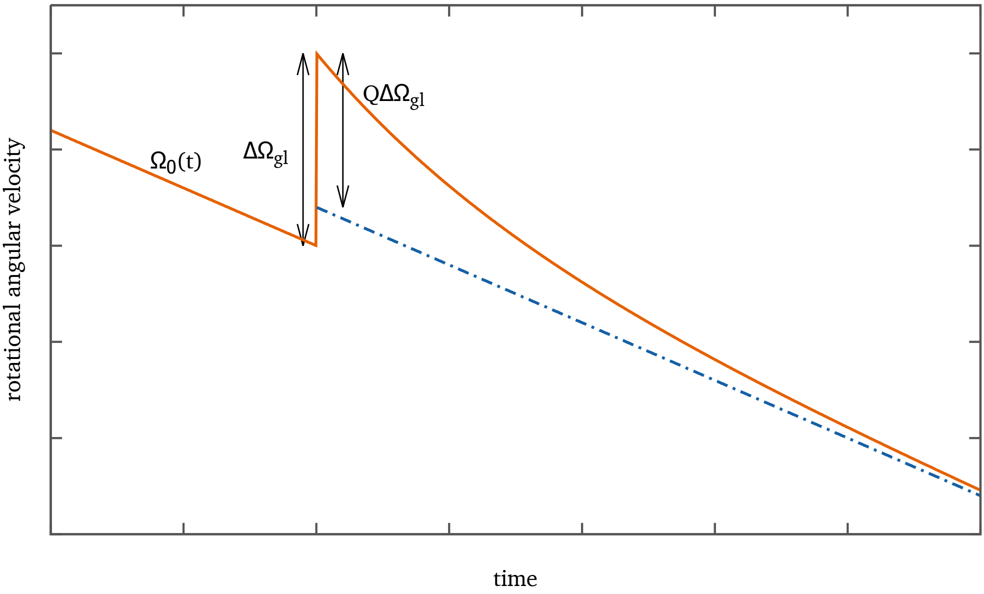

Figure B.1: Schematic representation of a glitch. $\Omega_0(t)$ is the pre–glitch slow down of the crust, and $\Delta\Omega_{\mathrm{gl}}$ is the jump size. Q is the healing parameter used in the global two components model to fit the post–glitch behavior.

APPENDIX **C**

Derivation of the multifluids formalism

C.1 Introduction

We want here to obtain the multifluids dynamic equations from a variational principle. As usual, the starting point is the analysis of an action on which applying the variational methods. Let $\mathcal{I}$ be the action that depends on the lagrangian $\mathcal{L}$ in the following way:

$$\mathcal{I} = \int \mathcal{L} \, dV \, dt \tag{C.1}$$

We introduce the two variables n and $\mathbf{n}$ where the first is the particle density of the fluid and the latter is defined as

$$\mathbf{n} = n\mathbf{v} \tag{C.2}$$

and represent the current density. Typically the lagrangian $\mathcal{L}$ will be a function of these variables, i.e. $\mathcal{L} = \mathcal{L}(n, n\mathbf{v})$. Writing the total differential of $\mathcal{L}$ we can define the dynamical quantities p_0 (energy) and $\mathbf{p}$:

$$d\mathcal{L} = \frac{\partial \mathcal{L}}{\partial n} dn + \frac{\partial \mathcal{L}}{\partial \mathbf{n}} d\mathbf{n} = p_0 dn + \mathbf{p} d\mathbf{n} \tag{C.3}$$

This idea can be used to describe a perfect barothropic fluid. In this case we know the total lagrangian, ie

$$\mathcal{L} = \frac{1}{2}\rho \mathbf{v}^2 - \mathcal{E}(\rho) \tag{C.4}$$

where $\mathcal{E}(\rho)$ is the internal energy which define also the pressure:

$$d\mathcal{E} = \tilde{\mu} d\rho \qquad\qquad P + \mathcal{E} = \rho \tilde{\mu} \tag{C.5}$$

If we apply the variational principle on this lagrangian, we find

$$\delta \mathcal{L} = \rho \mathbf{v} \cdot \delta \mathbf{v} + (\mathbf{v}^2/2 - \tilde{\mu})\delta\rho \tag{C.6}$$

This means that the equations of motion are $\rho \mathbf{v} = 0$ and $\tilde{\mu} = \mathbf{v}^2/2$. We cannot reproduce the Eulerian hydrodynamics in this way because the variational principle is over–constrained. The variational principle must be reformulated based on the concept of "flow lines". For each fluid particle, we can identify the initial position **a** and then the position $\mathbf{x} = \mathbf{x}(\mathbf{a}, t)$. The "Lin condition" is the requirement of conservation of the particle identity, i.e. $\partial_t \mathbf{a} + \mathbf{v} \cdot \nabla \mathbf{a} = 0$. Following this approach one can write the velocity **v** as $\mathbf{v} = \partial_t \mathbf{x}(\mathbf{a}, t)$ and the density as $\rho(\mathbf{x}, t) = \rho_0(\mathbf{a})/det(J^i_j)$, where $J^i_j = \partial x^i / \partial a^j$.

The same results can be obtained by imposing that the variation of the "eulerian" quantities is induced by variation (ξ, τ) of the underlining flow line.

$$\delta\rho = -\nabla(\rho\xi) \qquad\qquad \delta\mathbf{v} = \partial_t \xi + (\mathbf{v}\cdot\nabla)\xi - (\xi\cdot\nabla)\mathbf{v} \tag{C.7}$$

Sustituting these expressions in the action $\mathcal{I}$ and calculating the variation, one can find that

$$\delta\mathcal{I} = -\int \xi\left[\rho(\partial_t + \mathbf{v}\cdot\nabla)\mathbf{v} + \rho\nabla\tilde{\mu} + \mathbf{v}[\partial_t\rho + \nabla(\rho\mathbf{v})]\right] dV\, dt \tag{C.8}$$

The conservation of mass states that $\partial_t \rho + \nabla(\rho \mathbf{v}) = 0$ and so the final equation is

$$(\partial_t + \mathbf{v}\cdot\nabla)\mathbf{v} + \frac{1}{\rho}\nabla P = 0 \tag{C.9}$$

where we have defined $\nabla P = \rho\nabla\tilde{\mu}$. This equation is obtained from the quantity ξ that have three degrees of freedom and is linked to conservation of linear momentum. The variation based on the time shift τ would give the conservation of energy.

C.2 Multi–fluids systems: equations of motion

Form this point we identify with the subscript X the constituent indices, and with the superscripts $i \in [1, 2, 3]$ the single vector component of a quantity. If we apply a variation (ξ_X, τ_X) on the constituent X, we found

$$\delta n_X = -\nabla(n_x \xi_X) + \mathbf{n}_x \cdot \nabla\tau_X - \tau_X \partial_t n_X \tag{C.10}$$

$$\delta \mathbf{n}_X = n_X \partial_t \xi_X + (\mathbf{n}_X \cdot \nabla)\xi_X - (\xi_X \cdot \nabla)\mathbf{n}_X - \mathbf{n}_X(\nabla\cdot\xi_X) - \partial_t(\mathbf{n}_X \tau_X) \tag{C.11}$$

which leads to

$$\delta\mathcal{L} = \sum_X \left(g^X - \mathbf{f}^X \xi_X\right) + \partial_t R + \nabla\cdot\mathbf{R} \tag{C.12}$$

$$\mathbf{f}^X \equiv n_X(\partial_t \mathbf{p}^X - \nabla p^X_0) - \mathbf{n}_X \times (\nabla\times\mathbf{p}^X) + \mathbf{p}^X \Gamma_X \tag{C.13}$$

$$g^X \equiv \mathbf{v}_X \cdot (\mathbf{f}^X - \mathbf{p}^X\Gamma_X) - p^X_0 \Gamma_X \tag{C.14}$$

The last two terms in the first equation vanish in the action integration by appropriate boundary condition ($\xi = 0$ and $\tau = 0$ at the edges of the integration volume) so the action variation is

$$\delta\mathcal{I} = \sum_X \int \left(g^X \tau_X - \mathbf{f}^X \cdot \xi_X \right) dV\, dt \tag{C.15}$$

In these equation Γ_X is the particle creation rate for the constituent X and must be $\sum_X m_X \Gamma_X = 0$.

The equations of motion are obtained from the assumption that a common variation for all constituent $\xi_X = \xi$ and $\tau_X = \tau$ leads to a action variation that can be written as

$$\delta\mathcal{I} = \int \left(g_{\text{ext}} \tau - \mathbf{f}_{\text{ext}} \cdot \xi \right) dV\, dt \tag{C.16}$$

The consequences are the following equations of motion:

$$\sum_X \mathbf{f}^X = \mathbf{f}_{\text{ext}} \qquad\qquad \sum_X g^X = g_{\text{ext}} \tag{C.17}$$

C.3 Conservation laws

C.3.1 Conservation of mass

If $\rho = \sum_X \rho_X = \sum_X m_X n_X$ and $\rho^i = \sum_X n_X^i$ we can calculate the total mass as

$$M = \int_V \rho\, dV \tag{C.18}$$

and, for the Stoke's theorem, $\partial_t \rho + \nabla_i \rho_X^i = 0$. Back to the constituent we have

$$\partial_t n_X + \nabla_i n_X^i = \Gamma_X \qquad\qquad \sum_X m_X \Gamma_X = 0 \tag{C.19}$$

C.3.2 Conservation of linear momentum

We can rewrite the eq. (C.13) as

$$f_i^X = \partial_t (n_X p_i^X) + \nabla_j (n_X^j p_i^X) - (n_X \nabla_i p_0^X + n_X^j \nabla_i p_j^X) \tag{C.20}$$

where we have used the relation in eq. (C.19) to rewrite the term Γ_X as $\partial_t n_X + \nabla_i n_X^i$ and the vector identity $\mathbf{A} \times (\nabla \times \mathbf{B}) = \nabla_{\mathbf{B}}(\mathbf{A} \cdot \mathbf{B}) - (\mathbf{A} \cdot \nabla) \cdot \mathbf{B}$ which leads to the equation $(\mathbf{n}_X \times (\nabla \times \mathbf{p}_X))^i = n_X^j \nabla_i p_j^X - n_X^j \nabla_j p_i^X$. Now we define the generalized pressure Ψ as

$$\Psi = \mathcal{L} - \sum_X (n_X p_0^X + n_X^i p_i^X) \tag{C.21}$$

It's easy to find, starting from the definition in eq. (C.3), that

$$d\Psi = -\sum_X (n_X\, dp_0 + n^i_X\, dp^X_i) \tag{C.22}$$

If we calculate the sum of the eq. (C.20) for all the constituents we have the following relation

$$f^i_{\text{ext}} = \sum_X f^i_x = \partial_t \pi^i + \nabla_j (\sum_X n^j_X p^X_i) - \nabla^i \Psi \tag{C.23}$$

where we use the notation π_i to indicate the linear momentum density, ie

$$\pi_i = \sum_X p i^X_i = \sum_X n_X p^X_i . \tag{C.24}$$

As result we can write the conservation law for linear momentum

$$f^i_{\text{ext}} = \partial_t \pi_i + \nabla_j T^j{}_i \tag{C.25}$$

$$T^j{}_i = \sum_X (n^j_X p^X_i) + \Psi \delta^j_i \tag{C.26}$$

The energy conservation law can be obtained in a similar way, starting from the eq. (C.14):

$$g^X = n^i_X \partial_t p^X_i - n^i_X \nabla_i p^X_0 - (\partial_t n_X + \nabla_i n^i) p^X_0 \tag{C.27}$$

$$= \partial_t (n^i_X p^X_i) - \nabla_i (n^i_X p^X_0) - (p^X_0 \partial_t n_X + p^X_i \partial_t n^i_X) \tag{C.28}$$

$$= \partial_t (n^i_X p^X_i) - \nabla_i (n^i_X p^X_0) - \partial_t \mathcal{L} \tag{C.29}$$

The result is that we can write the following equation that express the energy conservation law:

$$g_{\text{ext}} = \sum_X g^x = \partial_t \mathcal{H} + \nabla_i Q^i \tag{C.30}$$

where $Q^i = -p^X_0 n^i_X$ and $\mathcal{H}$ represent the hamiltonian of the system

$$\mathcal{H} = \sum_X n^i_X p^X_i - \mathcal{L} \tag{C.31}$$

C.4 Application to neutron stars

In order to describe a neutron star core, we want to find the class of lagrangian density $\mathcal{L}$ which describe Newtonian hydrodynamics. We postulate that

$$\mathcal{L}(n_X, n^i_X) = \sum_X m^X \frac{g_{ij} n^i_X n^j_X}{2 n_X} - \mathcal{E} \tag{C.32}$$

where g_{ij} is the metric tensor (flat in our case, $g_{ij} = \delta_{ij}$), and $\mathcal{E}$ is the internal energy of the system. This implies that

$$-p_0^X = \frac{1}{2} m^X g_{ij} v_X^i v_X^j + \frac{\partial \mathcal{E}}{\partial n_X} \tag{C.33}$$

$$p_i^X = m^X g_{ij} v_X^j - \frac{\partial \mathcal{E}}{\partial n_X^i} \tag{C.34}$$

If we want our description to be invariant under a Galileian boost, the term $\mathcal{E}$ must be in the following form, as shown in (Prix, 2004):

$$\mathcal{E}(n_X, n_X^i) = \mathcal{E}(n_X, \Delta_{XY}^i) \tag{C.35}$$

where Δ_{XY}^i is the relative velocity between the fluids, i.e.

$$\Delta_{XY}^i = v_X^i - v_Y^i = \frac{n_X^i}{n_X} - \frac{n_Y^i}{n_Y} \tag{C.36}$$

The requirement of isotropy constrains again the form of $\mathcal{E}$ to be

$$\mathcal{E} = \mathcal{E}(n_X, \Delta_{XY}^2) \tag{C.37}$$

The total differential of the energy function will be

$$d\mathcal{E} = \sum_X \mu^X dn_X + \frac{1}{2} \sum_{X,Y} \alpha^{XY} d\Delta_{XY}^2 \tag{C.38}$$

This means that the linear momentum and energy density of the components are coupled by the term α^{XY} which encodes the entrainment effect.

$$p_i^X = m^X g_{ij} v_X^j - \sum_Y \frac{2\alpha^{XY}}{n_X} \Delta_{XY} \tag{C.39}$$

$$-p_0^X = \mu^X - m_X \frac{v_X^2}{2} + v_X^i p_i^X \tag{C.40}$$

From the definition of the generalized pressure Ψ, it follows that

$$\mathcal{E} + \Psi = \sum_X n_x \mu^X \qquad \Rightarrow \qquad d\Psi = \sum_X n_X d\mu^X - \frac{1}{2} \sum_{X,Y} \alpha^{XY} d\Delta_{XY}^2 \tag{C.41}$$

It’s easy now, from the relation in eq. (C.23), to write the equation of motion in this way

$$f_i^X = n_X(\partial_t + v_x^j \nabla_j) p_i^X + n_X \nabla_i \mu^X - \sum_Y 2\alpha^{XY} \Delta_{XY}^j \nabla_i v_j^X \tag{C.42}$$

Entropy

Entropy can be included easily in this formulation if we consider it as a constituent of the system. The corresponding density is $n_s = s$ and its current is $\mathbf{n}_s = s\mathbf{v}_s$. Of course entropy is massless ($m_s = 0$) and we have that $\mu_s = T$. The internal energy becomes

$$d\mathcal{E} = T ds + \sum_{X \neq s} \mu^X dn_X + \frac{1}{2} \sum_{X,Y} \alpha^{XY} d\Delta^2_{XY} \tag{C.43}$$

and the momenta are

$$\Theta_0 = p^s_0 = -T - v^i_s \Theta_i \tag{C.44}$$

$$\Theta_i = p^s_i = -\sum_Y \frac{2\alpha^{sY}}{s} \Delta^i_{sY} \tag{C.45}$$

We can see that, even if entropy has no mass, it has a linear momentum associated due to the entrainment effect with other fluid constituent. The corresponding equations of motion are:

$$f^s_i = s(\partial_t + v^j_x \nabla_j)\Theta_i + s\nabla_i T - \sum_Y 2\alpha^{sY} \Delta^j_{sY} \nabla_i v^s_j \tag{C.46}$$

$$g^s = v^i_s f^s_i + (T + v^i_s \Theta_i)\Gamma_s \tag{C.47}$$

Bibliography

Adams P., Cieplak M., Glaberson W. “Spin-up problem in superfluid ^{4}He”. *Phys. Rev. B*, **32**(1):171–177, 1985.
DOI: 10.1103/PhysRevB.32.171

Alpar M.A. “Pinning and Threading of Quantized Vortices in the Pulsar Crust Superfluid”. *Astrophys. J.*, **213**:527, 1977.
DOI: 10.1086/155183

Alpar M.A., Anderson P.W., Pines D., Shaham J. “Giant glitches and pinned vorticity in the VELA and other pulsars”. *Astrophys. J.*, **249**:L29, 1981.
DOI: 10.1086/183652

Alpar M.A., Anderson P.W., Pines D., Shaham J. “Vortex creep and the internal temperature of neutron stars. I. General theory”. *Astrophys. J.*, **276**, 1984a.

Alpar M.A., Anderson P.W., Pines D., Shaham J. “Vortex creep and the internal temperature of neutron stars. II. Vela pulsar”. *Astrophys. J.*, **278**, 1984b.

Alpar M.A., Chau H.F., Cheng K.S., Pines D. “Postglitch relaxation of the Crab pulsar: Evidence for crust cracking”. *Astrophys. J.*, **427**:L29, 1994.
DOI: 10.1086/187357

Alpar M.A., Chau H.F., Cheng K.S., Pines D. “Postglitch Relaxation of the Crab Pulsar after Its First Four Major Glitches: The Combined Effects of Crust Cracking, Formation of Vortex Depletion Region and Vortex Creep”. *Astrophys. J.*, **459**:706, 1996.
DOI: 10.1086/176935

Alpar M.A., Langer S.A., Sauls J.A. “Rapid postglitch spin-up of the superfluid core in pulsars”. *Astrophys. J.*, **282**:533, 1984c.
DOI: 10.1086/162232

Anderson P.W., Alpar M.A., Pines D., Shaham J. “The rheology of neutron stars. Vortex-line pinning in the crust superfluid”. *Philos. Mag. A*, **45**(2):227–238, 1982.

Anderson P.W., Itoh N. “Pulsar glitches and restlessness as a hard superfluidity phenomenon”. *Nature*, **256**(5512):25–27, 1975.
DOI: `10.1038/256025a0`

Andersson N., Comer G.L. “A flux-conservative formalism for convective and dissipative multi-fluid systems, with application to Newtonian superfluid neutron stars”. *Class. Quantum Gravity*, **23**(18):5505–5529, 2006.
DOI: `10.1088/0264-9381/23/18/003`

Andersson N., Glampedakis K., Ho W.C.G., Espinoza C.M. “Pulsar Glitches: The Crust is not Enough”. *Phys. Rev. Lett.*, **109**(24):241103, 2012.
DOI: `10.1103/PhysRevLett.109.241103`

Andersson N., Sidery T., Comer G.L. “Mutual friction in superfluid neutron stars”. *Mon. Not. R. Astron. Soc.*, **368**(1):162–170, 2006.
DOI: `10.1111/j.1365-2966.2006.10147.x`

Andersson N., Sidery T., Comer G.L. “Superfluid neutron star turbulence”. *Mon. Not. R. Astron. Soc.*, **381**(2):747–756, 2007.
DOI: `10.1111/j.1365-2966.2007.12251.x`

Antonelli M. *Automaton for spin evolution of isolated pulsar*. Master thesis, Università degli studi di Milano, 2014.

Avogadro P., Barranco F., Broglia R., Vigezzi E. “Quantum calculation of vortices in the inner crust of neutron stars”. *Phys. Rev. C*, **75**(1), 2007.
DOI: `10.1103/PhysRevC.75.012805`

Babaev E. “Unconventional Rotational Responses of Hadronic Superfluids in a Neutron Star Caused by Strong Entrainment and a Σ^- Hyperon Gap”. *Phys. Rev. Lett.*, **103**(23):231101, 2009.
DOI: `10.1103/PhysRevLett.103.231101`

Baym G., Pethick C.J., Pines D., Ruderman M. “Spin Up in Neutron Stars : The Future of the Vela Pulsar”. *Nature*, **224**(5222):872–874, 1969.
DOI: `10.1038/224872a0`

Bildsten L. “Gravitational Radiation and Rotation of Accreting Neutron Stars”. *Astrophys. J.*, **501**(1):L89–L93, 1998.
DOI: `10.1086/311440`

Carter B., Chamel N., Haensel P. “Entrainment coefficient and effective mass for conduction neutrons in neutron star crust: macroscopic treatment”. *Int. J. Mod. Phys. D*, **15**(05):777–803, 2006.
DOI: `10.1142/S0218271806008504`

Chamel N. “Effective mass of free neutrons in neutron star crust”. *Nucl. Phys. A*, **773**(3-4):263–278, 2006.
DOI: `10.1016/j.nuclphysa.2006.04.010`

Chamel N. “Two-fluid models of superfluid neutron star cores”. *Mon. Not. R. Astron. Soc.*, **388**(2):737–752, 2008.
DOI: `10.1111/j.1365-2966.2008.13426.x`

Chamel N. “Neutron conduction in the inner crust of a neutron star in the framework of the band theory of solids”. *Phys. Rev. C*, **85**(3):035801, 2012.
DOI: `10.1103/PhysRevC.85.035801`

Chamel N. “Crustal Entrainment and Pulsar Glitches”. *Phys. Rev. Lett.*, **110**(1):011101, 2013.
DOI: `10.1103/PhysRevLett.110.011101`

Chamel N., Carter B. “Effect of entrainment on stress and pulsar glitches in stratified neutron star crust”. *Mon. Not. R. Astron. Soc.*, **368**(2):796–808, 2006.
DOI: `10.1111/j.1365-2966.2006.10170.x`

Chamel N., Haensel P. “Physics of Neutron Star Crusts”. *Living Rev. Relativ.*, **11**, 2008.
DOI: `10.12942/lrr-2008-10`

Chau H.F., Cheng K.S., Ding K.Y. “Implications of 3P2 superfluidity in the interior of neutron stars”. *Astrophys. J.*, **399**:213, 1992.
DOI: `10.1086/171917`

Crawford F., Demiański M. “A Comparison of Measured Crab and Vela Glitch Healing Parameters with Predictions of Neutron Star Models”. *Astrophys. J.*, **595**(2):1052–1057, 2003.
DOI: `10.1086/377470`

Demorest P.B., Pennucci T., Ransom S.M., Roberts M.S.E., Hessels J.W.T. “A two-solar-mass neutron star measured using Shapiro delay.” *Nature*, **467**(7319):1081–3, 2010.
DOI: `10.1038/nature09466`

Dodson R.G., Lewis D., McCulloch P. “Two decades of pulsar timing of Vela”. *Astrophys. Space Sci.*, **308**(1-4):585–589, 2007.
DOI: `10.1007/s10509-007-9372-4`

Dodson R.G., McCulloch P.M., Lewis D.R. “High Time Resolution Observations of the January 2000 Glitch in the Vela Pulsar”. *Astrophys. J.*, **564**(2):L85–L88, 2002.
DOI: `10.1086/339068`

Donati P., Pizzochero P.M. “Is there Nuclear Pinning of Vortices in Superfluid Pulsars?” *Phys. Rev. Lett.*, **90**(21):4–7, 2003.
DOI: `10.1103/PhysRevLett.90.211101`

Donati P., Pizzochero P.M. “Fully consistent semi-classical treatment of vortex–nucleus interaction in rotating neutron stars”. *Nucl. Phys. A*, **742**(3-4):363–379, 2004.
DOI: `10.1016/j.nuclphysa.2004.07.002`

Donati P., Pizzochero P.M. “Realistic energies for vortex pinning in intermediate-density neutron star matter”. *Phys. Lett. B*, **640**(3):74–81, 2006.
DOI: `10.1016/j.physletb.2006.07.047`

Douchin F., Haensel P. “A unified equation of state of dense matter and neutron star structure”. *Astron. Astrophys.*, **380**:151–167, 2001.
DOI: `10.1051/0004-6361`

Elshamouty K.G., Heinke C.O., Sivakoff G.R., Ho W.C.G., Shternin P.S., Yakovlev D.G., Patnaude D.J., David L. “Measuring the cooling of the neutron star in Cassiopeia A with all Chandra X-ray observatory detectors”. *Astrophys. J.*, **777**(1):22, 2013.
DOI: `10.1088/0004-637X/777/1/22`

Epstein R.I., Baym G. “Vortex pinning in neutron stars”. *Astrophys. J.*, **328**:680, 1988.
DOI: `10.1086/166325`

Epstein R.I., Baym G. “Vortex drag and the spin-up time scale for pulsar glitches”. *Astrophys. J.*, **387**:276, 1992.
DOI: `10.1086/171079`

Espinoza C.M., Lyne a.G., Stappers B.W., Kramer M. “A study of 315 glitches in the rotation of 102 pulsars”. *Mon. Not. R. Astron. Soc.*, **414**(2):1679–1704, 2011.
DOI: `10.1111/j.1365-2966.2011.18503.x`

Fetter A. “Core Structure of a Quantized Vortex”. *Phys. Rev. Lett.*, **27**(15):986–988, 1971.
DOI: `10.1103/PhysRevLett.27.986`

Flanagan C. “Twelve years of Glitches in the VELA Pulsar”. *Pulsars Probl. progress. Astron. Soc. Pacific Conf. Ser.*, **105**, 1996.

Gandolfi S., Illarionov A., Fantoni S., Pederiva F., Schmidt K. “Equation of State of Superfluid Neutron Matter and the Calculation of the $^1S_0$ Pairing Gap”. *Phys. Rev. Lett.*, **101**(13):132501, 2008.
DOI: `10.1103/PhysRevLett.101.132501`

Gandolfi S., Illarionov A.Y., Schmidt K.E., Fantoni S. “Equation of state of low-density neutron matter, and the $^1S_0$ pairing gap”. *Phys. Rev. C*, **80**(4):045802, 2009.
DOI: `10.1103/PhysRevC.80.045802`

Glampedakis K., Andersson N. “Hydrodynamical Trigger Mechanism for Pulsar Glitches”. *Phys. Rev. Lett.*, **102**(14):5, 2009.
DOI: `10.1103/PhysRevLett.102.141101`

Glampedakis K., Andersson N. "Magneto-rotational neutron star evolution: the role of core vortex pinning". *Astrophys. J.*, **740**(2):L35, 2011.
DOI: `10.1088/2041-8205/740/2/L35`

Glendenning N., Moszkowski S. "Reconciliation of neutron-star masses and binding of the Λ in hypernuclei". *Phys. Rev. Lett.*, **67**(18):2414–2417, 1991.
DOI: `10.1103/PhysRevLett.67.2414`

Grill F. *Proprietà della materia superfluida in presenza del reticolo nucleare nella crosta interna delle stelle di neutroni*. Phd master thesis, Università degli studi di Milano, 2011.

Grill F., Pizzochero P.M. "Vortex-lattice interaction in Pulsar Glitches". *J. Phys. Conf. Ser.*, **342**:012004, 2012.
DOI: `10.1088/1742-6596/342/1/012004`

Gudmundsson E.H., Pethick C.J., Epstein R.I. "Structure of neutron star envelopes". *Astrophys. J.*, **272**:286, 1983.
DOI: `10.1086/161292`

Gügercinoğlu E., Alpar M.A. "Vortex creep against toroidal flux lines, crustal entrainment, and pulsar glitches". *Astrophys. J.*, **788**(1):L11, 2014.
DOI: `10.1088/2041-8205/788/1/L11`

Haensel P., Potekhin A.Y. "Analytical representations of unified equations of state of neutron-star matter". *Astron. Astrophys.*, **197**:191–197, 2004.
DOI: `10.1051/0004-6361`

Harvey J., Ruderman M., Shaham J. "Effects of neutron-star superconductivity on magnetic monopoles and core field decay". *Phys. Rev. D*, **33**(8):2084–2091, 1986.
DOI: `10.1103/PhysRevD.33.2084`

Haskell B., Andersson N., Comer G.L. "Dynamics of dissipative multifluid neutron star cores". *Phys. Rev. D*, **86**(6):063002, 2012a.
DOI: `10.1103/PhysRevD.86.063002`

Haskell B., Antonopoulou D. "Glitch recoveries in radio-pulsars and magnetars". *Mon. Not. R. Astron. Soc. Lett.*, **438**(1):L16–L20, 2013.
DOI: `10.1093/mnrasl/slt146`

Haskell B., Degenaar N., Ho W.C.G. "Constraining the physics of the r-mode instability in neutron stars with X-ray and ultraviolet observations". *Mon. Not. R. Astron. Soc.*, **424**(1):93–103, 2012b.
DOI: `10.1111/j.1365-2966.2012.21171.x`

Haskell B., Pizzochero P.M., Sidery T. "Modelling pulsar glitches with realistic pinning forces: a hydrodynamical approach". *Mon. Not. R. Astron. Soc.*, **420**:658–671, 2012c.
DOI: `10.1111/j.1365-2966.2011.20080.x`

Haskell B., Samuelsson L., Glampedakis K., Andersson N. "Modelling magnetically deformed neutron stars". *Mon. Not. R. Astron. Soc.*, **385**(1):531–542, 2008.
DOI: `10.1111/j.1365-2966.2008.12861.x`

Helfand D.J., Gotthelf E.V., Halpern J.P. "The Vela Pulsar and its Synchrotron Nebula". *Astrophys. J.*, **556**(380):16, 2001.
DOI: `10.1086/321533`

Ho W.C.G., Andersson N., Haskell B. "Revealing the Physics of r Modes in Low-Mass X-Ray Binaries". *Phys. Rev. Lett.*, **107**(10):101101, 2011.
DOI: `10.1103/PhysRevLett.107.101101`

Jones P.B. "Rotation of the neutron-drip superfluid in pulsars: period discontinuities and internal temperatures". *Mon. Not. R. Astron. Soc.*, **246**:315–323, 1990a.

Jones P.B. "Rotation of the neutron-drip superfluid in pulsars: the resistive force". *Mon. Not. R. Astron. Soc.*, **243**:257–262, 1990b.

Jones P.B. "Neutron superfluid spin-down and magnetic field decay in pulsars". *Mon. Not. R. Astron. Soc.*, **253**:279–286, 1991a.
DOI: `1991MNRAS.253..279J`

Jones P.B. "Rotation of the neutron-drip superfluid in pulsars - The interaction and pinning of vortices". *Astrophys. J.*, **373**:208, 1991b.
DOI: `10.1086/170038`

Jones P.B. "Rotation of the neutron-drip superfluid in pulsars: the Kelvin phonon contribution to dissipation". *Mon. Not. R. Astron. Soc.*, **257**:501–506, 1992.

Jones P.B. "Type I and two-gap superconductivity in neutron star magnetism". *Mon. Not. R. Astron. Soc.*, **371**(3):1327–1333, 2006.
DOI: `10.1111/j.1365-2966.2006.10754.x`

Kobyakov D., Pethick C.J. "Towards a Metallurgy of Neutron Star Crusts". *Phys. Rev. Lett.*, **112**(11):112504, 2014.
DOI: `10.1103/PhysRevLett.112.112504`

Lander S.K., Andersson N., Glampedakis K. "Magnetic neutron star equilibria with stratification and type II superconductivity". *Mon. Not. R. Astron. Soc.*, **419**(1):732–747, 2012.
DOI: `10.1111/j.1365-2966.2011.19720.x`

Larson M.B., Link B. “Simulations of glitches in isolated pulsars”. *Mon. Not. R. Astron. Soc.*, **333**(3):613–622, 2002.
DOI: `10.1046/j.1365-8711.2002.05439.x`

Link B. “Constraining Hadronic Superfluidity with Neutron Star Precession”. *Phys. Rev. Lett.*, **91**(10):10–13, 2003.
DOI: `10.1103/PhysRevLett.91.101101`

Link B. “Dynamics of Quantum Vorticity in a Random Potential”. *Phys. Rev. Lett.*, **102**(13):131101, 2009.
DOI: `10.1103/PhysRevLett.102.131101`

Link B. “Instability of superfluid flow in the neutron star core”. *Mon. Not. R. Astron. Soc.*, **421**(3):2682–2691, 2012a.
DOI: `10.1111/j.1365-2966.2012.20498.x`

Link B. “Instability of superfluid flow in the neutron star inner crust”. *Mon. Not. R. Astron. Soc.*, **422**(2):1640–1647, 2012b.
DOI: `10.1111/j.1365-2966.2012.20740.x`

Link B.K., Epstein R.I. “Mechanics and energetics of vortex unpinning in neutron stars”. *Astrophys. J.*, **373**:592, 1991.
DOI: `10.1086/170078`

Lombardo U., Schulze H.J. *Physics of Neutron Star Interiors*, volume 578 of *Lecture Notes in Physics*. Springer Berlin Heidelberg, Berlin, Heidelberg, 2001.
DOI: `10.1007/3-540-44578-1`

Lorenz C., Ravenhall D., Pethick C. “Neutron star crusts”. *Phys. Rev. Lett.*, **70**(4):379–382, 1993.
DOI: `10.1103/PhysRevLett.70.379`

Lyne a.G., Shemar S.L., Graham Smith F. “Statistical studies of pulsar glitches”. *Mon. Not. R. Astron. Soc.*, **315**(3):534–542, 2000.
DOI: `10.1046/j.1365-8711.2000.03415.x`

Manchester R.N., Hobbs G.B., Teoh A., Hobbs M. “The Australia Telescope National Facility Pulsar Catalogue”. *Astrophys. J.*, **129**:1993–2006, 2005.
DOI: `10.1086/428488`

Melatos A., Peralta C. “Superfluid Turbulence and Pulsar Glitch Statistics”. *Astrophys. J.*, **662**(2):L99–L102, 2007.
DOI: `10.1086/518598`

Melatos A., Peralta C., Wyithe J.S.B. “Avalanche Dynamics of Radio Pulsar Glitches”. 2008.
DOI: `10.1086/523349`

Melatos a., Warszawski L. “Superfluid vortex unpinning as a coherent noise process, and the scale invariance of pulsar glitches”. *Astrophys. J.*, **700**(2):1524–1540, 2009.
DOI: `10.1088/0004-637X/700/2/1524`

Mendell G. “Superfluid hydrodynamics in rotating neutron stars. I - Nondissipative equations. II - Dissipative effects”. *Astrophys. J.*, **380**:515, 1991.
DOI: `10.1086/170609`

Middleditch J., Marshall F.E., Wang Q.D., Gotthelf E.V., Zhang W. “Predicting the Starquakes in PSR J0537-6910”. *Astrophys. J.*, **652**(2):1531–1546, 2006.
DOI: `10.1086/508736`

Migdal A. “Superfluidity and the moments of inertia of nuclei”. *Nucl. Phys.*, **13**(5):655–674, 1959.
DOI: `10.1016/0029-5582(59)90264-0`

Negele J., Vautherin D. “Neutron star matter at sub-nuclear densities”. *Nucl. Phys. A*, **207**(2):298–320, 1973.
DOI: `10.1016/0375-9474(73)90349-7`

Page D., Prakash M., Lattimer J.M., Steiner A.W. “Rapid Cooling of the Neutron Star in Cassiopeia A Triggered by Neutron Superfluidity in Dense Matter”. *Phys. Rev. Lett.*, **106**(8):081101, 2011.
DOI: `10.1103/PhysRevLett.106.081101`

Peralta C., Melatos A. “An unstable superfluid stewartson layer in a differentially rotating neutron star”. *Astrophys. J.*, **701**(2):L75–L78, 2009.
DOI: `10.1088/0004-637X/701/2/L75`

Peralta C., Melatos A., Giacobello M., Ooi A. “Global Three-dimensional Flow of a Neutron Superfluid in a Spherical Shell in a Neutron Star”. *Astrophys. J.*, **635**(2):1224–1232, 2005.
DOI: `10.1086/497899`

Peralta C., Melatos A., Giacobello M., Ooi A. “Transitions between Turbulent and Laminar Superfluid Vorticity States in the Outer Core of a Neutron Star”. *Astrophys. J.*, **651**(2):1079–1091, 2006.
DOI: `10.1086/507576`

Piekarewicz J., Fattoyev F.J., Horowitz C.J. “Pulsar Glitches: The Crust may be Enough”, 2014. eprint: `arXiv:1404.2660` .

Pines D., Shaham J., Alpar M.A., Anderson P.W. “Pinned Vorticity in Rotating Superfluids, with Application to Neutron Stars”. *Suppl. Prog. Theor. Phys.*, **69**, 1980.

Pizzochero P.M. “Angular Momentum Transfer in Vela-Like Pulsar Glitches”. *Astrophys. J.*, **743**(1):L20, 2011.
DOI: `10.1088/2041-8205/743/1/L20`

Prix R. “Variational description of multifluid hydrodynamics: Uncharged fluids”. *Phys. Rev. D*, **69**(4), 2004.
DOI: `10.1103/PhysRevD.69.043001`

Ruderman M. “Neutron Starquakes and Pulsar Periods”. *Nature*, **223**(5206):597–598, 1969.
DOI: `10.1038/223597b0`

Ruderman M. “Crust-breaking by neutron superfluids and the VELA pulsar glitches”. *Astrophys. J.*, **203**:213, 1976.
DOI: `10.1086/154069`

Ruderman M., Zhu T., Chen K. “Neutron Star Magnetic Field Evolution, Crust Movement, and Glitches”. *Astrophys. J.*, **492**(1):267–280, 1998.
DOI: `10.1086/305026`

Ruderman M.A., Sutherland P.G. “Rotating Superfluid in Neutron Stars”. *Astrophys. J.*, **190**:137, 1974.
DOI: `10.1086/152857`

Sedrakian A. “Type-I superconductivity and neutron star precession”. *Phys. Rev. D*, **71**(8):8–13, 2005.
DOI: `10.1103/PhysRevD.71.083003`

Sedrakian a., Cordes J.M. “Vortex-interface interactions and generation of glitches in pulsars”. *Mon. Not. R. Astron. Soc.*, **307**(2):365–375, 1999.
DOI: `10.1046/j.1365-8711.1999.02638.x`

Shternin P.S., Yakovlev D.G., Heinke C.O., Ho W.C.G., Patnaude D.J. “Cooling neutron star in the Cassiopeia A supernova remnant: evidence for superfluidity in the core”. *Mon. Not. R. Astron. Soc. Lett.*, **412**(1):L108–L112, 2011.
DOI: `10.1111/j.1745-3933.2011.01015.x`

Sidery T., Alpar M.A. “The effect of quantized magnetic flux lines on the dynamics of superfluid neutron star cores”. *Mon. Not. R. Astron. Soc.*, **400**(4):1859–1867, 2009.
DOI: `10.1111/j.1365-2966.2009.15575.x`

Sidery T., Passamonti A., Andersson N. “The dynamics of pulsar glitches: contrasting phenomenology with numerical evolutions”. *Mon. Not. R. Astron. Soc.*, **1074**:1061–1074, 2010.
DOI: `10.1111/j.1365-2966.2010.16497.x`

Steiner A.W., Gandolfi S., Fattoyev F.J., Newton W.G. “Using Neutron Star Observations to Determine Crust Thicknesses, Moments of Inertia, and Tidal Deformabilities”, 2014. eprint: `arXiv:1403.7546` .

Thompson C., Duncan R.C. “The soft gamma repeaters as very strongly magnetized neutron stars - I. Radiative mechanism for outbursts”. *Mon. Not. R. Astron. Soc.*, **275**:255–300, 1995.
DOI: `10.1093/mnras/275.2.255`

Van Eysden C.A., Melatos A. “Pulsar glitch recovery and the superfluidity coefficients of bulk nuclear matter”. *Mon. Not. R. Astron. Soc.*, **409**(3):1253–1268, 2010.
DOI: `10.1111/j.1365-2966.2010.17387.x`

Warszawski L., Melatos A. “A cellular automaton model of pulsar glitches”. *Mon. Not. R. Astron. Soc.*, **390**(1):175–191, 2008.
DOI: `10.1111/j.1365-2966.2008.13662.x`

Warszawski L., Melatos A. “Gross-Pitaevskii model of pulsar glitches”. *Mon. Not. R. Astron. Soc.*, **415**(2):1611–1630, 2011.
DOI: `10.1111/j.1365-2966.2011.18803.x`

Warszawski L., Melatos A. “Gravitational-wave bursts and stochastic background from superfluid vortex avalanches during pulsar glitches”. *Mon. Not. R. Astron. Soc.*, **423**(3):2058–2074, 2012a.
DOI: `10.1111/j.1365-2966.2012.20977.x`

Warszawski L., Melatos A. “Knock-on processes in superfluid vortex avalanches and pulsar glitch statistics”. *Mon. Not. R. Astron. Soc.*, **428**(3):1911–1926, 2012b.
DOI: `10.1093/mnras/sts108`

Zhou X.R., Schulze H.J., Zhao E.G., Pan F., Draayer J. “Pairing gaps in neutron stars”. *Phys. Rev. C*, **70**(4):2–5, 2004.
DOI: `10.1103/PhysRevC.70.048802`

Zuo W., Li Z.H., Lu G.C., Li J.Q., Scheid W., Lombardo U., Schulze H.J., Shen C.W. “$^1S_0$ proton and neutron superfluidity in β-stable neutron star matter”. *Phys. Lett. B*, **595**(1-4):44–49, 2004.
DOI: `10.1016/j.physletb.2004.05.061`

List of Publications

As of December 2014

Refereed publications

- "The effect of realistic equations of state and general relativity on the 'snow-plough' model for pulsar glitches".
  Seveso S., Pizzochero P.M., Haskell B., *Mon. Not. R. Astron. Soc.*, **427**(2):1089–1101, 2012
  `10.1111/j.1365-2966.2012.21906.x`
  (Chapter 5)

- "Investigating superconductivity in neutron star interiors with glitch models"
  Haskell B., Pizzochero P.M., **Seveso S.**, *Astrophys. J. L.*, **764**(2):L25, 2013
  `10.1088/2041-8205/764/2/L25`
  (Chapter 6)

Publications under review

- "Mesoscopic pinning forces in neutron star crusts"
  Seveso S., Pizzochero P.M., Grill F., Haskell B., submitted to *Mon. Not. R. Astron. Soc.*
  eprint: `arXiv:1408.4298`
  (Chapter 3)

Publications in preparation

- "Mesoscopic pinning forces in neutron star cores"
  Seveso S., Pizzochero P.M., Haskell B., to be submitted to *Mon. Not. R. Astron. Soc.*
  (Chapter 4)

Acknowledgments

This work has been done during the Ph.D. program of “Università degli studi di Milano”, and was partially supported by INFN (Italy) and CompStar, a Research Network Programme of the European Science Foundation.

I would like to express my special thanks to my supervisor Prof. Pierre Pizzochero, for his patience, confidence and the help he has gave me: I’m very grateful that you have given me the opportunity of growing as a researcher. All the ideas in this thesis come from our meetings which have always been very fruitful moments, so again thank you.
I would also like to thank Brynmor Haskell for his comments, suggestions and for his brilliant advises that have been fundamental for my research.

Questi quattro anni di dottorato sono stati intensi, divertenti e molto soddisfacenti; a volte anche un po’ faticosi. Daniela però mi è sempre stata vicina con infinita pazienza mentre la nostra famiglia si è allargata due volte: grazie per aver tenuto duro e per accompagnarmi sempre. Anche Michela è stata molto paziente: questa tesi ha rubato un po’ del “nostro” tempo e so bene di essere in debito.. sono felicissimo adesso di poterla ripagare recuperando dei bei momenti per crescere insieme.
Grazie anche ai miei genitori per il sostegno, a mia sorella Elisa per il lavoro di correzione e a tutti quelli che hanno mostrato interesse per questa ricerca e mi sono stati vicini, è stato un aiuto prezioso.
E infine Eleonora... questa tesi è per te. Chissà se la leggerai mai quando sarai grande. Probabilmente no, ma non è questo il punto... qui ci puoi trovare solo qualche piccola cosa sulle stelle di neutroni, ma l’universo è enorme, ed è tutto lì per te. Buon viaggio!

Grazie. *Stefano*